EXTREME WAVE IMPACTS ON OFFSHORE AND COASTAL STRUCTURES

A Dissertation

by

WEI-LIANG CHUANG

Submitted to the Office of Graduate and Professional Studies of
Texas A&M University
in partial fulfillment of the requirements for the degree of

DOCTOR OF PHILOSOPHY

Chair of Committee,	Kuang-An Chang
Committee Members,	Richard Mercier
	Hamn-Ching Chen
	Achim Stossel
Head of Department,	Robin Autenrieth

December 2017

Major Subject: Civil Engineering

ABSTRACT

This dissertation presents an experimental investigation of three different scenarios on the interaction between extreme waves and offshore/coastal structures: (1) plunging breaking wave impingement on a tension-leg platform (TLP); (2) green water caused by focusing wave and random seas on an offshore platform in a large wave basin; and (3) tsunami bore impact on a coastal building. The bore, green water, or breaking wave is usually multiphase and highly turbulent. To quantify such flows, the bubble image velocimetry (BIV) technique was employed. In addition, the applicability of the BIV technique on moving structures as well as on two perpendicular view planes was validated. The void fraction (air volumetric fraction) in the aerated flows was obtained from the time series of phase transition measured by fiber optic reflectometer (FOR).

The green water occurs when waves overtop marine structures such as ships or offshore platforms. In this study, the green water generated by plunging breaking waves on a TLP in a wave flume and a fixed platform in a large wave basin were investigated. The green water events in random seas were also investigated, and categorization of green water type was made based on the similarity of flow behaviors. The green water velocities were measured, and the corresponding dominant velocities were determined. Furthermore, comparisons between measurements and dam break flow solution were performed. Prediction equations, based on the self-similar green water velocity profile, were obtained.

The variation in impact pressures due to breaking waves is associated with air compressibility, and entrained air bubbles are considered dominant in plunging breaking wave impacts. In this study, pressure, void fraction, and fluid velocity measurements were performed on the vertical wall of a moving structure under a plunging breaking wave impingement. By modeling the plunging breaking wave impact as a filling flow, the correlation of peak pressure and its corresponding void fraction and fluid velocity was examined and compared with an approximation solution. In addition, the portion of compressed air pressure was found proportional to the squared value of void fraction.

For the investigation on tsunami bore impact, a simplified model structure at four different headings on a 1/10 sloping beach was considered. A tsunami wave that can generate high run-up and inland inundation was employed as the input wave condition. Synchronized and repeated measurements of pressure, fluid velocity, and impact pressure were conducted. A comparison of the front velocity and the velocity profile between measurement and dam break flow solution was made. Furthermore, the measured and calculated time histories of surge force were compared.

DEDICATION

With Love and Respect,
To My Family Members: Father, Mother, Wife and Sister.

ACKNOWLEDGEMENTS

I would like to express my deepest and sincere gratitude to my dissertation advisor, Dr. Kuang-An Chang, for his advice, encouragement, enlightening guidance, and continuous support at all times.

I also would like to thank Dr. Richard Mercier, Dr. Hamn-Ching Chen and Dr. Achim Stossel for serving as committee members and for their profound and carefully aimed comments and suggestions to the course of this research. Special thanks are extended to Dr. Richard Mericer for his help, patience, valuable advice, and enlightening insight.

I wish to thank John Reed, Dr. Binbin Wang, Dr. Vadoud Dehkharghanian, Dr. Chris Lai while working in the Ocean Engineering Lab, and thank Dr. Youn Kyung Song for the aid in my initial understanding of laboratory methods. I would like to express my special thanks to Dr. Yunta Wu, Dr. Byoungjoon Na, Dr. Zhi-Cheng Huang, and Dr. Wen-Yang Hsu for their help and friendship.

Thanks also go to the staff at Offshore Technology Research Center, the staff in Tainan Hydraulics Laboratory at National Cheng Kung University, and the staff in Hinsdale Wave Research Laboratory at Oregon State University for their technical support and friendly aid.

I would like also thank the TAMU Taiwanese Student Association (TSA) and the TAMU TSA Softball team for making my time in College Station more varied.

I would like to extend my deepest gratitude to my father, mother, and sister for their unfailing support from overseas. Lastly, a special gratitude and love goes to my beloved wife for her love, patience, understanding, encouragement, kind support, and amazing culinary skill for making this work interesting and a success.

CONTRIBUTORS AND FUNDING SOURCES

Contributors

This work was supervised by a dissertation committee consisting of Dr. Kuang-An Chang (chair), Dr. Richard Mercier, and Dr. Hamn-Ching Chen of the Department of Civil Engineering, and Dr. Achim Stossel of the Department of Oceanography.

All work conducted for the dissertation was completed by the student independently.

Funding sources

Chapters 2, 3, and 4 were made possible by the research project funded by the Industry Consortium with a title "Implementation of Bubble Image Velocimetry in OTRC Wave Basin." Chapter 5 was made possible by the research project funded by the Texas A&M Engineering Program with a title "Building Capacities to Withstand Extreme Coastal Wave Forces."

TABLE OF CONTENTS

Page

LIST OF FIGURES

LIST OF TABLES

Page

CHAPTER I

INTRODUCTION

1.1 Flow characteristics of extreme waves interacting with marine structures

Extreme waves, such as tsunami, rogue wave, greatly threaten ships, offshore platforms, costal defense systems, and residential/commercial buildings. To offshore structures, in certain scenario, such as rough sea or hurricane, large waves may be high or strong enough (large momentum) to overtop a deck surface and create so-called green water, posting tremendous risking to the safety of the crew, the integrity of the structure, and the performance of the equipment. Green water often entrains air bubbles, and its flow behavior is highly turbulent. To coastal structures, tsunami wave is probably the most destructive wave. Tsunami is usually generated as a subsequence of geophysical forces (e.g., earthquake, submarine landslide, and volcanic eruption) or astronomical conditions (e.g., meteorite impact). Tsunami wave may break at near shore or inland and continue to propagate inland in a form of run-up or bore. Similar to green water, bore is highly aerated and turbulent. Such highly turbulent nature and discontinuous free surface of green water and bore flows hinder the progress of laboratory measurement. To quantify such complicated flows, Ryu et al. (2005) introduced the bubble image velocimetry (BIV) technique on the basis of the sophisticated particle image velocimetry (PIV). To date, several studies (e.g., Ryu et al. 2007a; Chang et al. 2011; Lin et al. 2012; Song et al. 2013) have successfully performed the application and robustness of the BIV technique on the aerated flows, such as sloshing, hydraulic jumps, breaking waves interacting with fixed 2-D or 3-D structures. With more and more ships and movable offshore platforms populated in the ocean, it is desired if the BIV technique can be applied to moving structures. If success is achieved, the BIV technique can not only provide valuable inputs for designs, but also advance the development of numerical modeling.

1.2 Wave impact pressure and role of compressed air

Evaluating the wave impact pressures caused by an extreme wave event is of great importance in designing or re-designing coastal and offshore structures. Over the years, the understanding of impact pressure caused by non-breaking waves has been well developed and incorporated into design process. However, with the challenge of turbulent and multiphase nature in either numerical modeling or laboratory measurement, the knowledge has been improved by numerous studies across the last eight decades, but the cause and the detailed mechanism of tremendous peak pressures due to breaking waves still remain inconclusive. Among them, Bagnold (1939) is probably the pioneer who conducted systematic laboratory investigation on breaking wave impact pressures. Some of the main conclusions and referenced literature related to breaking wave impacts are as follows:

a) The wave impact pressure greatly depends on the location of the impingement point relative to the structure (Ochi and Tsai 1984; Chan and Melville 1988; Hattori et al. 1994; Ariyarathne et al. 2012).
b) The wave impact pressure is deeply associated with the shape of incipient wave upon collision with the structure (Hattori et al. 1994; Hull and Muller 2002; Peregrine 2003; Bullock et al. 2007).
c) The wave impact peak pressure varies considerably even with an identical wave condition considered in the measurement (Hattori et al. 1994; Hull and Muller 2002; Peregrine 2003; Bullock et al. 2007).

Although the mechanisms have not yet been completely unveiled, it has generally been accepted that air entrapment increases the magnitude and variation of impact pressure maxima, while entrained air bubbles act as a cushion sandwiched by fluid and solid boundary and reduces the pressure magnitude (Peregrine 2003). In addition, 3-D, turbulent, and aerated flows with high nonlinearity leads to the lack of measured data set for advancing the development of numerical modeling and theoretical works. In particular, the knowledge of air volumetric fraction or void fraction is crucial to assess the fluid density variation, which is associated with the flow properties such as mass, momentum, and energy. Most studies ignored the variation in fluid density because of the difficulty in measuring void fraction. Nevertheless, there exist a few measurements of void fraction on breaking waves (e.g., Cox and Shin 2003; Blenkinsopp and Chaplin 2007), and very limited void fraction measurements on breaking waves interacting with structures (Chang et al. 2012; Song et al. 2015).

1.3 Scope of this dissertation

The present study presents a thorough experimental investigation of extreme waves interacting with coastal/offshore structures based on three different scenarios: (1) breaking wave impingement on a tension-leg platform; (2) green water caused by focusing breaking wave and random seas on an offshore platform in a large wave basin; and (3) tsunami bore impact on a coastal building.

In CHAPTER II, the attention is mainly drawn to the implementation of the BIV technique on a tension-leg platform (TLP) model in a laboratory wave flume and the investigation of the fluid kinematics. Fluid velocities and structure translation were measured simultaneously. The fluid velocities on two perpendicular view planes – side view and top view – were revealed and further analyzed to evaluate the turbulence intensity, verify the self-similarity, and compare with dam break flow solution. In addition, comparisons with the works done by similar input wave conditions on a 2-D (Ryu et al. 2007a, b) and a 3-D (Chang et al. 2011) fixed structures will be presented.

In CHAPTER III, as a continuous work of CHAPTER II, an experiment with simultaneous pressure, void fraction measured by fiber optic reflectometer (FOR), fluid velocity, wave elevation and structure motion measurements under the same test condition was performed. This part of the study is focused on the fluid dynamics and processes of plunging breaking wave impacts on the frontal vertical wall of a TLP model. The correlation between impact peak pressure, fluid velocity, void fraction, pressure rise time, and impingement location will be presented and discussed. Various approaches were used to obtain impact coefficients. In addition, the effect of air compressibility was examined by modeling the plunging breaking impact as a filling flow.

In CHAPTER IV, the green water on a fixed offshore platform in a large wave basin under focusing waves and random waves was experimentally studied. Two events, wall impingement event and deck impingement event, were generated by a focusing wave train. Simultaneous measurements of pressure, void fraction, fluid velocity, and wave elevation were carried out. The correlation between impact peak pressure, fluid velocity, void fraction, and pressure rise time will be shown and discussed. For random waves, the green water velocity was investigated. The random green water events were categorized into three groups according to the similarity of flow behaviors. The self-similarity of green water velocity profiles was examined and a prediction formula was obtained. Furthermore, modeling the random green water events as dam break flow will be presented.

In CHAPTER V, an experimental modeling of a tsunami bore impinging a costal building fixed on a sloping beach was performed. Four different headings were tested with identical wave condition. Pressure, fluid velocity, forces and motions were simultaneously measured. The spatial and temporal distributions of fluid velocity, turbulence intensity, impact pressure, and surge force for different headings will be demonstrated. Modeling the tsunami wave run-up as a dam break flow will be shown. The validity of Bernoulli equation in estimating impact peak pressure will be discussed. In addition, the comparison of measured and calculated surge forces will be exhibited.

Finally, the summary of this dissertation will be drawn in CHAPTER VI, and the recommendation for future works will be stated.

CHAPTER II

GREEN WATER VELOCITY DUE TO BREAKING WAVE IMPINGEMENT ON A TENSION LEG PLATFORM[*]

2.1 Introduction

Extreme waves have the potential to create violent impingement on offshore structures followed by adverse consequences such as green water runup and overtopping. Wave impingement can exert huge impact forces on structures and cause extensive damage and failure. Green water may appear when the approaching wave height exceeds the freeboard of the structure or the wave momentum is strong enough to push the water onto the structure deck. Green water has been a great concern to the safety of personnel, integrity of structures, and operation of equipment. With an increased number of permanently moored offshore structures being built and operating in the ocean while hurricanes potentially become more severe and frequent, the improved understanding of green water flow is essential to engineers.

For decades the green water flow has been numerically and experimentally investigated. Buchner (1995) experimentally investigated the green water effect on a model floating, production, storage, and offloading (FPSO) vessel in a laboratory. Hamoudi and Varyani (1998) studied the probability of green water occurrence as a function of Froude number and significant wave height by performing laboratory tests. Schoenberg & Rainey (2002) developed a potential flow-based boundary integral equation method to calculate the green water velocities on the deck of a vertically submerging shelf. Nielsen and Mayler (2004) employed a Navier-Stokes solver with the volume of fluid (VOF) approach to reconstruct and describe the free surface. They modeled a 2D fixed vessel, predicted the green water level in head seas, and found good agreement with the

---

[*] Content reported in this chapter is reprinted with permission from “Green water velocity due to breaking wave impingement on a tension leg platform” by Chuang et al. (2015). *Experiments in Fluids*, DOI: 10.1007/s00348-015-2010-y, Copyright [2015] Springer.

data from Buchner (1995). In their extension to 3D simulations, including vessel motion, they concluded that 3D effects were insignificant.

Buchner (1995) reported that the green water flow may be treated as a dam-break problem based on the qualitative observation that green water behaves similar to a bore. Industry has been using dam-break solutions for flow velocities in structural design and analysis of green water incidents (Schoenberg and Rainey 2002). However, the similarity between green water and dam-break flows had not been quantitatively verified until Ryu et al. (2007b). Ryu et al. employed the well-known, simple analytical solution of dam-break flow from Ritter (1892) to compare with their measured green water velocities obtained by using an image-based velocimetry technique. In their work, two approaches were introduced in an attempt to match the initial water depth required in Ritter's solution. Comparisons indicated that Ritter's solution describes the overall distribution of green water velocity surprisingly well in spite of neglecting the complex nature of the green water flow.

The multiphase, highly turbulent, and violent green water slowed the progress in laboratory measurements and made numerical modeling very challenging. To tackle the measurement of bubbly flow in the laboratory, an image-based technique called bubble image velocimetry (BIV) was introduced by Ryu et al. (2005) for velocity determination. BIV was derived from the principle of particle image velocimetry (PIV). BIV uses laser-emitting diode (LED) or equivalent for backlighting and generating shadow images from bubbles or droplets as tracers and, unlike traditional PIV, requires no lasers for illumination. Flow velocities are then determined by correlating textures in the images formed by the shadows of air-water interfaces. BIV has been successfully employed to perform velocity measurements in highly aerated flows, such as green water flows on a 2D structure (Ryu et al. 2005, 2007a, 2007b) and on a 3D structure (Chang et al. 2011; Ariyarathne et al. 2012), wave breaking on a sloping beach (Pedrozo-Acuña et al. 2011; Rivillas-Ospina 2012), aerated open channel flows and hydraulic jumps (Lin et al. 2008, 2012), and liquid sloshing (Song et al. 2013). Even though the BIV measurement technique has mostly been applied on small-scale models in laboratories, Song et al.

(2015) recently extended its application to model tests in a large-scale wave basin to investigate the green water surface velocity on a fixed deck structure. Applications using the BIV technique on a moving model structure have not yet been explored to date.

The present study implements the BIV technique on a simplified model TLP in a laboratory wave flume to simultaneously measure the full-field bubbly water velocity and the structure velocity. The objectives are: (1) to investigate the flow behavior and kinematics of a breaking wave impingement on a floating structure in an earth-fixed frame of reference (termed *global* coordinates hereafter); (2) to examine the green water flow kinematics in a platform-fixed frame of reference (termed *body-fixed* coordinates); (3) to evaluate the turbulence intensity; (4) to verify flow self-similarity and obtain the prediction equation of green water velocity; (5) to validate the dam-break prediction model through comparisons with Ritter's solution. In addition, measurements from the present study are also compared to those on a 2D (Ryu et al. 2007a, b) and a 3D (Chang et al. 2011) fixed structure with a similar model layout and a nearly identical wave condition. Two BIV measurement sets were carried out on two perpendicular measurement planes: side view (vertical measurement plane) and top view (horizontal measurement plane). The ensemble averaging method was applied using 30 repeated tests to obtain the mean flow fields and calculate the turbulence intensity distribution.

2.2 Experimental setup

2.2.1 Model and coordinate system

The experiment was carried out in a glass-walled wave tank located at the Zachry Department of Civil Engineering at Texas A&M University. This tank has a dimension of 36 m in length, 0.9 m in width, and 1.5 m in depth. The tank is equipped with a dry-back flap-type wavemaker at one end and a 1:5.5 sloping beach covered with a layer of horse hair at the other end to serve as a wave energy absorber and reflection reducer. The still water depth was kept at d = 0.80 m throughout the experiment.

The TLP model is a watertight, rectangular box-like structure with dimensions of 0.37 m in length, 0.85 m in width, and 0.31 m in height, built with Plexiglas of 9.53 mm (3/8") in thickness. The model was moored to the tank floor by a 1.6 mm (1/16") diameter wire rope tendon at each corner of the structure bottom with eyebolts on both ends of each wire rope. Buoyancy pre-tensioned the wire rope tendons; the model structure floated in water with a draft of 0.20 m. The model structure and mooring system were designed to mimic a geometry-simplified tension leg offshore platform. See Fig. 2.1(a) and 1.1(b) for the sketch and detailed dimensions and 1.1(c) for the photo of the model and setup. The coordinate system is also shown in Fig. 2.1(a) with x being the wave-propagating direction, y the cross tank direction, and z the vertically upward direction. The origin of the body-fixed coordinates (x_B, y_B, z_B) = (0, 0, 0) is set at the leading edge, 0.1 m from the front glass wall, and on the deck surface of the structure. The origin of the global coordinates (x_G, y_G, z_G) is referenced to (x_B, y_B, z_B) = (0, 0, 0) at the resting position. Note that the still water level is at z_G = -0.11 m. To be consistent with Ryu et al. (2007a) and Chang et al. (2011), the time t = 0 is defined as the moment when the green water wave front crosses the structure leading edge at x_B = 0.

The physical model described above is intended to simulate a simplified TLP with a 1:169 scale ratio on the basis of the Froude scaling. The mass of the model structure is 17 kg and the buoyancy is equivalent to 97.5 kg. The frontal vertical wall of the model is located 21.7 m from the wavemaker. There exists a 25-mm gap between the structure and each glass side wall so the structure can move freely without in contact with the tank walls. By examining the movies captured by a high speed camera from both side view and top view, the structure has major motion in surge (x-axis), minor motion in heave (y-axis), and negligible motions in the other four rigid body degrees of freedom.

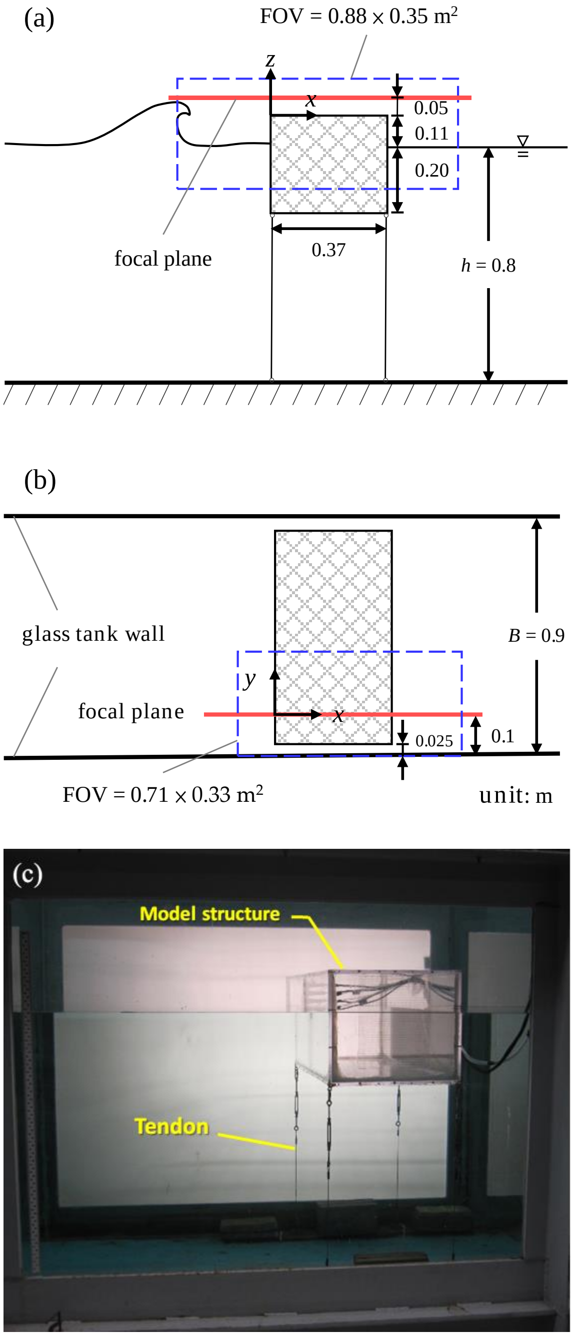

Figure 2.1 Diagrams and dimensions of the model setup for (a) side view measurement and (b) top view measurement. (c) Photo of model setup in the wave tank. The coordinate system and the BIV focal planes and FOVs are also shown in the figure.

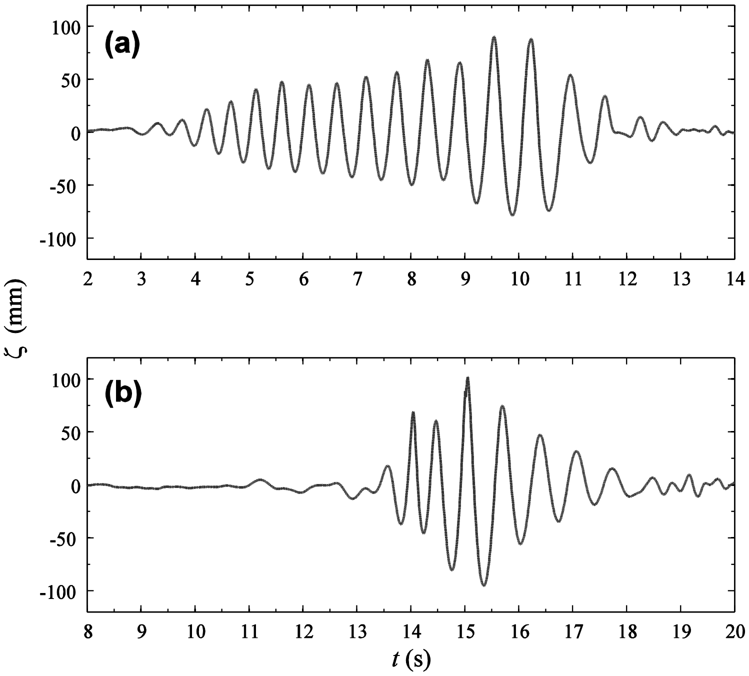

Figure 2.2 Free surface elevations measured at (a) 5.1 m (x_G = -16.6 m) and (b) 17.7 m (x_G = -4 m) from the wavemaker.

2.2.2 Wave condition

The present study focuses on the scenario of a plunging breaking wave impinging on the frontal wall of a marine structure near the still water level, equivalent to the wave condition in Ryu et al. (2007a) and the *wall impingement* case denoted by Chang et al. (2011). Plunging breakers were generated using the wave focusing method (Davis and Zarnick 1964; Perlin et al. 1996; Ryu et al. 2005, 2007a). The wave train, as shown in Fig. 2.2(a), consists of various frequencies ranging from 0.7 to 1.3 Hz. The waves are nearly identical to that used in Ryu et al. (2007a) and Chang et al. (2011). The free surface elevations shown in Fig. 2.2 were measured using double-wired resistance-type wave gauges located at 5 m (x_G = -16.5 m) and 17.7 m (x_G = -4 m) from the wavemaker. The primary wave that leads to the only breaking event is the wave with the largest amplitude in the wave train. The wave height (H), period (T), and phase speed (C) of the primary wave are H = 0.17 m (equivalent to 28.7 m in prototype on the basis of 1:169 Froude scaling), T = 1.32 s (17.2 s in prototype), and C = 2.05 m/s (26.7 m/s or 96 km/hr in prototype) respectively. The zero up-crossing method was applied to the wave gauge data at x_G = -16.5 m to determine the wave period and wave height of the primary wave. The phase speed was calculated based on the linear dispersion relationship. At a scale ratio of 1:169, the primary wave approximates the scaled-down wave condition of the measured maximum wave height during Hurricane Ivan reported by Wang et al. (2005).

The impinging point of the breaking waves, defined as the location where the tongue of the overturning wave touched its front wave surface, was adjusted by fine tuning the period of the wave train on an order of μs to make it close to the structure vertical wall. By inspecting the images at a framing rate of 1000 frames per second (fps), the impinging points distributed within a 50-mm range in front of the structure vertical wall.

2.2.3 Velocity measurement

Breaking wave impingement on a structure often results in a highly turbulent and aerated flow. The BIV technique introduced by Ryu et al. (2005) was employed to quantify the flow. The principle of BIV is to combine PIV and the shadowgraphy technique with a controlled narrow depth of field (DOF) for image acquisition. It then correlates shadow textures generated by air-water interfaces (i.e., bubbles and water droplets) in the images for velocity determination. The BIV technique does not require the use of a laser light sheet. For the side view measurements, a thin, translucent acrylic sheet was placed on the rear glass wall of the wave tank. The sheet was illuminated from behind by 600 W light bulbs to mimic the backlit effect of light emitting diode (LED). Similarly, for the top view measurements, a thin, white plastic sheet was fixed at the tank bottom. A bright background designated for the down-looking camera was created by projecting light onto the plastic sheet from the same light bulbs through the side walls in an inclined angle. Note that the model structure is transparent so the overtopping green water can be illuminated from the bright tank bottom. A high-speed camera (Vision Research, Phantom M340) mounted with a Nikon 50-mm f/1.4 focal lens was used to capture images. The camera has a maximum framing rate of 800 fps at a 2560 × 1600 pixel full resolution and 12-bit dynamic range.

The DOF, controlled by adjusting the camera aperture and the distance (ℓ) from the camera lens to the measurement plane, was carefully adjusted to make it narrow enough so displacements in the images can be translated to velocity with a reasonable error caused by this narrow DOF. According to Ray (2002), the DOF was calculated as $D = S - R$, where S is the farthest limit $S = \ell f_c^2 \big/ \left(f_c^2 - N\ell C_c \right)$ and R is the nearest limit $R = \ell f_c^2 \big/ \left(f_c^2 + N\ell C_c \right)$. In the present study, the focal length of the camera focal lens is $f_c = 50 \text{ mm}$, the circle of confusion is $C_c = 0.0175 \text{ mm}$, and the *f*-number of the camera lens aperture gives $N = 1.4$. Objects within the DOF appear sharp, whereas objects outside the DOF are blurred. Ryu et al. (2005) reported that blurred images make insignificant contribution in comparison to sharp images in the cross-correlation process for velocity determination. In other words, sharp images have greater weight in the correlation process than blurred ones. The error caused by the limited depth in BIV can be estimated as $\varepsilon = D / 2\ell$, implying the uncertainty increases with a wider DOF from the use of a greater *f*-number or a shorter lens-to-focal-plane distance.

Table 2.1 Summary of image recording setup for the two measurement planes. The camera framing rate was fixed at 1000 fps.

Measurement Plane	Resolution (pixels)	FOV size (mm^2)	Spatial Resolution (mm^2)	D (mm)	ℓ (m)	ε (%)
Side view	2560 × 1000	883 × 345	5.5 × 5.5	68	1.86	1.8
Top view	2560 × 1200	711× 333	4.4 × 4.4	99	1.33	3.7

As shown in Fig. 2.1, the velocity measurements were performed on two perpendicular planes – the side view *x*-*z* plane and the top view *x*-*y* plane – and measurements on each plane were conducted independently. The side view plane is centered at 0.1 m behind the front glass wall and the top view plane at 0.05 m above the model deck surface. The errors caused by the limited DOF were estimated as 1.8 % and

3.7 %, respectively. The camera resolution, FOV, spatial resolution, DOF (D), ℓ, and ε as well as the framing rate for both measurement planes are listed in Table 2.1. More details on the principles, validation, and discussion regarding the BIV technique can be found in Ryu et al. (2005), Chang et al. (2011), Lin et al. (2012), and Song et al. (2013).

Based on the measurements in Ryu et al. (2007a) and Chang et al. (2011) and the observed maximum velocity in the present study, the framing rate in the BIV measurements was set at 1000 fps throughout the experiment. Commercial software from LaVision Inc. (DaVis 8) and MPIV developed by Mori and Chang (2003) was employed to process the images for velocity determination, post process the velocity maps by removing spurious vectors with a median filter, and fill the removed vectors using Kriging interpolation. An adaptive multi-pass algorithm was adopted in the cross-correlation process, beginning from an interrogation window size of 64 × 64 pixels and ending with a window size of 16 × 16 pixels with a 50% overlap between adjacent windows. That is equivalent to a 5.5 × 5.5 mm^2 and 4.4 × 4.4 mm^2 spatial resolution for the side view plane and top view plane velocity measurements, respectively.

For each measurement plane, the BIV measurements were repeated 30 times with the same initial and boundary conditions. The ensemble-average method was then used to calculate the mean velocities based on the 30 repeated instantaneous BIV measurements, i.e.

$$U_i = \frac{1}{N}\sum_{j=1}^{N} u_i^j \qquad (2\text{-}1)$$

where U_i is the i-component mean velocity, u_i^j is the i-component instantaneous velocity of the j^{th} repeated measurement, and N is the total number of repeated tests ($N = 30$ in the present study). Regarding the proper choice of N, Chang and Liu (1999) suggested that $N \geq 16$ is required for the measurement of mean velocity in breaking wave studies. By reviewing the BIV measurements reported by Ryu et al. (2007a) and Chang et al. (2011), $N = 30$ seems to be adequate and was thus selected in the present study. Since two coordinate systems were used in the study, hereafter the physical quantities referring to the body-fixed coordinates will be denoted with the subscript B, e.g., (U_B, V_B, W_B), while those referring to the global coordinates will be denoted with the subscript *G*, e.g., (U_G, V_G, W_G).

In the ensemble-averaging process the instantaneous velocity was decomposed into the mean velocity (U_i) and turbulent fluctuation (u_i'), i.e. $u_i = U_i + u_i'$. Since only two velocity components were measured at a time on each measurement plane, the turbulence intensity for each plane is defined as

$$I_{side} = \langle u'u' + w'w' \rangle^{1/2} \qquad \text{for side view plane} \qquad (2\text{-}2)$$

$$I_{top} = \langle u'u' + v'v' \rangle^{1/2} \qquad \text{for top view plane} \qquad (2\text{-}3)$$

A low pass filter was subsequently applied to filter out any sudden changes of the turbulence intensity map.

2.3 Green water velocity and structure motion

2.3.1 Wave impingement and runup

The evolution of the green water flow caused by breaking wave impingement on the model structure can be categorized into three sequential phases: (1) *wave impingement*; (2) *runup of splashing jet*; and (3) *overtopping green water*. The flow kinematics of the first two phases are firstly demonstrated. Figure 2.3 shows the mean flow fields and turbulence intensity for the plunging breaker impingement on the model structure. In the figure, four subplots are included at each moment of interest: mean velocity vectors (*left column*) and turbulence intensity contour normalized by *C* (*right column*) for the side view measurement (*top row*) and the top view measurement (*bottom row*). The global coordinate system is referenced here. In the BIV measurements, only vectors in the aerated region can be determined due to the existence of bubbles. Since it is difficult to acquire a large number of samples to accurately determine the flow turbulence in such a transient flow, the turbulence intensity contour is thus embedded with a high uncertainty. Nevertheless, it at least provides an order-of-magnitude estimate for the turbulence level. In the figure, the ensemble-averaged mean images are blurry so instantaneous images were arbitrarily selected to superimpose with the vectors and contour plots. This results in slight mismatches between the images and the vectors at some instants.

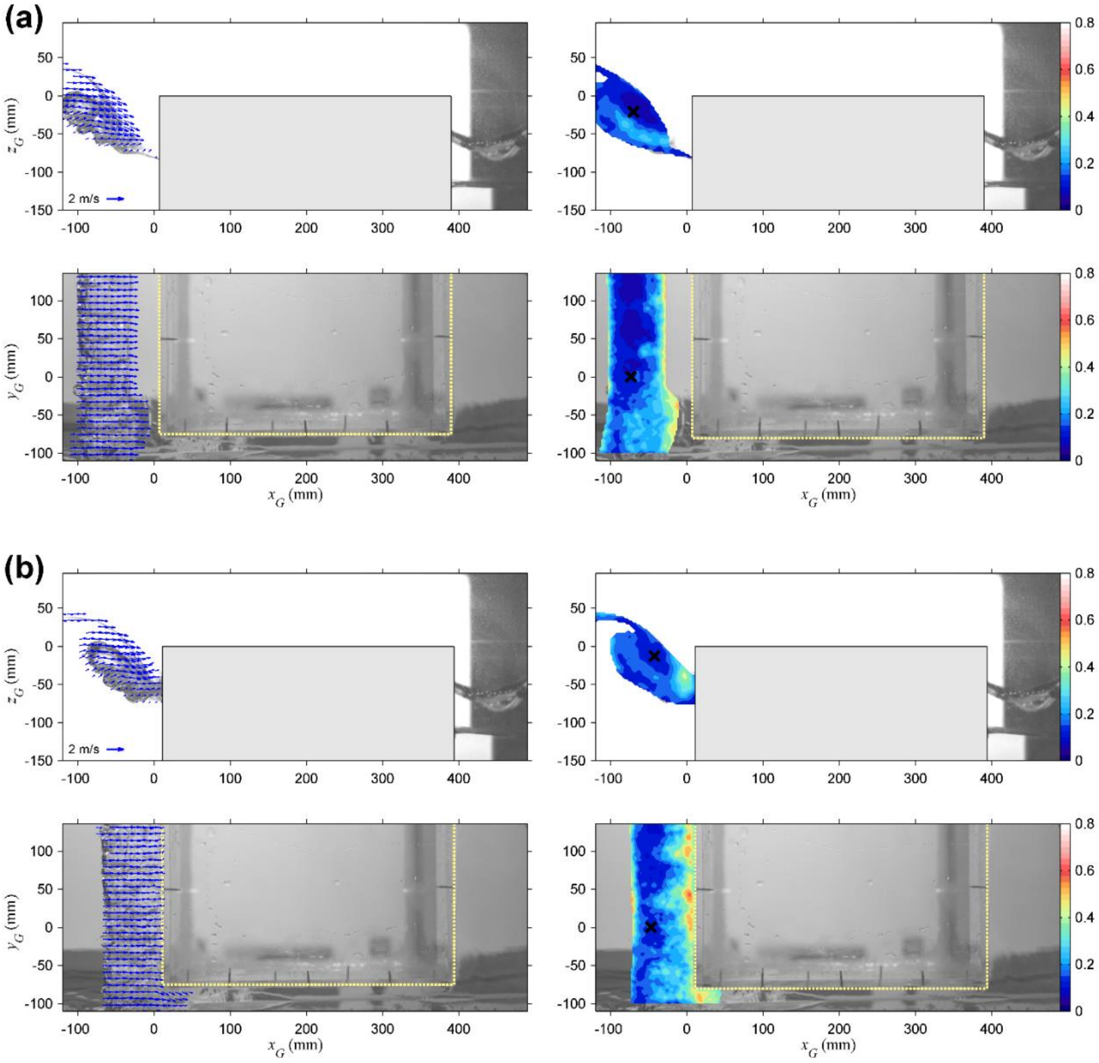

Figure 2.3 Mean velocity field and turbulence intensity at **a** t = -0.04 s, **b** t = -0.02 s, **c** t = 0.00 s, **d** t = 0.01 s, **e** t = 0.05 s, **f** t = 0.12 s, **g** t = 0.17 s, **h** t = 0.22 s. *Top row*: side view measurement; *bottom row*: top view measurement; *left column*: velocity vectors; *right column*: turbulence intensity contours (normalized by C). “ x ” indicates the location

of maximum velocity on $y_G = 0$. Note that the images and data are referenced to the global coordinate system.

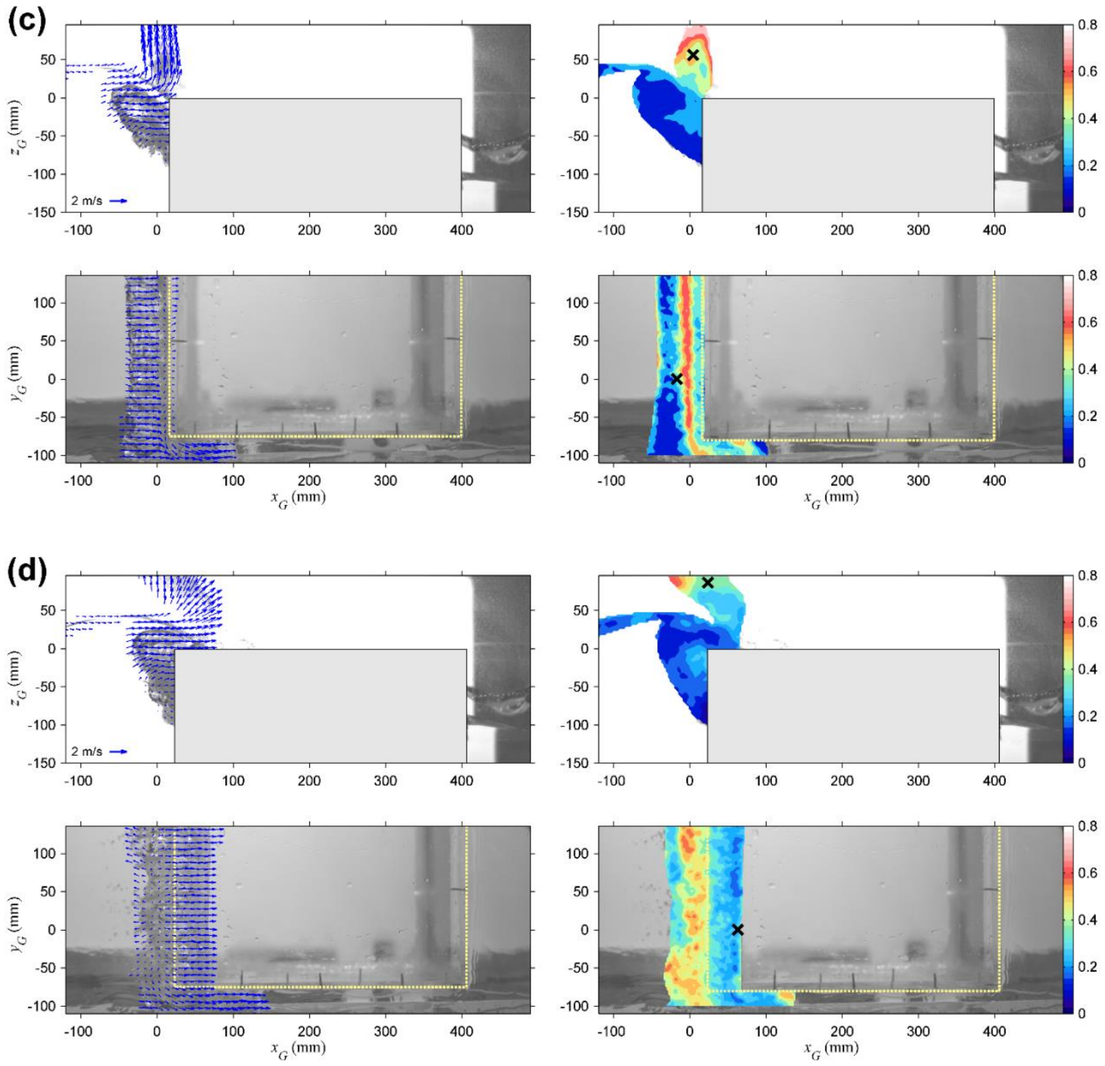

Figure 2.3 Continued

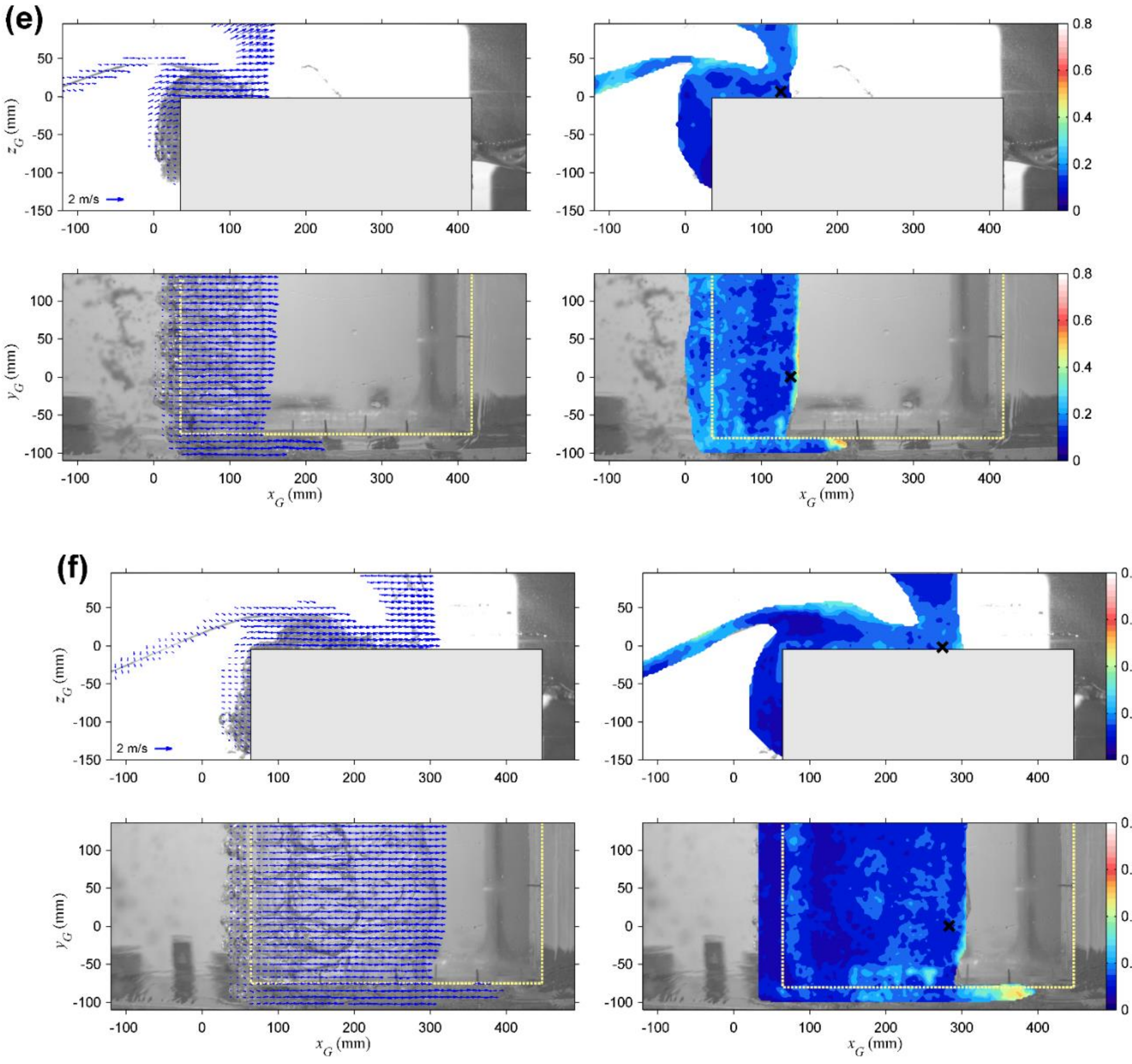

Figure 2.3 Continued

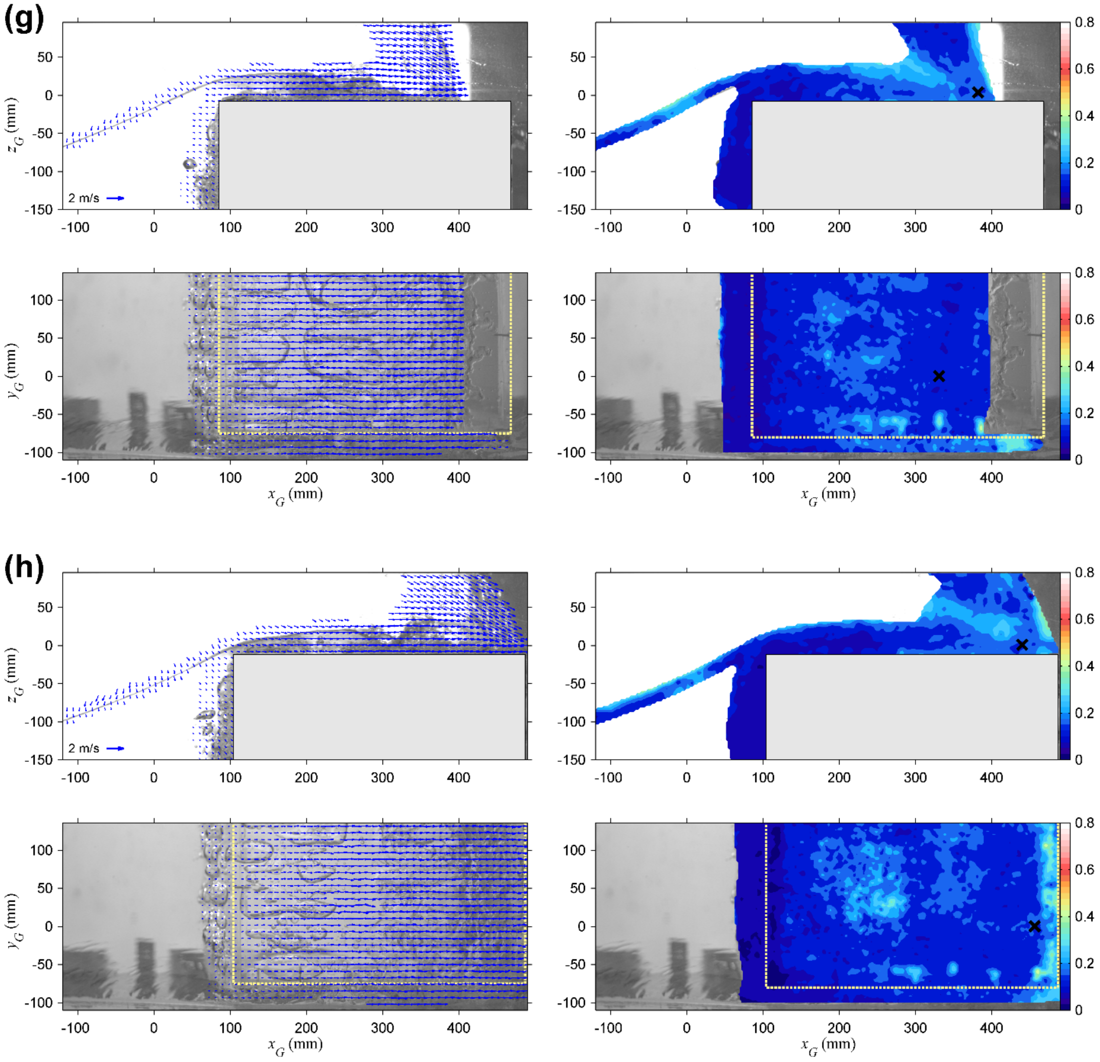

Figure 2.3 Continued

The mean velocity and turbulence intensity fields are shown in Fig. 2.3, while the horizontal velocity contours at certain instances are shown in Fig. 2.4. Figure 2.3(a) shows the moment the tongue of the overturning breaking wave impinged on the frontal water surface and the vertical wall of the model structure. As seen from the top view measurements, both the breaking wave front and the U velocity are uniformly distributed along the y axis except near the gap region between the structure and the glass wall of the wave flume. The FOV in the top view measurements was deliberately set to cover the gap region so the boundary or gap effect can be clearly seen. The boundary effect led to a slightly earlier wave breaking near the wall than that away from the wall. The corresponding U velocity contours, plotted in Fig. 2.4(a), shows that the reduction in velocity magnitude and fluctuation near the wall boundary due to the wall effect is apparent, but the effect does not influence the plane of interest, i.e. the plane at $y_G = 0$ (or 0.1 m away from the wall). Furthermore, the contours reveal that the maximum U velocity resides at the middle of the overturning wave. The corresponding turbulence intensity contour indicates that relatively strong velocity fluctuations appeared inside the overturning roller and at the wave front. In addition, the location of the structure front wall was no longer at $x_G = 0$, indicating the model structure was moving downstream (in the positive x_G direction).

The flow in Fig. 2.3(a), referred as the impinging phase, was horizontally dominated with a maximum velocity of $U_G = 1.14C$ which is lower than the maximum velocity of $1.5C$ observed on a fixed structure in Ryu et al. (2007a). Because of structure motion, these two values were not expected to be identical. Having that said, if the maximum U_G value is evaluated by averaging the 30 instantaneous maximum horizontal velocities over the 30 repeated runs, then the $U_G = 1.4C$ will be obtained and this value becomes consistent with that in Ryu et al (2007a). An interesting question is then raised: what caused the reduction in maximum U_G at the wave impingement phase in the present study? As mentioned earlier, the impinging points were distributed within a 50-mm range in front of the frontal wall of the structure. That implies the maximum horizontal velocities may not occur at the same moment and location but with a slight difference among the 30 repeated runs. By examining the videos, the structure motion was found also varied slightly over the 30 repeated runs. Such small variations may be caused by the nature of turbulence. These two factors (i.e., the slight variation in impinging point and structure motion) combined can introduce spatial variation that causes slight phase difference which in turn reduces the magnitude of the averaged maximum velocity in the ensemble-averaging process. In addition, in spite of the use of identical incoming waves, possible effects such as wave instability and imperfect mechanical control of the wavemaker could also lead to a slight spatial variation of the wave impinging point. Notice that a moving structure is employed in the present study. The structure motion somewhat acts like a passive wavemaker in response to the incoming wave train. This exercise will introduce wave radiation which the breaking waves are very sensitive to. Therefore, the structure motion is considered as the major contributing factor for the reduction of U_G in comparison to that value on the fixed structure in Ryu et al. (2007a). It should be pointed out that the definition of $t = 0$ makes the average-out effect much less significant in the green water flow after the impinging phase

Shortly after the instant shown in Fig. 2.3(a), the breaking wave front slammed on the structure vertical wall and started to rush upward, as shown in Fig. 2.3(b). Based on the video images, a lot of water droplets and a few air bubbles splashed upward by the impingement right in front of the vertical wall. According to the top view measurements, the concentration of higher turbulence intensity appeared at the wave front, with the magnitude reaching about 0.5C. In addition, the effect of the gap (around y_G = -100 mm) can be observed from the larger V_G velocities in Figs. 2.3(b), (c) and Fig. 2.4(d), showing that water in the vicinity was deflected and entering the gap. At $t = 0$, corresponding to the moment in Fig. 2.3(c) and Fig. 2.4(b), the strong, upward splashing jet reached a maximum mean vertical velocity of 2.8C. This maximum velocity is consistent with the magnitude of 2.9C reported by Ryu et al. (2007a) on a fixed structure. If scaled up, this up-rushing water mass would reach a speed of 269 km/h or 167 mph. Such a high speed could pose a tremendous risk if there is a protruding structure or equipment from the vertical surface on an offshore platform. It should be pointed out that the translating motion of the structure (to be discussed later) plays a relatively minor role in comparison to the fluid velocities at this initial impingement stage. Nevertheless, impact pressures caused by the green water flow are proportional to the square of the relative horizontal fluid velocity, based on the dimensional argument supported by Ariyarathne et al. (2012) and Song et al. (2013), and are of great concern to industrial practice. Consideration of structure translation may be necessary in order to accurately determine the relative fluid velocity for dynamic pressure estimation.

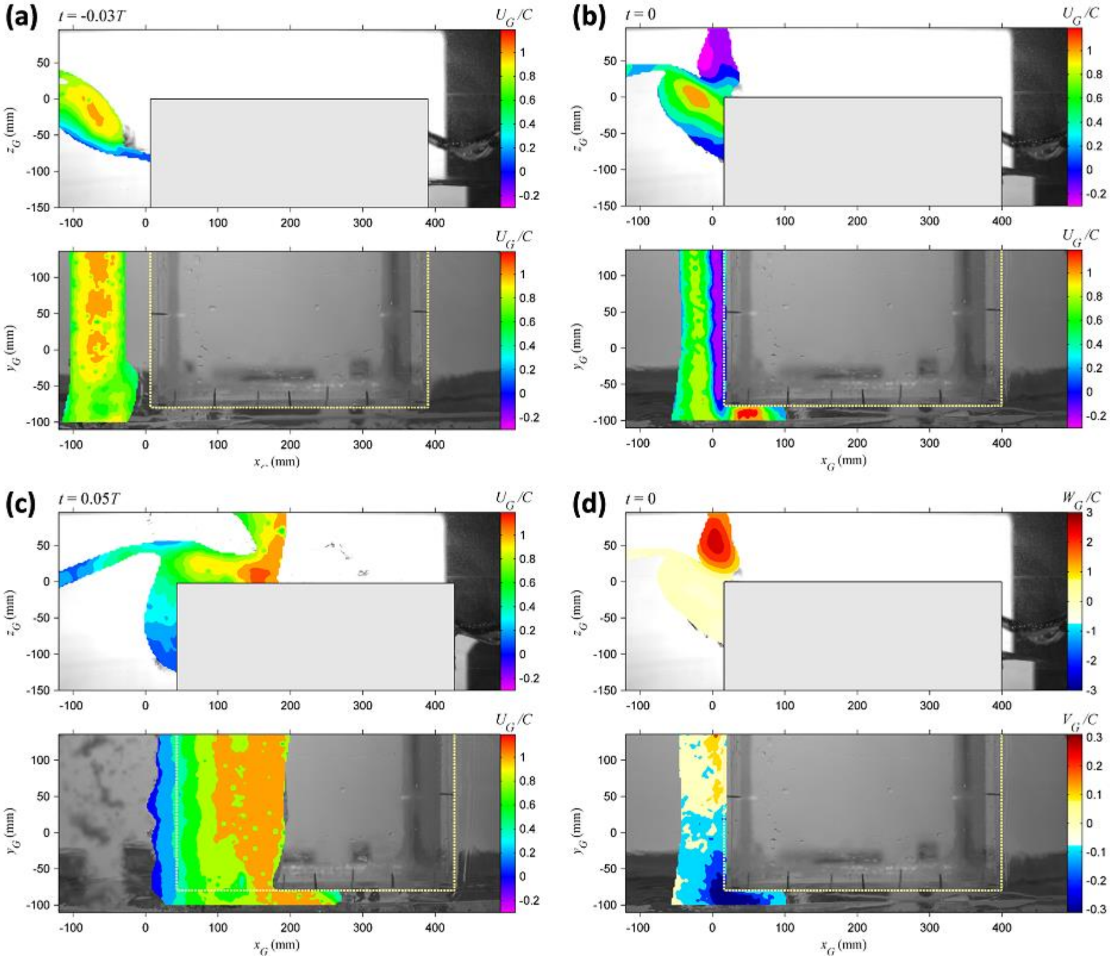

Figure 2.4 Normalized U_G velocity contours (by C) at t = (a) -0.03T, (b) 0, and (c) 0.05T. (d) The normalized W_G velocity contour (*top*) and V_G velocity contour (*bottom*) at t = 0.

It is interesting to point out that the up-rushing jet features negative U velocities at $t = 0$, as shown in Fig. 2.3(c) and Fig. 2.4(b). Before $t = 0$, the maximum structure velocity is merely $0.08C$, much less than the water particle velocities (up to $1.4C$). The water seems to be bounced back following the impact on the vertical wall, causing the negative U velocities in Fig. 2.4(b).

2.3.2 Overtopping green water flow

Here the behavior of the green water flow onto the deck of the TLP model is described. It is worth pointing out that Ryu et al. (2007a) and Chang et al. (2011) both observed, based on the recorded images, the elevation of the breaking wave crest at $t = 0$ was approximately level with the deck surface, whereas the elevation of the wave crest exceeded the deck surface by 44 mm or roughly 1/4 wave height in the present study. It is somewhat surprising since nearly identical wave conditions were used to generate the breaking waves among the three studies. This discrepancy may be attributed to the compliance of the moored structure, which affects the amplitude and phase of the wave reflection from the frontal surface and introduces wave radiation effects, manifested in both propagating and evanescent modes.

In the green water process, the overtopping flow reached the deck after $t = 0$ and the fluid motion was predominantly in the x_G direction. It is worth mentioning that the pattern of the green water flow observed in the fixed-structure experiment by Ryu et al. (2007a) is more like a jet shooting upward and then moving forward in a roughly 45 degree angle; its front was not in contact with the deck surface until the front reached more than halfway along the deck. On the contrary, Fig. 2.3(d) to Fig. 2.3(g) show that, based on the vertical plane measurements, a dam-like flow traveled onto the deck with a maximum U_G velocity of $1.4C$ and the flow seemed to have full contact with the deck surface all along the way. Noticeable splashing water was pushed forward in the positive x_G direction by the water body right behind it and travelling in the air with a speed comparable to that of the green water front, as demonstrated in Fig. 2.4(c). The velocity of this travelling water body on and above the deck was primarily in the x_G direction with little upward z_G direction movement except for that at the higher elevation splash-up jet created by the wave impingement on the vertical structure wall as shown in Fig. 2.3(c-d). The upward momentum of the wave gradually transferred to potential energy before t = 0.17 s at the instant of Fig. 2.3(g), and then started to fall onto the deck as shown in Fig. 2.3(h). Based on the top view measurements, the U_G velocity profiles are uniformly distributed along the y_G axis. Figure 2.3(h) denotes the moment the green water front reached the end of the deck and started to fall back to the "sea".

Based on the top view measurements in Fig. 2.3(g), several large bubbles located between x_G = 100 mm and x_G = 300 mm had a tremendous x_G direction span size of nearly 100 mm yet the vertical dimension was relatively thin – no more than a centimeter or two based on the corresponding side view images. These stretched long and flat bubbles formed when the air cavity of the overturning breaking wave was enclosed and trapped by the deck surface as green water reached and passed through the deck leading edge. Comparing the top-view images between Fig. 2.3(f) and Fig. 2.3(g), the x_G-direction span dimension of those long bubbles remained nearly the same, whereas their y_G-direction span dimension kept growing, probably due to either merging with the adjacent bubbles or a lateral expansion. The lateral expansion of the bubbles might contribute to the non-zero (but small) V_G velocity. It also enhanced the local velocity fluctuations due to the random nature of the bubbles and contributed to the relatively high turbulence intensity contour, as shown in Fig. 2.3(h) between x_G = 200 mm and x_G = 300 mm on the top view measurements.

The small scale experiment for multiphase green water flow in the present study obviously suffers from scale effect since Froude scaling does not account for bubbles. However, the green water inertial force is much greater than the buoyancy force since typical bubble sizes are less than 10 mm at the region of interest (i.e., near the front of the green water where the velocity is the highest).

2.3.3 Maximum fluid velocity

Understanding of maximum mean velocities in a violent flow is important for evaluating the potential for damage. In the present study, extracting maximum velocities also allows us to compare and validate the U_G velocity measurements since the measurements were taken on two perpendicular planes. The maximum mean velocities on both measurement planes were extracted from the velocity maps and their temporal variation is presented in Fig. 2.5(a). The figure illustrates the time history of normalized (by C) maximum mean velocities, U_{GM}, V_{GM}, and W_{GM}. Note that U_{GM} and W_{GM} were measured on the side view plane and another U_{GM} and V_{GM} were determined on the top view plane along $y_G = 0$.

Since the measurements were independently conducted on two perpendicular measurement planes, both measurement planes resulted in velocities in the x direction so one U_{GM} was defined on each measurement plane. Note that U_M obtained from the top view measurements is mostly velocity on the upper water surface, while U_M obtained in the side view measurements can be velocity inside the water body. The values of U_{GM} obtained from the two measurement planes are not expected to be identical, but the comparison in Fig. 2.5(a) shows that their values are very close to each other except during the runup stage. Since there exists only one U_{GM} at a given instant in the flow, the larger U_{GM} value is likely the actual U_{GM} value.

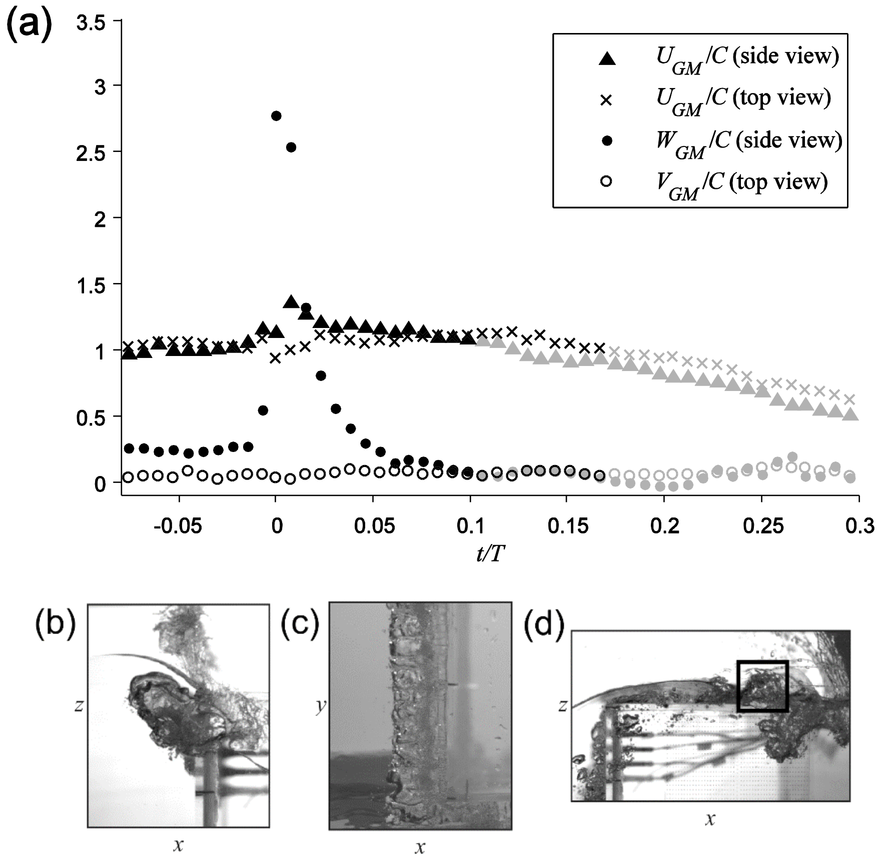

Figure 2.5 (a) Maximum fluid velocities normalized by *C*. Note that U_{GM} in the top view measurements was chosen along $y_G = 0$ and the grey data points are considered as less reliable. Snapshots from (b) the side view plane and (c) the top view plane at $t = 0.004T$. (d) Snapshot from the side view plane at $t = 0.16T$.

Before time $t = -0.01T$ when the wave was approaching the model structure, the flow was horizontally dominant. The magnitude of U_{GM} is roughly *C*, as observed from measurements in both planes that are evidently within 0.06*C* of each other. Subsequently, the wave front arrived at the vertical wall of the structure and moved vertically upward due to the presence of the structure. The magnitude of W_{GM} soared to 2.8*C* at $t = 0$ while the flow became vertically dominant for a very short period of approximately 0.02*T*, then returned to horizontally dominant again. During $t = 0 \sim 0.03T$, a lower velocity magnitude for U_{GM} was observed on the top view plane. What led to this discrepancy can be referred to Fig. 2.5(b) and Fig. 2.5(c). These two snapshots at $t = 0.004T$ provide a close-up of the vicinity of the structure leading edge. The cloud of splashing water and droplets right above the structure leading edge shown in Fig. 2.5(b) blocked the green water front, as shown in Fig. 2.5(c). As a result, velocities measured on the top view plane were indeed the up-splashing droplet cloud, not the water front close to the deck surface that has a higher horizontal velocity. After $t = 0.03T$, the two U_{GM} profiles are again nearly convergent, but the U_{GM} in the top view measurements is slightly lower than that in the side view measurements. That is because the maximum velocity is located not on the upper surface of the green water front but at the lower portion of the front, as shown in Fig. 2.4(d). A similar observation was also reported in Chang et al. (2011). They pointed out that the measured velocities on the top view plane represent the particle velocity on the upper water surface, but the maximum velocity appears near the lower water front where the measurements cannot be made from the top view. By comparing both measurement sets, the maximum difference is only $0.06C$ at the wave approaching stage, $0.38C$ at the impingement and runup stage, and $0.14C$ in the overtopping green water flow.

The U_{GM} in the side view measurements after $t = 0.1T$ tends to have a lower magnitude due to some water arising from the gap between the glass tank wall and the model structure. A snapshot in Fig. 2.5(d) highlights that part of the green water flow was obstructed by a small mass of air-water mixture as highlighted in the figure. Although the DOF is merely 68 mm, the blockage is thick enough to prevent us from obtaining the velocities at the plane of interest. Therefore, the measured U_{GM} from the side view plane after $t = 0.1T$ are considered less reliable.

2.3.4 Average turbulence intensity

Since the number of samples is small in the ensemble average process, we use spatially averaged turbulence intensity (I_{avg}) to represent the turbulence level in the flow to smooth out noise. Measurements in the violent air-water mixture, such as overturning wave, up-rushing jet, and overtopping green water, were used to determine I_{avg}. In the averaging, rules were applied to exclude the turbulence free regions, specifically: (i) prior to the W-velocity dominated runup stage at $t < -0.008T$, only the overturning wave is considered, (ii) after the runup stage at $t = 0.015T$, only the green water is considered, (iii) during the runup stage between $t = -0.008T$ and $0.015T$, both the overturning wave region [*blue-colored* area illustrated in Fig. 2.6(a)] and the up-rushing jet region [*red-colored* area illustrated in Fig. 2.6(a)] are considered, (iv) for top view measurements, the data at $y_G \geq 0$ is considered to avoid the wall effect.

Figure 2.6 presents the I_{avg} value (normalized by C) and the corresponding turbulence level relative to the maximum mean velocity at each measurement moment. Only data within the period of interest are discussed here; they are otherwise not shown in the plots. After $t = 0.17T$, the green water front passed the structure and started to fall into the sea, gaining certain fluctuations unrelated to the overtopping flow. Therefore, data after $t = 0.17T$ for both measurement planes were intentionally neglected in the plots. The unreliable data due to blocking in top view images were marked as *open circles* in the figure.

Figure 2.6(a) demonstrates the time history of I_{avg} for both measurement sets. By examining both measurements (*cross* and *filled circle* in the plot) their magnitudes before and after the W-velocity dominated runup stage (*grey* background) are in a narrow range between $0.12C$ and $0.25C$. The peak magnitude for both measurements occurred during the runup stage – approximately $0.31C$ for both measurements. Since only the up-rushing jet featured a high W velocity at the runup stage and the overturning wave remained U-velocity dominated, an attempt, as illustrated in Fig. 2.6(b), is given to compare I_{avg} in the overturning wave (marked as *square* in Fig. 2.6) and I_{avg} in the up-rushing jet (marked as *triangle* in Fig. 2.6) with the combined I_{avg} (calculated over both regions). In Fig. 2.6(a), I_{avg} in the up-rushing jet reaches $0.64C$ at $t = -0.008T$, compared to the value of $0.20C$ in the overturning wave. The I_{avg} value in the overturning wave shows no abrupt pattern, more or less continuing the trend from the previous moments. In short, the combined I_{avg}

seems not quite representative since the two regions feature two different directions in the dominant velocity.

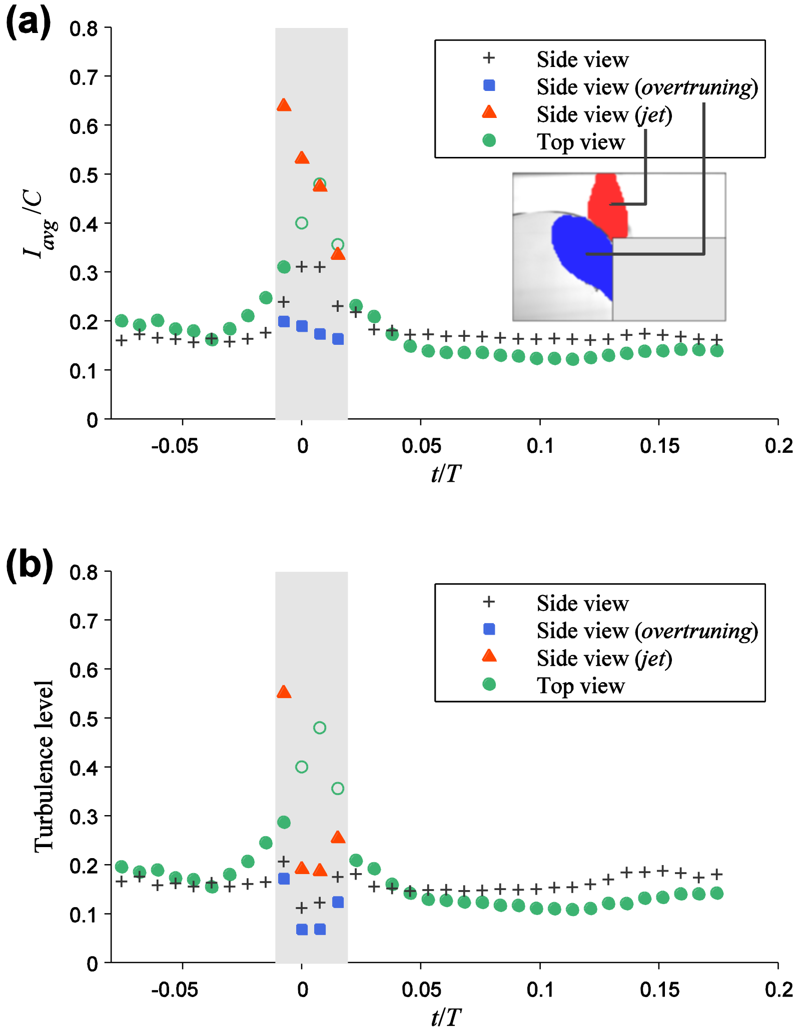

Figure 2.6 (a) Average turbulence intensity (I_{avg}) normalized by C and (b) turbulence levels for side view measurements and the top view measurements. The *open circle* is considered as unreliable data in the top view measurements due to blocking in images. The shadow region represents the runup stage. Note that "jet" in the legend denotes that the region of up-rushing jet was used in the calculation, while "overturning" denotes that the region of overturning wave was used.

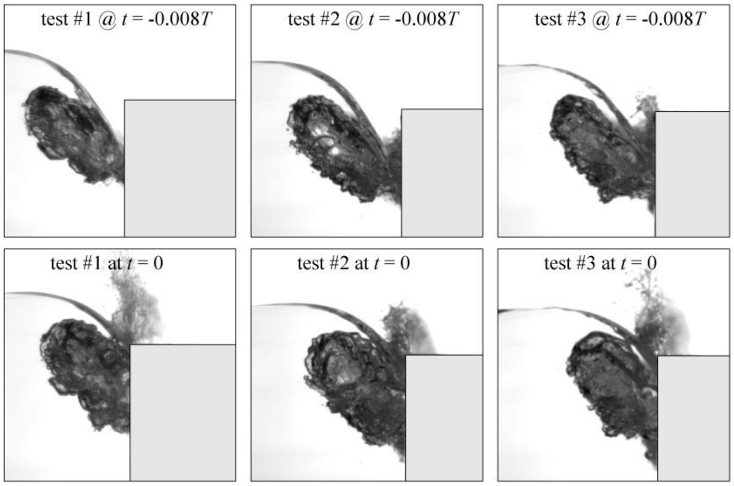

Figure 2.7 Snapshots from the side view plane at t = -0.008T (*upper row*) and t = 0 (*lower row*) for three selected tests.

Figure 2.6(b) shows the corresponding turbulence level relative to the maximum velocity of the entire flow. By neglecting the W-velocity dominated runup stage, the turbulence levels for both measurement sets vary between 0.1 and 0.2 with an average level of 0.16 for the side view measurements and 0.18 for the top view measurements. The high level observed in the top view measurements during the runup stage is mostly related to the chaotic flow motion in front of the structure wall. For the side view measurements, the peak value, greater than 0.5 at t = -0.008T, is caused by unexpectedly large vertical velocity fluctuations in some tests contributing to the ensemble average process as described below. To identify the cause, corresponding images over the 30 repeated tests were examined. Three representative images are shown in Fig. 2.7 to demonstrate the effect. At t = -0.008T, the figure shows that the runup started a bit late in test #1, but started in test #2, and reached the deck surface in test #3. Among them, high W_G velocities (greater than 2C) were observed only in test #3. This slight spatial and temporal variations result in a very high w' in the ensemble-average process. Moving forward to the next instant 0.008T later, the jet in test #1 splashed up higher than the other two tests, while all of them appeared to have a very high but similar vertical velocity magnitude. In addition, it was found that the cases with an impinging point closer to the vertical wall led to a slower initiation but quicker development in forming the up-rushing jet.

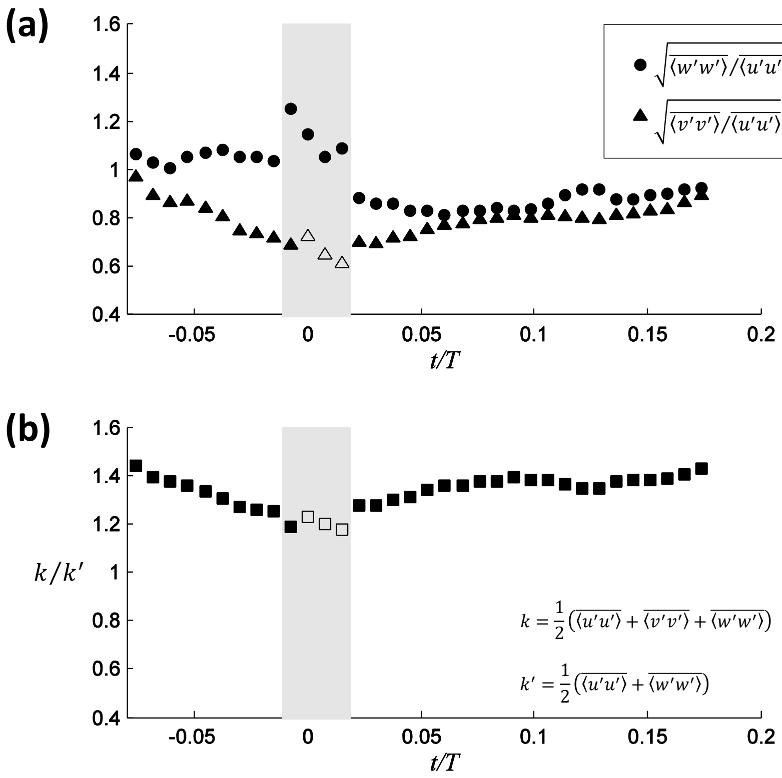

Figure 2.8 (a) Time history of the square root ratio of the spatially-averaged root-mean-square velocity fluctuations for both the side view (*filled circle*) and top view (*filled triangle*) measurements. (b) Time history of *k*/*k*'. The *grey* background represents the runup stage. The *open triangle* and *open square* are considered as unreliable data in the top view measurements due to image blocking.

2.3.5 Ratio of k/k'

Since the velocity fluctuations on two perpendicular view planes were obtained, we examined the relationships among $\langle u'u'\rangle$, $\langle v'v'\rangle$, and $\langle w'w'\rangle$. The goal is to come up with the average ratio of k/k' where k is the turbulent kinetic energy per unit mass, defined as:

$$k = \frac{1}{2}\left(\langle u'u'\rangle + \langle v'v'\rangle + \langle w'w'\rangle\right) \tag{2-4}$$

and k' is the part of k determined by two-dimensional measurements and written as:

$$k' = \frac{1}{2}\left(\langle u'u'\rangle + \langle w'w'\rangle\right) \tag{2-5}$$

Note that k' is the only available quantity in most experimental measurements and many numerical computations so knowing the ratio of k/k' is useful in estimating the kinetic energy in two-dimensional studies. The spatial average was obtained by following the same approach established in the previous section to calculate the average turbulence intensity and express those averaged quantities as $\overline{\langle u'u'\rangle}$, $\overline{\langle v'v'\rangle}$, and $\overline{\langle w'w'\rangle}$ where the overbar represents spatial averaging. Figure 2.8(a) plots the time history of $\sqrt{\overline{\langle w'w'\rangle}/\overline{\langle u'u'\rangle}}$ for the side view measurements and $\sqrt{\overline{\langle v'v'\rangle}/\overline{\langle u'u'\rangle}}$ for the top view measurements. Before and after the W-velocity dominated runup stage, the $\sqrt{\overline{\langle w'w'\rangle}/\overline{\langle u'u'\rangle}}$ ratio is nearly constant, while a decreasing trend in $\sqrt{\overline{\langle v'v'\rangle}/\overline{\langle u'u'\rangle}}$ against time was observed until the end of the runup stage. By examining the contours of $\langle v'v'\rangle/\langle u'u'\rangle$ before the runup stage, it was found that both components of velocity fluctuations increase rapidly as the wave front approaches the structure wall. However, the magnitude of u' grows much faster than that of v', leading to a decrease of $\sqrt{\overline{\langle v'v'\rangle}/\overline{\langle u'u'\rangle}}$.

Based on the results shown in Fig. 2.8(a), the ratio of k/k' can be obtained and the result is shown in Fig. 2.8(b). The trend of k/k' decreases against time until the end of the runup stage. After that, the k/k' ratio in the green water overtopping stage shows a gradually increasing trend. It is interesting to point out that the k/k' ratio during the runup stage (including the unreliable data in the gray area) has an average value of 1.20. The average ratios of k/k' before and after the runup stage are 1.33 and 1.36, respectively. The

k/k' ratio varies within a narrow range between 1.18 and 1.44 and the average ratio over the entire time history (excluding the unreliable data) is 1.35. The k/k' ratio found in the present study closely agrees with the widely-used coefficient of 1.33 based on the assumption that breaking waves features similar turbulence characteristics to that of the plane wake (Svendsen, 1987). The k/k' coefficient helps provide a reasonable estimate of the turbulent kinetic energy from two-dimensional modeling for both spilling and plunging breakers (e.g., Lin and Liu, 1998; Christensen, 2006). Based on Svendsen (1987), using the coefficient of 1.33 is based on the similarity between a spilling breaker and a plane wake. Based on our observation, the coefficient of 1.33 is applicable to green water flows caused by plunging breakers. Accordingly, the coefficient is likely applicable to both plunging breakers and spilling breakers.

2.3.6 Structure velocity

The present study considers a moored model in two-dimensional surge, heave and pitch motion. Similar to the fluid velocity, the structure displacement and velocity were measured using the BIV technique by adding numerous black dots on the lateral wall of the model structure. The dots mimic the shadow texture required in BIV correlation analysis. Velocities for both the structure and the fluid were measured simultaneously on the side view plane so 30 repeated tests were used to obtain the mean structure and fluid velocities. It should be noted that the eyebolts were installed in an appropriate direction to cancel out most of the pitch motion, providing all the tendons remained fully tensioned at all time. Movies captured by a high speed camera confirm that the pitch motion was insignificant whereas the surge motion was dominant.

Figure 2.9(a) shows the time history of the mean structure velocities U_{GS} and W_{GS}. When the breaking wave front was approaching the frontal wall of the model structure at t = -0.08T to -0.02T, the structure constantly accelerated in the x_G direction with a magnitude of about 0.11g with g being the gravitational acceleration. Subsequently, wave impingement and runup occurred and the structure acceleration reached its maximum

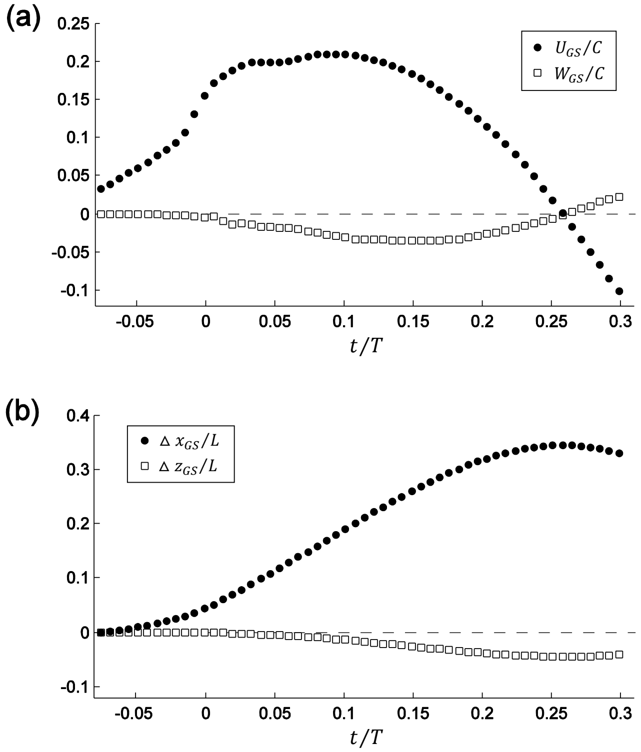

Figure 2.9 (a) Mean structure velocities normalized by the phase velocity *C*. (b) Mean structure displacements normalized by the deck length *L*. *Filled circle*, the *x*-direction component; *Open square*, the *z*-direction component. The temporal resolution is 8 ms.

magnitude of 0.34*g* at around $t = 0$ due to the arrival of the wave crest. The structure continued to accelerate and its maximum velocity U_{GS} reached 0.43 m/s (or 0.21*C*) at $t \sim 0.08T$. The *x*-direction wave momentum transferred to the structure overcame the TLP restoring force and pushed the structure further downstream until $t = 0.11T$. Once the primary wave passed the structure, the potential to restore the static stability became dominant and acted as a brake. After reaching the maximum displacement in the *x* direction at $t = 0.26T$, the restoring force induced by the inverse pendulum started to drive the structure backward (i.e., with a negative U_{GS}). It should be noted that both structure velocity components reversed their directions at about the same instant. After $t = 0.26T$, the structure moved back and forth (the entire history is not shown here) until the kinetic energy was fully dissipated by damping. By integrating the velocities with respect to time, the corresponding mean structure displacements were obtained and plotted in Fig. 2.9(b). According to Fig. 2.9(b), the maximum mean structure displacements in the x_G and z_G directions are 0.34*L* and 0.04*L*, respectively, with *L* being the deck length.

2.4 Modeling green water as a dam-break flow

By assuming hydrostatic pressure and uniform velocity distribution over the depth in one-dimensional flow, Ritter (1892) proposed an analytical solution to the Saint Venant equations for the free surface elevation, η_d , and the horizontal velocity, *U*, of a dam-break flow as:

$$\eta_d = \frac{1}{9g}\left(2\sqrt{gh_0} - \frac{x}{t}\right)^2 \tag{2-6}$$

$$U = \frac{2}{3}\left(\sqrt{gh_0} + \frac{x}{t}\right) \tag{2-7}$$

where h_0 is the initial water depth of the reservoir, *t* is time with $t = 0$ being the moment when the dam breaks, *x* is positive in the downstream direction with $x = 0$ at the dam, and the solutions are valid over $-\sqrt{gh_0} < x/t < 2\sqrt{gh_0}$. In order to compare the dam-break flow with the green water flow, matching the analytical solution with measured results is required initially. Following Ryu et al. (2007b), we follow the definition of $t = 0$ being the moment corresponding to the instant of dam removal and $x_B = 0$ the location of the dam in the dam-break problem. Since a moving structure is present in the experiment, it may be appropriate to use the relative velocity (U_B, V_B, W_B) to evaluate the kinematic behavior of the green water flow. Therefore, all discussion and results hereafter are referred to the body-fixed coordinates.

To model the complex green water velocity as a simplified dam-break flow by applying the dam-break solution in Eq. (2-7), the initial water depth h_0 needs to be determined. There are two approaches for estimating h_0 as follows.

(i) Traditional approach – calculating the elevation difference between the wave height and the free board (S_{deck}): $h_0 = H - S_{deck}$

(ii) Ryu et al.'s (2007b) approach – matching the analytical dam-break front velocity ($= 2\sqrt{gh_0}$) and the measured front velocity of green water (U_{BFG}): $h_0 = (0.5U_{BFG})^2 / g$.

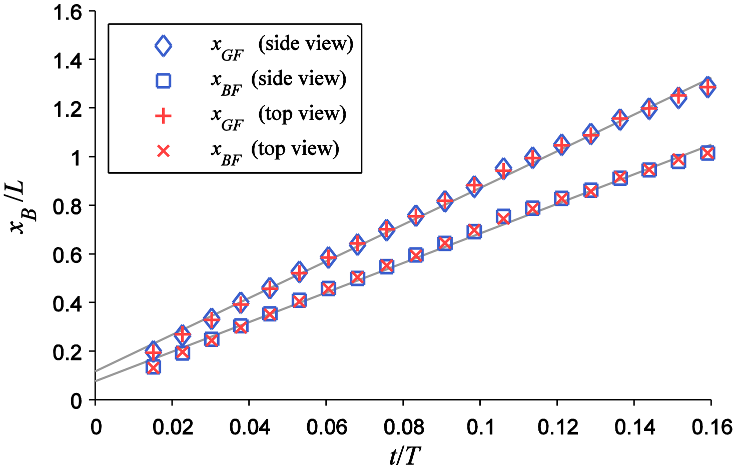

Figure 2.10 Green water front position versus time. x_{GF} and x_{BF} are referenced to the global coordinates and the body-fixed coordinates, respectively. Data for the top view plane was based on $y_B = 0$.

As mentioned earlier in the discussion of the flow pattern, an exceedance of the wave crest above the deck level was observed at the initial stage of green water. Although the wave crest is not all that similar to a dam-break, the exceedance may be used as a direct input to the determination of h_0 to replace the first approach [approach (i) above] in which a perfect wave reflection and linear behavior were assumed. The value from the first approach is 60 mm. It is interesting to point out that an exceedance was observed as 44 mm; this value could be used as another approach for estimating h_0. Having said that, we expect the wave momentum may still be strong enough to push the water onto the deck and form an overtopping green water flow even if the exceedance is zero or negative. Based on such an argument, the use of the exceedance is probably not physically sound. In practice, the wave height and the freeboard information are likely to be available in design and risk assessment because they are the key parameters for offshore structures. Therefore, the present study followed the traditional approach and the approach proposed by Ryu et al. (2007b).

In the second approach, h_0 is determined based on the assumption that the front velocity of the green water flow is steady and independent of time. From their laboratory observation, Ryu et al. (2007b) showed that was the case for fixed structures. For moored TLP models such as the one in the present study, the assumption needs to be further validated. The measured green water front position (normalized by the deck length, L) based on the images taken from both side view and top view planes, plotted against time (normalized by T) is shown in Fig. 2.10. Curve fitting was performed over these two distinct data sets – one with a steeper slope referenced to the global coordinates and the other with a milder slope referenced to the body-fixed coordinates. The results show that the front velocities are nearly constant for both coordinate systems and indistinguishable between the two measurement planes. The relative front velocity of green water (i.e., body-fixed coordinates) with respect to the model structure is $U_{BFG} = 0.83C$ and the measured global coordinate based front velocity is $1.03C$. These two front velocities are 14% and 31% lower than the magnitude of $1.2C$ observed on the fixed structure in Ryu et al. (2007a). In practice, the body-fixed relative velocity should be used since it better represents the damage potential on the structure deck. Accordingly, the calculated h_0 based on the second approach of $h_0 = \left(0.5U_{BFG}\right)^2 / g$ is 74 mm. It is very interesting that this h_0 value is unexpectedly close to the value of 60 mm based on the first approach of $h_0 = H - S_{deck}$. Comparing to the h_0 value of 140 mm obtained by Ryu et al. (2007b) on the fixed structure with a nearly identical wave condition and free board, the green-water front velocity is reduced by about 30% mainly due to the structure motion. Therefore, if applying the second approach to calculate the green water velocity, using a fixed structure can be considered as a conservative estimate.

For the side view measurements, the horizontal velocity U_B varies in the z_B direction. In order to compare with the one-dimensional Ritter's solution, the maximum velocity in each vertical profile, termed cross-sectional velocity U_{BC} following Ryu et al.'s (2007b) approach, and the depth-averaged velocity U_{BD} were used to represent the equivalent one-dimensional velocity. For the top view measurements, the horizontal velocity U_B measured at the water surface was defined at $y_B = 0$ and denoted as U_{BS}. Figure 2.11 illustrates the comparisons among the measured data, including U_{BC} and U_{BD} from the side view measurements, U_B from the top view measurements, and Ritter's solution with $h_0 = 60$ mm and $h_0 = 74$ mm determined from the two approaches. The velocities and locations are referenced to the body-fixed coordinates and normalized by the phase velocity of the primary wave C and the deck length L, respectively. Note that the figure covers only the region within the range of the deck, i.e. $x_B = [0, L]$. According to the figure, it is obvious that the difference between the two parallel, straight lines obtained from the two different h_0 values is negligibly small – a magnitude of merely $0.04C$. Note that if Ritter's solution for $h_0 = 44$ mm based on the exceedance were added, the difference would also be nearly indistinguishable.

In Fig. 2.11(a), Ritter's solution well represents the green water front velocity for U_{BD} and U_{BS}, although it under-predicts U_{BC} except its front and maximum velocity. The subsequent moment in Fig. 2.11(b) the solution fails to predict the distribution of green water but it again predicts the front velocity well. After that moment, Ritter's solution captures the overall trend and magnitude throughout the overtopping process surprisingly well. Ryu et al. (2007b) showed that h_0 obtained from the second approach performs better in predicting the overall green water distribution while h_0 obtained from the first approach predicts the front and maximum velocities better. Note that the green water velocity profiles in the present study seem to be more linearly distributed than those in Ryu et al.'s measurements on a fixed structure. They concluded the second approach is a better choice in predicting green water velocity using the dam-break solution. However, for a TLP structure such as the one in the present study, both approaches for h_0 determination result in only slight differences; practically they both predict green water velocity very well.

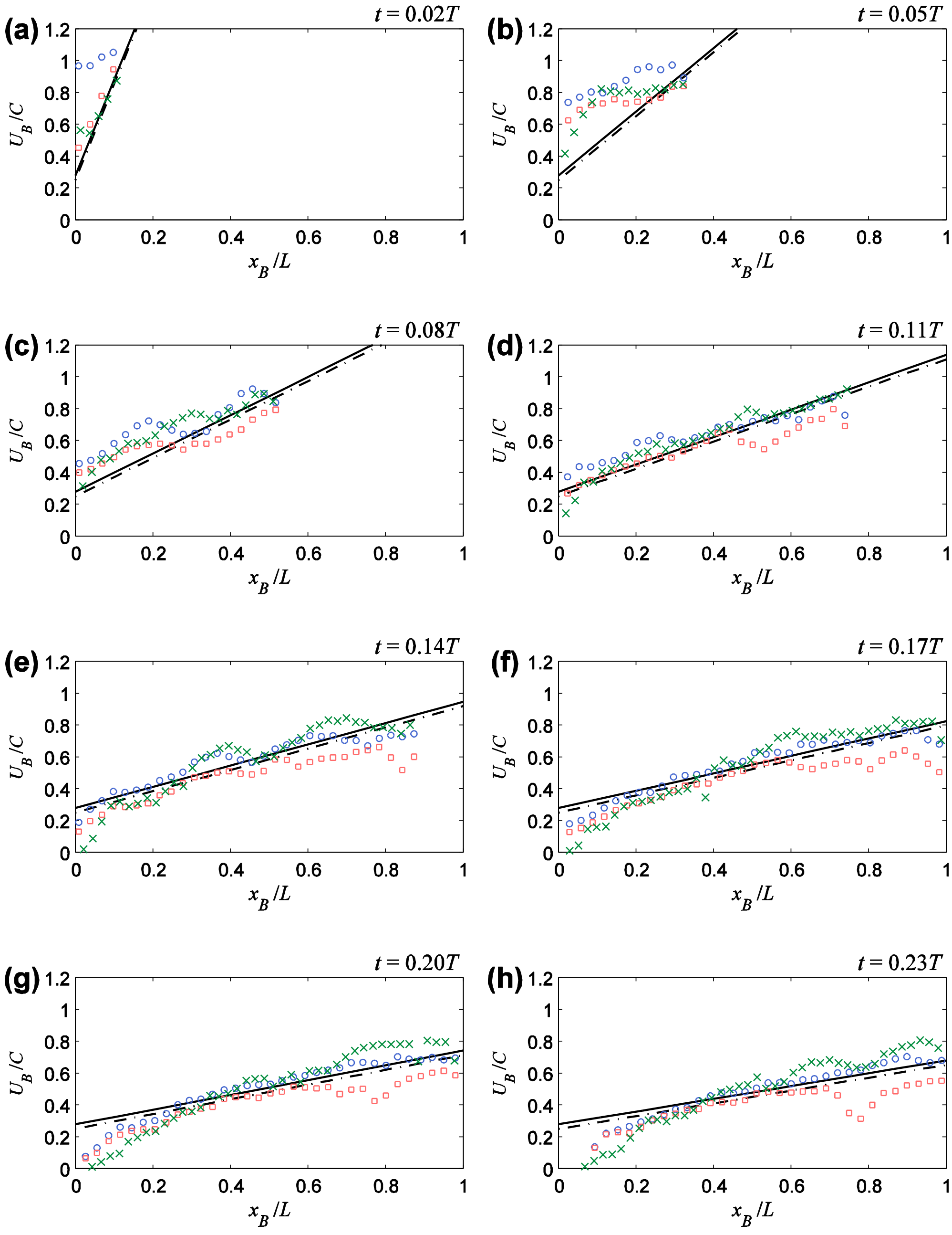

Figure 2.11 Comparisons of dam-break solution and measurements. *Blue circle*, relative cross-sectional horizontal velocity U_{BC} from the side view measurements; *red square*, relative depth-averaged horizontal velocity U_{BD} from the side view measurements; green cross, relative horizontal velocity U_{BS} along $y_B = 0$ from the top view measurements. Solid line, Ritter's solution with h_0 = 74 mm; dot-dash line, Ritter's solution with h_0 = 60 mm.

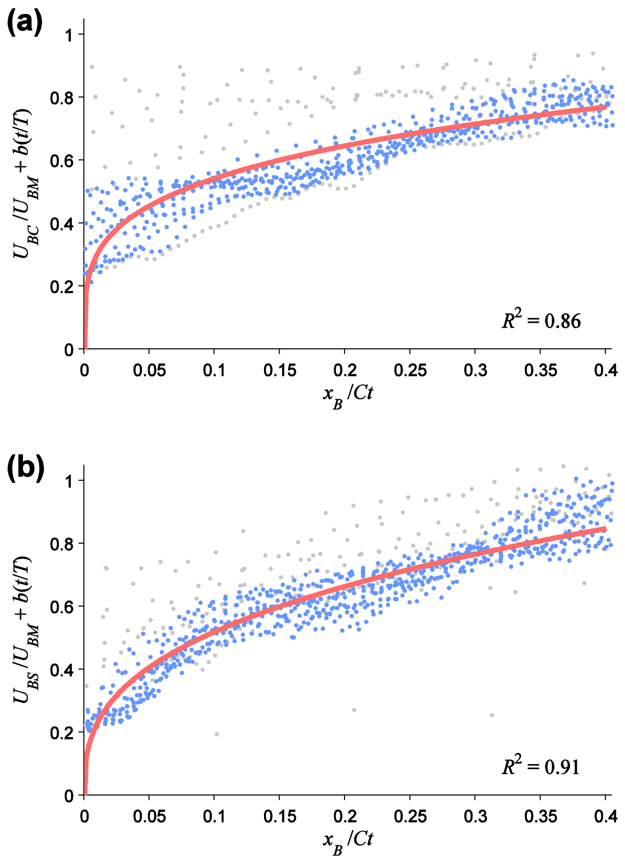

Figure 2.12 Self-similar profiles for (a) the side view measurements and (b) the top view measurements. *Blue dots*, data collected from $t = 0.07T \sim 0.16T$; *gray dots*, data collected from $t = 0 \sim 0.07T$; *red line*, fitting curve determined by least square regression using the data marked as *blue dots*.

2.5 Self-similar velocity distribution

Ryu et al. (2007a) observed similar U_{BC} distributions at various instants and examined the self-similar profiles for the green water flow on a fixed structure. They proposed an equation to predict the green water velocity distribution along the deck based on dimension analysis. The prediction equation is expressed as:

$$\frac{U_{BC}}{U_{BM}} + b\left(\frac{t}{T}\right) = a\left(\frac{x}{Ct}\right)^n \tag{2-8}$$

where U_{BM} is the maximum velocity at each time step and a, b, and n are empirical constants determined by curve fitting. Ryu et al. (2007a) found that U_{BM} is constant and independent of time so they applied a constant U_{BM} of $1.2C$ to their prediction equation. In the present study, a constant U_{BM} was observed in the top view measurements, whereas a decreasing U_{BM} was found in the side view measurements (to be discussed later). As a result, we applied the U_{BM} values corresponding to each time step in curving fitting for both measurement sets.

Figure 2.12 shows the self-similar profiles for the side view measured velocities U_{BC} and the top view measured velocities U_{BS}. Figure 2.12(a) shows the measured velocities and least square regression fitted curve for U_{BC}. Only the data marked as *blue dots* were used in the curve fitting; the data points before $t = 0.07T$ (plotted in grey) were considered as outliers and not used in the fitting. Similarly only data points after $t = 0.07T$ (plotted in blue) were used in curve fitting in Fig. 2.12(b) for U_{BS}. The outliers are from the earlier stage of the green water flow that was undergoing a rapid transition from vertically dominant to horizontally dominant. The developing green water flow exhibits U_{BC} and U_{BS} distributions that do not feature self-similar patterns until $t = 0.08T$. This can be clearly seen by examining the sequential plots in Fig. 2.11.

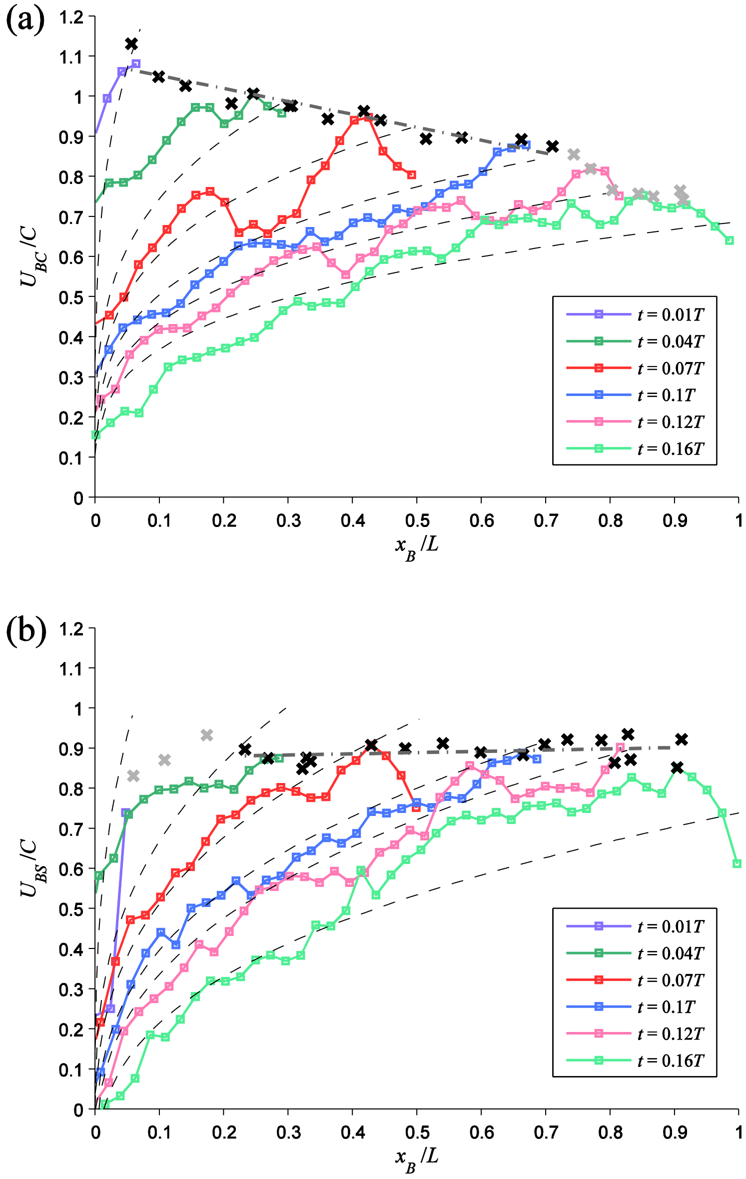

Figure 2.13 (a) Relative cross-sectional horizontal velocity U_{BC} along the deck based on the side view measurements. (b) Relative horizontal velocity U_{BS} along the deck at $y_B = 0$ based on the top view measurements. *Square-line*, distributions of U_{BC} or U_{BS}; *cross*, maximum relative horizontal velocity U_{BM}; *dot-dash line*, curve fitting obtained using the U_{BM} (*black cross*); *dash lines*, predicted profile obtained by Eq. (2-9) or Eq. (2-10). Possible outliers in U_{BM} are plotted in grey.

Based on the fitted curves, the constants in Eq. (2-8) are a = 0.97, b = 0.17, and n = 0.26 with a coefficient of determination R^2 = 0.87 for the side view measurements (U_{BC}) and a = 1.17, b = 1.54, and n = 0.35 with R^2 = 0.91 for the top view measurements (U_{BS}), i.e.

$$\frac{U_{BC}}{U_{BM}} + 0.17\left(\frac{t}{T}\right) = 0.97\left(\frac{x}{Ct}\right)^{0.26} \qquad \text{for the side view measurements} \qquad (2\text{-}9)$$

$$\frac{U_{BS}}{U_{BM}} + 1.54\left(\frac{t}{T}\right) = 1.17\left(\frac{x}{Ct}\right)^{0.35} \qquad \text{for the top view measurements} \qquad (2\text{-}10)$$

It is worth pointing out that the coefficients obtained for U_{BS} agree to a certain degree with a = 1.02, b = 1.2, and n = 0.34 reported by Ryu et al. (2007a) using a fixed structure. The prediction equations are likely to be flow dependent and not expected to be the same among different green water flows with different structure characteristics and incoming wave conditions.

Figure 2.13 plots U_{BC} and U_{BS} at several time instants for the overtopping green water flow and the corresponding maximum velocity, U_{BM}, used in Eq. (2-9) and Eq. (2-10) for the prediction equations. Note that the prediction equations above are applicable before the green water front falls back to the sea after reaching the rear end of the deck at t = 0.16T. Data with uncertainty in U_{BM} due to possible water blockage coming up from the gap between the structure and glass wall and obstruction of splashing droplets are plotted in grey. These data were not used in examining the trend of U_{BM}. Based on the U_{BM} distributions obtained from U_{BC} and U_{BS} and the U velocity contour demonstrated in Fig. 2.4(c), it is clear that U_{BM} locates at or near the green water front. That agrees with the findings in Ryu et al. (2007a) and Chang et al. (2011). In the top view measurements shown in Fig. 2.13(b), a constant U_{BM} was found. Note that this velocity represents the surface velocity. The observed constant velocity agrees with that reported in Ryu et al. (2007a), although with a lower magnitude due to the use of the relative velocity in the present study. In addition, U_{BM} in the side view measurements is 0.98C, approximately 10% higher than the value of 0.89C in the top view measurements.

On the contrary, Fig. 2.13(a) shows that U_{BM} obtained based on the side view measurements is not constant but decreases gradually. Although we are not sure the exact reason, friction may be a possible cause. At $t = 0.01T$, the U_{BM} value is 1.15C, identical to the constant U_M reported in Ryu et al. (2007a). Ryu et al. observed a jet-like green water flow on the deck, so flow deceleration due to friction may not be an issue or obvious. However, the green water flow in the present study was, as mentioned earlier, moving in close contact with the deck surface so that friction may play a role in decelerating the water particles near the no-slip boundary. In addition, most U_{BM} data were found at a lower elevation where the friction effect may be significant.

2.6 Conclusions

Experimental modeling of a moored TLP structure interacting with a plunging breaker was carried out in a laboratory. The evolution of the flow involves three phases – *impingement*, *runup*, and *overtopping green water*. The BIV technique was used to quantify the aerated flow velocities as well as determine the structure motion. Measurements were taken from two orthogonal measurement planes, side view and top view, and repeated 30 times to obtain the mean velocity and turbulence intensity using ensemble averaging. Some findings are summarized as follows:

(1) The overall flow pattern on this moving structure is similar to that on a fixed structure with two main differences for this flow: the exceedance of the wave crest above the deck level at the initial stage of green water is much higher and the dam-break-like green water flow is in full contact with the deck surface throughout the overtopping process.

(2) The dominant velocities referenced to global coordinates for the three phases are 1.4C for impingement, 2.8C for runup, and 1.4C for the overtopping green water. All three dominant velocities are consistent and very close to those found on a fixed structure in Ryu et al. (2007a) with differences within 0.2C.

(3) The difference in maximum velocities between the side view measurement and the top view measurement is negligibly small for the approaching wave, about $0.4C$ for wave impingement, and $0.1C$ for overtopping green water. Note that the top view measurements are unable to obtain the runup velocity.

(4) The average turbulence levels (normalized by the time-varying maximum velocities), excluding the runup stage, are 0.16 and 0.18 for the side view measurements and the top view measurements, respectively, and the magnitude varies between 0.1 and 0.2.

(5) The ratio k/k' based on three-dimensional and two-dimensional measurements averaged over the entire time history is 1.35. This ratio closely agrees with the coefficient 1.33 widely used in two-dimensional breaking wave modeling.

(6) The Ritter dam-break solution predicts the green water flow surprising well on the present moving structure. That agrees well with what Ryu et al. (2007b) reported on a fixed structure. The two approaches for determining the initial water depth h_0 required in the Ritter dam-break solution result in nearly indistinguishable predictions.

(7) The overtopping greenwater has a constant maximum surface velocity, based on the top view measurement. That is in agreement with Ryu et al.'s (2007a) observation on a fixed structure. However, the side view measurement shows a gradual decrease of the maximum velocity over time with an average magnitude about the same as that from the top view measured constant velocity.

(8) Two prediction equations were obtained using data from the two measurement planes based on the self-similar velocity profiles. The green water velocity distributions on the TLP structure are slightly different to those on a fixed structure.

The present study shows that both measurement sets are in quantitative agreement for the approaching wave and green water flow, but only the side view measurements are able to capture the runup process which is the most violent part throughout the flow evolution. Deciding which measurement plane would work better is likely to depend on the physical phenomena of interest. For example, the side view measurements allow us to investigate fluid impingement on a vertical surface, such as wave runup (Ryu et al. 2007a) and slamming and the liquid sloshing problems (Song et al. 2013). On the other hand, the top view measurements allow us to examine the horizontally deflected green water flow induced by a 3D structure (e.g., Chang et al. 2011) or directional waves. Of course, combining the side view and top view measurements is probably more ideal, especially in a relatively narrow flume with glass side walls for optical access.

CHAPTER III

IMPACT PRESSURE AND VOID FRACTION DUE TO PLUNGING BREAKING WAVE IMPACT ON A TWO-DIMENSIONAL TLP STRUCTURE[*]

3.1 Introduction

High impulsive pressures created by extreme wave impacts are of great concern to the integrity and safety of marine structures in the ocean, such as ships, production platforms, offshore wind farms, and coastal defense systems. Wave impingements may exert heavy loadings and affect the dynamic balance of the structures. For ships, offshore production platforms (e.g., spar, semi-submersible, tension-leg platform), and vessels serving as FPSOs (floating production storage and offloading systems), some local waves may be high enough to overtop their lower or even the top deck and create so-called green water, threatening equipment, facilities and personnel on the decks. A local intensive impact, such as wave slamming and green water, could cause localized damage and, subsequently, extensive failure of the structure. Recent records indicate a possibility that devastating hurricanes may become more frequent in a changing climate (Wuebbles et al. 2014). As a result, an increase in wave heights may boost the occurrence of green water and intensify the violent wave impact.

The mechanism of wave impingement must be properly understood to address the risk in engineering design. To date the knowledge of impact pressure caused by non-breaking waves has been well developed and integrated into practical designs. On the other hand, with the complex nature involving discontinuous free surface, turbulence, and multiphase air-water mixture, and hurdles in measuring the phenomena, the cause and consequence of violent impact pressures due to breaking waves are still not well understood. It is well known from previous laboratory observations that the wave impact pressure depends on not only the location of the impingement point relative to the structure (Bagnold 1939;

---

[*] Partial content reported in this chapter is reprinted with permission from "Impact pressure and void fraction due to plunging breaking wave impact on a 2D TLP structure." by Chuang et al. (2017). *Experiments in Fluids*, DOI: 10.1007/s00348-017-2356-4, Copyright [2017] Springer.

Ochi and Tsai 1984; Chan and Melville 1988; Hattori et al. 1994; Ariyarathne et al. 2012), but also on the shape of the incipient wave upon collision against the structure (Bagnold 1939; Hattori et al. 1994; Hull and Muller 2002; Peregrine 2003; Bullock et al. 2007). Furthermore, even under nominally identical incoming wave conditions, the magnitude of the measured peak impact pressure varies considerably (Bagnold 1939; Chan and Melville 1988; Zhou et al. 1991).

Numerous studies have shown that entrained and entrapped air plays a crucial role in the impact pressure variation. Chan and Melville (1988) and Zhou et al. (1991) suggested that the randomness of entrapped air in wave impact may be the main cause of the maximum pressure variation. Peregrine (2003) reviewed the role of entrained and trapped air in the generation of various impact pressures. Hattori et al. (1994) studied the breaking wave impact pressures on vertical walls under four different colliding conditions. Their observations indicate that the impact pressures increase considerably when a small amount of air is trapped between the waves and the structure wall. They also found that the magnitude of the impact pressure reduces and the corresponding pressure rise time increases when a large volume of air is entrapped. Peregrine and Thais (1996) theoretically investigated the cushioning effect of air entrainment by modelling the flip-through wave impact as a filling flow in a liquid container with the air bubble compressibility being accounted for. They concluded that a high level of air entrainment tends to reduce the pressure maximum.

Bullock et al. (2001) carried out a series of drop tests in both freshwater and seawater to examine the influence of the aeration level. Their experimental results indicate that a high level of aeration not only reduces the pressure maximum but also increases the pressure rise time. The same conclusion was also reported by Ma et al. (2016) in which numerical and experimental works were conducted by considering a rigid square flat plate falling into pure and aerated water. Bullock et al. (2007) later evaluated the magnitude of the pressure impulse by integrating the pressure with respect to its rise time for different types of breakers. They concluded that a high level of aeration does not always reduce peak pressure but it seems to increase the rise time. Their work also shows that, in comparison to the pressure variation, the level of impulse variation was far lower among the repeated tests. Wood et al. (2000) reported that an air pocket may create a higher impulse due to the rebound of the water. Lugni et al. (2006) observed that the pressure time history, after reaching the peak pressure, oscillates with the presence of air entrapment, whereas no clear oscillations were observed when there was no air entrapment. Subsequently, Lugni et al. (2010a, 2010b) studied the formation of the air cavity during wave impact. Their results show that the oscillation frequency in the measured pressure time history is associated with the air pocket.

Bredmose et al. (2009) numerically investigated the effect of air using an incompressible potential-flow model combined with a compressible aerated-flow model. Their simulations show that the highest impact pressures are associated with the entrapment of small air pockets. Cuomo et al. (2010a) derived a Bagnold–Mitsuyasu scaling law that accounts for the scale effect of an air pocket upon wave impact. Subsequently, Bredmose et al. (2015) numerically and analytically investigated the effects of scale and aeration, and compared the outcomes from the Froude law and the Bagnold–Mitsuyasu law. By comparing with the approximate solution derived by Peregrine and Thais (1996), they found that a high level of aeration reduces the maximum impact pressure, maximum force, and impulse for three types of wave impact – flip through, low aeration, and high aeration. Furthermore, although in practical applications the wave impacts generally occur in seawater, most laboratory studies have been carried out using freshwater. To examine the issue, Bullock et al. (2001) conducted laboratory and field measurements in both freshwater and seawater to investigate the effect of ambient aeration level on impact pressure. They observed that prominent air bubbles in seawater took several wave periods to diminish, compared to only one period in freshwater. The aeration level is one order of magnitude greater in seawater than that in freshwater, implying that the aeration effect is sensitive to the working fluid.

When a wave breaks, the free surface flow evolves into chaotic motion of gas-liquid mixture, leading to fluid density variation and affecting flow properties such as mass, momentum, and energy. Therefore, measuring void fraction using a phase transition detection technique is necessary to account for the fluid density variation. A small number of studies (e.g., Cox and Shin 2003; Blenkinsopp and Chaplin 2007; Lim et al. 2015; Na et al. 2016) have performed direct void fraction measurements on breaking waves in the laboratory. Ryu et al. (2008) examined the void faction of green water flow following a broken wave impact by using the fiber optic reflectometer (FOR) technique developed by Chang et al. (2003). The FOR technique enables measurement of rapid phase transitions based on detection of refractive index changes. Subsequently, Ariyarathne et al. (2012) applied the FOR technique to measure void fraction in the green water flow on a 3D model structure. However, void fraction measurements on moving structures under breaking wave impacts are still rare.

Researchers have attempted to relate the impact pressure to flow momentum flux during wave-structure interaction. By correlating the impact pressure with the square of the wave phase speed, Chan and Melville (1988) summarized the impact coefficients obtained from previous research works, and reported that the coefficients vary widely from 0.5 to 40. Even though the use of the incident wave phase speed as a scaling parameter is most convenient, it hardly represents the flow velocity coincident with the shock pressure. Instead of using the wave phase speed, Ochi and Tsai (1984) conducted experiments to confirm that the impact pressure is proportional to the squared impact velocity (i.e., the water particle velocity) for breaking wave impact on a surface-piercing cylinder. Azarmsa et al. (2001) tested spilling and plunging breakers and concluded that the occurrence of impact pressure is closely related to the internal kinematics of breaking waves. For green water on a 3D structure created by breaking wave impact (Ariyarathne et al. 2012; Song et al. 2015) and breaking wave impact due to liquid sloshing (Song et al. 2013), the impact pressure maxima are found to be proportional to the square of the maximum flow velocity measured around the pressure measurement points. Moreover, with void fraction measurements available, Ariyarathne et al. (2012) accounted for the fluid density variation in formulating the relationship between the peak impact pressure and the maximum flow velocity.

Studies of wave impact pressure have been mostly performed using fixed structures, such as cylinders and vertical or inclined walls. Literature relevant to the wave impact pressure on movable marine structures is mostly directed at evaluating the structural dynamic response (e.g., Johannessen et al., 2006; Buchner et al., 2007; Rudman and Cleary, 2013). Xu et al. (2008) experimentally investigated the impact pressures caused by steep waves on a bow structure and the associated structural dynamic response. Subsequently, Xu and Barltrop (2008) conducted a reliability analysis to determine an appropriate safety factor for engineering design. For numerical modeling, Veldman et al. (2011) employed a Navier-Stokes equation based model with air compressibility being taken into account in order to simulate impact pressures due to sloshing and wave impact on a semi-submersible. However, as far as the authors know, simultaneous pressure measurements along with void fraction and velocity measurements on moving structures have not been reported. As a result, the present and likely near future numerical models still lack measurement data for validation.

To determine the instantaneous velocity field in highly aerated turbulent flows such as breaking waves and hydraulic jumps, Ryu et al. (2005) introduced the bubble image velocimetry (BIV) technique that combines the shadowgraphy method and the particle image velocimetry (PIV) technique. The BIV technique has been successfully applied to measure the velocity fields in turbulent bubbly flows such as wave breaking on a sloping beach (Pedrozo-Acuña et al. 2011; Rivillas-Ospina et al. 2012), hydraulic jumps (Lin et al. 2012), free overfall in open channels (Lin et al. 2008), liquid sloshing (Song et al. 2013), and wave breaking wave in deep water (Lim et al. 2015; Na et al. 2016). The technique is also capable of quantifying the aerated green water flow velocities during breaking wave impingement on either 2D (Ryu et al. 2005, 2007a, 2007b) or 3D (Chang et al. 2011; Ariyarathne et al. 2012; Song et al. 2015) structures. More recently, Chuang et al. (2015) extended the application to breaking wave impinging on a moving structure and simultaneously determined the structure motion and the fluid velocity field of the aerated flow.

The present experimental study continues Chuang et al.’s (2015) work on a plunging breaking wave impinging on a tension-leg platform (TLP) model with a simplified geometry in a laboratory wave tank. To the best of the authors' knowledge, this is the first attempt to perform simultaneous pressure, void fraction, fluid velocity, and structure motion measurements on the turbulent aerated free surface flow interacting with a structure in wave-induced motion. The BIV technique was employed to quantify the instantaneous fluid velocity field in the aerated region and the structure motion. Instantaneous void fraction was obtained by analyzing the phase transition time histories measured by FOR while pressures were measured using differential pressure sensors. The objectives of the present study are: (1) to investigate the correlation between impact pressure maxima and the velocity, pressure rise time, void fraction, impingement location, and mean kinetic energy of the flow; (2) to compare the impact coefficients evaluated from different approaches and establish a formula to predict the maximum probable impact pressure as a function of the incoming wave condition and structure motion; (3) to investigate the pressure-aeration relationship and the effect of air entrainment.

3.2 Experimental setup

3.2.1 Model setup

The experiment was conducted in a two-dimensional glass-walled wave tank located in the Zachry Department of Civil Engineering at Texas A&M University. The tank has dimensions of 36 m in length, 0.9 m in width, and 1.5 m in depth. It is equipped with a dry-back flap-type wavemaker at one end and a 1:5.5 sloping beach covered with a horsehair layer as the wave energy absorber at the other end. The tank was filled with freshwater to a constant depth of h = 0.80 m throughout the experiment. A rectangular floating model structure made of Plexiglas was built watertight with dimensions of 0.37 m in length, 0.85 m in width, and 0.31 m in height. In calm water the structure had a freeboard (F) of 0.11 m. The model structure was moored to the tank bottom by vertical wire rope tendons attached to its four corners. Hull buoyancy pre-tensioned the wire rope

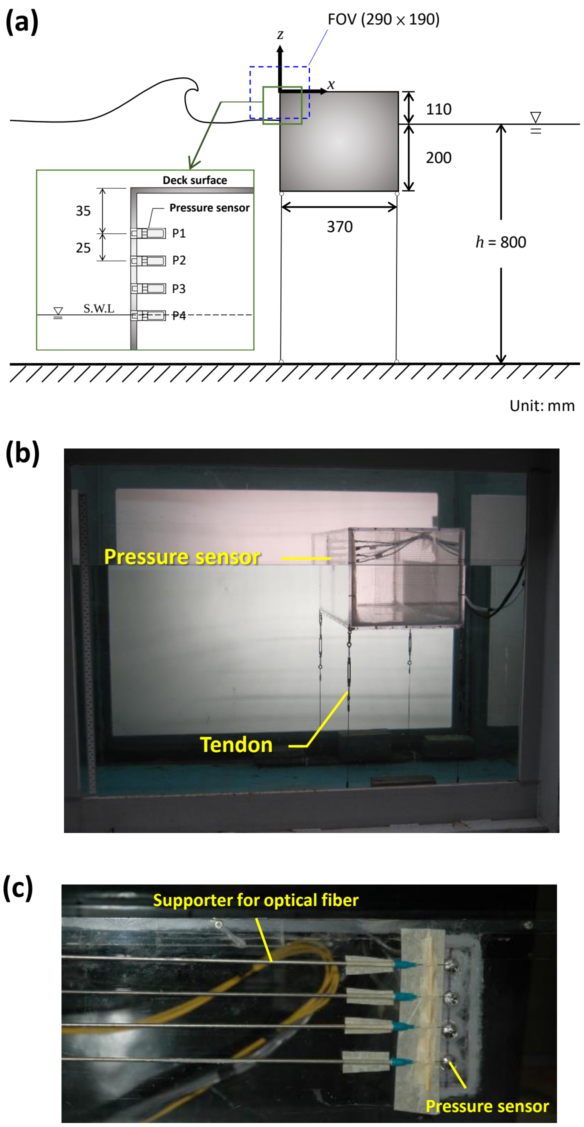

Figure 3.1 (a) Skematic diagram and dimensions of model setup and coordinate system. *Blue dashed line* indicates the field of view (FOV). Photos of (b) model structure in still water and (c) setup of FOR probes and pressure sensors taken from the upstream.

tendons, thus rendering the model structure a tension-leg platform (TLP), albeit one in a scaled water depth that is unusually shallow compared to most installed TLPs used to support oil and gas production facilities. It is recognized that the plunging breaking wave investigated in this study is not representative of the type of wave breaking that occurs in deep water, however the measurement techniques and physical mechanisms discussed herein are relevant and directly applicable to wave impacts against floating platforms in deep water.

The model setup is sketched in Fig. 3.1(a) and a photo of the model structure in the wave tank is shown in Fig. 3.1(b). The model structure is designed to mimic a tension-leg platform or tendon-moored marine structure with a simplified geometry at a scale ratio of 1:169. The Froude similitude was applied to scale down the characteristics of the incident wave in a hurricane that generates the breaking wave impact studied herein. At 1:169 scale, the 0.80 m water depth in the tank corresponds to a full scale depth of 135 m, which is comparable to the 147 m depth in which the Hutton TLP was installed. The body-fixed coordinate system (i.e., the fixed coordinate system on the moving structure) is defined such that x is the horizontal direction along the wave propagation, y is the cross-tank direction, and z is the vertical upward direction. The origin of the coordinate system $(x, y, z) = (0, 0, 0)$ is set at the leading edge of the model structure, 0.1 m from the front glass wall, and on the deck surface of the model structure at the resting position, respectively, as shown in the figure. Note that the results and discussions are primarily presented in the body-fixed coordinate frame unless otherwise specified. The time $t = 0$ is defined as the moment when the green water wave front passes $x = 0$. The same model structure setup was also used in Chuang et al. (2015).

3.2.2 Velocity measurement

Chuang et al. (2015) applied the BIV technique to quantify the aerated flow field on a moving structure interacting with breaking waves. The present study adopted a similar setup but using a smaller field of view (FOV) to achieve a finer spatial resolution. As depicted in Fig. 3.1(a), a fixed FOV was set as 0.29 m by 0.19 m, centered at the leading edge of the model structure in calm water. A high-speed camera (Vision Research Phantom M340) mounted with a 50-mm focal lens was used for image recording at a framing rate of 1000 frames per second (fps) with a resolution of 2240 × 1440 pixels and 12-bit dynamic range. In the process of breaking wave impingement, trackable shadow textures were created by air-water interfaces, such as air bubbles and water droplets, through a backlit source/screen. The BIV technique utilizes the shadowgraphy technique to acquire images through a controlled, narrow depth of field (DOF). The flow velocity can thus be readily determined by cross-correlating the trackable textures in consecutive images.

In the present study, the backlit screen was created by a thin, translucent acrylic sheet attached to the rear glass tank wall, illuminated by 600 W light bulbs from behind. A vertical focal plane was set 0.1 m behind the frontal tank glass wall. The DOF for air bubble images was 10.3 mm, and the estimated geometric error due to the limited DOF is 0.71%. Image processing software from LaVision Inc. and MPIV (Mori and Chang 2003) were employed to determine the fluid velocity in the aerated region by cross-correlating consecutive images. In the cross-correlation process, an adaptive multi-pass algorithm was adopted with an initial interrogation window size of 64 × 64 pixels, and a final interrogation window size of 16 × 16 pixels with 50% overlap between adjacent windows. The resulting spatial resolution for velocity maps is 2.1 × 2.1 mm^2. In addition to fluid velocity, the BIV technique was employed to simultaneously determine the structure displacement and velocity with artificial texture printed on the lateral wall of the structure as tracers. More details regarding the image recording and setup are summarized in Table 3.1. More details on the principle and validation of BIV, determination of the DOF (*D*), and estimation of the geometric error (ε) can be found in Ryu et al. (2005), Lin et al. (2012), Song et al. (2013), and Chuang et al. (2015).

Table 3.1 Summary of image recording setup. *D* is the DOF, ℓ is the distance between the camera and the focal plane, and ε is the error.

Field of view (pixels)	Field of view (mm^2)	Spatial resolution (mm/16 pixels)	Framing rate (fps)	D (mm)	ℓ (mm)	ε (%)
2240 × 1440	290 × 190	2.1 × 2.1	1000	10.3	725	0.7

3.2.3 Pressure measurement

Pressure measurements were taken at four points (named P1 to P4) along the frontal wall of the model structure as shown in Fig. 3.1. P1 is 35 mm below the deck surface while P4 is at the still water level. The pressure sensors are evenly spaced with an interval of 25 mm, covering a vertical range from z = -35 mm to z = -110 mm or from the still water level to 75 mm above it (or from 0 to 0.44H above the still water level with H being the breaking wave height). These four piezoresistive differential pressure sensors (Kistler 4053A1) were mounted, facing the incoming waves, at the desired locations on the vertical structure wall with great care to ensure that each end face of the 12-mm-diameter sensor was flush with the wall surface. The sensors measure the pressure differential referenced to the surrounding atmospheric pressure and cover the range up to 1 bar with a sensitivity of 200 Pa/mV and a natural frequency higher than 15 kHz. The pressure measurements in the present experiment were sampled at 10 kHz throughout the experiment. Since the flow due to breaking wave impact was highly turbulent, an appropriate repetition number for pressure measurements was performed. Ariyarathne et al. (2012) applied bootstrap analysis (Efron and Tibshirani, 1993) to quantify the errors over different repetitions. They suggested that at least 5 repetitions are required for an acceptable reliability in estimating the mean maximum pressure. Accordingly, the present study set the repetition number to 30 with an estimated error less than 1%.

3.2.4 Void fraction measurement

In addition to velocity and pressure measurements, the FOR technique was employed for void fraction measurements. The optical fiber used in the present experiment is 125 μm in diameter. To support and protect the fiber probes against strong wave forces, stainless steel tubes were built to enclose the optical fibers. A flat-cut end needle, with 25 mm in length and 0.5 mm in outer dimension, was connected to each tube to house and direct the optical fiber tip. The optical fiber tip was intentionally exposed out of the needle (and initially in the air during the measurements) by a 5-mm length to minimize the surface tension effect around the needle end and keep the fiber end tip stiff. Each FOR probe was anchored to the vertical wall of the model structure with its end tip precisely 5 mm in front of the center of a corresponding pressure sensor. Figure 3.1(c) shows the relative locations between the pressure sensors and the FOR probes.

The FOR technique measures the time histories of phase transition by detecting changes of the refractive indices between two different media (air and water in the present study) at the tip of the optical fiber. With the time histories of phase transition, the void fraction (α) at a given measurement point can be determined by calculating the ratio of the fractional air-phase residence time (T_{air}) over the duration of air-water mixture (T_{mix}), i.e.,

$$\alpha = \frac{T_{\mathrm{air}}}{T_{\mathrm{mix}}} \tag{3-1}$$

in which $\alpha = 0$ represents that the fiber tip is fully immersed in water, whereas $\alpha = 1$ represents that the tip is surrounded by air. Following Ariyarathne et al. (2012) and Lim et al. (2015), the FOR sampling rate was set at 100 kHz and T_{mix} was set at 1 ms throughout the experiment. This results in a final temporal resolution of 1 kHz in the void fraction measurements. Further details on the principles, validation, and applications of the FOR technique can be found in Chang et al. (2003), Lim et al. (2008), Ryu and Chang (2008), Lim et al. (2015), and Na et al. (2016).

3.2.5 Wave condition

The present study employed a wave focusing method (e.g., Perlin et al. 1996; Ryu et al. 2005, 2007a; Chuang et al. 2015) to generate a plunging breaker in a flat-bottom wave tank. A wave packet with modulated frequencies ranging from 0.7 to 1.3 Hz was generated. The wave packet was programed to generate only one very steep wave (called primary wave) from the component waves of different frequencies which later become a plunging breaker. The primary wave in the present study is intended to simulate the recorded maximum wave height reported by Wang et al. (2005) during Hurricane Ivan at a scale ratio of 1:169.

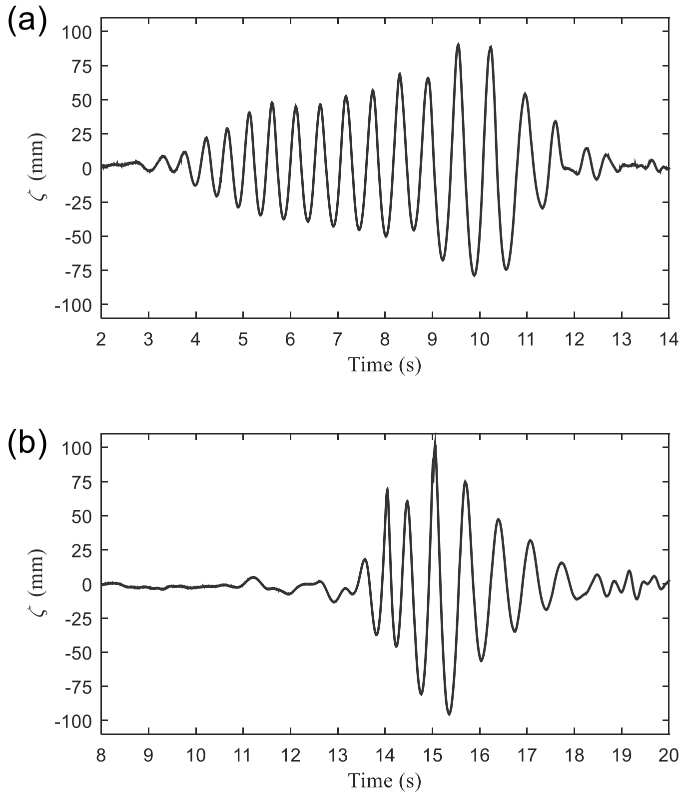

Figure 3.2 Free surface elevations measured at (a) 16.7 m and (b) 4.0 m upstream from the frontal wall of the model structure.

Figure 3.2 shows the wave elevation measured using double-wired resistance-type wave gauges located at 5 m (x = -16.7 m) and 17.7 m (x = -4.0 m) from the neutral position of the wavemaker paddle. The properties of the primary wave obtained using zero-upcrossing analysis and the linear dispersion relationship are: wave height H = 0.17 m, wave period T = 1.32, and phase speed C = 2.05 m/s. The generated waves are identical to those used in Chuang et al. (2015). The wave impingement point, defined as the location where the tongue of an overturning breaking wave touches its front water surface, can be adjusted by tuning the period of the waves on the order of μs (Chuang et al. 2015). In the present study the impingement point was set on the structure vertical wall at the still water level, also denoted as the *wall impingement* condition by Chang et al. (2011). It is well known that breaking point is highly sensitive. For plunging breaking wave generation, it is extremely difficult to have a constant impingement point even though an identical wave condition is employed. The structure-induced wave reflection may disturb the breaking point resulting in a wider range of the impingement point. In the present study, only one single breaking wave was generated in a wave train. By inspecting the high-speed video images, the mean impingement location was 46 mm (0.27*H*) in front of the structure vertical wall, with a standard deviation of 20 mm (0.12*H*). Comparing to that (mean location of 8 mm with the standard deviation of 9 mm) in Chang et al. (2011) on a fixed structure, the breaking wave in the present experiment is considered highly repeatable, especially with a moving structure.

3.2.6 Synchronization

In order to evaluate the ensemble-averaged quantities, image recording and signal acquisition were synchronized while 30 repetitions with identical wave and boundary conditions were performed. To cope with the limited image recording duration (about 2.6 seconds with 3.2 million pixels per frame at 1000 fps with 12-bit depth) of the high speed camera used herein, a rising-edge signal with a fixed delay time was generated to trigger the recording so that the physical process of interest can be fully captured. However, it was found that a small random time lag existed between images and signals among the repeated tests. The FOR signals were utilized to eliminate the random time lag. The FOR signals feature a sudden drop, indicating the phase change (a high signal represents the gas phase and a low signal represents the liquid phase) when the tip of a probe is in contact with water. Figure 3.3 demonstrates what was observed at measurement points P1 and P2. Note that the phase change takes less than 10 μs, comparing to the frame rate of 1000 fps in the image recording. As a result, a refined synchronization was performed on both record images and acquired signals by matching the timestamp of the FOR signals to the corresponding images.

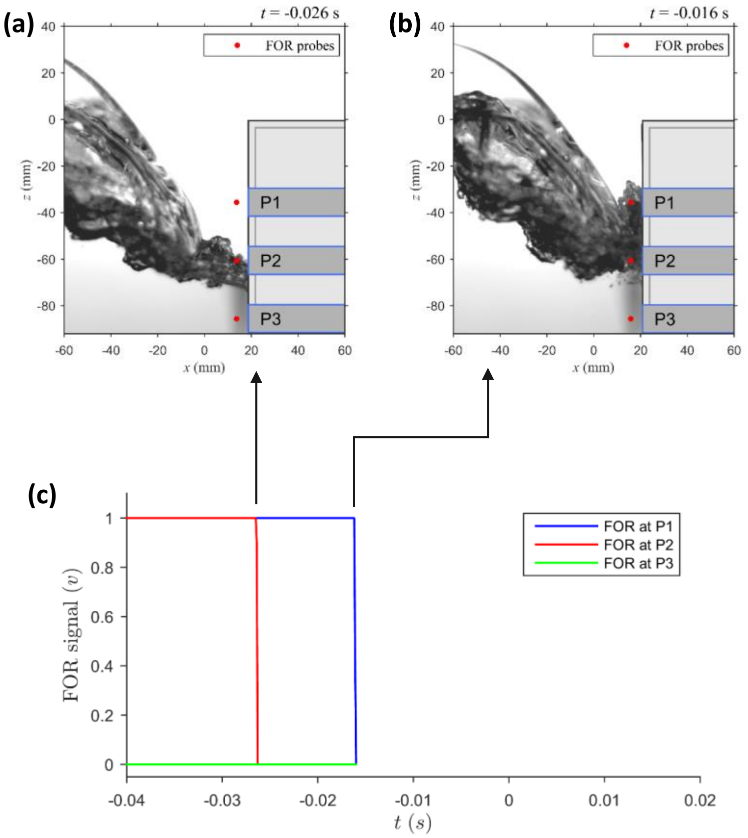

Figure 3.3 (a) and (b) are the snapshots corresponding to the initial moments when the breaking wave touched the sensing tips of the FOR probes at P1 and P2. (c) The corresponding FOR signal time series with the signals dropping to zero indicating a phase change from air to water. Note that the sample test run was randomly selected over the 30 repeats.

3.3 Results and discussions

The following presentation will examine results obtained from individual test realizations as well as quantities obtained by averaging over the 30 repeated tests. It is important to distinguish between instantaneous or time-dependent parameters measured from individual impact events (such as maximum instantaneous impact pressure $p_{\max}$, pressure rise time t_r, local u velocity, and void fraction α), and ensemble-averaged parameters (such as maximum ensemble-averaged pressure P_{max} and ensemble-averaged void fraction A). Note that the subscript r denotes the quantity averaged over rise time.

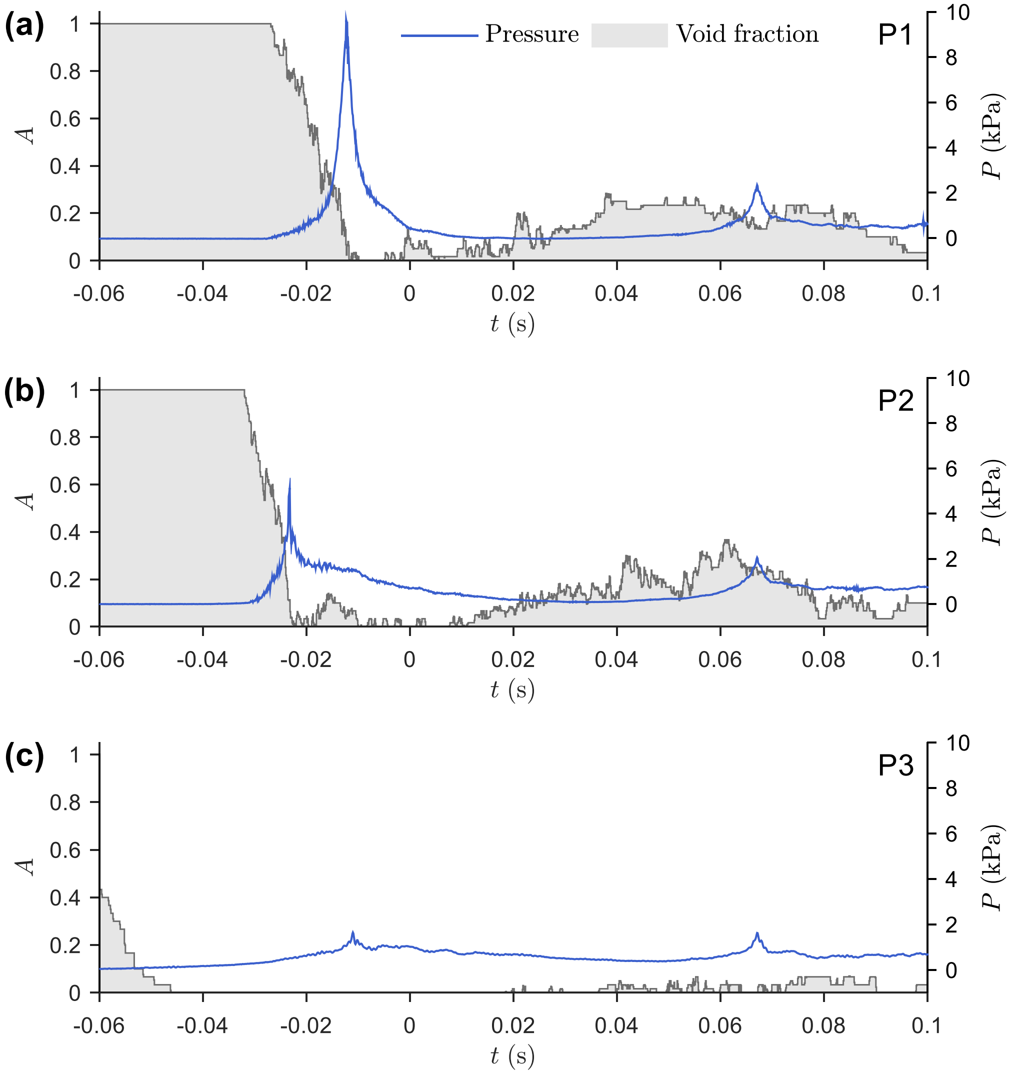

Figure 3.4 Time histories of ensemble-averaged pressure and void fraction at measurement points (a) P1, (b) P2, and (c) P3.

3.3.1 Impact pressure and void fraction

The ensemble-averaged pressure (P) and void fraction (A) at measurement points P1, P2 and P3 are shown in Figure 3.4. Note that the hydrodynamic behavior at P4 is similar to that at P3 so the results at P4 are not presented. In the figure, before $t = 0$ prominent pressure peaks are found at P1 and P2 which may be characterized as the zone of wave impact (Chan and Melville 1988). On the contrary, the peaks below the wave impact zone at P3 and P4 are insignificant in magnitude. Although the pressure sensors P1 and P2 are not far from each other (only 25 mm or $0.15H$ apart), their magnitudes and temporal distributions are noticeably different. The pressure evolution at P1 features a typical church roof profile (Peregrine 2003), nearly symmetric with respect to the peak pressure. At P2, a steep rise but a gradual fall after reaching the peak pressure is observed. Although no negative pressures appear in the ensemble-averaged results at any of these four measurement points, negative pressures occurred near the beginning of pressure rise at P1 and P2 in some of the instantaneous pressure measurements. However, based on examination of the pressure time histories over 30 repeats, the negative pressures do not seem to affect the peak pressures. The maximum mean pressures ($P_{\max}$) at P1 and P2 are estimated as 9.63 kPa ($2.3\rho C^2$) and 5.14 kPa ($1.2\rho C^2$), respectively, with ρ being the water density. The rise time (t_r) is estimated as 8.5 ms for P1 and 6.5 ms for P2. Note that P1 and P2 were emerged before the breaking wave impact, whereas P3 and P4 were submerged (by the rising wave trough) before the impact.

Table 3.2 Summary of pressure and void fraction measurements.

Measurement point	z (mm)	$P_{\max}$ (Pa)	$\frac{P_{\max}}{\rho C^2}$	$\left(\frac{dP}{dt}\right)\Big/\left(\frac{0.5\rho U_{\max}^2}{T}\right)$	t_r (ms)	A_r
P1	-35	9631	2.3	448	8.5	0.30
P2	-60	5135	1.2	293	6.5	0.44
P3	-85	1651	0.39	14	43	0
P4	-110	1532	0.36	2	196	0

Table 3.2 summarizes the location, magnitude and rise time of the maximum mean pressure, the averaged void fraction in pressure rise time (A_r), and the *impulsiveness* measured for all pressure measurement points. Ariyarathne et al. (2012) proposed *impulsiveness* as a measure of impact by normalizing the pressure rise rate (dP / dt) by the wave period (T), fluid density (ρ), and squared maximum mean horizontal flow velocity ($U_{\max}^2$). They proposed a threshold value for impulsive impacts as:

$$\left(\frac{dP}{dt}\right) \Big/ \left(\frac{0.5\rho U_{\max}^2}{T}\right) > 100 \tag{3-2}$$

The $U_{\max}$ value was estimated as 1.3C (i.e., the dominant velocity of the approaching wave) in the present experiment. The values of impulsiveness for both measurement points P1 and P2 are over 100, indicating the breaking wave impacts are of impulsive type. On the contrary, the values at P3 and P4 are way below the threshold value. As a result, as expected, these impacts are non-impulsive. Furthermore, high speed images and FOR signals both indicate that P3 and P4 were fully submerged throughout the wave breaking event, implying that the pressures at P3 and P4 are hydrostatically dominated.

Unlike an overturning structure observed on a fixed structure in Ryu et al. (2007a), the bubble cloud in the present study mainly moved in the direction of wave propagation and expanded vertically downward. The horizontal fluid velocities at P1 and P2 were so high that the air bubbles were pushed toward the wall and then forced to move up or down (vertical expansion of the bubble cloud). As a result, the measured void fraction in Figs. 4(a) and 4(b) reflected what the optical fibers sensed at the measurement points P1 and P2. The void fraction at P3 is, however, relatively low, as shown in Fig. 3.4(c). The cause is likely associated with the moving structure. According to the velocity map presented by Ryu et al. (2007a), if the structure is fixed, the air bubbles in front of P3 will move horizontally against the wall. The measured void fraction at P3 would probably be as high as what P1 and P2 experienced. In the present study, the structure is moving. The forward moving structure drove fluid to fill in the wake region that was originally occupied by the structure. Accordingly, the bubble cloud moved at a velocity very close to the structure U velocity along the positive x direction. We infer that a water film (very low aeration) existed between the structure wall and the lower portion of the bubble cloud (the water film could not be observed right in front of the wall due to the blockage created by an aerated flow entering the 25-mm clearance between the lateral structure wall and the front tank wall). Based on that, the bubble cloud at P3 and below had little chance to reach the structure wall so that the measured void fraction at P3 was relatively low.

High speed images show that the overturning jet of the breaking wave made contact with the frontal water surface within an 80-mm range in front of the vertical structure wall. As shown in Fig. 3.5(a), the overturning jet impinged the front water surface and entrained air. Shortly after the impingement, the rising wave trough and the overturning jet converged at P2 and caused a rapid rise of impact pressure. Figure 3.5(b) shows the moment of the peak pressure at P2. One can see that the wave trough reached P2 before the wave front impinged the vertical wall. The wave trough provided a cushioning effect against the direct impact at P2. In comparison, Fig. 3.5(c) shows the wave front had a direct impact at P1. Although sandwiched by water droplets and air bubbles, their relatively low mass density shown in the figure seems unable to weaken the strong impact pressure, which reached a level nearly twice of that at P2.

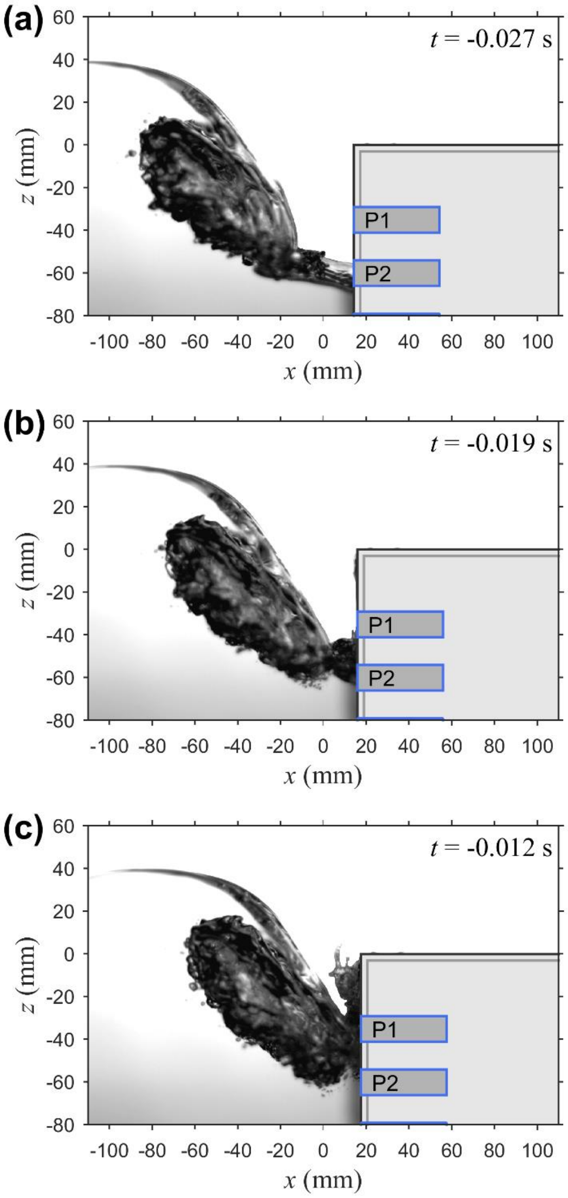

Figure 3.5 Demonstration of the water cushion at P2 during the breaking wave impact.

Based on the 30 repeated measurements, correlations between the instantaneous peak pressures ($p_{\max}$) at P1 and P2 and the distance of the breaking wave impingement points from the vertical wall (x_{imp}) are plotted in Fig. 3.6. At P1, $p_{\max}$ and x_{imp} are negatively correlated: $p_{\max}$ increases as x_{imp} decreases. The observation is in agreement with Chan and Melville (1988). On the contrary, at P2 which is near the lowest bound of the breaking wave impact zone, no clear correlation is observed. Chan and Melville (1988) reported a similar observation that the variation of the pressure maximum at the lower bound of the breaking wave impact zone did not increase with the decreasing x_{imp}. Furthermore, a small number of the test realizations at P2 have maximum pressures higher than that at P1. Examination of high-speed images reveals that in these tests the wave trough did not arrive at P2 in time before the breaking wave front collided with P2. The impact mechanism in these tests is similar to that at P1, and so is the pressure magnitude.

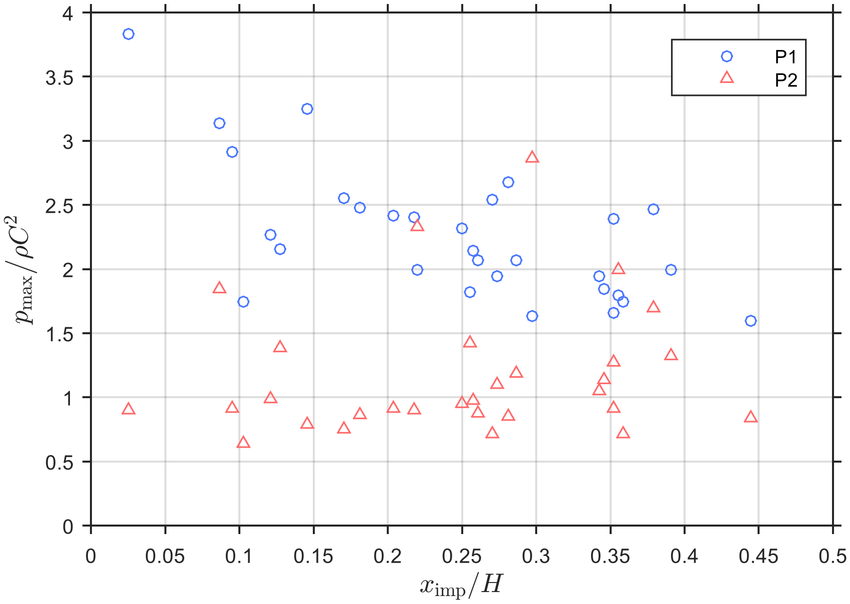

Figure 3.6 Relation between normalized breaking wave impingement points x_{imp} and impact pressure maxima p_{max} at measurement points P1 and P2.

Figure 3.7(a) examines the variation of the pressure maxima in box plot for all four measurement points. With an identical wave condition applied, the pressure maxima at P3 and P4 have only a minor variation, whereas the pressure maxima vary significantly at P1 and P2. The standard deviations for P1 and P2 are 2.19 kPa ($0.52\rho C^2$ or 23% of P_{max} at

P1) and 2.16 kPa ($0.51\rho C^2$ or 42% of $P_{\max}$ at P2), respectively. Song et al. (2015) found that the variation of the relative impact pressure maxima due to broken wave impact could be approximately represented as a Gaussian distribution. Following their conclusion, the normality of the present measured pressure maxima was examined and presented in Fig. 3.7(b). Note that the data used in the figure is the instantaneous pressure maxima normalized by the mean pressure maximum at each measurement point. It is clear that the probability distribution is slightly left-skewed with a heavy tail toward increasing peak pressure. The same heavy tail feature is also observed in the occurrence rate distribution measured by Song et al. (2015). To a certain extent, it may be acceptable to state that the distribution of maximum pressures is close to Gaussian. However, it is interesting to fit the pressure maxima with other well-known probability distributions. Figure 3.7(c) presents the comparison of various probability distribution fits, including normal, lognormal, Weibull, Rayleigh, and gamma distributions. Among them, the lognormal and gamma distributions are able to capture the left-skewed extreme, while the lognormal distribution seems to fit the best in the comparison. On the other hand, the Rayleigh distribution fails to enclose most measured data, but it describes the heavy tail better than other distributions. Since only one wave condition was considered and the scale effect was not evaluated, the lognormal distribution or the Rayleigh distribution may not be directly applicable to engineering design. In addition, a sufficient number of data is needed to reduce the level of uncertainty in identifying a suitable probability distribution model. In the absence of such additional data, however, the lognormal or similarly skewed distribution is reasonable for purposes of estimating the probable maximum pressure.

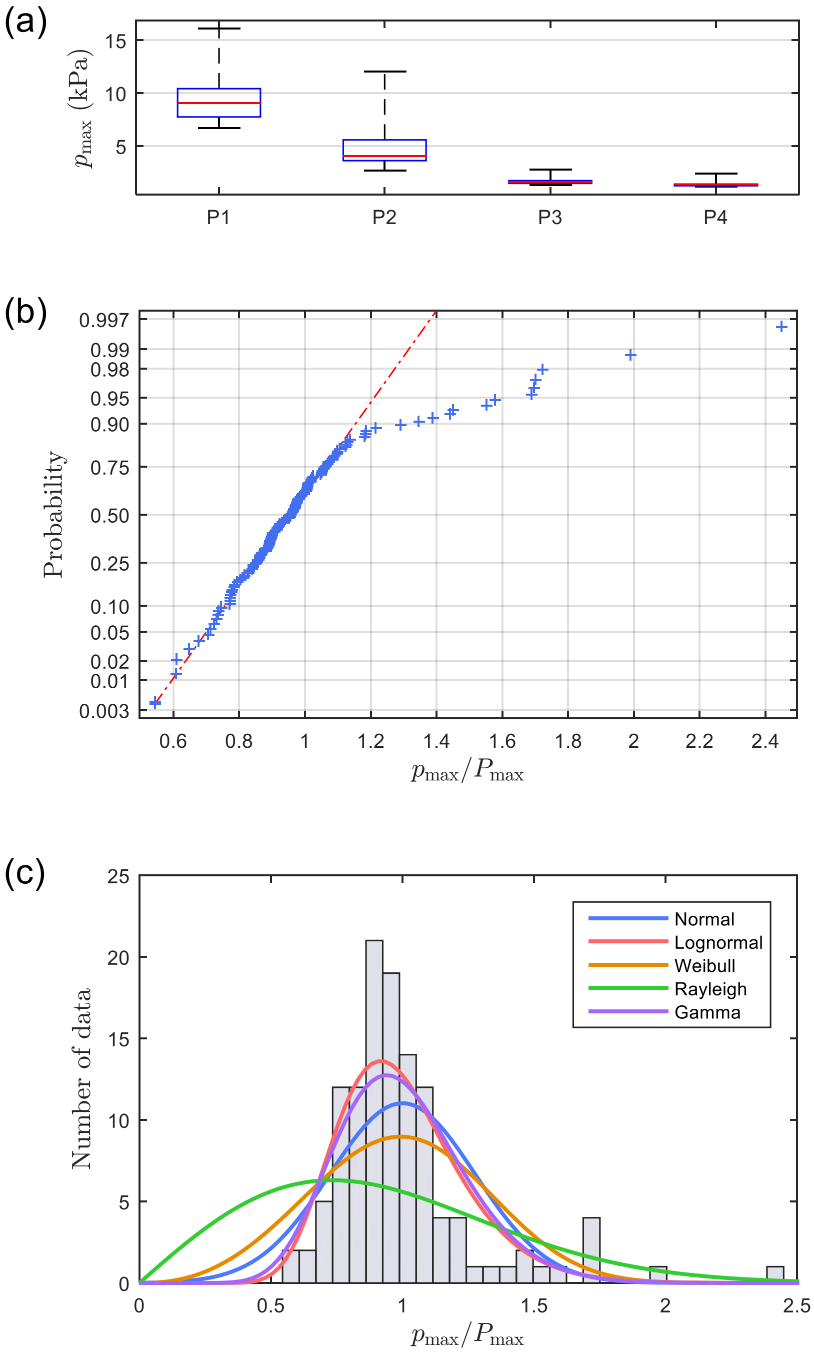

Figure 3.7 (a) Box plot of all measured pressure maxima. (b) Normal plot. (c) Normalized maximum pressure historgram fitted with typical probability distributions.

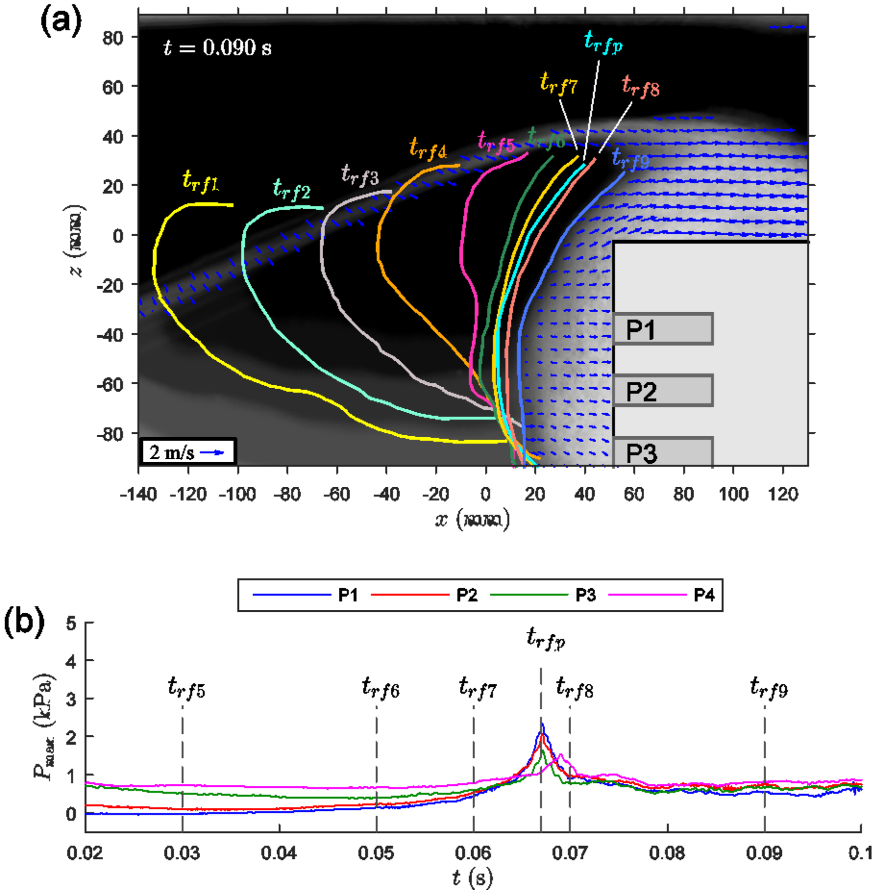

Figure 3.8 (a) Evolution of the rear face of the overturning breaking wave. (b) Selected moments on the time series of mean pressure time histories.

In Fig. 3.4, a double-peak pressure time history (with the second peak at around t = 0.07 s for P1 to P3) was observed. As mentioned earlier, the first peak was caused by breaking wave front impact on the structure, so the second peak occurred after the passing of the broken wave crest. A similar pressure signature was observed by Chan et al. (1995), but the cause of the second peak was not elucidated. With the aid of the high-speed images, the evolution of the rear face of the overturning breaking wave (i.e., the rear side of the entrained air pocket as clearly shown in Fig. 3.5) is demonstrated in Fig. 3.8(a). By matching Fig. 3.8(a) with the measured pressure time histories in Fig. 3.8(b), one can conclude that the impact of the rear face led to the rise of the second peak. After the first impact due to the breaking wave crest, pressure sensors P1 to P3 simultaneously recorded the second peak at around t = 0.067 s, while a 2 ms delay was observed at P4. The magnitude of the second peak decreases from P1 (2.34 kPa or $0.56\rho C^2$) to P4 (1.10 kPa or $0.26\rho C^2$). All the second peak profiles are church-roof like, and all the pressure sensors and FOR probes were below the wave crest and in full contact with the bubble cloud formed by the overturning broken waves. Hence what the pressure sensors measured was the impact formed by wave momentum, air compressibility, and hydrostatic pressure.

3.3.2 Relationship between peak impact pressure and pressure rise time

The relationship between the peak impact pressure ($p_{\max}$) and the pressure rise time (t_r) has been examined by researchers (e.g., Weggel and Maxwell 1970; Blackmore and Hewson 1984; Kirkgoz 1990; Hattori et al. 1994; Cuomo et al. 2010(b); Ariyarathne et al. 2012; Song et al. 2015) using an empirical form:

$$p_{\max} = a t_r^b \tag{3-3}$$

where a and b are empirical coefficients determined by curve fitting. Since this relationship is not written in non-dimensional form, the coefficients a and b are scale dependent. It is thus difficult to apply the formula to evaluate the full-scale $p_{\max}$ versus t_r relationship based on results obtained from scaled-down physical model tests. As a result, Kisacik et al. (2012) proposed a dimensionless form of the formula by normalizing t_r with the wave period and $p_{\max}$ with the maximum hydrodynamic pressure estimated from non-breaking waves (Goda 2000; Oumeraci et al. 2001). For breaking waves, a time scale derived from the wave phase speed and wave height may be considered as more relevant than the wave period in producing high impulsiveness. Furthermore, the phase speed is more relevant to the dynamic pressure in breaking waves. As a result, a new dimensionless relationship with scale independent coefficients a' and b' is expressed as:

$$\frac{p_{\max}}{\rho C^2} = a'\left(\frac{t_r C}{H}\right)^{b'} \qquad (3\text{-}4)$$

Note that the left hand side term is the equivalent of the impact coefficient denoted in Song et al. (2015). The present study uses *H/C* as the normalization time scale for t_r in Eq. (3-4).

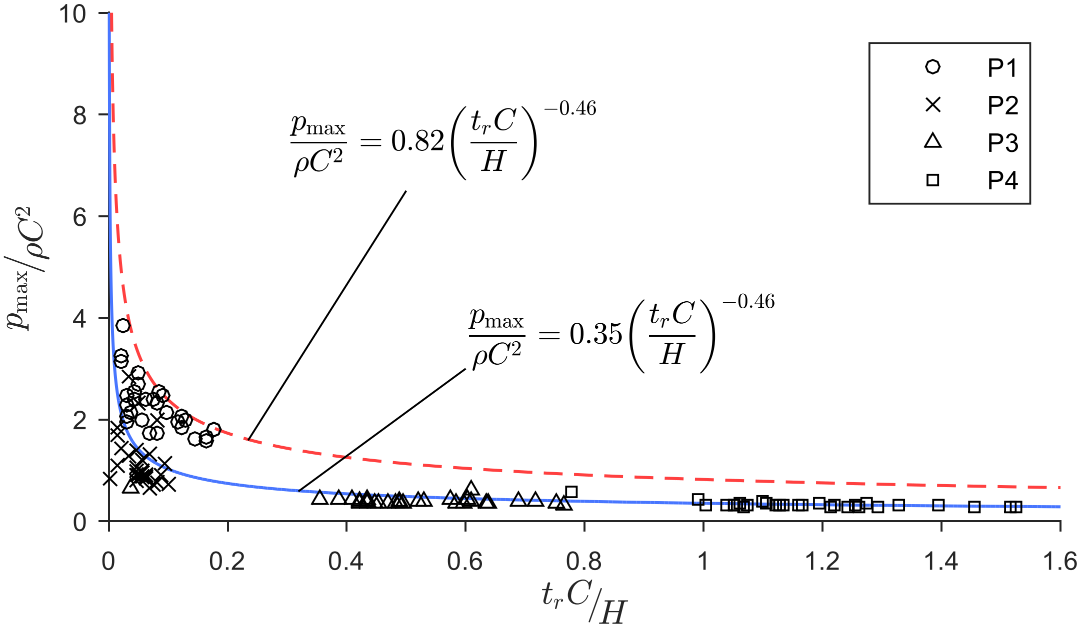

Figure 3.9 Relation between the rise times t_r (normalized by *H*/*C*) and the impact pressure maxima p_{max} normalized by ρC^2. *Blue solid line* represents the curve fit of the data, while *red dashed line* is the envelope of the data.

Using instantaneous pressure measurements from all four sensors, Fig. 3.9 plots the normalized $p_{\max}$ against the normalized t_r with a least square regression fit of $a' = 0.35$ and $b' = -0.46$ based on Eq. (3-4). An upper envelope curve with coefficients $a' = 0.82$ and $b' = -0.46$ was also obtained by shifting the regression curve up to enclose all the data points. In the literature, reported values of *b* vary from -0.33 to -1, while the value of *a* varies more considerably. In the present study, the value of b' obtained from the normalized $p_{\max}$ versus t_r relationship still stays within the range. In addition, $a' = 0.35$ is consistent with the value of 0.24 reported by Kisacik et al. (2012) as well as 0.22 and 0.35 reported by Kisacik et al. (2014). For impulsive impacts, t_r at P1 and P2 is shorter than 15 and 8 ms (or $0.18H/C$ and $0.10H/C$), respectively. For non-impulsive impacts, a fairly wide range of t_r at P3 was observed, ranging from 30 to 64 ms (or $0.36H/C$ to $0.77H/C$), while an even wider range of 65 to 127 ms (or $0.78H/C$ to $1.53H/C$) was found at P4.

In summary, the present experiment shows that $p_{\max}$ is negatively correlated with t_r in the event of breaking wave impact on a TLP model structure. The observation is in agreement with previous findings based on fixed model structures. Moreover, the aeration level may affect the coefficients in Eq. (3-3) (Song et al. 2015). Since the void fraction measurements are available, the instantaneous fluid density variation $(1-\alpha_r)$ averaged over the pressure rise time may be incorporated in the pressure coefficient as a correction to the mass density, i.e., $p_{\max}\Big/\left[(1-\alpha_r)\rho C^2\right]$. The consideration of fluid density variation changes the value of b' slightly to -0.63, but it seems to have an insignificant effect on the value of a' in the curve fit.

3.3.3 Correlation between impact pressure and flow velocity

Since the velocities are measured with a high spatial resolution using BIV, it would be useful if the impact pressures can be estimated using the measured velocities. The present study follows Ariyarathne et al. (2012) and Song et al. (2013, 2015) in which the maximum pressures were related to the kinetic energy of the flow by the so-called impact coefficient (c_i). According to Ariyarathne et al. (2012), the correlation between $P_{\max}$ and $U_{\max}$ is formulated as:

$$P_{\max} = c_i \rho U_{\max}^2 \tag{3-5}$$

where $U_{\max}$ is evaluated from the entire flow field. The use of only the horizontal velocity (u or U) is justified by the orientation of the pressure sensors (facing the $-x$ direction). Moreover, the wave propagation also infers that the u or U velocity plays a dominant role in creating the maximum impact pressure against the vertical wall.

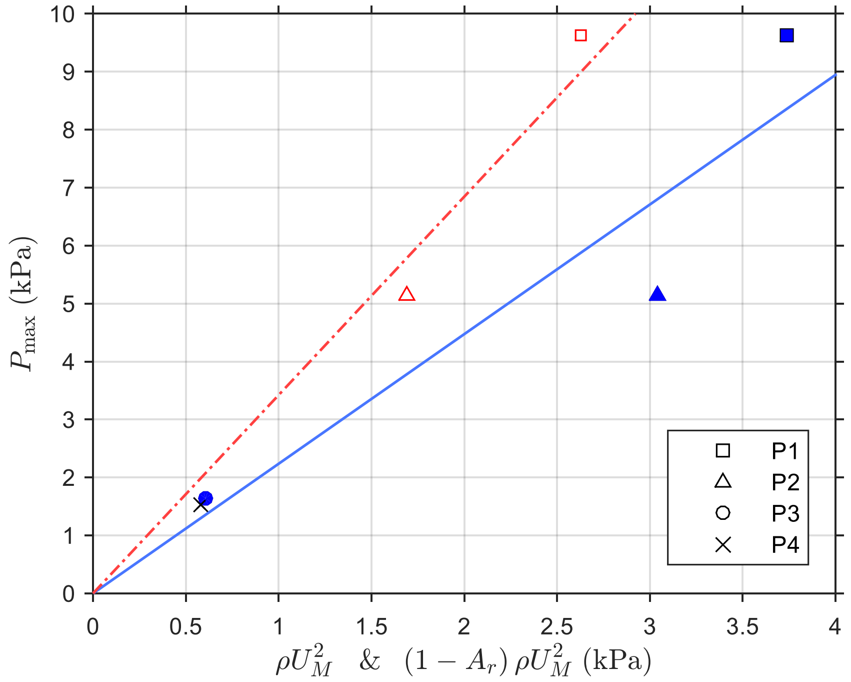

Figure 3.10 Relation between the impact pressure maxima and the local kinetic energy density determined by the maximum local horizontal fluid velocity. *Red empty markers* and *blue filled markers* represent the consideration with and without fluid density variation, respectively.

In the present study, we replaced $U_{\max}$ with U_M which is defined as the maximum local U velocity at a pressure sensor. The local U velocity (U_L) is evaluated by averaging the horizontal velocity vectors in a small window of 0.5d × 1d in front of a pressure sensor end face with d (= 12 mm) being the diameter of the pressure sensor end face. The impact coefficient thus becomes the ratio of the pressure maximum and the local kinetic energy density maximum in front of each pressure sensor end face. Confirmed by examining the high speed images and the void fraction evolution presented in Fig. 3.4(c), the velocities at P3 and P4 are not available because of a lack of air-water interfaces at P3 and below during the breaking wave impact. By assuming a uniform U velocity profile over a 20-mm vertical distance, the impact velocity at P3 was approximated by the available vectors

10 mm above its measurement point. The impact velocity at P4 was approximated by extending the linear wave theory above the still water level and calculating the *U* velocity at its measurement point.

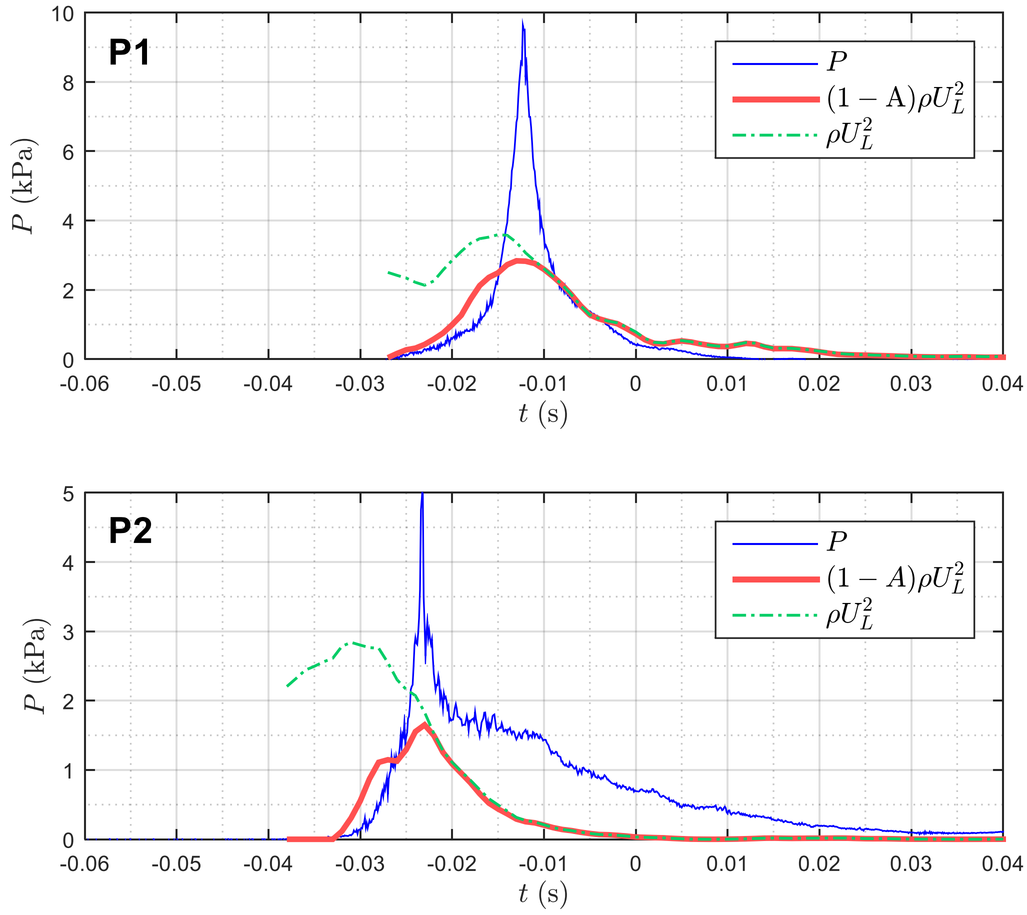

Figure 3.11 Time histories of mean pressure and local kinetic energy density with and without fluid density correction at P1 and P2.

In the process of breaking wave impingement, air bubbles are entrained and cause the flow to become multiphase so an assumption of zero void fraction (i.e., 100% water) may not be appropriate. Hence a modification to Eq. (3-5) by correcting the fluid density with A_r may be needed. Accordingly, the revision can be written as:

$$P_{\max} = c_i\left(1 - A_r\right)\rho U_M^2 \tag{3-6}$$

where c_i is the impact coefficient. Figure 3.10 plots the impact pressure maxima against the corresponding local kinetic energy density with and without the consideration of fluid density variation. The values of impact coefficient are 3.4 and 2.2 with and without the fluid density correction, respectively, determined by linear least-square regression. The value with the fluid density correction is roughly 50% higher.

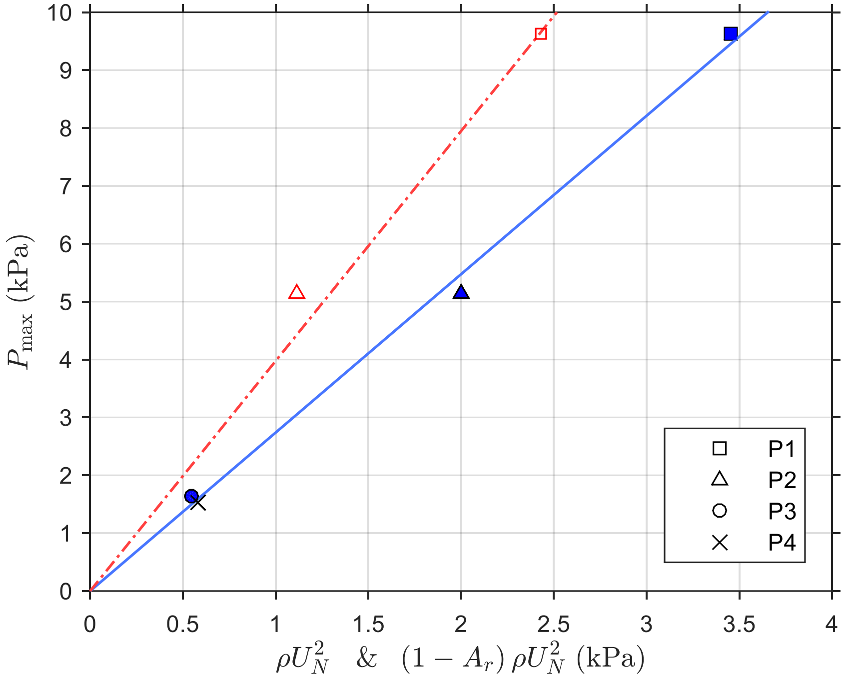

Figure 3.12 Relation between the impact pressure maxima and the local kinetic energy density determined by the corresponding local horizontal fluid velocity. *Red empty markers* and *blue filled markers* represent the consideration with and without fluid density variation, respectively.

Figure 3.11 presents the time histories of the mean pressure and the mean local kinetic energy density with and without the consideration of void fraction at P1 and P2. The figure shows that the mean pressure maxima and mean maximum kinetic energy densities without density correction did not occur simultaneously at both measurement locations.

On the contrary, after the correction of fluid density variation the mean pressure maxima were coincident in occurrence with the mean maximum kinetic energy densities (with a lag of about only 1 ms). However, the simultaneous occurrence of the maxima was not always observed from the instantaneous data with a corrected fluid density. At P1, 18 of the 30 test runs show that both peaks are coincident without the corrected fluid density, while the number increases slightly to 21 with the corrected fluid density. At P2, only 1 out of the 30 runs is coincident without the corrected fluid density, but the number increases significantly to 18 with the consideration of void fraction. Based on the observation and discussion above, it may be more appropriate to replace the velocity term in Eq. (3-5) and Eq. (3-6) with the local U velocity coincident to $P_{\max}$ (i.e., U_N). The results are plotted in Fig. 3.12. With a lower local kinetic energy density calculated using U_N, the value of averaged impact coefficient increases to 2.8 (without the corrected fluid density) and 4.0 (with the corrected fluid density). The linear regressions also demonstrate a higher correlation between the pressure maximum and the local kinetic energy density when compared with Fig. 3.10, especially when the density variation is not considered.

The instantaneous impact coefficients of the impulsive impacts at P1, P2 and P3 evaluated from the instantaneous pressure maxima ($p_{\max}$), the local u velocity coincident to $p_{\max}$ (i.e., u_N), and α_r were examined and are plotted in Fig. 3.13(a) in the form of mean points with a shaded area. Note that the shaded area represents the confidence interval within one standard deviation. The value of the instantaneous impact coefficient ranges from 0.6 to 4.3 with an average of 1.8 obtained from linear regression over 90 instantaneous data points. If the fluid density variation is considered, as shown in Fig. 3.13(b), the confidence interval becomes narrower. The value of the instantaneous impact coefficient ranges from 1.3 to 9.7 (with the $\alpha_r = 1$ data points being neglected). Comparing to the peak pressure variation as presented in Fig. 3.7(a), it is expected that the complex nature of the breaking wave impact caused scattering of the instantaneous values. The

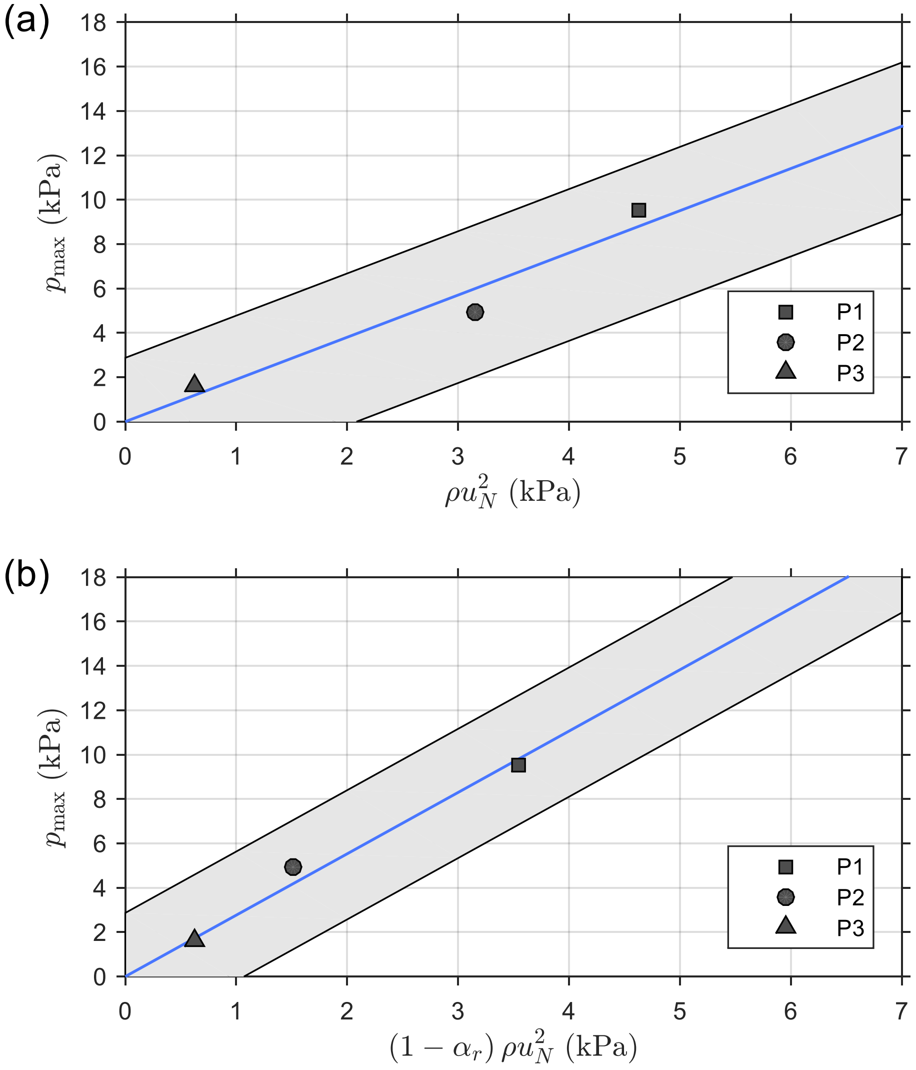

Figure 3.13 Relation between the instantaneous impact pressure maxima and their corresponding local kinetic energy densities without (a) and with (b) the consideration of fluid density variation. Note that the shaded area represents the confidence interval within one standard deviation.

overall trend of the instantaneous values can still be captured by the lines derived from Eq. 5 and Eq. 6. However, one should be cautious that the extreme value may be averaged out. For example, the maximum impact coefficient derived from the instantaneous values is twice the mean value.

Table 3.3 Summary of the impact coefficients at measurement points P1 and P2 evaluated by different approaches.

	P1		P2	
Consider fluid density variation?	Yes	No	Yes	No
$\frac{P_{\max}}{\rho(C-S)^2}$	4.1	2.9	2.7	1.5
$\frac{P_{\max}}{\rho U_M^2}$	3.7	2.6	3.0	1.7
$\frac{P_{\max}}{\rho U_N^2}$	4.0	2.8	4.6	2.6
$\frac{p_{\max}}{\rho u_N^2}$	1.5 ~ 6.1	1.3 ~ 4.3	1.3 ~ 9.7	0.6 ~ 3.9

Table 3.3 summarizes the impact coefficients evaluated by different approaches in the present study, and Table 3.4 summarizes the average impact coefficients among those approaches. The average impact coefficients obtained in the present study are up to twice those reported by Ariyarathne et al. (2012) and Song et al. (2015). These two studies examined the impact pressures due to the green water flow generated by breaking wave impingements at two different physical scales. Ochi and Tsai (1984) reported impact coefficients between 2.74 (broken wave impact) and 5.98 (breaking wave impact) from measurements. The range agrees with what was found in the present study. Chan and Melville (1988) reported a considerable variation of impact coefficient, ranging between 0.5 and 40, evaluated from wave impact on plates and cylinders with the pressure normalized by ρC^2. Based on the comparison, the present study confirms that the pressure maximum is proportional to the squared local flow velocity for a moving structure under breaking wave impacts. However, detailed information on the local velocities related to the structure motion, such as U_M, U_N, and u_N, and void fraction may not be readily

available. For practical applications, obtaining the phase speed C is relatively straightforward.

Table 3.4 Summary of the averaged impact coefficients evaluated by different approaches.

Consider fluid density variation?	$\frac{P_{\max}}{\rho U_M^2}$	$\frac{P_{\max}}{\rho U_N^2}$	$\frac{p_{\max}}{\rho u_N^2}$
Yes	3.4	3.9	2.5
No	2.2	2.7	1.8

It is worth pointing out that in random seas a floating structure may move in or opposite to the wave propagation direction. The effect of the structure motion thus needs to be considered. A modified expression for $P_{\max}$ with the consideration of the corresponding horizontal structure velocity (S) as well as void fraction can be formulated as:

$$P_{\max} = c_i' \rho \left(C - S\right)^2 \tag{3-7}$$

where c_i' is for impulsive type impact coefficient with and without the fluid density correction with its values summarized in Table 3.3. According to the table, $c_i' = 2.9$ may be used for evaluating the pressure maximum due to the breaking wave impact on the vertical surface of a moving structure.

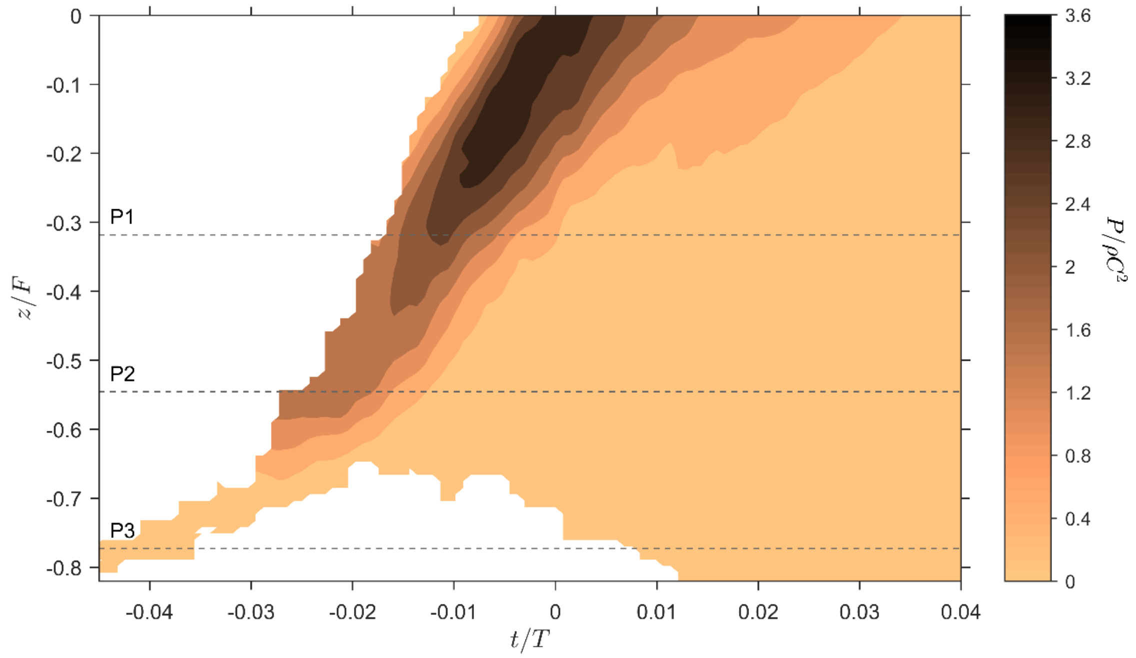

Figure 3.14 Temporal and spatial distribution of the calculated pressure $P = 2.9\rho U_L^2$ (normalized by ρC^2) on the vertical wall of the model structure. Note that the *dashed lines* represent the pressure measurement points, and the vertical and horizontal coordinates are normalized by freeboard (*F*) and wave period (*T*), respectively.

Figure 3.14 further shows the spatial and temporal pressure distribution along the structure frontal wall calculated using the BIV velocities and the averaged impact coefficient (c_i = 2.9) using Eq. (3-5) but replacing $U_{\max}$ with U_L. In the figure, the magnitude of pressure decreases from the deck surface level to the still water level, consistent with the direct pressure measurements. From the contour, it is anticipated that the highest pressures on the structure wall are between the deck surface and the measurement point P1, equivalent to from *H*/2 above the still water level to the deck surface level. The calculated pressure in this region reaches up to $3.4\rho C^2$, nearly 50% higher than the maximum measured pressure of $2.3\rho C^2$. The calculated results indicate that evaluating the probable maximum pressure by breaking wave impacts on the vertical surface of a floating platform may be conducted by placing pressure sensors right below the deck level.

3.3.4 Correlation between impulsive impact pressure and void fraction

Many studies have shown that air bubbles and pockets in breaking waves play a crucial role in the magnitude and temporal distribution of impact pressures. However, existing pressure-aeration measurements under breaking wave impacts are very limited, and attempts to correlate the impact pressure and aeration level are rare. A few valuable measurements were conducted by Bullock et al. (2001) on field measurements at different elevations of a breakwater and Bullock et al. (2007) in a large-scale laboratory wave tank. In both studies the pressure-aeration data were obtained using a pressure-aeration device which senses the change in the electrical conductivity of the intervening volume. The device is very sensitive to environmental factors such as salinity and temperature (Bird et al. 1998). Bullock et al. (2001) examined the correlation between the impact pressure and the aeration level. Interestingly, they found no clear trends regardless whether the corresponding aeration level (coincident to the pressure maximum) or the ambient aeration level (equivalent to the averaged void fraction in the pressure rise time) was used in correlating with the pressure maximum. Their scattered plots may also indicate the absence of elevation dependence.

In the present study, the void fraction measurements using FOR are less sensitive to the environment factors because the probes detect the difference in refractive indices between water and air, which is fairly large. Similar to the approach and observation in Bullock et al. (2001), a direct correlation between $p_{\max}$ and α_r, as shown in Fig. 3.15(a), results in a scattering plot as well. However, if considering all data points in the figure but neglecting the ones with zero void fraction, the overall trend seems to show a somewhat negative pressure-aeration relationship. In other words, a high aeration level seems to reduce the pressure maximum, implying the cushioning effect due to air bubbles may be a cause.

Bullock et al. (2001) confirmed the pressure-aeration relationship through drop tests and suggested a pressure reduction factor, but it is unclear whether their physical model represents the scenario of a plunging breaking wave impact. Peregrine and Thais (1996) derived approximate solutions by modeling the flip-through wave impact as filling flow in a liquid container to address the entrained air effect in wave impact. The filling flow cannot represent wave propagation, but it may be able to resemble the local process of breaking wave impact (Peregrine and Thais 1996; Bredmose et al. 2015) based on the similarity of the flow rapidly filling a confined region. Therefore, the present study attempted to model the plunging breaking wave impact as a filling flow and compared the measured data with the available approximate solutions.

Peregrine and Thais (1996) extended the work of Peregrine and Kalliadasis (1996) for the filling flow by modeling the compressibility effects with the assumption that incompressible water contains homogeneously distributed small air bubbles. In addition, by assuming an adiabatic process in the polytropic law, a pressure-density relation for the equation of state was obtained for compressible air bubbles. An approximate solution for the excess pressure (p') in the filling flows was derived as:

$$\frac{p' - p_0}{0.5\rho u_0^2} = \frac{2}{\left(\varepsilon + \beta_0\right)} \qquad (3\text{-}8)$$

where p_0 is the atmospheric pressure, u_0 is the velocity of the incoming jet, β_0 is the volume fraction of air bubbles at atmospheric pressure, and the subscript 0 refers to the initial condition of the incoming jet. The parameter ε ($= 1 - e/E$) is a measure of the violence of the incoming jet, where e is the thickness of the incoming jet and E is the height of the container being filled. For p' at the stagnation point (termed as p_s'), the solution becomes:

$$\frac{p_s' - p_0}{0.5\rho u_0^2} = \frac{1}{\left(\varepsilon + \beta_0\right)^2} \qquad (3\text{-}9)$$

In order to perform a comparison, matching the variables between the solutions and the present study is required. The measured $p_{\max}$ of impulsive impact is used as input in both $p' - p_0$ and $p_s' - p_0$, u_0 is replaced by u_N (instantaneous u velocity corresponding to

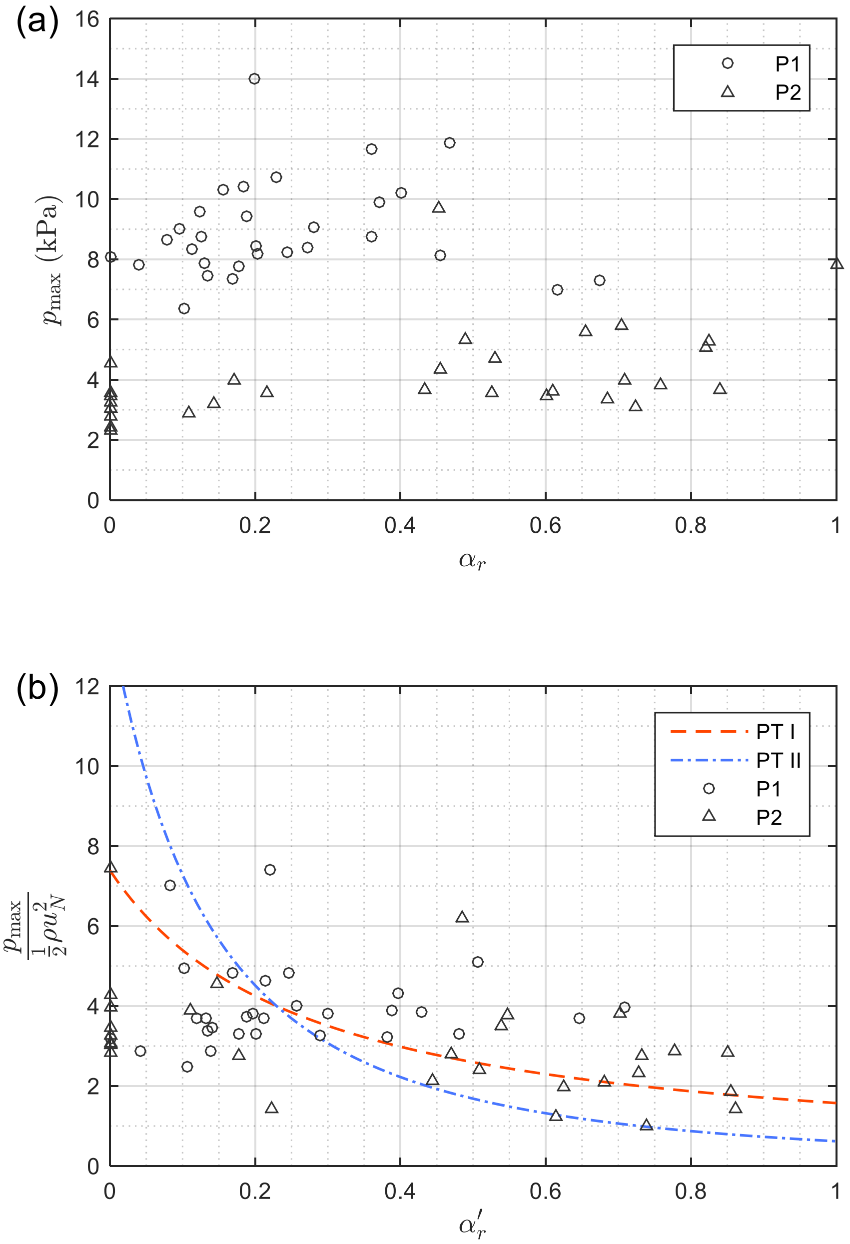

Figure 3.15 (a) Instantaneous pressure maxima versus void fraction at measurement points P1 and P2. (b) Comparison of the measured data (characterized as impulsive type) and the approximate solutions of Peregrine & Thais (1996). *Red dashed curve* (PT I) represents the relationship between the excess pressure (p') in the filled portion of the space and α'_r; *blue dash-dot curve* (PT II) represents the relationship between p' at the stagnation point (p'_s) and α'_r.

$p_{\max}$), and β_0 is replaced by $\alpha_r' = \alpha_r \left(1 + p_{\max}/p_0\right)^{\gamma}$ with an assumption of the ideal gas and adiabatic behavior ($\gamma = 1.4$). Note that α_r' represents α_r at the atmospheric pressure. To evaluate ε, E is approximated as H, while e is approximated as the thickness of the plunging breaking wave jet.

Figure 3.15(b) plots the normalized pressure maxima against void fraction at atmospheric pressure with the curves from Eq. (3-8) (denoted as PT I) and Eq. (3-9) (denoted as PT II). Unlike the scatter in Fig. 3.15(a), the pressure coefficients for measurement points P1 and P2 are closer in magnitude, and the scatter is significantly reduced at lower α_r'. Comparing with the approximate solutions, the curve for the filling pressure (PT I) fits the data better than that for the stagnation pressure (PI II). Based on the Bernoulli equation, the stagnation point is the point with a zero velocity in all directions. However, as the maximum impulsive-type pressures occur, non-zero vertical velocities are found in front of the pressure sensor for all the tests. As a result, modelling the breaking wave impact as filling pressure may be more appropriate. According to the approximate solutions, a zero aeration level is expected to generate the least cushioning effect. For the data points with zero void fraction measured at P2, as mentioned earlier, the wave trough reached P2 slightly ahead of the overturning wave impact. In this scenario, P2 was cushioned, at least to some degree, by the surface of the wave trough instead of the entrained air bubbles. Nonetheless, there is a deviated high pressure point at P2 with a zero void fraction staying on the curve (PT I). After inspecting the high speed images, it is indeed the case when the wave front and wave trough coincided at P2 nearly simultaneously.

Assuming that the impact pressure is primarily dominated by the combined effect of fluid kinetic energy density and compressed air pressure, the ratio of the compressed air pressure to the corresponding fluid kinetic energy density can be evaluated as:

$$\xi = \frac{p_{\max}}{0.5\rho\left(1-\alpha_r'\right)u_N^2} - 1 \qquad (3\text{-}10)$$

Figure 3.16 shows ξ versus α_r' with a parabolic fit. The figure shows that the compressed air pressure portion gains with a higher aeration level, and the increment seems to follow $\alpha_r'^2$. Future work is needed to investigate the relationship and the cause. Furthermore, all the values of ξ are greater than zero, indicating that the compressible air pressure always applies to the breaking wave impact. Even though air compressibility is likely the main source of the non-zero ξ values, it is interesting to see that ξ is also nonzero even with a zero void fraction, as shown in Fig. 3.16. As mentioned in the previous section, there is a good chance that the optical fiber might miss some air bubbles/pockets which impacted the corresponding pressure sensor due to the size difference between the FOR probe and the pressure sensor. However, it is possible to detect the presence of air entrapment by observing the pressure time histories (Lugni et al. 2006). For example, out of the 9 pressure time histories with a zero α_r', intensive oscillations similar to that observed by Lugni et al. (2006) were observed in 6 of them, implying the presence of air entrapment.

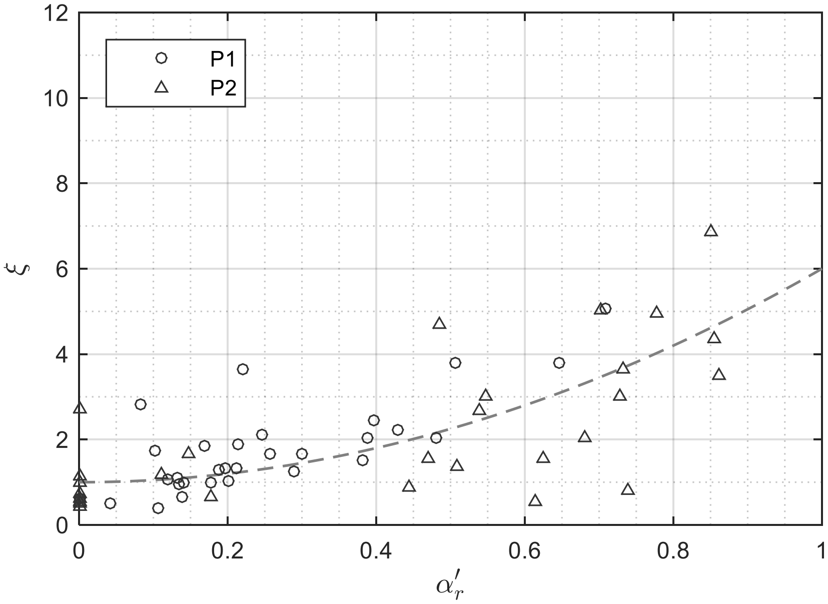

Figure 3.16 Void fraction at the atmospheric pressure versus the ratio of pressure excess to fluid kinetic energy density. The line is a parabolic fit to the data.

It is worth pointing out that air entrapment, although tiny in amount, may occur due to the geometric limitation of the instrument. The end faces of typical pressure sensors are usually not perfectly flat, including the ones used in the present study. This may potentially lead to formation of entrapped air during the initial impact with breaking waves. The tiny air entrapment may then be sensed by the pressure sensor as oscillatory signals. Unfortunately, the FOR probes are unable to detect that phase transition since each optical fiber tip was kept at 5 mm off the corresponding pressure sensor face. On the other hand, the entrapped air is usually associated with an increase in impact pressure (Bagnold 1939; Hattori et al. 1994; Peregrine 2003). The mixed effect of air entrainment and entrapment could be the cause of the scattered data in Fig. 3.15(b) and the insignificant cushioning effect at lower aeration level. However, applying Eq. (3-10) is insufficient to separate these effects. Accordingly, developing new pressure measurement techniques and data processing algorithms to distinguish the effects of air entrainment and entrapment, or simply to minimize one of the effects, on wave impact pressures will be a challenging topic for future studies.

Although the Froude similitude was applied to design the present physical model, it should be especially noted that the physical quantities derived in the present study may not be directly scaled up. For simulating the air bubble dynamics, at least two typical dimensionless quantities – Mach number (for air compressibility) and Weber number – were not considered. The Bagnold-Mitsuyasu scaling law proposed by Cuomo et al. (2010a) may be a solution to correct the factor of the Froude law, but it is derived by only considering the air entrapment effect and requires more validation. As discussed earlier, the air entrainment effect during the plunging breaking wave impact is significant, and unfortunately, no scaling law is valid. Therefore, a scaling law(s) for both air bubble induced effects is very important and desirable.

3.4 Conclusions

Simultaneous pressure, void fraction, fluid velocity, and structure motion measurements were performed on a 2D TLP model structure under a plunging breaking wave impact. Four pressure measurement points with four corresponding void fraction measurements, P1-P4, were located from the still water level to $0.44H$ above the still water level, respectively. The measured quantities were ensemble averaged from 30 repeated tests with identical test conditions. The time histories of pressure and void fraction were presented. The probability distribution of the variation between repeated tests of the relative peak pressure for impulsive impacts was further examined. Correlations between pressure maxima and flow velocity, void fraction, pressure rise time, impingement location, and mean kinetic energy were exhibited and discussed. A dimensionless formula relating the peak impact pressure and its corresponding pressure rise time was obtained. A prediction equation for maximum peak pressure in terms of the structure motion and the wave phase speed is proposed. The pressure-aeration relationship was examined and compared with approximation solutions from Peregrine and Thais (1996). Some conclusions are summarized below:

(1) Double peaks were observed in the pressure time histories at all the measurement points. Breaking wave impact accounts for the first peak, while the second peak is caused by the impact of the rear face of the broken wave (i.e. the rear side of the entrained air pocket).

(2) During the breaking wave impact, the impulsive impact pressures featured a rise time $t_r < 15$ ms (or $t_r < 0.18H/C$). The maximum mean impact pressure reached $2.3\rho C^2$.

(3) The probable maximum pressure may be estimated by using a lognormal or similarly skewed extreme value distribution.

(4) The impact pressure maxima are negatively correlated with the pressure rise time in the event of breaking wave impact on the model TLP structure.

(5) The value of the impact coefficients evaluated by correlating the impact pressure maxima and the fluid velocities, with and without correcting the fluid density,

ranges from 1.5 to 4.6 for ensemble-averaged quantities and from 0.6 to 9.7 for instantaneous quantities. With the correlation of fluid density, the instantaneous quantities show a narrower confidence interval for the instantaneous impact coefficients.

(6) For engineering purposes, $P_{\max} = c_i' \rho (C - S)^2$ may be suggested by including the structure translation velocity (S) and the breaking wave phase speed (C).

(7) With the correlation between pressure and velocities obtained, the entire pressure contour can be estimated. The highest pressures on the structure wall are predicted between $H/2$ above the still water level and the deck surface level.

(8) By modeling the plunging breaking wave impact as a filling flow, it was observed that the pressure maxima were negatively correlated with the aeration level, implying cushioning effects from the entrained air bubbles.

CHAPTER IV

KINEMATICS AND DYNAMICS OF GREEN WATER ON A FIXED PLATFORM IN A LARGE WAVE BASIN UNDER FOCUSING WAVES AND RANDOM WAVES

4.1 Introduction

Extreme wave impingements on marine structures are a greatly concerned hydrodynamic issue to coastal and ocean engineering structures, such as oil rigs, FPSOs (floating production storage and offloading systems), offshore wind farms, ships, coast and harbor, and coastal defense structures. Under certain circumstances, high wave crests could overtop a deck and create so-called green water. Green water flows have been numerically and experimentally investigated for decades. Notably, Buchner (1995) performed an experimental investigation on a scaled FPSO. Nielsen and Mayler (2004) utilized a Navier-Stokes solver by treating the free surface with the volume of fluid (VOF) method, and their 2D simulations show good agreement with the data from Buchner (1995). When extending to 3D simulations and accounting for vessel dynamics, they concluded that 3D effects are insignificant.

To study green water, obtaining the green water velocities is crucial to improve our understanding of the flow. However, green water flows are in general aerated and highly turbulent in nature which makes velocity measurements very difficult. To measure the aerated flow field, Ryu et al. (2005) introduced the bubble image velocimetry (BIV) technique based on particle image velocimetry (PIV). Unlike PIV that requires a laser light sheet, BIV only needs a uniformly illuminated background, like laser-emitting diode (LED), to enhance the shadow contrast created by air-water interfaces. The shadow texture is then employed as tracer in cross-correlation for velocity determination. In the last decade, the BIV technique has been successfully applied to various violent aerated flow problems, including liquid sloshing (Song et al. 2013), hydraulic jump (Lin et al. 2008), deep-water plunging breaking wave processes (Lim et al. 2015; Na et al. 2016), and plunging breaking wave impingements on fixed structures (Ryu et al. 2007a, 2007b, 2008;

Chang et al. 2011; Ariyarathne et al. 2012; Song et al. 2015) and on a moving structure (Chuang et al. 2015, 2017). In most of these studies, high speed photography was employed over a limited duration of image acquisition (generally 2 to 3 seconds for a full resolution setting). As a result, they used focusing waves or a prescribed flow condition that allow the repeatable flows and events to be recorded for subsequent analysis. Mori and Cox (2003) developed a statistical model to predict wave overtopping volume and occurrence rate of extreme waves on a fixed deck. To remedy the deficiencies of linear random wave theory and nonlinear regular wave theory in estimating maximum velocity, they concluded the need to investigate statistical characteristics of green water flow velocities under random waves. However, the application of BIV to random green water events (i.e., green water generated by random waves) remains to be explored.

Based on qualitative observation, Buchner (1995) proposed that green water may be modeled as a dam break flow. Green water has since been routinely modeled as a dam break flow to determine the flow velocity in structural design (Schoenberg and Rainey 2002). However, a quantitative verification on the similarity between green water flows and dam break flows was not available until Ryu et al. (2007b) in which the Ritter solution (Ritter 1892) was employed to compare the green water flow on a fixed structure. Chuang et al. (2015) further showed the validity of Ritter solution in quantitatively describing the green water velocity distribution on a moving structure. Nevertheless, both Ryu et al. (2007b) and Chuang et al. (2015) only considered the green water scenario caused by plunging breaking waves generated using a wave focusing method in a laboratory. The appropriateness of the Ritter solution remains unclear for the green water events under random waves. In addition to verifying dam break flow similarity, Ryu et al. (2007b) and Chuang et al. (2015) both obtained nonlinear prediction functions based on dimensional analysis and self-similar flow velocities proposed by Ryu et al. (2007b). Similarly, the applicability of the prediction functions for green water flows under random wave events remains unclear.

When a structure is impinged by large waves, the high impact pressures may cause local damage and in turn threaten the structural integrity. Our evaluation on the impact pressures caused by non-breaking waves has become more accurate and routine in the engineering designs. For breaking waves, on the other hand, our knowledge and understanding on such impact processes and induced pressures and forces are still in the development stage due to the complex nature of the flow that are highly turbulent and multiphase, and involves a deformed and discontinued free surface. Such a complex flow not only hinders the development of numerical and theoretical models to simulate the flow, it also hampers efforts to measure the flow quantitatively in laboratory. However, from Bagnold's (1939) early pioneer, systematic laboratory investigation on breaking wave impact pressures to the recent advances and development of new measurement techniques, our understanding of breaking wave impact pressures has been greatly improved. Below are some important works and conclusions related to breaking wave impacts: (1) the wave impact pressures greatly depend on the location of the impingement point relative to the structure (Ochi and Tsai 1984; Chan and Melville 1988; Hattori et al. 1994; Ariyarathne et al. 2012). (2) The wave impact pressures are deeply associated with the shape of incipient waves upon collision with the structure (Hattori et al. 1994; Hull and Muller 2002; Peregrine 2003; Bullock et al. 2007). (3) The wave impact peak pressures vary considerably even if an identical wave condition is applied to the measurements (Hattori et al. 1994; Hull and Muller 2002; Peregrine 2003; Bullock et al. 2007).

Compressibility of air plays an important role in the breaking wave impact process. Some researchers (e.g., Chan and Melville 1988; Zhou et al. 1991) suggested that the peak pressure variation in the process may be caused by air entrapment occurring on a solid boundary. Chan and Melville (1988) reported a systematic study on impact pressures due to plunging breaking wave impinging on a vertical wall. They concluded that air entrapped between the waves and the vertical wall gave rise to a considerable gain in the pressure magnitude. With theoretical work and numerical modeling, Peregrine and Thais (1996) and Bredmose et al. (2009) addressed the effect of entrained air bubbles in the wave impact process. They concluded that the entrained air bubbles play a role in cushioning large wave impact and leading to a reduction in the impact pressure. Furthermore, Bullock et al. (2001) and Ma et al. (2016) carried out drop tests at two different scales and provided an experimental validation on the assumption of cushion effect. However, laboratory and field measurements on breaking wave impacts reported by Bullock et al. (2001) showed no clear relationship between the impact pressure and the aeration level. On the contrary, using the fiber optic reflectometer (FOR) technique (Chang et al. 2003) which allows the measurements of phase transition at the fiber tip located right in front of a pressure sensor, Chuang et al. (2017) showed that the effect of the entrained air bubbles is significant to plunging breaking wave impacts on a moving vertical wall.

The present study experimentally investigates the kinematics and dynamics of green water on a fixed offshore platform in a large wave basin. Both focusing wave condition and random wave condition were tested. A focusing wave train was generated to create two large waves with difference impingement locations. One large wave broke and impinged on the water surface right in front of the vertical wall of the platform, referred as the wall impingement event (Chang et al. 2011). The second large wave directly overtopped the deck and impinged at roughly the mid-deck, referred as the deck impingement event (Chang et al. 2011). For random waves, the JOSWAP spectrum was employed to generate waves with a significant wave height roughly equals to the freeboard.

Free surface elevations and fluid velocities on two perpendicular planes were measured for both wave conditions using wave gauges and BIV. For the focusing wave condition, pressure and void fraction were also measured and synchronized with the free surface and velocity measurements. The focusing wave condition was repeated 20 times in order to calculate ensemble averages. For the random wave condition, the same realization (i.e., an identical wave train) was repeated 5 times to collect a sufficient number of events (179 in the study) for categorization and statistical analysis. Only flow kinematics (i.e., free surface elevations and velocities) were investigated for the random wave condition. Using the dam-break flow to model the green water flows will be presented and discussed. A statistical distribution of maximum velocities over the random green water events will be exhibited, and correlation between the peak pressure and the aeration level will be demonstrated.

4.2 Experiment setup

4.2.1 Wave basin and model structure

Experiments were carried out in a deep-water wave basin housed in the Offshore Technology Research Center (OTRC) located at Texas A&M University. The wave basin is 45.7 m long, 30.5 m wide, and 5.8 m deep, with a 16.8-m deep pit located at the center of the basin. A wavemaker consisting of 48 individually controlled hinged flap paddles is located at one end of the basin and controlled by an integrated and synchronized data acquisition system. The other end of the basin is stacked with a cluster of vertical stainless steel screens that serve as an efficient wave absorber and reflection reducer. A cubic-shaped, fixed platform model was built with a side length of L = 0.74 m. The freeboard (S) was set to 0.26 m with the coordinate z = 0 being at the deck surface, so the still water level is at z = – 0.26 m. x = 0 was set at the leading edge of the model structure which is 20.9 m from the neutral position of the wave paddles. To accord with the recorded images (to be described later), the direction of the coordinate system has the positive x-axis pointing to the left. The coordinate y is in the cross tank direction with y = 0 being defined at 0.1 m from one of the model's lateral edge which is also the BIV vertical measurement plane. Figure 4.1(a) shows a picture of the model structure and the instruments, including wave gauges and high speed cameras in the wave basin.

4.2.2 Velocity measurement

Images on three measurement planes (top view, side view I, and side view II) were captured by three identical high speed cameras (Vision Research Phantom M340) at a framing rate of 1000 frames per second. The top view measurement plane was focused on the horizontal plane 0.1 m above the deck surface (z = 0.1 m). The side view I and side view II measurements shared the same focal plane that was set on the vertical plane y = 0. Cameras capturing the top view and side view I measurement planes were mounted with Nikon 50-mm f/1.4 focal lenses with the *f*-number set to 1.4 throughout the experiments.

Camera targeting on the side view II measurement plane was mounted with a Nikon 105-mm f/1.8 focal lens, with the *f*-number set to 1.8 throughout the experiments.

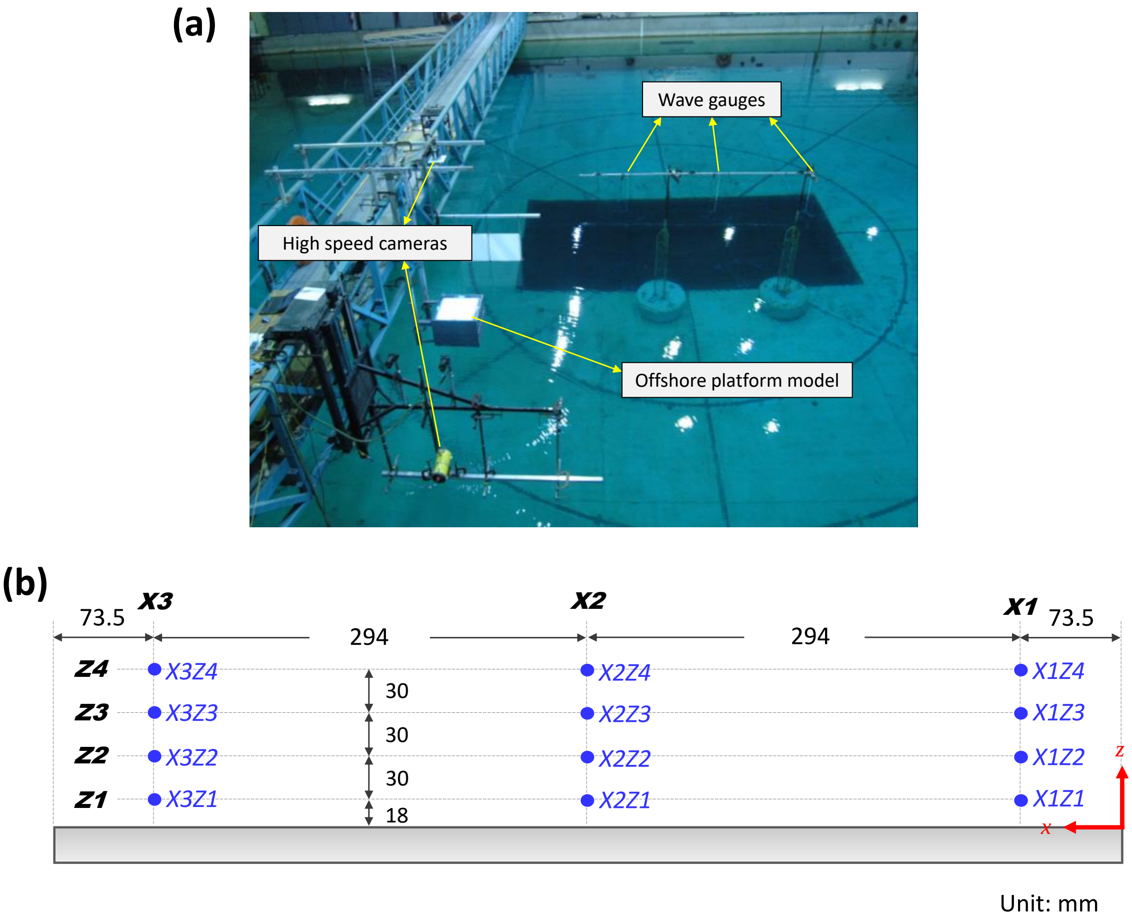

Figure 4.1 (a) Experiment setup in the wave basin. (b) Sketch of the coordinate system and the measurement points on the side view plane (x-z plane). Note that waves propagate from right to left.

Highly turbulent and aerated flows of breaking wave impingement and green water were quantified by using the BIV technique that cross-correlates shadow textures in consecutive high speed images. The shadow textures are contrast created by the air-water interfaces such as air bubbles and water droplets. The textures can be enhanced by using a high-sensitive camera and/or providing a uniformly illuminated background. In the present experiment, additional illumination is only necessary for top view measurements - a bright deck surface (see Fig. 4.1a) was built by framing a light-emitting diode (LED) panel and sealing it inside of the top of the model structure. For BIV image analysis, the interrogation window was set at 32 pixels with a 50% overlap with the adjacent windows. Table 4.1 summarizes the image recording setup and the estimated geometric error for each measurement plane. More details on the principles, validation, and applications of the BIV technique can be found in Ryu et al. (2005, 2007a), Chang et al. (2011), Lin et al. (2012), Song et al. (2013), and Chuang et al. (2015).

Table 4.1 Summary of setup for high-speed photography. *D* is the depth of field (DOF), ℓ is the distance between camera lens and focal plane, and ε is the geometric error due to limited DOF.

Measurement Plane	Resolution (pixels)	FOV size (m^2)	Spatial Resolution (mm^2)	ℓ (m)	D (m)	ε (%)
Side view I	2560 × 1600	1.54 × 0.72	9.6 × 9.6	3.00	0.18	2.94
Side view II	2560 × 1600	1.73 × 0.81	10.8 × 10.8	7.09	0.29	2.94
Top view	1920 × 1600	0.99× 0.83	8.3 × 8.3	2.58	0.13	2.53

4.2.3 Pressure and void fraction measurements

Pressure measurements were taken at 12 measurement points as sketched in Fig. 4.1(b) – three horizontal sections (x = 0.074 m, 0.368 m, and 0.662 m) and four elevations (z = 0.018 m, 0.048 m, 0.078 m, and 0.108 m). Pressure at each point was measured by a piezoresistive sensor (Kistler 4053A1) sensing pressure differential to the atmospheric pressure, and installed facing towards the incoming waves (or the negative x-axis). The pressures were sampled at 10 kHz throughout the tests. In addition, fiber optic reflectometer (FOR) was used to measure phase transition and determine void fraction. The optical fiber is 125 μm in diameter, supported and directed by a needle-shaped, stainless steel tube with a 5-mm protrusion to avoid surface tension effect while staying stiff in the violent flows. Each FOR probe was placed perpendicularly to the wave propagation and with a 5-mm spacing in front of each pressure sensor. FOR distinguishes different media by detecting the signal level corresponding to the refractive index of a medium. The refractive indices of air and water are very different so the signal changes (or phase changes) are readily distinguishable. Once the time series of phase transition is obtained, the void fraction (α) at each measurement point can be determined by calculating the resident time of the air phase (T_{air}) over the duration of the air-water mixture (T_{mix}), i.e.

$$\alpha = \frac{T_{air}}{T_{mix}} \tag{4-1}$$

In the experiments, the phase transition signals were sampled at 100 kHz, T_{mix} was set to 1 ms (averaged over 100 point), so the void fraction sampling rate is 1 kHz.

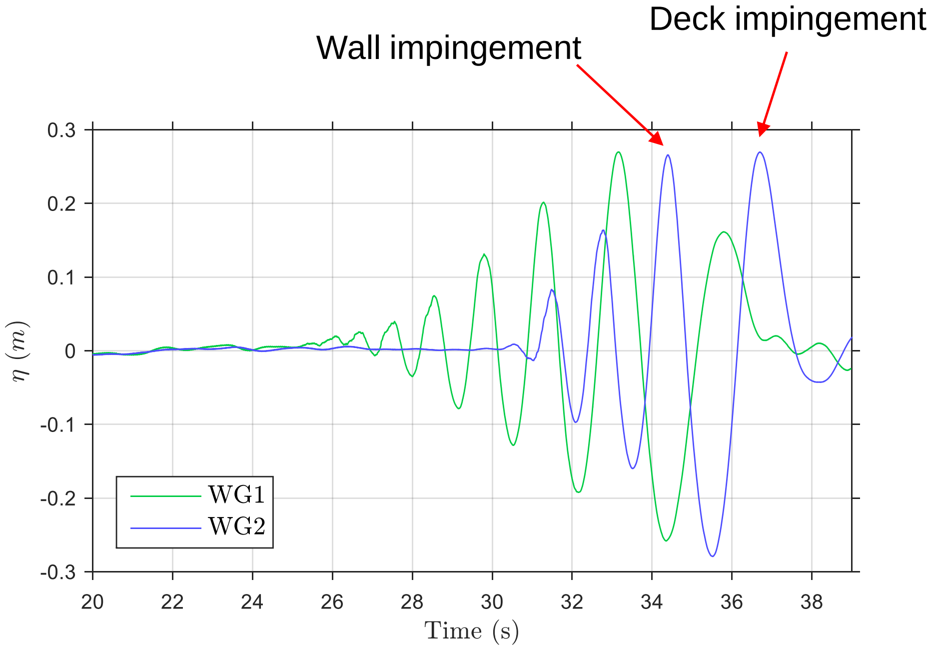

Figure 4.2 Measured free surface elevation at 10.6 m (WG1, green line) and 2.6 m (WG2, blue line) in front of the leading edge of the model structure.

Table 4.2 Position of wave gauges

Wave gauge	x (m)	y (m)
WG1	-2.64	-4.50
WG2	-4.62	-4.50
WG3	-6.60	-4.50

Table 4.3 Summary of properties of the primary breaking waves for the two impingement events as well as the maximum velocities during the impingement.

	W1	W2
Impingement event	Wall impingement	Deck impingement
Wave height, H (m)	$H_1 = 0.43$	$H_2 = 0.55$
Wavelength, (m)	4.84	11.64
Wave period, T (s)	$T_1 = 1.76$	$T_2 = 2.73$
Phase speed, C (m/s)	$C_1 = 2.75$	$C_2 = 4.26$
$U_{\max}$	$0.76C_1$	$1.32C_2$
$V_{\max}$	$0.36C_1$	$0.37C_2$
$W_{\max}$	$1.21C_1$	–

4.2.4 Wave conditions and green water events

The free surface elevation was measured using three double-wired capacitance-type wave gauges with their locations shown in Table 4.2. The present study considers two wave conditions: focusing wave and random waves. For the focusing wave condition, a wave train consisting of wave frequencies ranging from 0.7 to 1.3 Hz was generated. The wave train then formed a plunging breaker that broke right in front of the model structure, creating the *wall impingement* event (Chang et al. 2011). The breaking wave was immediately followed by a larger wave with a longer period that overtopped the deck and directly impinged on the deck surface, resulting in the *deck impingement* event (Chang et al. 2011). Figure 4.2 shows the measured wave elevations at two measurement points with indication that points out the corresponding impingement event. The properties of the primary waves representing both impingement events, such as wave height (H), wave period (T), and wave phase speed (C), are summarized in Table 4.3.

The random wave condition was generated using the JONSWAP spectrum with a duration of 1500 s. The significant wave height (H_s) and the peak wave period (T_p) measured at wave gauge WG1 are 0.30 m and 2.33 s, respectively. Each wave train contains 492 waves with η_{rms} being 0.08 m where η is the free surface elevation. An image-based auto-trigger method was employed to detect green water event and trigger image recording. This method utilizes contrast or brightness change over a preselected area within the field of view to detect the arrival of green water. Preliminary tests shows that 3% change in contrast is sufficient to detect any extent of green water events. Note that the cameras (with a 12-bit dynamic range) used in the present study provide 2^{12} grayscale intervals so they are sufficiently sensitive for the purpose. When the image-based trigger mode is on, the camera continues to record high-speed images but not save the images (due to limited storage space) until a trigger signal is received. In the experiments, the specified area is set between the leading edge of the model and x = 3 mm on the deck surface, and the threshold of contrast change is set as 3% (or 123 grayscale intervals). Note that it is impossible to record all green water events since each image-saving cycle takes about 20 s for 600 frames. To obtain a sufficient number of green water events for statistical analysis, the same random wave train was thus repeated 5 times – resulting in a recording of more than 300 captured events.

4.2.5 Measurement procedure

For the focusing wave tests, image recording and data acquisition were synchronized. To evaluate the mean quantities in such a highly turbulent flow, identical initial and boundary conditions were repeated 20 times and ensemble average was performed to all the measured data. Note that the recorded images on top view and side view I measurement planes were used for further analysis.

For the random wave tests, as mentioned earlier, five repetitions were performed with the same time series of the random wave signals. Image recording was taken on the side view II measurement plane. A total of 300 green water events were captured. Further manual examination was performed to remove events with false triggering or insignificant wave overtopping. Note that an insignificant wave overtopping in the present study was defined as that the water front did not reach 1/3 of the deck length. As a result, 179 events were selected for velocity determination and further analysis.

In the following presentation, the results obtained from individual test realizations as well as quantities obtained by averaging over the 20 repetition will be examined and discussed. To avoid confusion, the instantaneous parameters measured from individual impingement events use small letter (such as local u velocity, impact pressure p, and void fraction α), while the ensemble-averaged parameters use capital letter (such as local U velocity, impact pressure P, and void fraction A). Note that $t = 0$ is defined at the moment that overtopping wave passed the leading edge of the deck (green water took place), and t was reset for individual event such that ensemble average was done by matching $t = 0$.

4.3 Kinematics and dynamics of the green water under focusing waves

4.3.1 Green water velocity

Figure 4.3 shows instantaneous images superimposed with mean velocity maps on the top view and side view measurement planes for the wall impingement event. Similar to the case of plunging breaking wave impingements on a fixed (Ryu et al. 2007a) or moving (Chuang et al. 2015) structures with a vertical front wall, the flow features three stages: approach wave, vertical runup (Figs. 4.3a-b), and green water overtopping (Figs. 4.3c-e). Except the runup stage in which the flow was vertically dominated, the flow at the approaching wave stage and the green water stage were horizontally dominated. The dominant velocities for the three flow stages are $1.28C_1$ ($U_{\max}$), $1.21C_1$ ($W_{\max}$), and $0.76C_1$

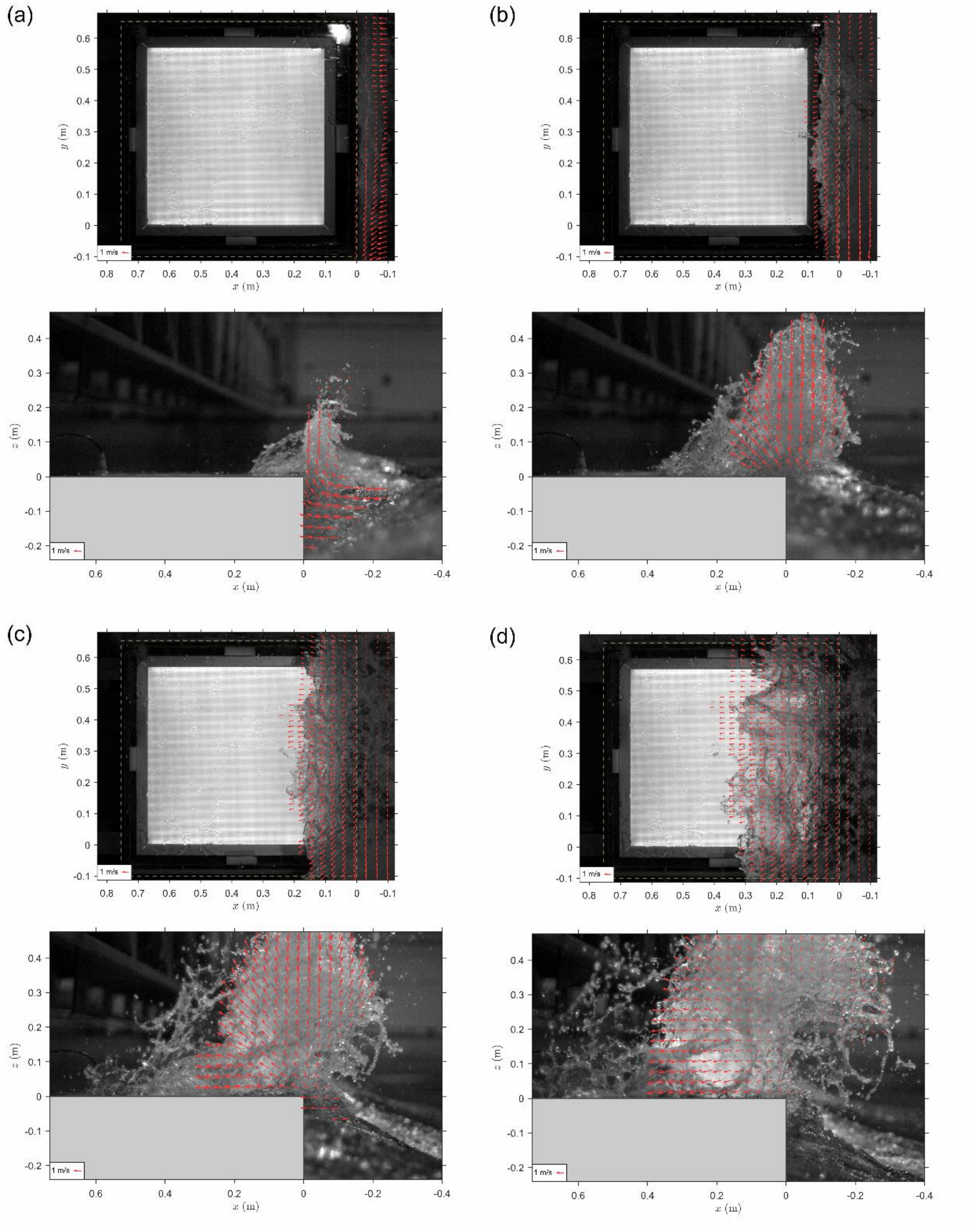

Figure 4.3 Wall impingement event: velocity maps on the side view (top panel) and top view (bottom panel) measurement planes at (a) t = 0, (b) t = 0.10 s, (c) t = 0.18 s, (d) t = 0.28 s, (e) t = 0.38 s, and (f) t = 0.54 s. Note that the vectors representing the water off the structure sidewall (not green water) was removed.

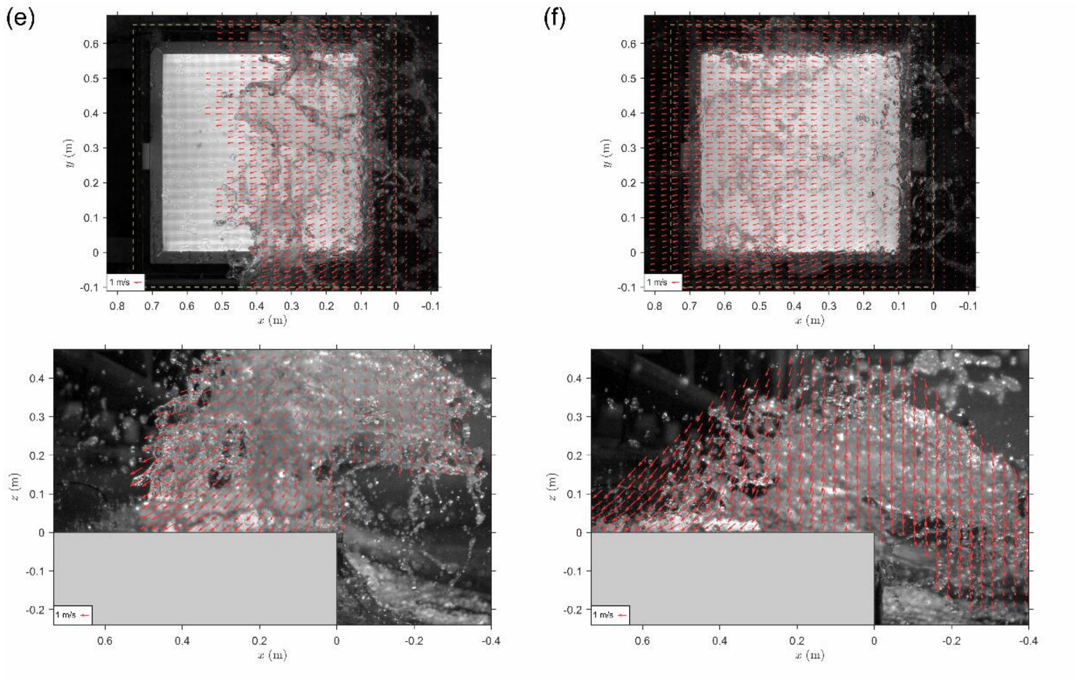

Figure 4.3 Continued.

($U_{\max}$), respectively, with C_1 (= 2.75 m/s) being the phase speed of the wave that caused the wall impingement event.

Comparing to the dominant green water velocity reported by Ryu et al. (2007a) and Chuang et al. (2015), the magnitude in the present experiment is about 40% lower. The impingement point relative to the vertical wall of the structure is the primary cause of the discrepancy. By examining the videos captured from both standard and high speed cameras, in the present study the breaking wave impinged on the water surface within a distance of 0.4 m to the front vertical wall of the model structure, in comparison to the range of 0.05 m (or equivalent to 0.13 m at the present scale through Froude scaling) reported by Chuang et al. (2015). With the impingement point farther away from the vertical wall, according to the deep-water plunging breaker processes described by Lim et al. (2015), some wave energy was dissipated in the splash-up roller formed upon the overturning breaking jet impinging on its front water surface. On the contrary, the breaking waves in Ryu et al. (2007a) and Chuang et al. (2015) impinged on the structure wall before the splash-up roller took shape and the green water retained most of its

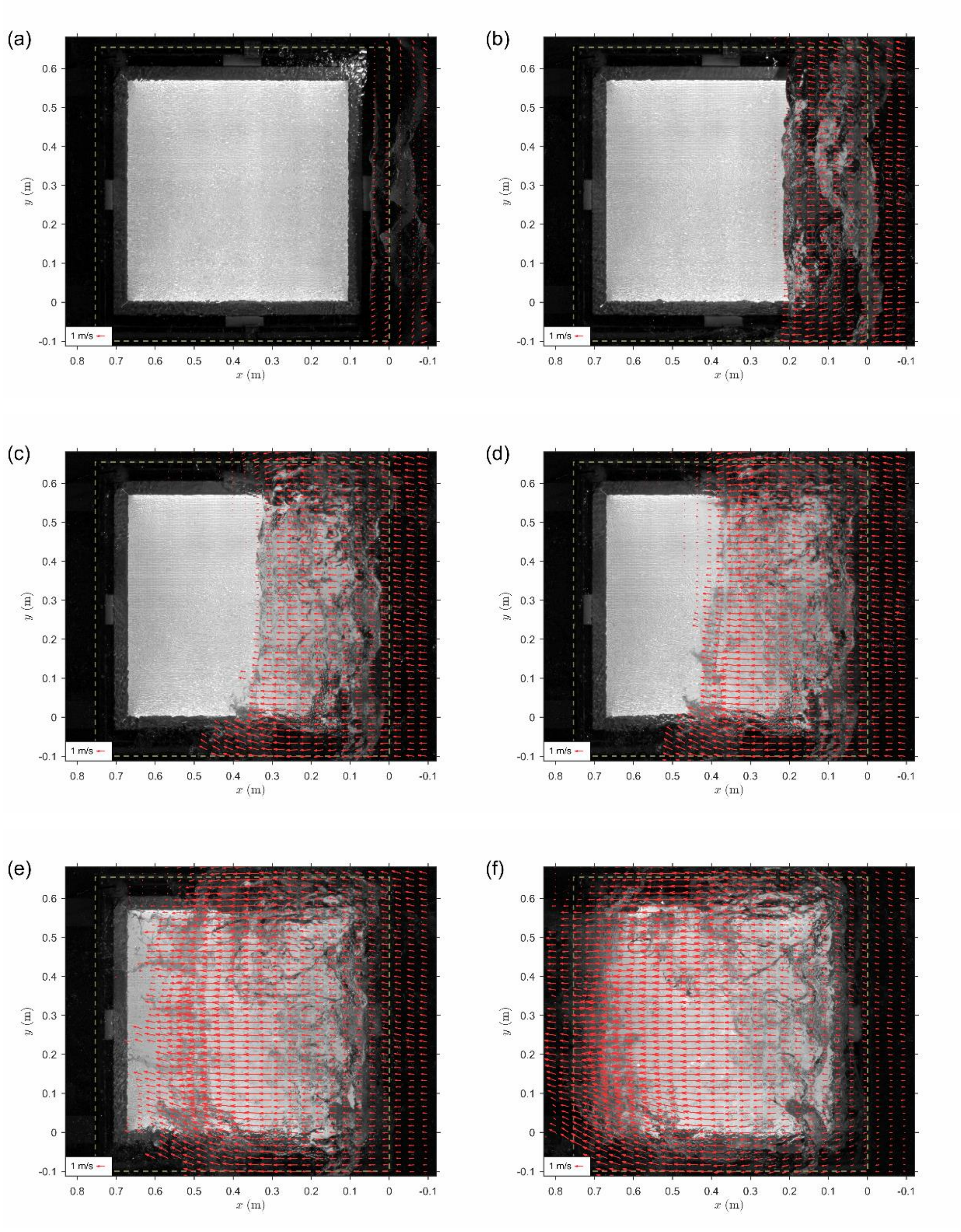

Figure 4.4 Deck impingement event: velocity maps on the top view measurement plane at (a) t = 0.02 s, (b) t = 0.16 s, (c) t = 0.24 s, (d) t = 0.26 s, (e) t = 0.30 s, and (f) t = 0.36 s.

horizontal momentum even after the runup stage. Nevertheless, the breaking wave in the present wall impingement event was still strong enough to overtop the deck, propel bulk of splashing water, and form an overtopping green water flow. As expected, the horizontal momentum was moderately reduced and the green water velocity is thus lower. Interestingly, the green water flow in the present study was mostly formed by the fall of splashing water on the deck, in comparison to a jet-like flow in Ryu et al. (2007a) or a bore propagation in Chuang et al. (2015).

Figure 4.4 presents instantaneous images superimposed with mean velocity maps on the top view measurement plane for the deck impingement event. Note that velocity measurements on the side view measurement plane were not available because water immersed the housing of the side-looking camera. Unlike the wall impingement event, in the deck impingement event the breaking wave directly overtopped the deck with its front touching down on the deck surface at about the middle of the deck. In addition, the deck impingement event involves only two stages: approaching wave and green water overtopping. As the wave touched down on the deck surface, a jet-like flow shoot out of the wave front, and then the wave collapsed and traveled on the deck somewhat similar to a dam break flow. The dominant green water velocity is $1.32C_2$ ($U_{\max}$) with C_2 (= 4.26 m/s) being the phase speed of the wave that causes the deck impingement event. The dominant green water velocity is slightly higher than the value of $1.2C_2$ reported by Chang et al. (2011) in which the plunging breaking wave impingement on a 3D ship-like structure.

Figure 4.5 plots the time history of the maximum velocities for both impingement events. For the wall impingement event shown in Fig. 4.5(a), initially the vertical structure wall obstructed the incoming breaking wave and forced the wave to run up, creating a bulk of splashing water with a high W velocity. Shortly after $t = 0.13T_1$, the $U_{\max}$ velocity became dominant with a magnitude remained nearly constant (~ $0.7C_1$) even after the green water front passed the rear edge of the deck. The large $V_{\max}$ velocity (reached $0.36C_1$), comparing to the x-direction green water velocity, implies that 3-D effects due to the limited width of the deck could significant if directional wave is considered. For the deck impingement event shown in Fig. 4.5(b), both the $U_{\max}$ and $V_{\max}$ velocities showed a sudden rise upon the wave front impingement on the deck surface at about $t = 0.08T_2$. In particular, the high U_{max} corresponded to the formation of the jet flow upon impingement as mentioned earlier. On the other hand, the V_{max} velocity nearly remained constant after reaching the peak value of $0.37C_2$.

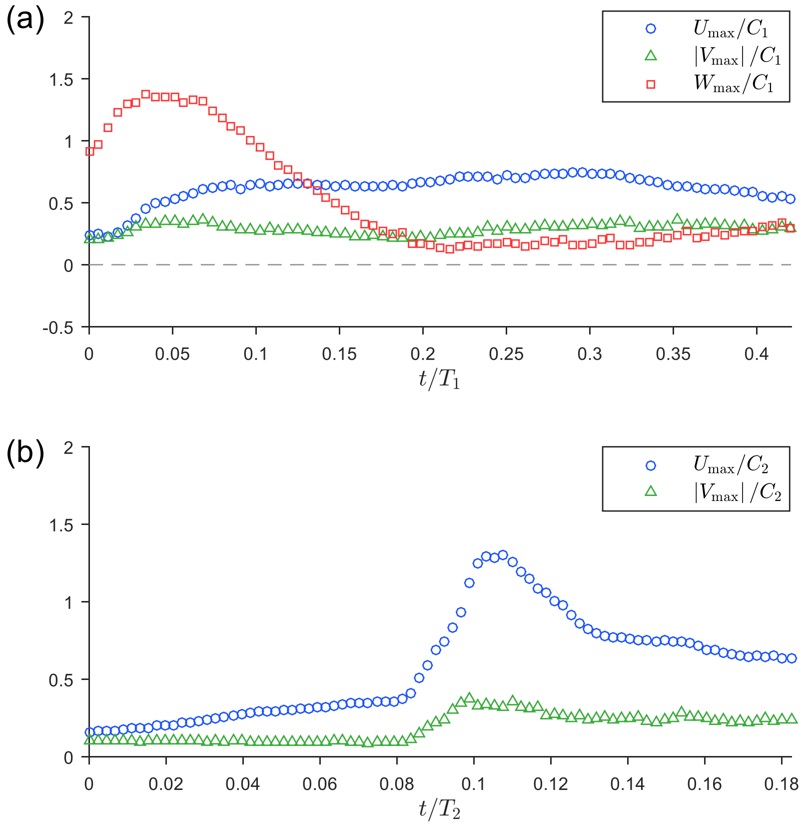

Figure 4.5 Time history of maximum velocities for (a) wall impingement event and (b) deck impingement event.

The peak magnitudes of V_{max} measured from both impingement events are nearly identical. Nevertheless, the behaviors of the large lateral velocities in both impingement events are opposite - a divergence of green water flowing from the deck centerline was observed in the wall impingement event, whereas a convergence of green water flowing towards the deck centerline was observed in the deck impingement event.

4.3.2 Modeling green water as a dam break flow

Ryu et al. (2007b) and Chuang et al. (2015) quantitatively examined the dam break modeling of green water on fixed and floating structures in 2D flumes, and showed that the simple Ritter's solution may be applicable to describe the green water velocity distribution. Based on their conclusions, the present study further examines whether the Ritter's solution can be applied to green water caused by both the wall and deck impingement events in a large-scale wave basin.

Ritter (1892) proposed an analytical solution to the Saint-Venant equations for the velocity, U, of a dam-break flow as:

$$U = \frac{2}{3}\left(\sqrt{gh_0} + \frac{x_d}{t_d}\right) \qquad \text{for } -\sqrt{gh_0} < x_d/t_d < 2\sqrt{gh_0} \tag{4-2}$$

where x_d represents the downstream direction with $x_d = 0$ being the location of the dam, t_d is time with $t_d = 0$ being the moment of dam removal, and h_0 is the initial water depth of the reservoir. In the present study, x_d and t_d are matched with x and t, respectively. To match h_0 in the green water flow, we followed the two approaches used by Ryu *et al.* (2007b). The first is the traditional approach that uses the elevation difference between wave height and freeboard, i.e.

$$h_0 = H - S \tag{4-3}$$

The second approach is to back-calculate h_0 by equating the measured green water front velocity (U_f) to Eq. (4-2):

$$h_0 = \left(0.5U_f\right)^2 / g \tag{4-4}$$

Figure 4.6(a) shows the green water front position in the wall impingement event, traveling at approximately a constant speed of $U_f = 0.54C_1$ based on the linear fit. For the deck impingement event, Fig. 4.6(b) shows the front position which again travelled approximately at constant speed except it accelerated when the green water front appeared to impinge on the deck surface. As a result, the green water front traveled at two constant speeds: $U_f = 0.33C_2$ before the impingement and $U_f = 1.09C_2$ after the impingement.

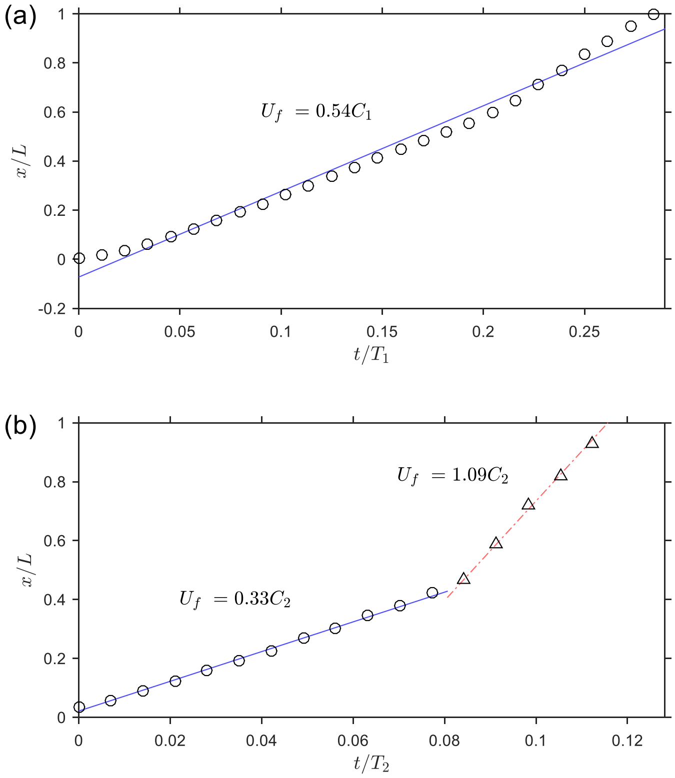

Figure 4.6 Time history of green water front for (a) the wall impingement event and (b) the deck impingement event. Note that the slope of the linear fit represents the green water front velocity (U_f).

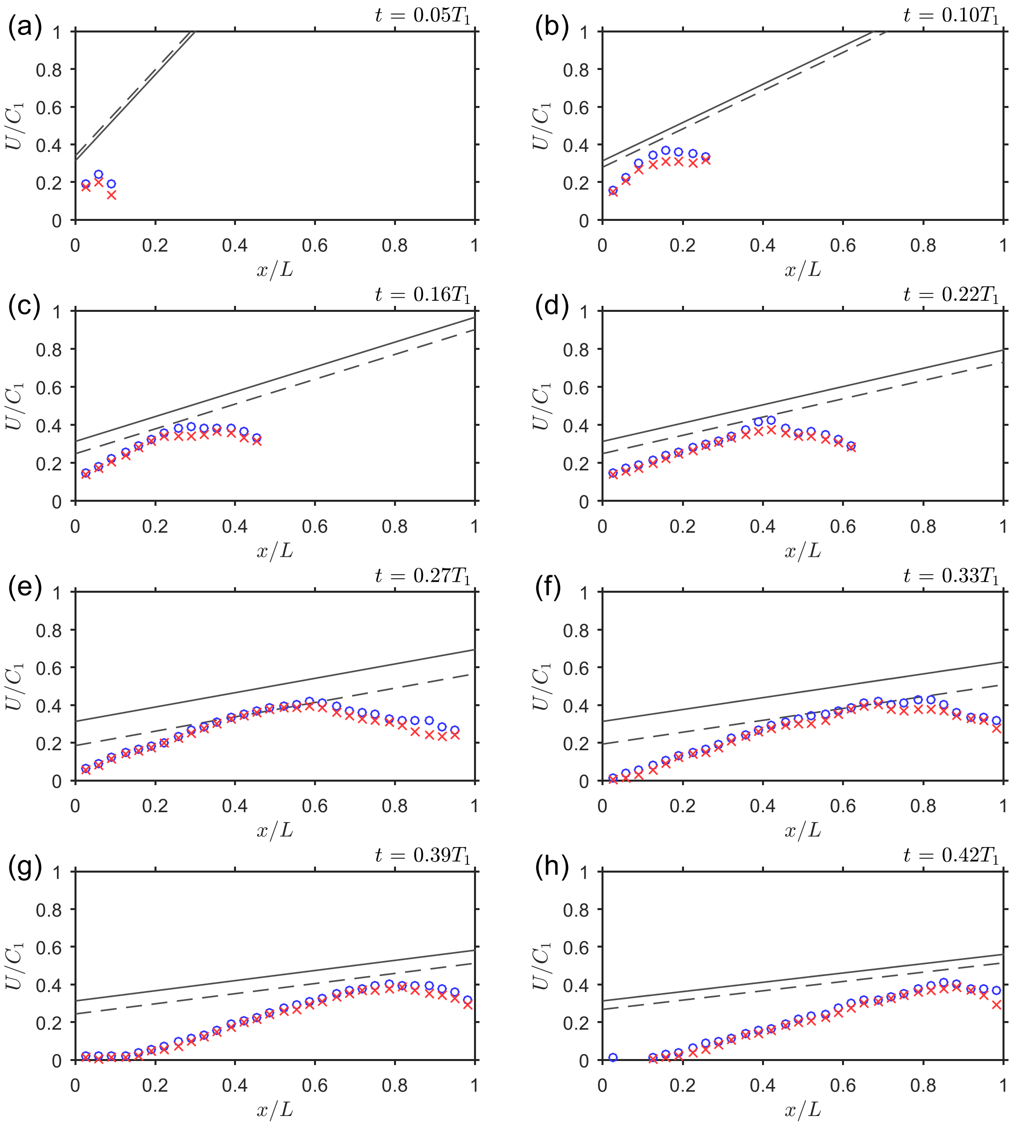

Figure 4.7 Comparisons of measured velocities and Ritter's solution for the wall impingement event. *Blue circle*, cross-sectional velocity U_c; *red cross*, width-averaged velocity U_w; *solid line*, Ritter's solution with $h_0 = H_1 - S$; *dotted-dashed line*, Ritter's solution with the h_0 back-calculated from the green water front velocity in Fig. 5(a).

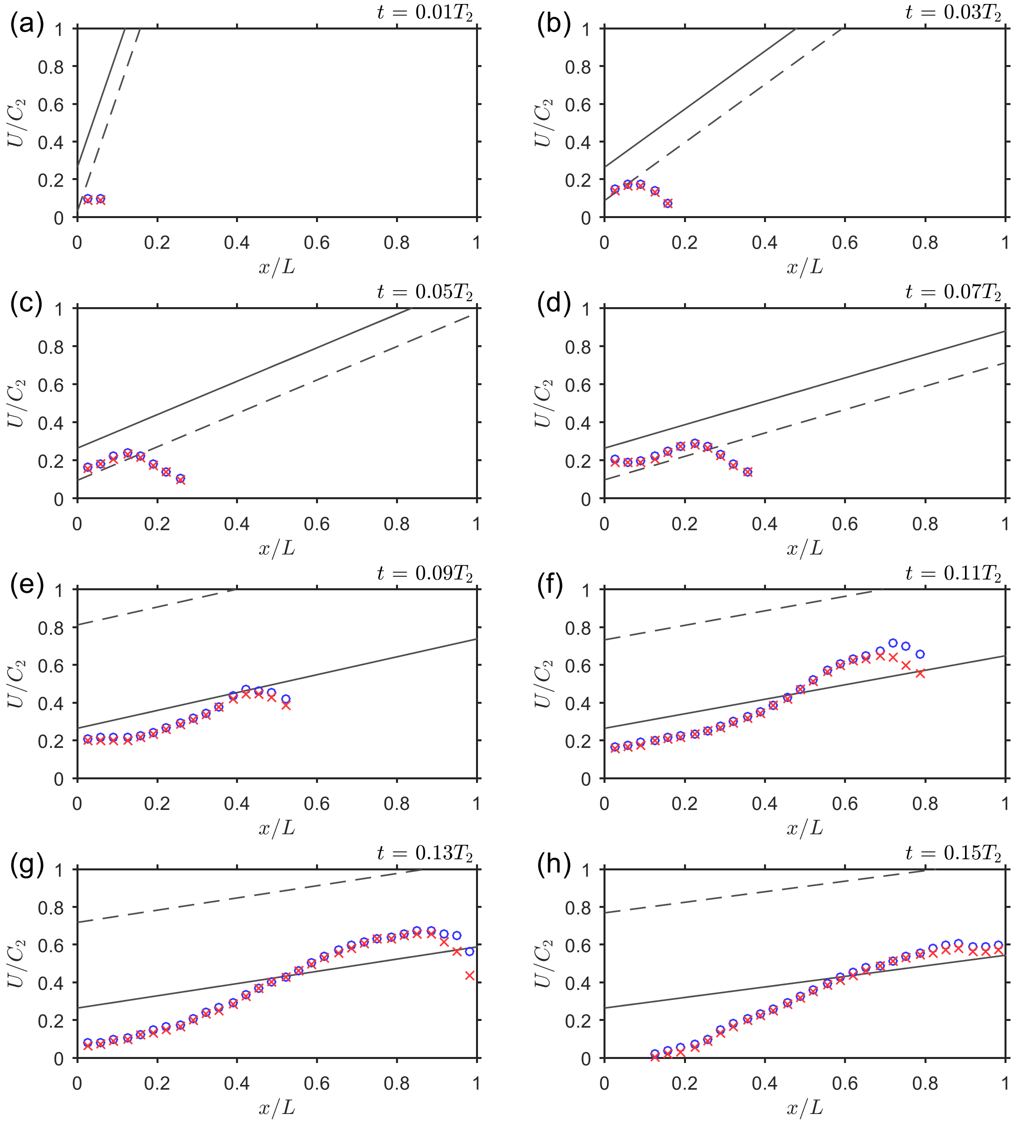

Figure 4.8 Comparisons of measured velocities and Ritter's solution for the deck impingement event. *Blue circle*, cross-sectional velocity U_c; *red cross*, width-averaged velocity U_w; *solid line*, Ritter's solution with $h_0 = H_2 - S$; and *dotted-dashed line*, Ritter's solution with the h_0 back-calculated from the green water front velocities in Fig. 5(b).

To compare with Ritter's 1D solution, the 2D green water U velocity distribution was further processed to form the "cross-sectional" U velocity (U_c) and the width-averaged U velocity (U_w). Note that only the top view measurements were used in the comparisons. Following Ryu et al. (2007a), U_c is defined as the maximum U velocity along each y column. Furthermore, U_w is the mean U velocity averaged within $y = \pm L/3$ along the centerline of the deck. Figures 4.7 and 4.8 present comparisons between the measured data and Ritter's solution for the wall impingement event and the deck impingement event, respectively. Overall the use of Eq. (4-4) captures the measured data better for the wall impingement event, as shown in Figure 4.7. The traditional approach of using Eq. (4-3) turns out to be overly conservative. On the contrary, the measured data seems to be sandwiched between the two lines of different h_0 using Ritter's solution, as shown in Figure 4.8, but the traditional approach seems to capture the measured data slightly better. Note that in Figure 4.8 the front velocity changes - both the velocities in Figure 4.6(b) were used as inputs to Eq. (4-4), depending on the moment being calculated, and the velocity significantly increases in magnitude after the impingement on the deck. In summary, the comparisons from the two impingement events show that Ritter's solution with both Eq. (4-3) and Eq. (4-4) gives reasonable approximation to the green water flow, but overall Eq. (4-3) seems to be slightly better in describing the velocity distribution.

4.3.3 Green water impact pressure

Figures 4.9 and 4.10 show the time histories of pressure and void fraction at measurement points depicted in Figure 4.1(b) for both the wall and deck impingement events. Note that the plots were arranged in a way that matches the measurement points with wave coming from right to left. Table 4.4 and 4.5 summarize the peak pressure (P_{max}), pressure rise time (t_r), aeration level (A_r, defined as the averaged void fraction over the pressure rise time), and impulsiveness at each measurement point for both impingement events. An impulsive pressure is generally recognized as a sudden rise of high pressure.

Ariyarathne et al. (2012) first proposed an index to quantify the threshold for impulsive pressure. The index or impulsiveness is defined as:

$$\left(\frac{P_{\max}}{t_r}\right)\Bigg/\left(\frac{0.5\rho_w U_{\max}^2}{T}\right) \tag{4-5}$$

where T is the wave period and ρ_w is the water density. For the wall impingement event, the pressure sensors at *X1Z2-Z4* and *X2Z1-Z2* experienced impulsive pressure. For the deck impingement event, measurement points at *X1Z3-Z4* and *X2Z1-Z2* sensed impulsive pressure. The highest peak pressure is 2.68 kPa or $0.35\rho_w C_1^2$ (measured at *X1Z4*) for the wall impingement event, and a much higher peak pressure of 11.23 kPa or $0.62\rho_w C_2^2$ (measured at *X2Z1*) for the deck impingement event.

The large green water impacts in the deck impingement event show a typical feature of wave impact pressure: a sudden rise to a high peak pressure followed by a gradual fall of pressure magnitude. Similar characteristics were also observed by Bullock et al. (2001), Bullock et al. (2007), and Chuang et al. (2017) during breaking wave impacts on a vertical surface. On the contrary, the splashing water-dominated green water in the wall impingement event only gave rise to moderate pressure at measurement points close to the structure leading edge. From these time histories, especially in the deck impingement event, the void fraction drops tremendously upon the rising pressure during the impact.

Table 4.4 Summary of pressure and void fraction measurements for the wall impingement event.

Measurement point			$P_{\max}$ (kPa)	$\frac{P_{\max}}{\rho_w C_1^{\ 2}}$	$\left(\frac{dP}{dt}\right) \Big/ \left(\frac{0.5\rho_w U_{\max}^2}{T_1}\right)$	t_r (ms)	A_r
	x (mm)	z (mm)					
X1Z1	73.5	18	1.06	0.14	26	33	0.3
X1Z2	73.5	48	1.2	0.16	84	12	0.17
X1Z3	73.5	78	2.15	0.28	315	5	0.16
X1Z4	73.5	108	2.68	0.35	332	6	0.27
X2Z1	367.5	18	1.63	0.22	97	13	0.29
X2Z2	367.5	48	1.18	0.16	112	9	0.43
X2Z3	367.5	78	0.53	0.07	41	10	0.62
X2Z4	367.5	108	0.58	0.08	85	5	0.58
X3Z1	661.5	18	0.83	0.11	25	26	0.79
X3Z2	661.5	48	0.48	0.06	37	10	0.88
X3Z3	661.5	78	0.16	0.02	7	19	0.93
X3Z4	661.5	108	0.29	0.04	17	13	0.81

Table 4.5 Summary of pressure and void fraction measurements for the deck impingement event. Note that the magnitude of the $P_{\max}$ measured at *X3Z4* is negative.

Measurement point			$P_{\max}$ (kPa)	$\frac{P_{\max}}{\rho_w C_2^{\ 2}}$	$\left(\frac{dP}{dt}\right) \Big/ \left(\frac{0.5\rho_w U_{\max}^2}{T_2}\right)$	t_r (ms)	A_r
	x (mm)	z (mm)					
X1Z1	73.5	18	2.54	0.14	4	102	0.38
X1Z2	73.5	48	3.22	0.18	22	25	0.71
X1Z3	73.5	78	5.9	0.32	145	7	0.54
X1Z4	73.5	108	4.34	0.24	83	9	0.65
X2Z1	367.5	18	11.23	0.62	194	10	0.53
X2Z2	367.5	48	8.2	0.45	101	14	0.37
X2Z3	367.5	78	6.71	0.37	61	19	0.3
X2Z4	367.5	108	4.37	0.24	47	16	0.2
X3Z1	661.5	18	8.33	0.46	48	30	0.39
X3Z2	661.5	48	5.56	0.31	32	30	0.27
X3Z3	661.5	78	2.33	0.13	18	22	0.05
X3Z4	661.5	108	-1.34	-0.07	-3	91	0.41

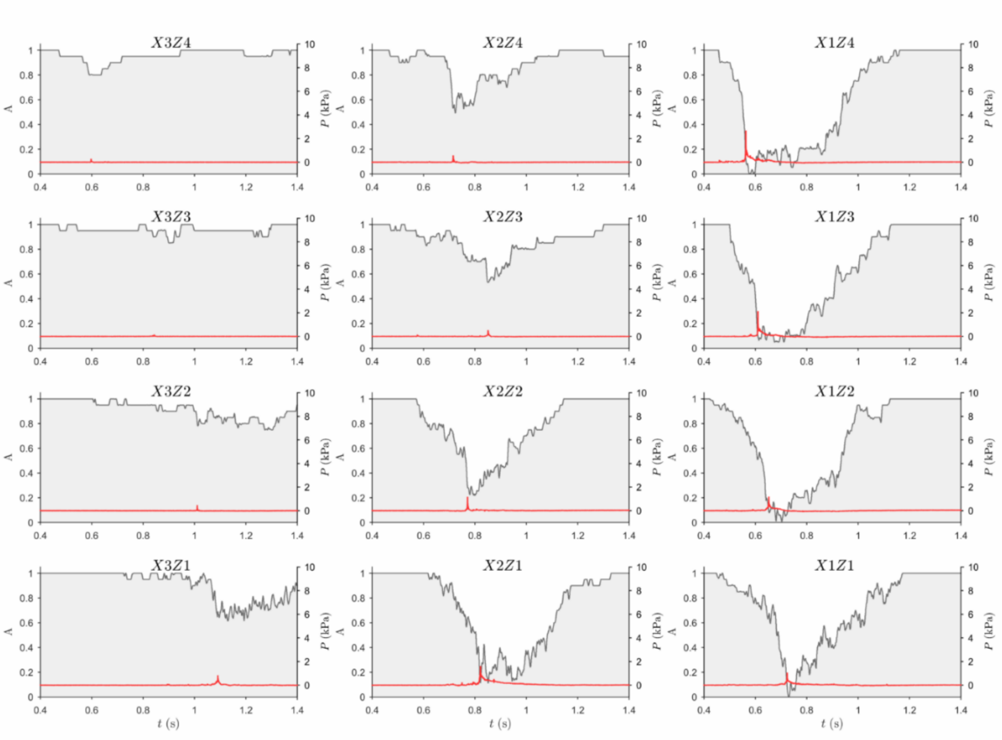

Figure 4.9 Time history of pressure and void fraction for wall impingement event.

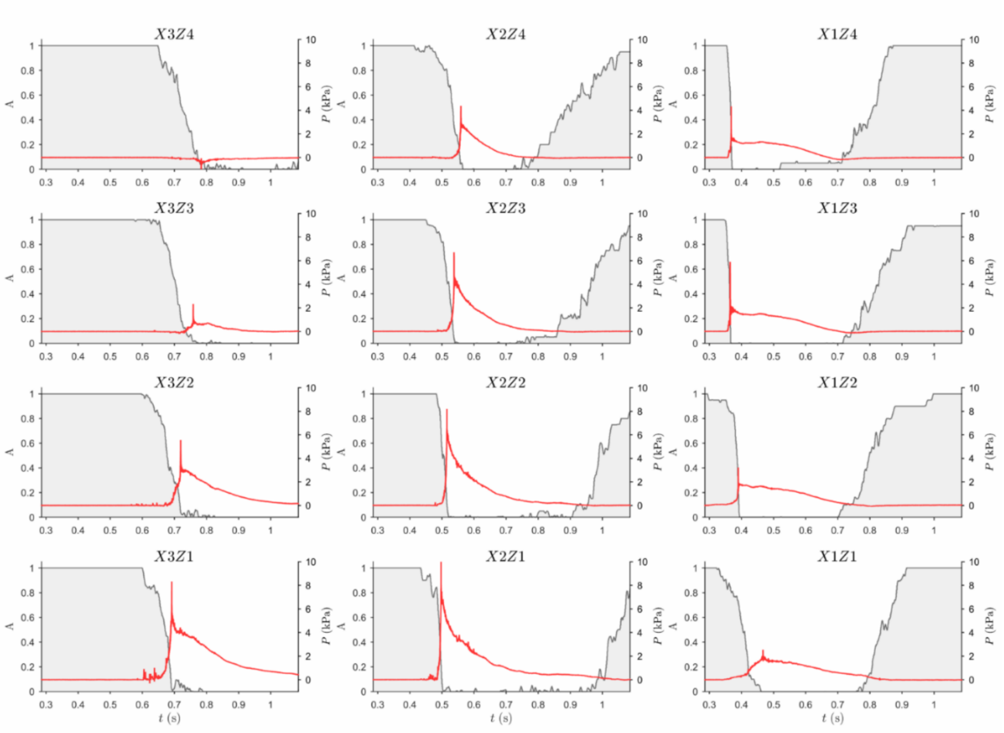

Figure 4.10 Time history of pressure and void fraction for deck impingement event.

Figures 4.11 and 4.12 present the vertical profiles of peak pressure, rise time, and aeration level for both impingement events. For the peak pressure profiles, the trend at *X1* is quite different from that at *X2* and *X3* for both impingement events. Based on the high speed videos, the leading edge of the deck is responsible for the difference. As the breaking waves overtopped, the lower surface of the green water flow was separated by the leading edge of the model structure. This separation led to a weaker flow momentum at the level below *Z2*, resulting in a lower pressure magnitude at *Z1* and *Z2* at the measurement location *X1*. As the green water continued to propagate downstream to *X2* and *X3*, the flow resembles a dam break flow or a bore and the vertical pressure profile is close to hydrostatic. At *X3Z4* (not plotted), the maximum pressure magnitude was negative. The negative pressure may be associated with cavitation effect. However, the present experiment was not designed to examine such phenomenon. This mechanism remains to be explored in the future study.

For the vertical profiles of the rise time and aeration level, the effect of flow separation caused by the leading edge seems to strongly to have a significant effect at *Z1*, especially for the deck impingement event. The trend of the rise time profile and the aeration level profile at *X1* is quite different from that at *X2* and *X3*.

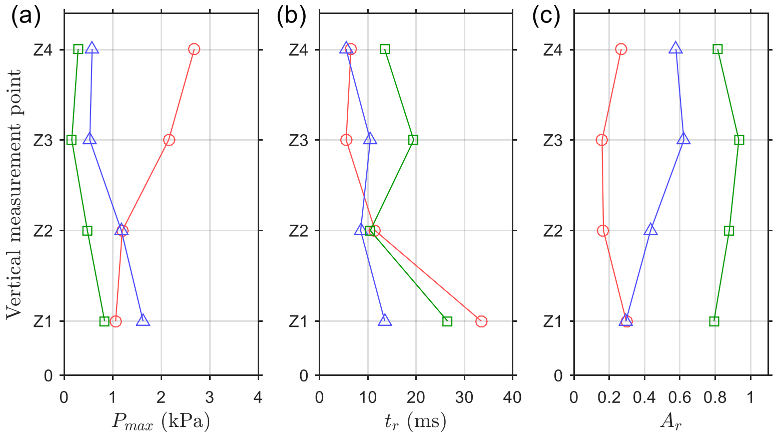

Figure 4.11 Wall impingement event: vertical distributions of (a) peak pressure, (b) rise time, and (c) aeration level. *Red circle*, *X1*; *blue triangle*, *X2*; and *green square*, *X3*.

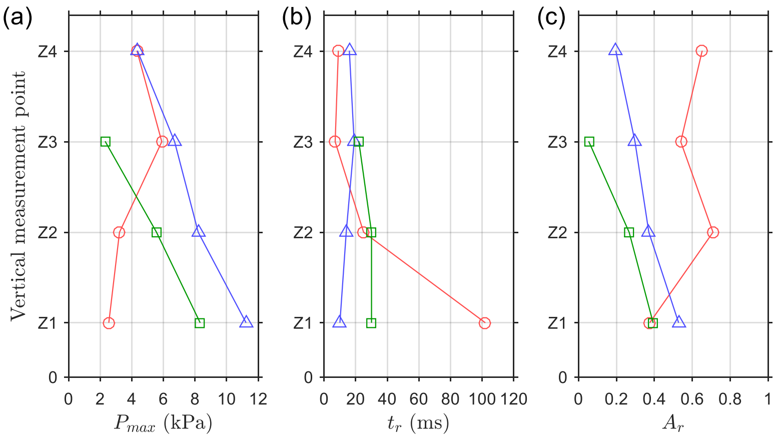

Figure 4.12 Deck impingement event: vertical distributions of (a) peak pressure, (b) rise time, and (c) aeration level. *Red circle*, *X1*; *blue triangle*, *X2*; and *green square*, *X3*.

4.3.4 Relation between peak pressure and rise time

The present study shows that the deck impingement event mostly led to impulsive pressures with a high intensity – a great concern in practical design. Hence, relation between the pressure maximum and the pressure rise time was further examined. Figure 4.13 plots the instantaneous impact pressure ($p_{\max}$) against the corresponding rise time (t_r) for the deck impingement event over the 20 repeated tests. A negative trend was found and in agreement with previous studies (e.g., Hattori et al. 1994; Cuomo et al. 2010a, b; Ariyarathne et al. 2012; Song et al. 2015; Chuang et al. 2017). To describe the relationship, a formula was proposed by Chuang et al. (2016, 2017) based on dimensional argument as:

$$\frac{p_{\max}}{\rho_w C^2} = a\left(\frac{t_r C}{H}\right)^b \tag{4-6}$$

where the impact pressure maximum is normalized by the water density and the wave phase speed, while the rise time is normalized by the wave height (H) and the wave phase speed. Two coefficients, a and b, were obtained by fitting the measured data with Eq. (4-6) with least squares regression. Two curves were obtained and plotted in Fig. 4.13: the solid curve represents the least square fitting curve with $a = 0.33$ and $b = -0.34$, and the dashed curve represent the envelope curve with $a = 0.10$ and $b = -0.34$. Comparing to the coefficients reported by Chuang et al. (2017) in which a breaking wave impingement on a moving structure in a 2D wave flume was studied, both coefficient sets are on the same order of magnitude. Accordingly, Eq. (4-6) seems to be a reasonable approach to formulate the pressure maximum-rise time relationship. However, due to the complexity of the green water flow and impacts, more measurement data at various scales and under different impact scenarios are still needed to verify the applicability of Eq. (4-6).

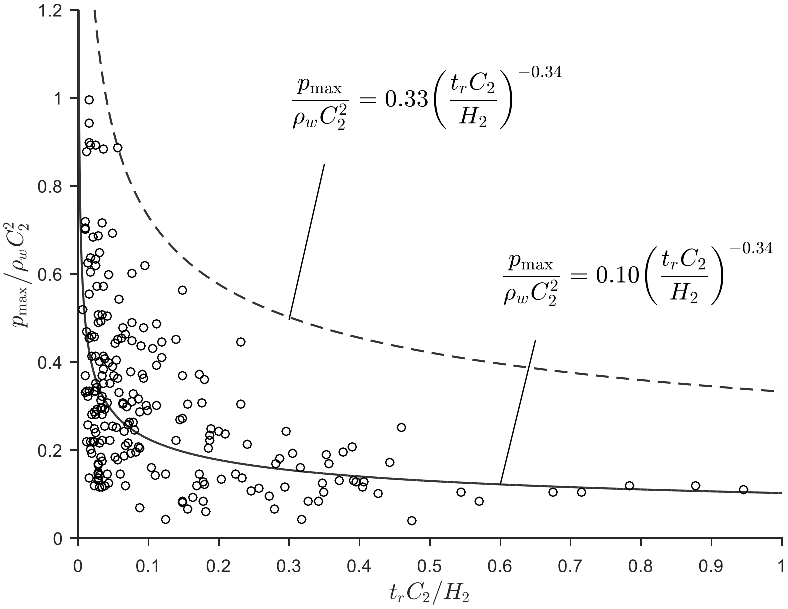

Figure 4.13 Peak impact pressure (normalized by $\rho_w C_2^2$) versus pressure rise time (normalized by C_2/H) for the deck impingement event. The *solid line* is the least squire fit of the data, while the *dashed line* is the envelope.

4.3.5 Relation between peak pressure and aeration level

Several studies (e.g., Peregrine 2003; Bullock et al. 2007) concluded that air bubbles/pockets play an important role in affecting the peak impact pressure variation during breaking wave impacts. It has been generally accepted that entrained air bubbles reduce impact pressure (cushioning effect) while entrapped air pockets lead to higher impact pressure and greater temporal variation. For a multiphase flow, the air compressibility effect in green water impacts was, however, less addressed in the literature. With the void fraction measurements, the present study examined the relation between the aeration level and the normalized peak pressure and plotted the results in Figure 4.14. For the wall impingement event, Fig. 4.14(a) demonstrates a negative correlation with a straight fitted line between these two quantities. As a matter of fact, the negative linear trend has nothing to do with the effect of entrained air bubbles. Instead, based on video observation, the green water impact pressure was mostly dominated by the "chance of contact" or momentum with the splashing water over the deck. A lower void fraction means a higher chance of contact with water and therefore a higher momentum. This can also been seen from Figure 4.9 in which void fraction stayed above zero during the impact, in comparison to the zero or near-zero void fraction when and after reaching the peak pressure in the deck impingement event in Figure 4.10.

Figure 4.14(b) shows the relation for the deck impingement event. The pattern is totally different from that for the wall impingement event. Two groups of data can be identified and separated in the plot: data points at *X1* and date points at both *X2* and *X3*. The three date points at *X1* with $A_r > 0.5$ show a clear negative (and nearly linear) trend, while the fourth data point (at *X1Z1*) deviated from the trend. The negative relationship is associated with the effect of entrained air bubbles because the non-breaking overtopping wave (before impinging on the deck) contained residual air bubbles from the previous breaking wave (that caused the wall impingement event). However, as mentioned earlier, the lowest measurement point *Z1* at *X1* experienced flow separation due to the leading edge of the deck. Such a flow resulted in a much smaller momentum flux and deviated the data point from the negative trend.

For data points at *X2* and *X3* in Fig. 4.14(b), the overtopping wave has already impinged on the deck and turned into a bore-like flow. The probes at these two locations sensed a fully-developed green water flow. Interestingly, the combined data points at *X2* and *X3* form a nearly perfect, positive linear trend with a higher impact pressure corresponds to a higher aeration level. The positive trend is totally opposite to the negative trend of cushioning effect by entrained air bubbles observed in breaking wave impacts.

The positive trend seems to make more sense physically and intuitively since the green water flow is bubbly. However, the positive trend may indicate a deformed or irregular green water front that entrapped air on the vertical wall surface (i.e., on a pressure sensor end face in the experiment). The entrapped air then exerted high pressure on the model surface as it experienced compression by the moving liquid with a high momentum flux.

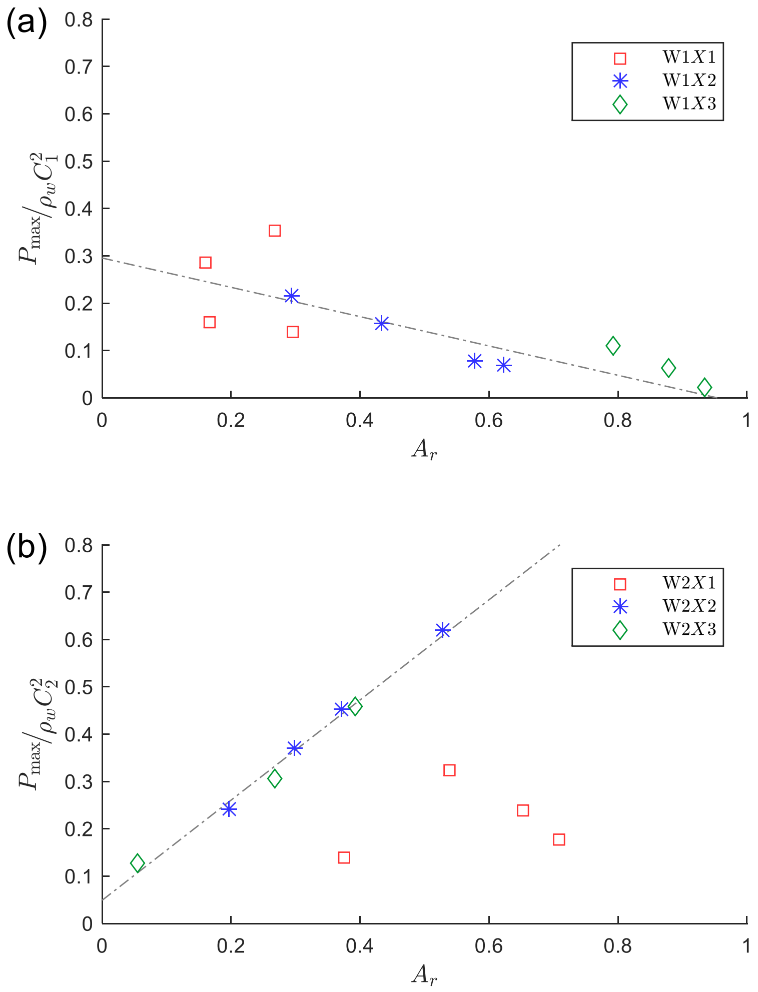

Figure 4.14 Aeration level versus normalized peak impact pressure for (a) wall impingement event (W1) and (b) deck impingement event (W2). Dot-dashed line is the linear fit of the data. Note that all data points in (a) were used in linear fit, and the data points from W2*X2* and W2*X3* were only used in linear fit.

4.4 Kinematics of the green water under random waves

4.4.1 Characteristics of random green water events

A total of 179 significant green water events, collected from a random wave realization repeated five times, were processed for velocity determination using the BIV technique. Although random green water events are highly turbulent, visual examination based on videos recording at 1000 fps shows that the green water events can be categorized into three types based on similarity of flow characteristics. The description for each type is as follows:

I. *Collapse of overtopping wave*: featuring a water mass overtopping the front deck and piling up on or near the front deck. Subsequently, as sketched in Fig. 4.15, the water mass collapses in a way very similar to a dam break and then travels downstream on the deck. In some cases, the overtopping wave front was separated at its lower surface by the leading edge of the deck. As a result, a high-speed horizontal jet emerges when the wave front falls and impinges on the deck surface, as demonstrated in Fig. 4.15.

II. *Fall of bulk water*: as sketched and demonstrated in Fig. 4.16, a bulky water was thrust up into the air as a form of wave jet by the vertical momentum transferred from the horizontal wave momentum due to the obstruction of the vertical structure wall. As soon as the bulky water reached its peak potential energy, the bulk water fell back on the deck and created turbulent and aerated green water.

III. *Breaking wave crest*: distinguished by a large breaking wave directly overtopping onto the deck. Figure 4.17 demonstrates a flow created by the breaking wave crest and involved into a highly turbulent and aerated flow. Much of this event is generated when a large breaking wave impinges on structure with the wave crest higher than the deck level.

In the present study, the probability of occurrence for each type is 69% (Type I), 26% (Type II), and 5% (Type III), respectively. According to the green water events observed on a FPSO model reported by Buchner (1995), the Type I green water flow seems to be the most representative case and resemble the formation of a dam break flow well. Although the Type II flow emerges less frequent than Type I, it should be pointed out that the high water and bulk mass could cause serious local damage and affect structure dynamics when it falls on the deck. The Type III flow is undoubtedly the most destructive which should be avoided, if possible, or carefully evaluated in designed and operation.

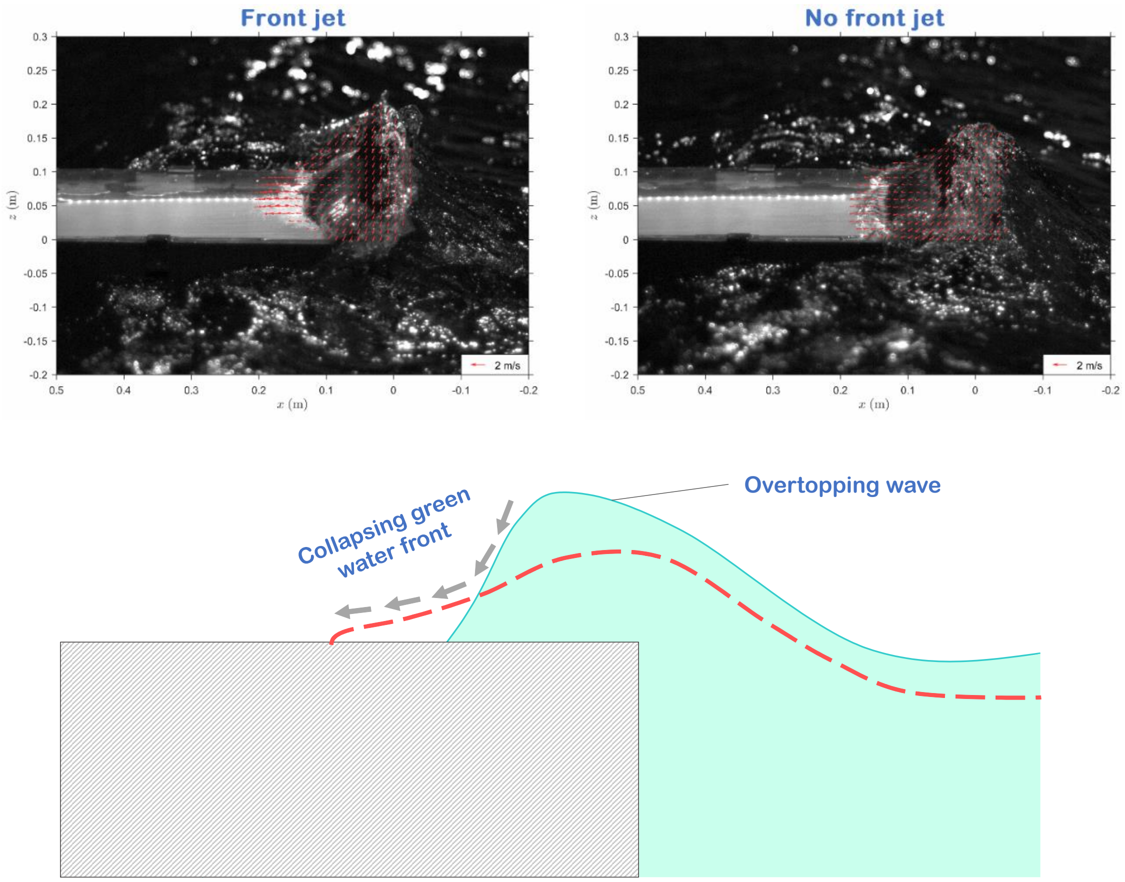

Figure 4.15 Type I green water – collapse of overtopping wave. The upper panel shows the snapshots with and without front jet. The bottom panel sketches the flow and its follow-up (*red dashed line*).

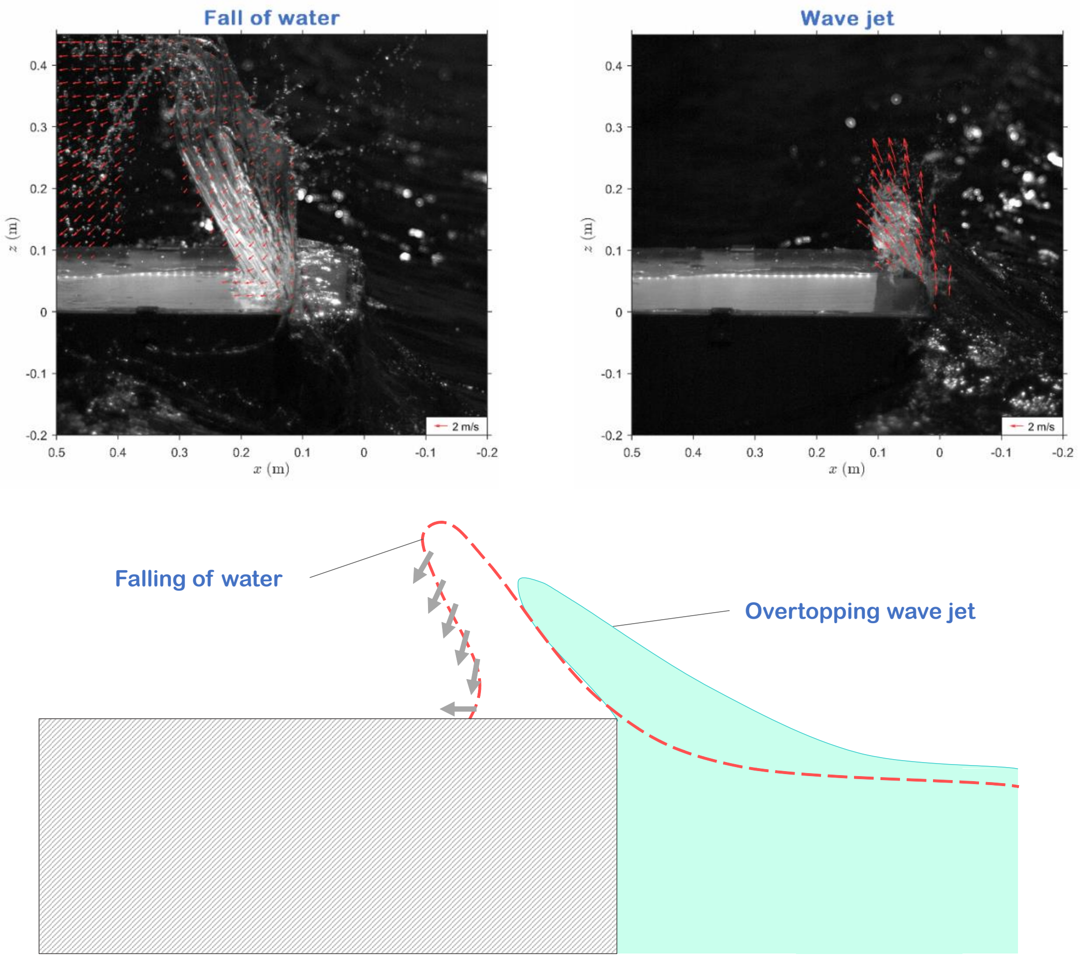

Figure 4.16 Type II green water – fall of bulk water. The upper panel shows the snapshots of wave jet and fall of water. The bottom panel sketches the flow and its follow-up (*red dashed line*).

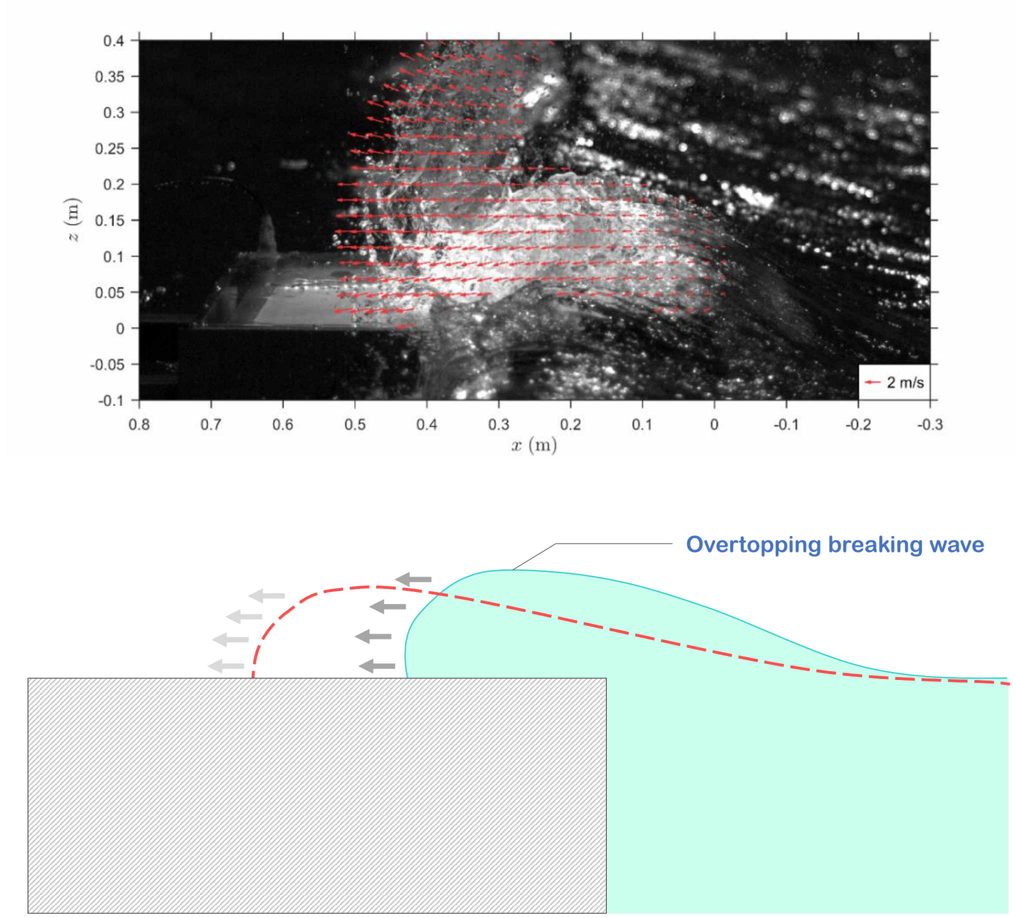

Figure 4.17 Type III green water – breaking wave crest. The upper panel shows a snapshot, while the bottom panel sketches the flow and its follow-up (*red dashed line*).

4.4.2 Statistical distribution of maximum green water velocities

Figure 4.18 plots the histogram of the maximum *u* velocity over the 179 events fitted with four typical distribution, including the normal, lognormal, Weibull, and Rayleigh distributions. The data show a left-skewed trend with a tail reaching u_{max} = 3.79 m/s. The values of u_{max} > 2.5 m/s are all found from the Type III events. Among the fittings in the figure, the lognormal distribution seems to be the best fit. By comparing the $U_{\max}$ value (1.32C_2 or 5.62 m/s) measured in the deck impingement event under a focusing wave, that deck impingement event presents a conservative estimate to the largest u_{max} to the random green water events.

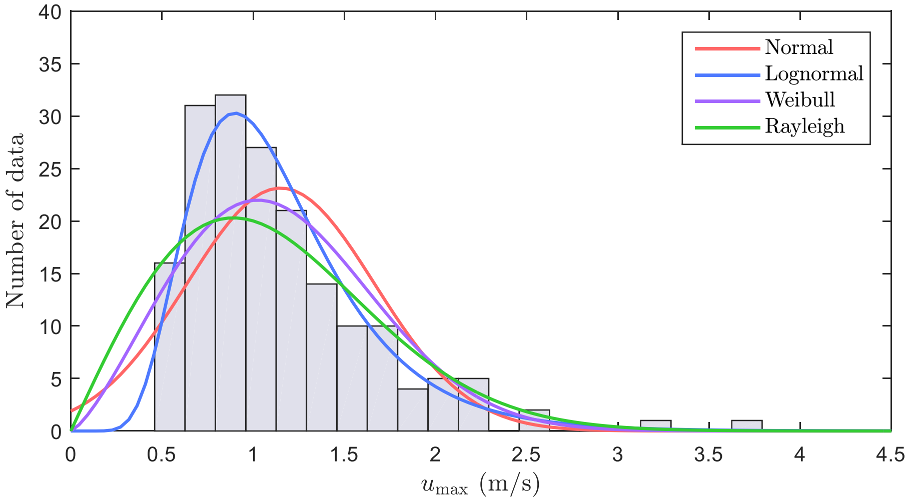

Figure 4.18 Histogram of $u_{\max}$ for the random green water events with four probability distributions

4.3 Prediction function for the velocity distribution under random waves

Based on the observation of self-similarity in the horizontal U velocity distribution of green water induced by plunging breaking wave impingement, Ryu et al. (2007a) performed a dimension analysis and proposed a prediction equation as follows:

$$\frac{U_c}{U_m} + k\left(\frac{t}{T}\right) = m\left(\frac{x}{Ct}\right)^n \qquad (4\text{-}7)$$

where U_m is the maximum green water velocity at each time step and k, m, and n are empirical constants determined by curve fitting. By considering a general application of prediction equation in random waves, the significant wave height (H_s) and peak wave period (T_p) are used to replace C and T in (7). With the use of instantaneous velocities [the cross-sectional u velocity (u_c) and the maximum u velocity (u_m)], the prediction equation becomes:

$$\frac{u_c}{u_m} + k'\left(\frac{t}{T_p}\right) = m'\left(\frac{x/t}{H_s/T_p}\right)^{n'} \tag{4-8}$$

where *k*′, *m*′, and *n*′ are empirical constants determined by curve fitting. Physically, the left hand side of Eq. (4-8) represents the momentum balance between green water velocity (u_c/u_m) and green water front propagation (t/T_p); while the right hand side represents the ratio of the local fluid particle velocity (x/t) and the significant intensity of incoming waves (H_s/T_p). Note that u_c or the cross-sectional *u* velocity represents the maximum *u* velocity along each vertical (*z*-axis) profile.

Data from all the 179 random wave causing green water events were used to obtain the empirical coefficients in Eq. (4-8) by applying a least squares regression. The prediction equation is shown in Fig. 4.19 with the predicted equation plotted against the measured data (more than 5×10^5 data points). In the figure, the prediction curve fits the mean points very well for $(x/t)\big/\left(H_s/T_p\right) \le 6$, indicating a self-similar *u* velocity distribution in the random green water events. For $(x/t)\big/\left(H_s/T_p\right) > 6$, the measured data start to decrease, whereas the prediction curve continues to increase. The frictionless assumption to Eq. (4-8) may mainly be responsible for the discrepancy. Table 4.6 further shows comparisons with the empirical coefficients obtained in previous studies performed in a 2D flume. Although the values are different, most of the coefficients do not deviate much, and all the coefficients are on the same order of magnitude. This may imply that the normalization quantities may be predicted using the equations regardless the test facilities.

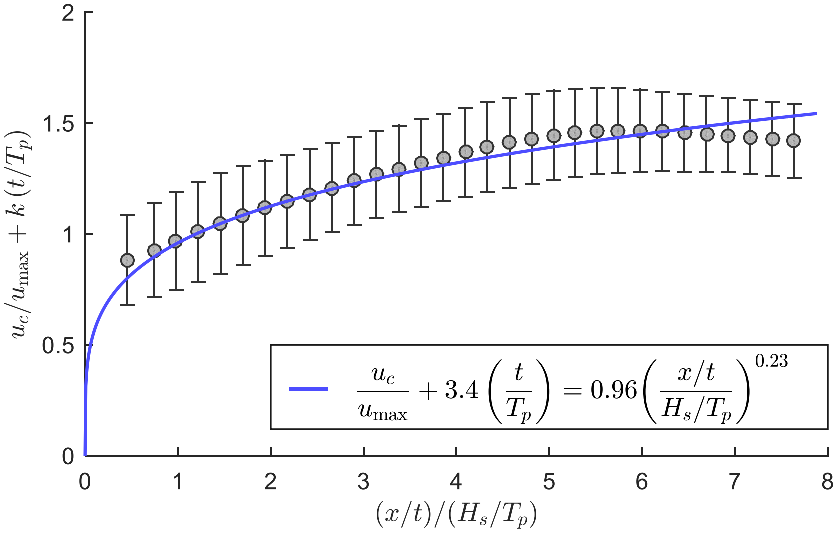

Figure 4.19 The self-similar *u* velocity profile for the random green water events. The *blue line* is based on Eq. (8) with the coefficients obtained from least square regression of the measured data. Note that the data points are plotted as mean values with error bars.

4.4.4 Modelling the random green water events as a dam-break flow

Following the approach presented in Section 3.2 in which the green water flow was modelled as a dam break flow, Ritter's solution was again employed to model the *u* velocity distribution in the random green water events. Figure 4.20 shows comparisons of

Table 4.6 Summary of the coefficients for Eq. (4.7) and Eq. (4.8).

Investigators	*m*	*k*	*n*	Test condition
Ryu et al. (2007b)	1.03	1.20	0.34	Plunging breaker on fixed structure
Chuang et al. (2015)	1.17	1.54	0.35	Plunging breaker on moving structure with two measurement planes
	m′	*k′*	*n′*	
Present study	0.96	3.40	0.23	Random waves on fixed structure in large basin

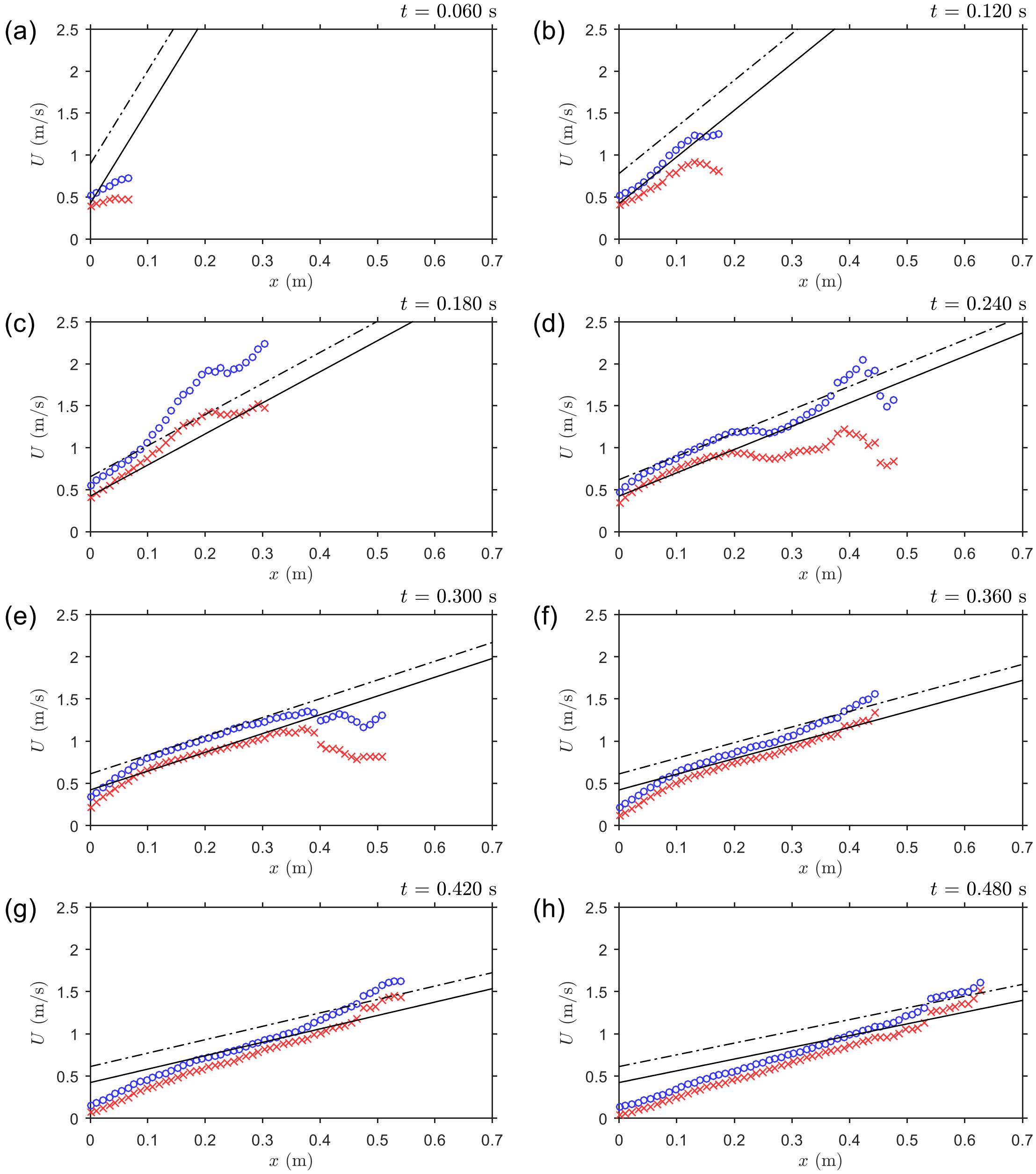

Figure 4.20 Comparisons of measured data and Ritter's solution for random green water events. *Blue circle*, cross-sectional velocity U_c; *red cross*, width-averaged velocity U_w; *solid line*, Ritter's solution with $h_0 = H_s - S$ from Eq. (3); and *dotted-dashed line*, Ritter's solution with the h_0 back-calculated from the mean green water front velocity from Eq. (4). Note that the data points are mean quantities.

the cross sectional velocity (u_c) and the width-averaged velocity (u_w) plotted against Ritter's solution at selected moments. Note that the data points in the figure are averaged quantities from all the 179 random green water events. Following the same approach, the significant weight was used to determine the initial water depth of the dam break flow, i.e., $h_0 = H_s - S$, in Ritter's solution in Eq. (4-3). Furthermore, the mean green water front velocity (U_f) averaged from all the 179 random green water events was used to in Eq. (4-4) to back-calculate the initial depth h_0. As a result, two h_0 values from the two different approaches were applied to Ritter's solution and plotted against the measurement data as shown in Fig. 4.20.

Upon the inception of green water on the deck, the transition from wave overtopping to a fully-developed green water flow encountered the momentum transfer from being vertically-dominated to horizontally-dominated, so the measured U is relatively low, as shown in Fig. 4.20(a). Shortly after, the developing green water flow became quite complex – the collapse of overtopping waves (Type I), especially for the events the feature a high-speed jet created by the impingement between the wave front and the deck, and the fall of bulk water (Type II), often created a sudden increase of the u velocity at the moment when as it fell on the deck. Figures 4.22(b-c) reflect the abrupt increase of the U velocity, especially for U_c. Note that Ritter's solution does not account for the effects described above thus the solution fails to represent the measured data. However, as the green water flow became more fully developed and horizontally dominated, Ritter's solution captures the U velocity distribution fairly well, as shown in Figures 4.22(d-h). Overall, the choice of h_0 evaluated from either Eq. (4-3) or Eq. (4-4) makes little difference for the fully-developed green water.

4.5 Conclusions

The present study experimentally investigates the kinematics and dynamics of green water on a simplified geometry, fixed model platform in a large wave basin with the green water flow generated by both focusing waves and random waves. For the focusing wave condition, wall impingement event and deck impingement event were both tested. Synchronized measurements of pressures, fluid velocities, void fraction, and free surface elevations were repeated 20 times with identical input wave condition and boundary conditions, and ensemble averaged for mean quantitates. The measured maximum U and W velocities were $0.76C_1$ and $1.21C_1$, respectively, and these magnitudes are lower than previously reported values obtained in a 2D flume due to the fact that the impingement point is farther from the vertical structure wall in the present study. For the deck impingement event, the maximum U velocity reached $1.32C_2$, close to the previously reported values.

The peak pressure reached 11.23 kPa or $0.62\rho_w C_2^2$ in the deck impingement event, measured at the middle section of the deck and close to the deck surface. The relationship between the peak impact pressure and the pressure rise time was examined using a dimensionless empirical formula. For a splashing-like green water in the wall impingement event, the peak impact pressure gained with higher contact chance with water (lower aeration level). For the deck impingement event, before impingement, the residual entrained air bubbles in the non-breaking overtopping wave tend to reduce impact pressure, resulting in negative correlation between peak pressure and aeration level. However, an opposite behavior was observed in the full-developed green water flow after impingement on deck. In this case, the higher pressure may be associated with more entrapped air being compressed by the liquid flow with large flux momentum.

Random waves was generated using the JOSWAP spectrum with the significant wave height roughly equal to the freeboard. By examining the 179 recorded random green water events recorded by high speed cameras, the events may be categorized into three types: (I) collapse of overtopping wave, (II) fall of bulk water, and (III) breaking wave crest. In particular, the Type I events not only occurred frequently, they also behaved like a dam-break flow. The maximum horizontal velocities demonstrate a lognormal distribution. A modified prediction equation based on self-similarity and featured common wave properties was successfully applied to model the velocity distribution on the deck for the random green water events. Ritter's solution was found to be able to quantitatively model the green water velocity distribution on the deck for both the focusing wave condition and the random wave condition.

CHAPTER V

TSUNAMI BORE IMPACT ON AN INLAND STRUCTURE

5.1 Introduction

Tsunami is a very long wave traveling in the ocean and mostly generated as a subsequence of geophysical forces, such as earthquake, submarine landslide, and volcanic eruption, or astronomical conditions, such meteorite impact. By causing extensive casualties and destruction to the coastal communities, the 2004 Indian Ocean and 2011 Tohoku tsunamis have raised public awareness of the improperness of existing designs for evaluating the forces and impacts generated by tsunamis. Several post-tsunami surveys for the 2004 Indian Ocean Tsunami (Fritz et al. 2006; Ghobarah et al 2006; Tomita et al. 2006) and the 2011 Tohoku Tsunami (Shimozono et al. 2012; Liu et al. 2013) reported the damages to the inland structures, such as transport facilities, coastal defense systems, and houses. Those survey results provide useful and substantial information to prepare the future investigation of the interaction between tsunami waves and coastal structures.

St-Germain et al. (2014) addressed four types of tsunami inland intrusions categorized by Takahashi et al. (2011) from the 2011 Tohoku Tsunami post-survey: overtopping, breaking wave, slowly varying, and high run-up. Overtopping type happens in port area when tsunami wave overtops the quay wall without breaking, and in this case very large flow velocity would occur. Breaking wave type features a scenario similar to surging breaker that a tsunami wave breaks at or near a shoreline and runs up on the mild-sloping beach. The run-up or so-called bore can reach up to several kilometers inland over low-lying landscape. Slowly-varying type emerges when a tsunami wave encounters a steep cliff in a deep water and bounces back (without breaking) in a relatively smooth up-and-down motion. High run-up type is characterized as a tsunami wave breaking inland on a relatively steep-sloping beach and reaching a significant run-up height at a high velocity. Many studies on the tsunami bore impacts (e.g., Linton et al. 2013; Robertson et al. 2011, 2013; Kihara et al. 2015; Chinnarasri et al. 2013; Moon et al. 2014; Rahman et al. 2014; Shafiei et al 2016) took breaking wave type into major account. However, studies on the tsunami wave impacts of overtopping and high run-up type, which are a more serious threat to coastal communities, are quite few.

Numerous laboratory works have been performed to improve the knowledge of the interaction between tsunami wave and coastal structures for breaking wave type. Some researchers studied the tsunami bore impact on the front wall by considering the vertical wall blocking the flume width (Cross, 1967; Linton et al. 2013; Robertson et al. 2011, 2013; Kihara et al. 2015). Some drew the attention to the low-crested coastal structure with wave overtopping under tsunami wave impact (Asakura et al. 2000; Thusyanthan and Madabhushi 2008; Fujima et al. 2009; Chinnarasri et al. 2013; Moon et al. 2014; Rahman et al. 2014). To examine the 3-D tsunami impact on lateral structure wall without overtopping, Palermo et al. (2012) considered square and circular cylinders with a height that wave overtopping never occurred. From their measured force time histories, three phases of horizontal forcing were identified: impulsive, run-up, and quasi-steady hydrodynamic. With respect to vertical forces, Yeh (2007) reported that impulsive, hydrodynamic drag, hydrodynamic lift, and buoyant force have been identified. As partially inspired by Cawley (2014) who pointed out the need of investigating the tsunami loadings to different building shapes and orientations, Shafiei et al (2016) performed a comprehensive experimental investigation of tsunami bore impact on a square prism with six different orientations. They examined the relation between bore heights and bore velocities, and numerically modelled the steam-wise (surge) and upward maximum forces. Furthermore, relevant drag coefficients at each heading were determined.

High pressures caused by tsunami wave impacts could lead to local damage that may deteriorate the structural integrity and result in structure failure. Palermo et al. (2012) suggested that the hydrostatic pressure may be used to approximate the pressure distribution on the upstream face of a square structure. On the contrary, both Nouri et al. (2010) and Kihara et al. (2015) identified two types of exerted pressure during the tsunami impact: (a) an impulsive pressure with a short duration on O(ms), and (b) a quasi-steady pressure with a longer duration on O(s). The quasi-steady pressure is associated with hydrostatic pressure, while the impulsive pressure is similar to the breaking wave impacts

(Bagnold 1939; Peregrine 2003) that often gives rise to large pressure magnitude. On the other hand, the surge force may be estimated with measured pressure. In addition to examining the pressure maxima on the wall face at different headings, Shafiei et al (2016) successfully calculated the time history of surge force using measured pressure time history by assuming uniform pressure distribution over the width of the structure. In addition, Robertson et al. (2011, 2013) suggested that considering the additional surge force caused by reverse flow is needed to accurately estimate the surge force maxima with measure pressure maxima.

Knowing the tsunami impact velocity is crucial to determine the hydrodynamic pressure or force acting on the structure wall. Kihara et al. (2015) addressed that the ideal flow model of Ritter (1892) can be used to describe the bore flow velocity profile along propagation. However, Shafiei et al. (2016) showed that the tip region of the bore is better described by a real fluid model with friction slope taken into account (Chanson 2006a). The dam break models by Ritter (1892) and Chanson (2006a) provide formulas to estimate the bore front celerity under different circumstances, but the 1-D assumption limits their applications to the realistic tsunami-structure interactions in which realistic flows are mostly 3-D. On the other hand, the bore velocity can be determined by bore height. However, researchers (Murty 1977; Kirkoz 1983; Bryant 2001; Matsutomi 2010; Shafiei et al. 2016) have shown that the empirical coefficients are affected by the Froude number of bore flow. Palermo et al. (2012) concluded that a proper assessment of momentum flux is needed to accurately predict the time history of hydrodynamic pressure/force. To achieve that, advanced approaches or measurement techniques are desired to determine the time-varying, full-field velocities in 2-D or even 3-D sense.

The tsunami-induced bore is often highly turbulent and aerated, and this kind of flow hampers the use of the particle image velocimetry (PIV) technique (Kihara et al. 2015) that has been well established in quantifying instantaneous flows. To reveal the fluid velocity in the aerated region of turbulent flows, such as plunging breaking wave, Ryu et al. (2005) introduced an image-based technique called bubble image velocimetry (BIV). In fact, BIV was derived from the principle of particle image velocimetry (PIV). Unlike

PIV that illuminates seeding particles with high-power laser, BIV only requires a uniform, light background illuminated by normal light bulbs to enhance the shadow texture created by the air and water interfaces. The shadow texture then serves as tracers for tracking the fluid particle displacement by cross-correlating two consecutive images. Many studies have successfully employed BIV to perform the velocity measurements in highly aerated flow, such as the greenwater due to breaking wave impingement on offshore structures (Ryu et al. 2005, 2007a, 2007b; Chang et al. 2011; Song et al. 2015; Chuang et al. 2015), wave run-up on a sloping beach (Pedrozo-Acuña et al. 2011), open channel flows (Lin et al. 2008) and sloshing (Song et al. 2013).

The present study considers the tsunami wave impact of high run-up intrusion type (Takahashi et al. 2011; St-Germain et al. 2014): a scenario that a tsunami wave propagates onshore, breaks inland on a 1/10 sloping beach, runs up as a bore, and impinges a coastal structure. By referencing to Shafiei et al (2016), four different structure headings, 0°, 15°, 30° and 45°, were considered in the present experiment. The instantaneous, full-field fluid velocity was revealed by the BIV technique. Pressure measurement was taken at four fixed points on the wall face of the model structure. The surge forces were measured by a multi-axis load call, and comparison with the surge forces calculated from measured pressure was made. To obtain ensemble averages, identical tsunami wave condition was repeated 20 times for each heading. The flow kinematics and hydrodynamics of the tsunami bore impact on a structure at four headings will be presented and discussed.

5.2 Experiment setup

5.2.1 Facility and model structure

The experiment was conducted in a three-dimensional wave basin housed in O.H. Hinsdale Wave Research Laboratory (HWRL) at Oregon State University. The dimensions of the wave basin are 48.8 m long, 26.5 m wide, and 2.1 m deep. A multidirectional, piston-type wavemaker, capable of generating maximum wave height of 0.8 m with a maximum stroke of 2.1 m, is installed at one end of the wave basin. The wave basin contains a 1/10 sloping beach ($\theta_s = 5.71^\circ$) where its toe is at 24 m from the original position of the wavemaker paddles.

The wave basin was filled with freshwater to a constant depth of $h = 0.50$ m throughout the experiment. A simplified model structure was constructed and located on the sloping beach at where its front wall is 8.39 m from the toe of the sloping beach, as shown in Fig. 5.1. The dimension of the model structure is $0.63 \times 0.63 \times 0.61$ m^3. As sketched in Fig. 5.2(a), to spatially describe the physical process around a model sitting on a slope, two coordinate systems, earth-fixed coordinates (x_E, y_E, z_E) and slope-fixed coordinates (x, y, z) may be needed. Figure. 5.2(b) depicts the model structure at the four different headings – $\theta_b = 0^\circ$, $\theta_b = 15^\circ$, $\theta_b = 30^\circ$, and $\theta_b = 45^\circ$. To be consistent, the slope-fixed coordinates will be referred to throughout the data processing and analysis. However, for demonstration purpose to avoid distortion in background image, the axes of image will remain in earth-fixed coordinates, but the physical quantities presented in the figure are still in slope-fixed coordinates.

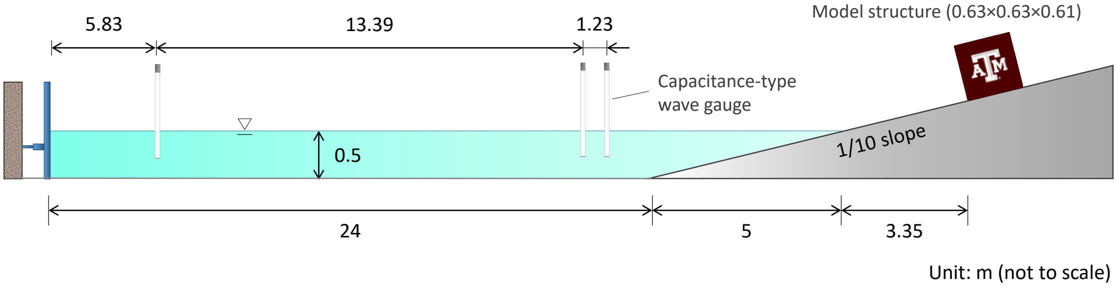

Figure 5.1 Schematic diagram of the model setup and wave gauge in the wave basin from lateral view.

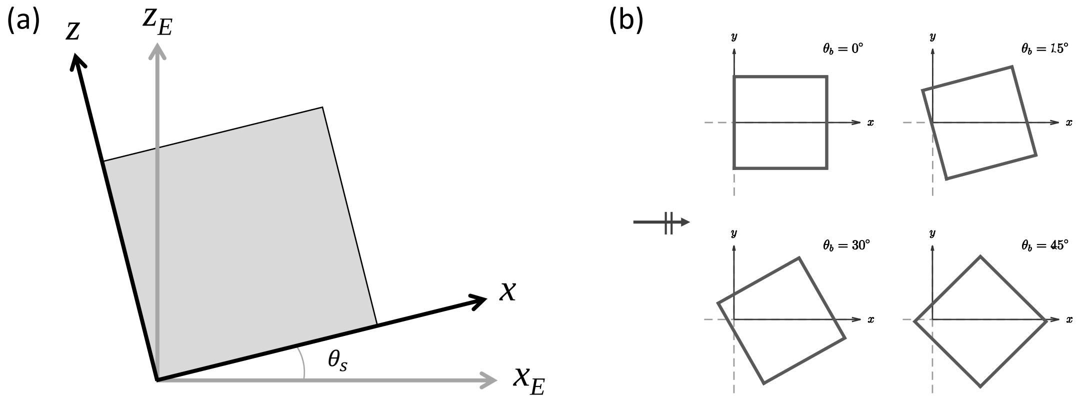

Figure 5.2 (a) Definition of the earth-fixed coordinate system ($x_E - y_E$ plane) and the slope-fixed coordinate system (*x*-*z* plane). (b) Box model heading corresponding to the slope-fixed coordinate system. Note that the wave propagates from left to right.

5.2.2 Fluid velocity measurement

A down-looking high speed camera (Phantom M340, Vision Research) was installed 5.19 m high from the toe of the model frontal wall at $\theta_b = 0^\circ$, covering a field of view (FOV) of 2.66×1.66 m^2 with the highest resolution of 2560×1600 pixels. The high speed images were recorded at a frame rate of 500 frames per second throughout the experiment. A Nikon 50-mm *f*/1.4 focal lens was mounted, and the focal plane was set to the horizontal plane 0.1 m above the beach face at the front toe of the model at the $\theta_b = 0^\circ$ heading. The focal plane is parallel to the $x_E - y_E$ plane.

The bubble image velocimetry (BIV) technique, introduced by Ryu et al. (2005) was employed to measure the instantaneous flow field. Preliminary tests indicated that no additional illumination is necessary. The M340 is of very high dynamic range (12 bits), capable of detecting fine shadow texture or so-called contrast created by the interfaces in multiple-phase flow. For example, the present study utilizes the contrast created by air bubbles and water droplets relative to the background in the aerate flow. The concept of BIV technique is to employ the shadow texture within depth of field (DOF) as tracers. As a result, these tracers in two consecutive images can be cross-correlated to obtained the displacement and determine the fluid velocity. The DOF was set to 0.53 m with *f*-number equal to 1.4, and this enabled a sufficient coverage in vertical direction with 5.1% of geometric error on the measured velocity magnitude. The interrogation window was set to 32×32 pixels with 50% overlaps, resulting in 17×17 mm^2 in spatial resolution. Table 5.1 summarizes the image recording setup. More details on the principles, validation, applications, and discussions regarding the BIV technique can be found in Ryu et al. (2005, 2007a), Chang et al. (2011), Lin et al. (2012), Song et al. (2013), Chuang et al. (2015). It should be noted that the fluid velocities measured on $x_E - y_E$ plane were transformed on *x*-*y* plane before plotting and further analyses.

Table 5.1 Summary of image recording setup. Note that the camera framing rate was fixed at 500 fps.

Measurement Plane	Resolution (pixels)	FOV size (m^2)	Spatial Resolution (mm^2)	D (m)	ℓ (m)	ε (%)
Side view	2560 × 1600	2.65× 1.66	17 × 17	0.53	5.19	5.1

5.2.3 Pressure measurement

Pressure measurements were taken at four evenly-spaced measurement points, P1 $(z = 20\text{ mm})$, P2 $(z = 50\text{ mm})$, P3 $(z = 80\text{ mm})$, and P4 $(z = 110\text{ mm})$. Four piezoresistive differential pressure sensors (Kistler 4053A1) were mounted facing offshore at $\theta_b = 0^\circ$. Careful work was done to ensure that the frontal wall with pressure sensors mounted remained flush. The present sensor measures the pressure differential referenced to the surrounding atmospheric pressure and cover a measurement range up to 1 bar with a sensitivity of 200 Pa/mV and a natural frequency higher than 15 kHz. In the present experiment, pressure measurements were sampled at 10 kHz.

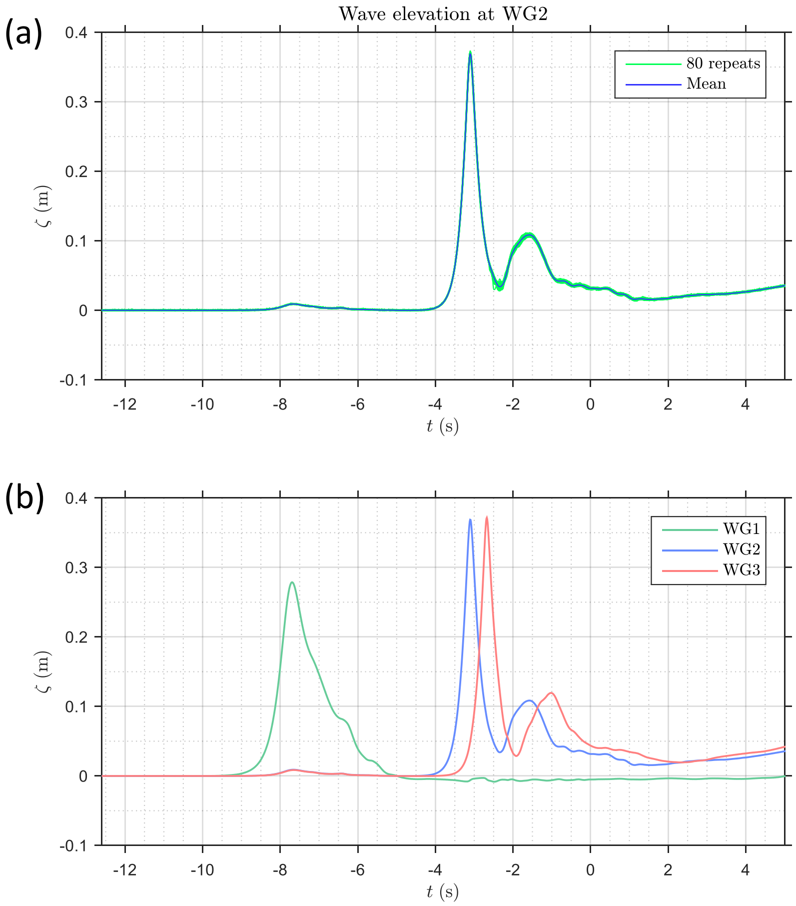

Figure 5.3 (a) Mean and instantaneous wave elevations measured at WG2. (b) Mean wave elevations measured at three wave gauges.

5.2.4 Force measurement

A multi-axis force transducer (UDW3-500) was used to measure forces and moments. One end of the force transducer was attached to a sturdy steel bar that stood normal to the beach face; while the inner wall of the model structure was mounted to the other side of the force transducer. In doing so, the force transducer measured what the model structure actually sensed. It should be specially mentioned that the model heading was changed by rotating the base of the steel bar. The axes of the measured forces and moments were transformed to the slope-fixed coordinate system before analysis. In the present experiment, force and moment measurements were sampled at 500 Hz. Note that the natural frequency of this force transducer is higher than 700 Hz.

5.2.5 Wave condition

The tsunami wave was generated with a wavemaker input signal programed as a single position surge using an error function designed to maximize the full stroke of the wavemaker paddle in 6 s. As a result, a tsunami wave with a wave amplitude $A = 0.37$ m was generated, and broke inland on the sloping beach where the impingement was observed very close to the still water line. The wave elevation was recorded using capacitance-type wave gauge at three locations (as sketched in Fig. 5.1), and the measurement was summarized in Table 5.2. Figure 5.3(a) plots the mean and repeated waves measured at WG2 and shows that the wave of interest is highly repeatable. Figure 5.3(b) further plots the mean wave elevation measured at three locations.

Table 5.2 Summary of wave gauge position, wave height, and wave speed.

Wave gauge	x_E position (m)	Wave amplitude, A (m)	Wave speed (m/s)
WG1	$x_E = 26.52$ m	0.28	2.76
WG2	$x_E = 39.91$ m	0.37	2.92
WG3	$x_E = 41.14$ m	0.37	2.92

5.2.6 Measurement procedure

Velocity, wave, pressure, forces, and moments measurements were simultaneously performed, and the synchronization over various instruments was achieved with a rising-edge signal sent 20 s before the wavemaker initiation. Since the recorded period of the high speed images for each event is very limited (only 4 sec), a delay was programed in the camera control software to tackle this issue. All measurements as well as identical initial and boundary conditions were repeated 20 times for each heading. As a result, a total of 80 identical waves were tested. Before further examination and analysis, the measured velocity, forces, and moments were transformed to the slope-fixed coordinate system. In addition to instantaneous data, the ensemble averages were obtained by averaging the measured data over 20 repeats. The $t = 0$ is defined as the moment that the tsunami bore reached the frontal wall of the model structure at the $\theta_b = 0^\circ$ heading.

5.3 Results and discussions

5.3.1 Flow pattern and maximum velocity

The mean velocity field of a tsunami bore interacting with a simplified coastal building at different headings was revealed by the BIV technique over 20 repeated tests. The mean velocity maps are displayed in Appendix I. To better visualize the flow pattern, Fig. 5.4 plots the streamline maps calculated from the velocity fields. Note that the streamlines map is superimposed with a background image set randomly selected from 20 repeated tests. Before impingement on structure by 0.15 s, as shown in Fig. 5.4(a), the streamline maps among different headings indicate that the flow is positive x-direction dominant. Comparing the bore front over the repeated tests, the waterline is highly non-uniform and unsteady. According to Yeh (1991), the irregularity and three-dimensional effects of turbulent flows mainly accounts for such formation. Except the velocity variation along the bore waterline, the rough shape could entrap air on solid boundary upon the impact on vertical wall. Upon the impact, as shown from Fig. 5.4(b) to (d), it is clearly demonstrated through the streamline maps that the flow patterns were being affected by the geometry due to the angle of heading. As expected, the $\theta_b = 0^\circ$ heading and $\theta_b = 45^\circ$ heading create quite symmetric flow patterns. The U velocity contour maps and the V velocity contour maps, as respectively presented in Fig. 5.5 and Fig. 5.6, also show symmetric distribution of velocity magnitude.

Comparing the flow patterns (Fig. 5.4) and *U* velocity contour maps (Fig. 5.5), the $\theta_b = 0^\circ$ heading undoubtedly created strongest reverse flow in front of the frontal wall. With the model structure more orientated, the more area of reverse flow shrinks, and more *x*-direction dominant flow was being directed to the lateral direction instead of bouncing off the structure wall to fuel the reverse flow. When the structure was at the $\theta_b = 45^\circ$ heading, the flow pattern became symmetric again, but with the least reverse flow being created due to the separation at the tip. The less violent reverse flow might also imply a weaker surge force sensed by the model structure. On the other hand, the flow patterns and velocity contour maps both point out that the unaffected area behind the structure increases with larger angle of heading up to 45°.

For a tsunami bore, it is expected that maximum *U* velocity is located at or near the bore front. The *U* velocity magnitude distribution in Fig 5.5 shows that the front velocity right along the waterline is relatively small instead. What accounts for this is the spatial variation of the waterline among 20 repeated tests averages out the velocity magnitude at and near the bore front. The variation in magnitude can be quantified as turbulence intensity, and more details and discussions will be presented in the next section.

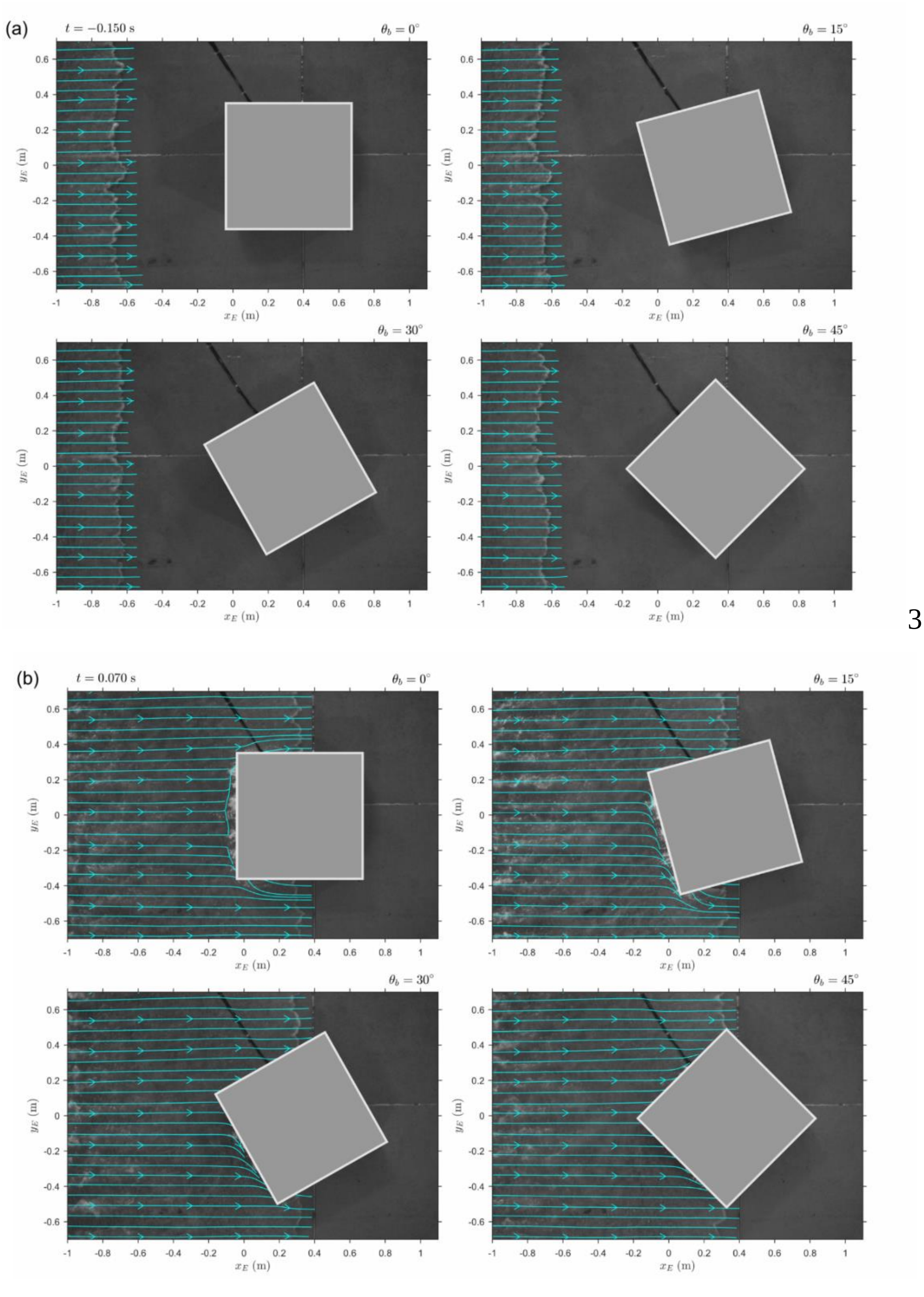

3.

Figure 5.4 Streamline map at (a) *t* = -0.15 s, (b) *t* = 0.07 s, (c) *t* = 0.20 s, (d) *t* = 0.33s.

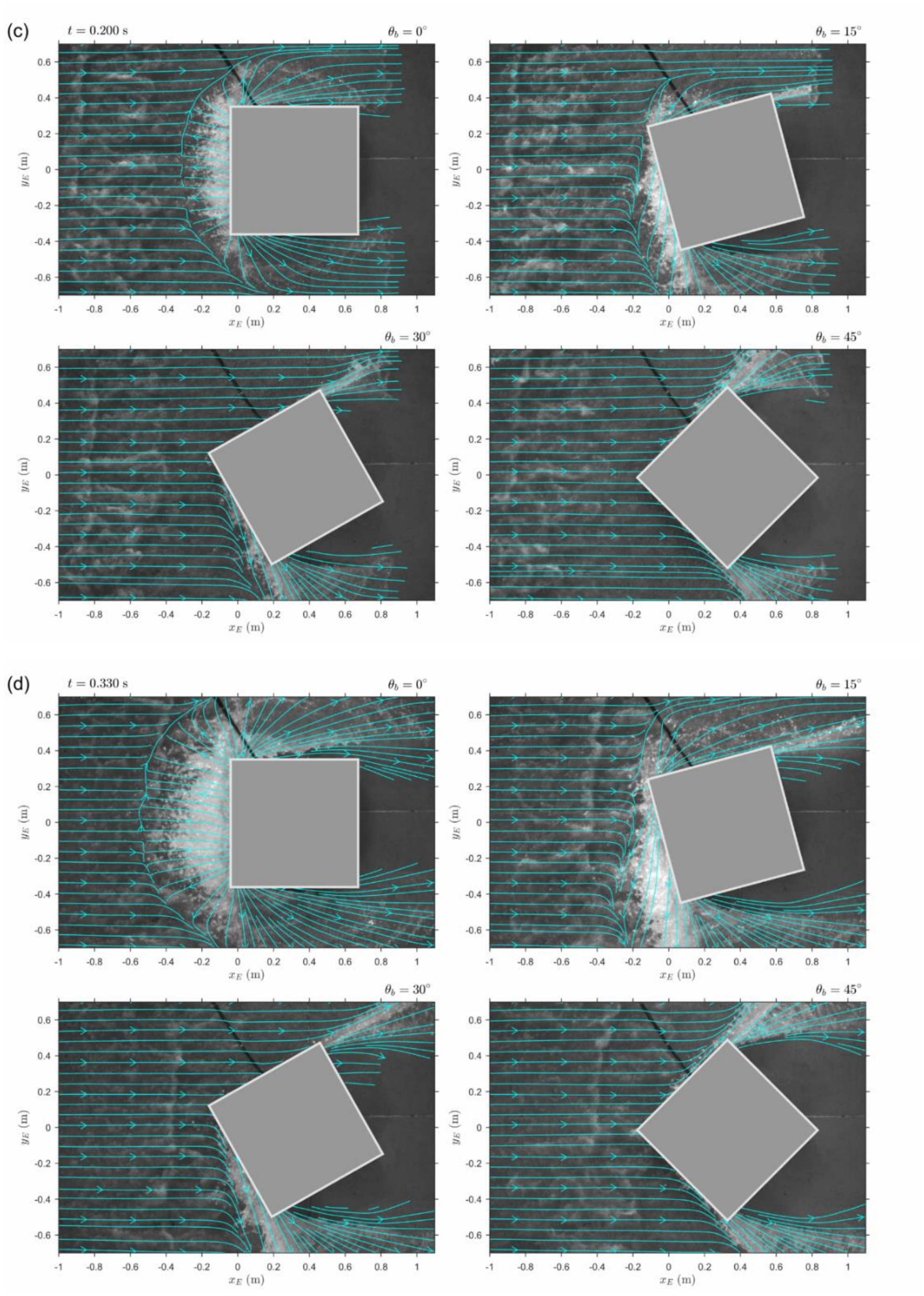

Figure 5.4 Continued.

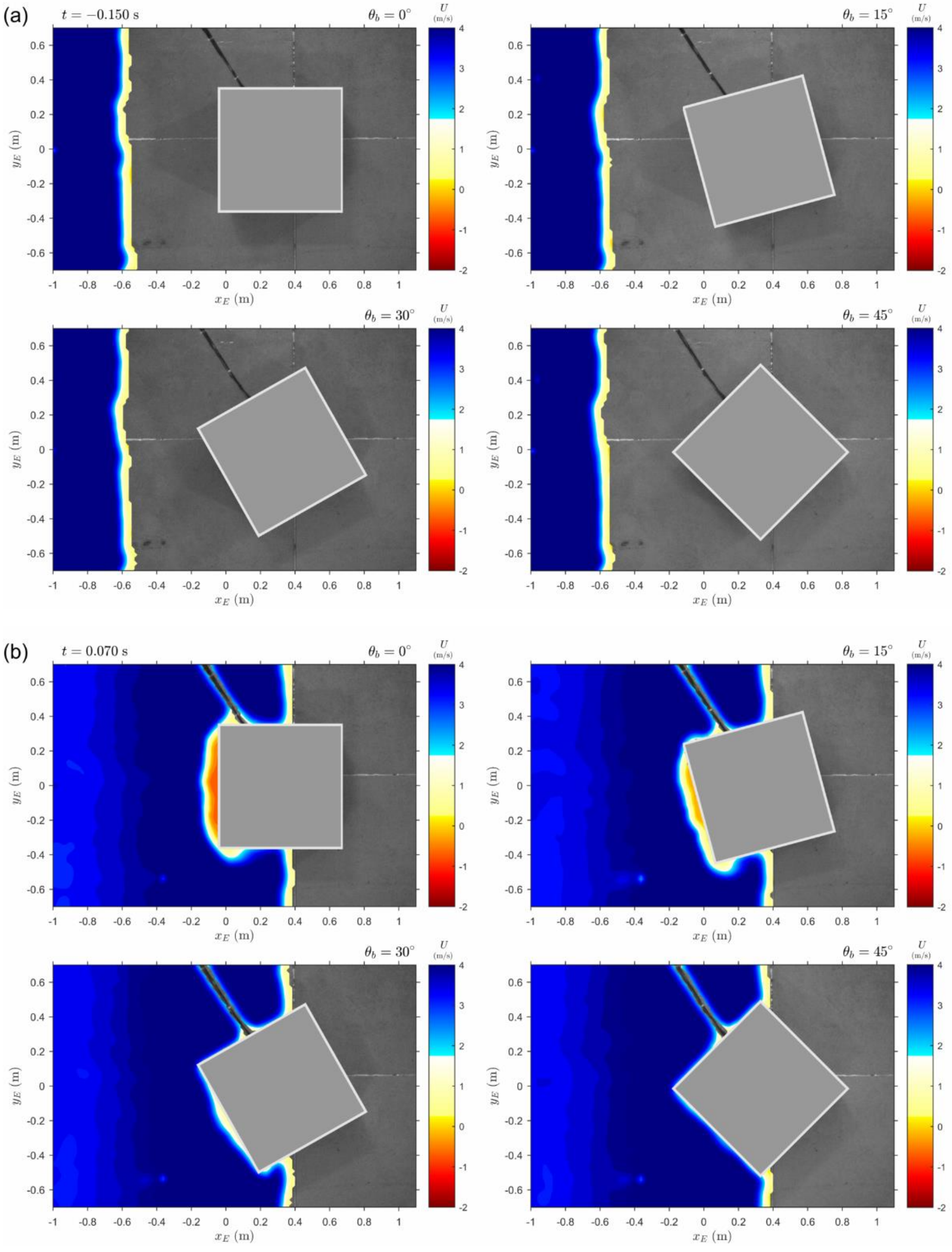

Figure 5.5 *U* velocity contour maps at (a) t = -0.15 s, (b) t = 0.07 s, (c) t = 0.20 s, (d) t = 0.33 s.

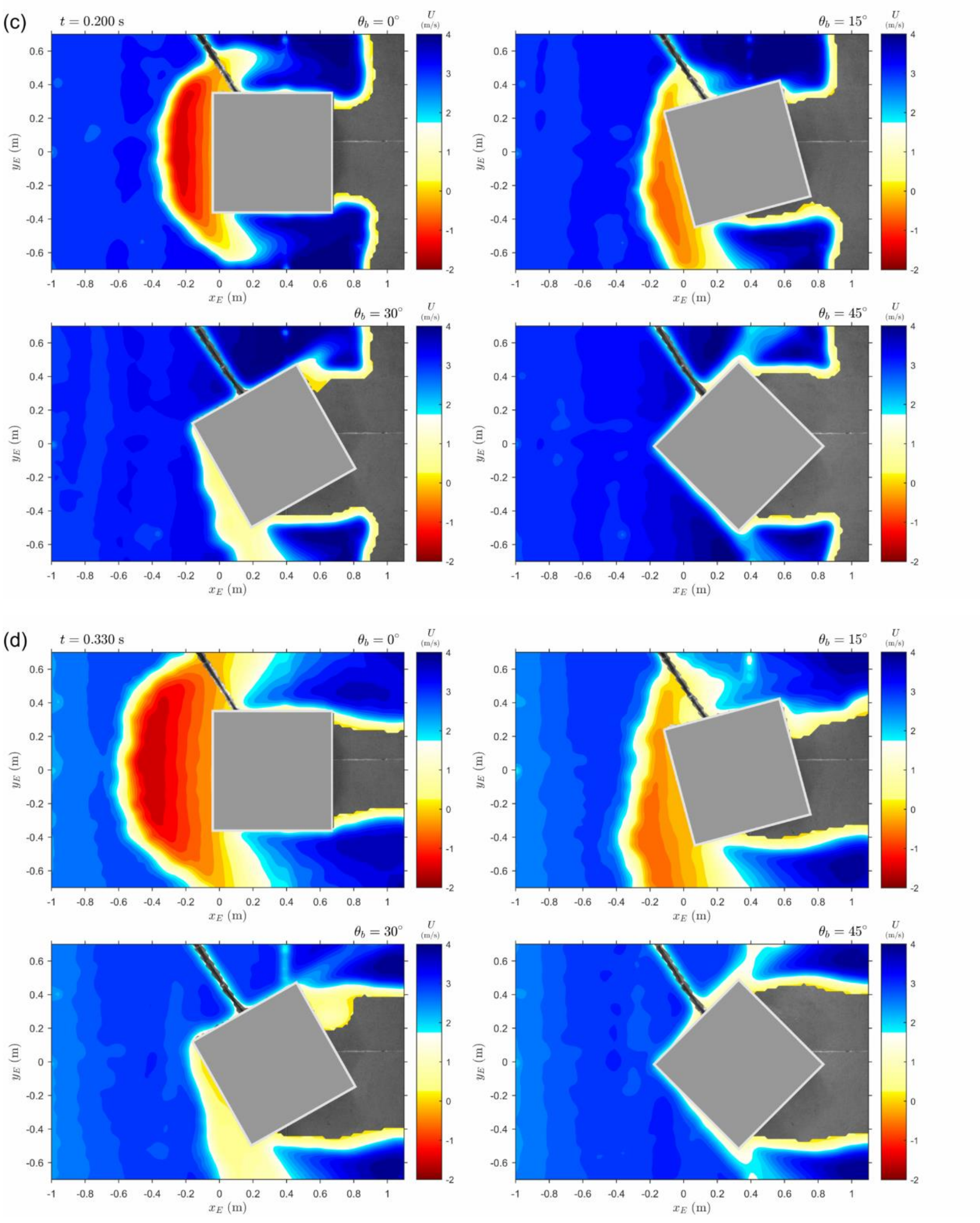

Figure 5.5 Continued.

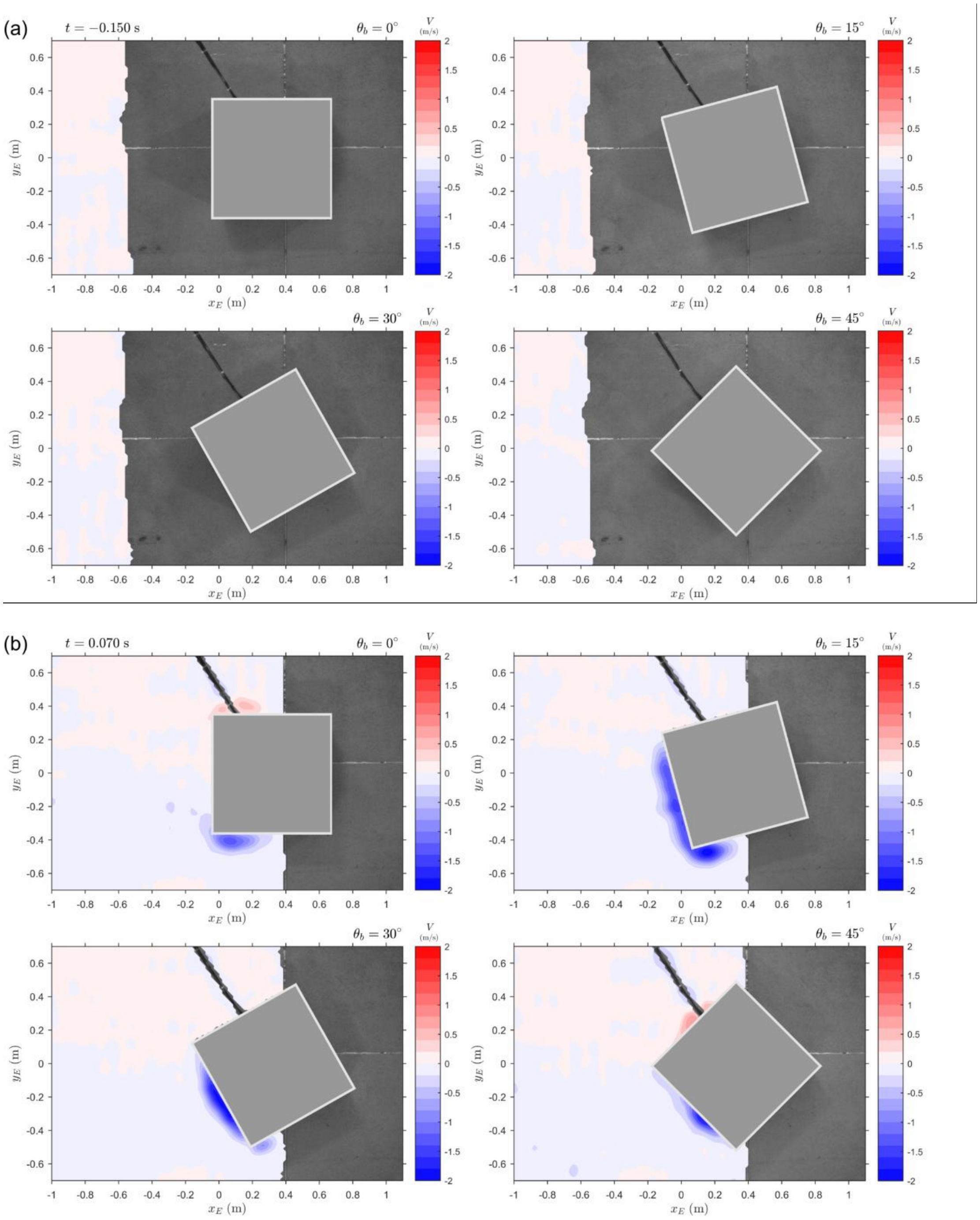

Figure 5.6 *W* velocity contour maps at (a) *t* = -0.15 s, (b) *t* = 0.07 s, (c) *t* = 0.20 s, (d) *t* = 0.33 s.

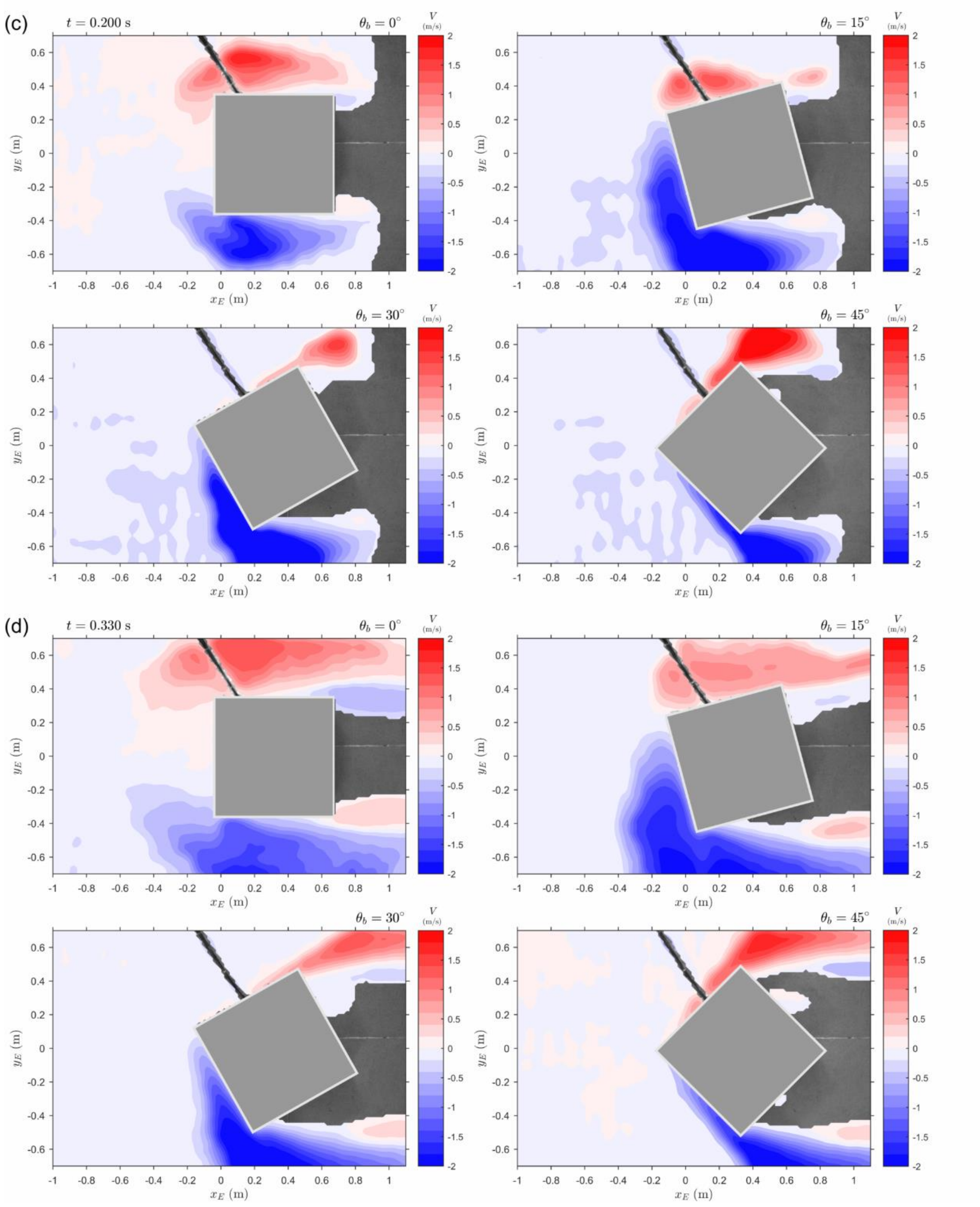

Figure 5.6 Continued.

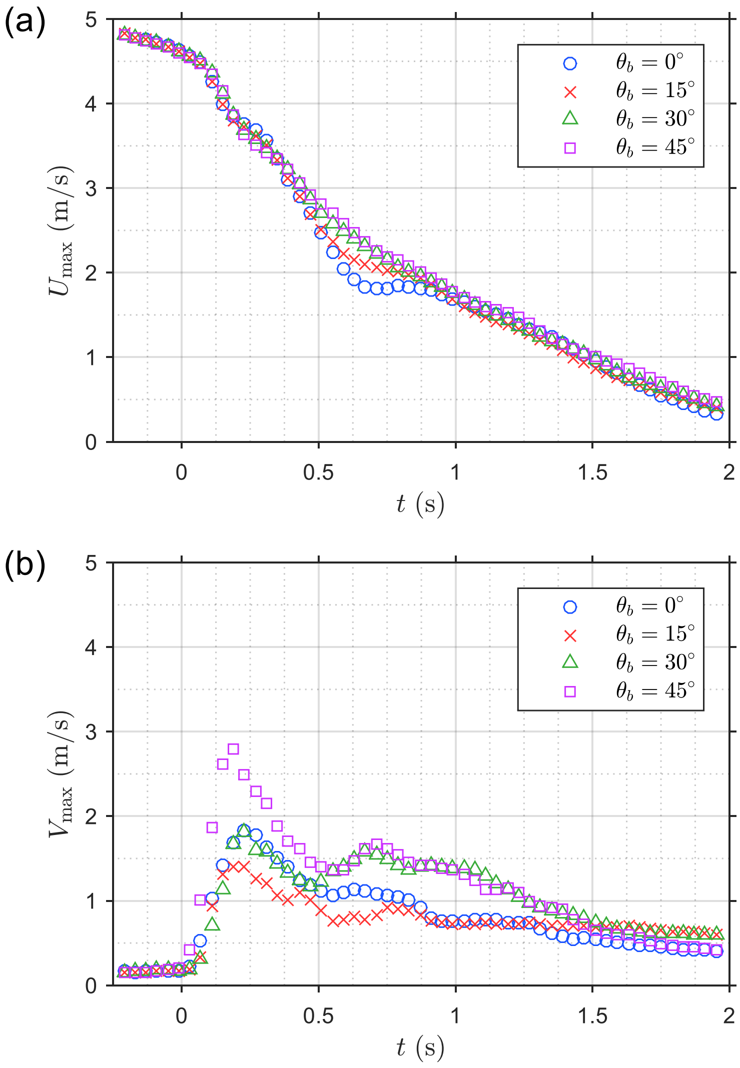

Figure 5.7 Time history of (a) maximum *U* velocities and (b) maximum *V* velocities for four headings.

Figure 5.7 exhibits the comparison of the time histories of maximum *U* velocity ($U_{\max}$) and maximum *V* velocity ($V_{\max}$) for four different headings. As shown in Fig 5.7(a), the $U_{\max}$ was decreasing as the tsunami bore was propagating on a sloping beach, and its magnitude is 4.6 m/s at $t = 0$. Note that 4.6 m/s is defined as the $U_{\max}$ used in further analysis. By examining the *U* velocity contour maps in Fig. 5.5, it can be seen that the dominant *U* velocity always appears near the bore front. The comparison between Fig. 5.5 and Fig. 5.7(a) shows that the magnitude of dominant *U* velocity does not vary among different headings until the bore front passed the right bound of the field of view. According to Fig. 5.7(b), the largest $V_{\max}$ is found at the $\theta_b = 45^\circ$ heading with a magnitude up to 2.79 m/s (~ 0.61 $U_{\max}$); while the smallest $V_{\max}$ is found at the $\theta_b = 15^\circ$ heading with a magnitude of 1.41 m/s (~ 0.31 $U_{\max}$).

5.3.2 Turbulence intensity

In the ensemble-averaging process the instantaneous velocity was decomposed into the mean velocity and turbulent fluctuation (u'), i.e. $u = U + u'$. The computation of turbulence intensity can be expressed as:

$$I = \langle u'u' + v'v' \rangle^{1/2} \tag{5-1}$$

where $\langle \ \rangle$ denotes the sum of the values from repeated tests at any given point.

Figure 5.8 displays the turbulence intensity contour maps at four selected moments for four different headings. Note that the turbulence intensity is normalized by the $U_{\max}$ at $t = 0$. Before impact, large turbulence intensity mostly located near the bore front with a magnitude up $0.3U_{\max}$. Upon the impingement, even larger turbulence intensity was found in the reverse flow, and the magnitude is positively related to the violence of reverse flow as well as the angle of heading. At the $\theta_b = 45^\circ$ heading, the flow-straightening geometry produced the least turbulence intensity in the interaction between bore and structure. Figure 5.9 further exhibited the time histories of I_{max} (normalized by $U_{\max}$) for different headings. The largest I_{max} is found 0.39 $U_{\max}$ at the $\theta_b = 0^\circ$ heading after impingement.

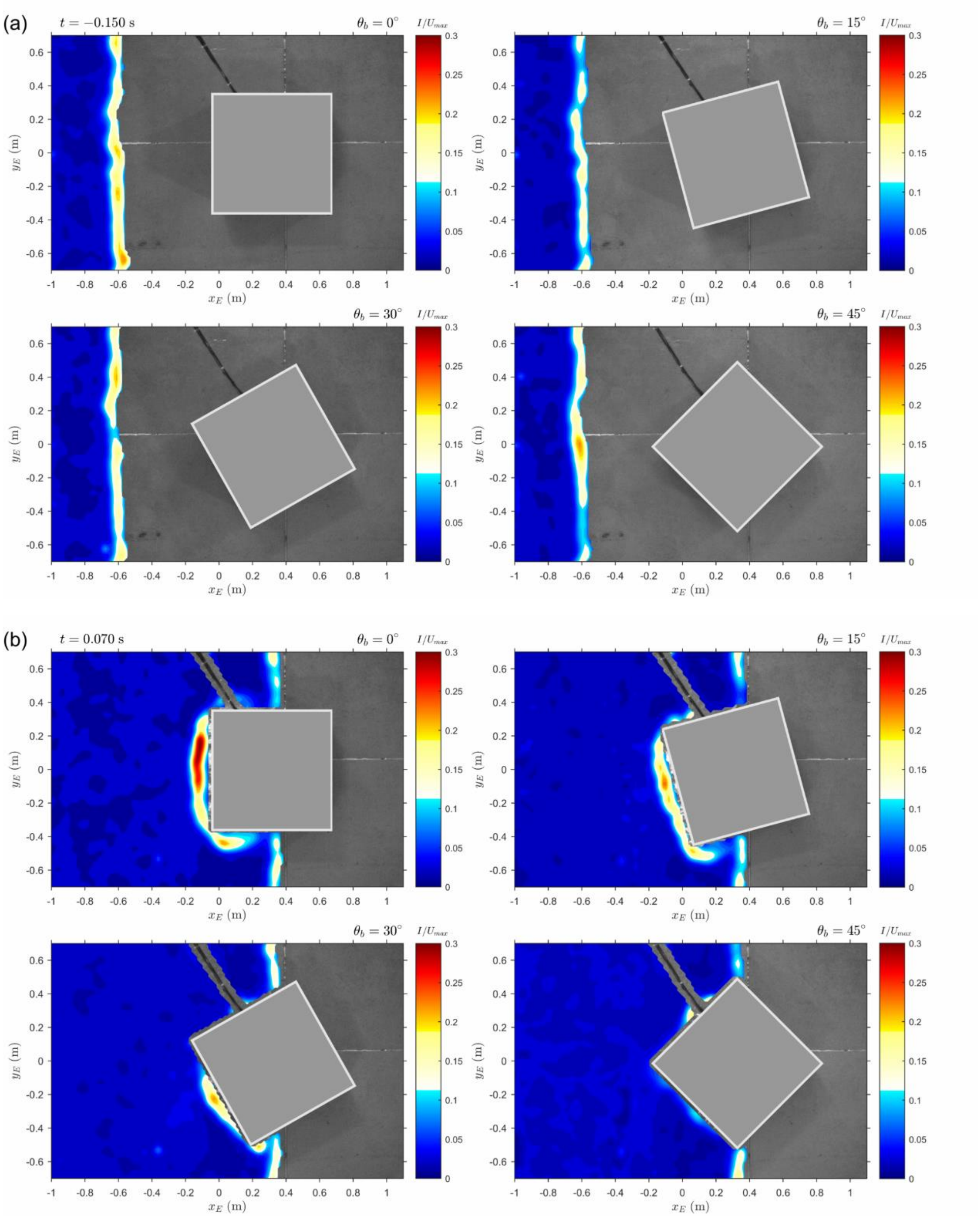

Figure 5.8 Turbulence intensity contour maps at (a) *t* = -0.15 s, (b) *t* = 0.07 s, (c) *t* = 0.20 s, (d) *t* = 0.33 s.

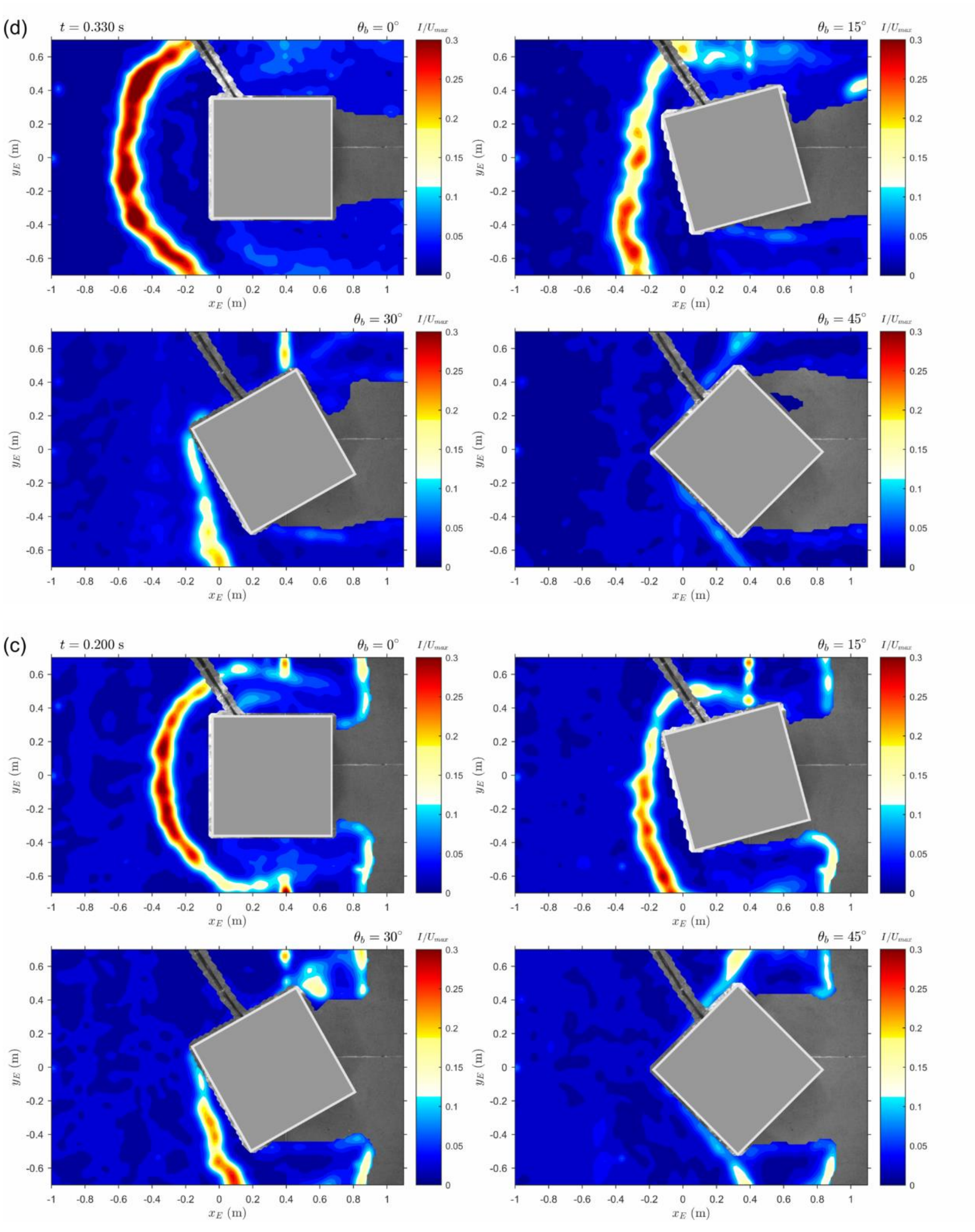

Figure 5.8 Continued

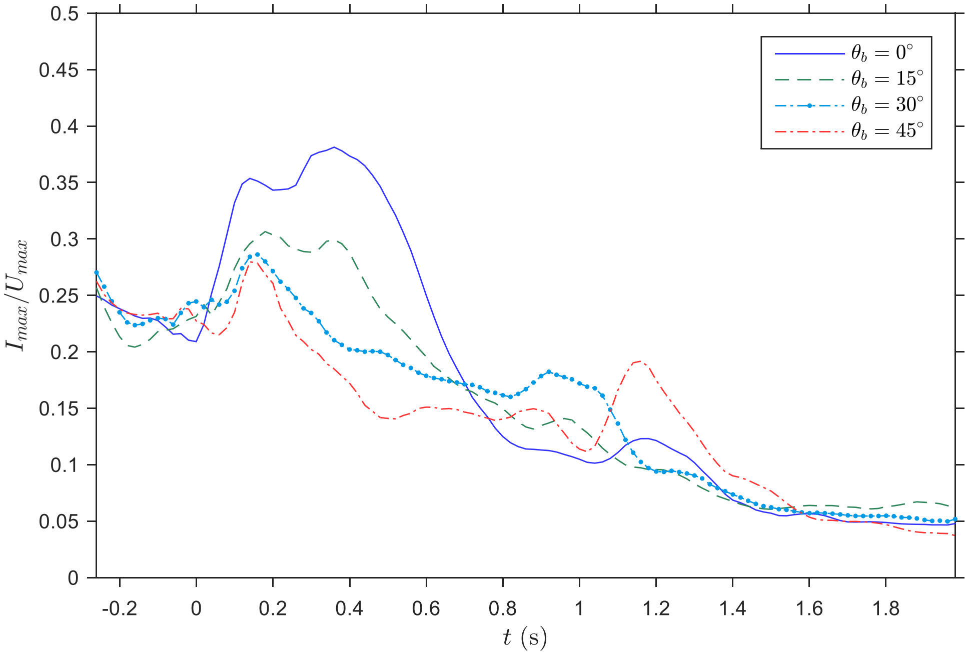

Figure 5.9 Time history of maximum turbulence intensity

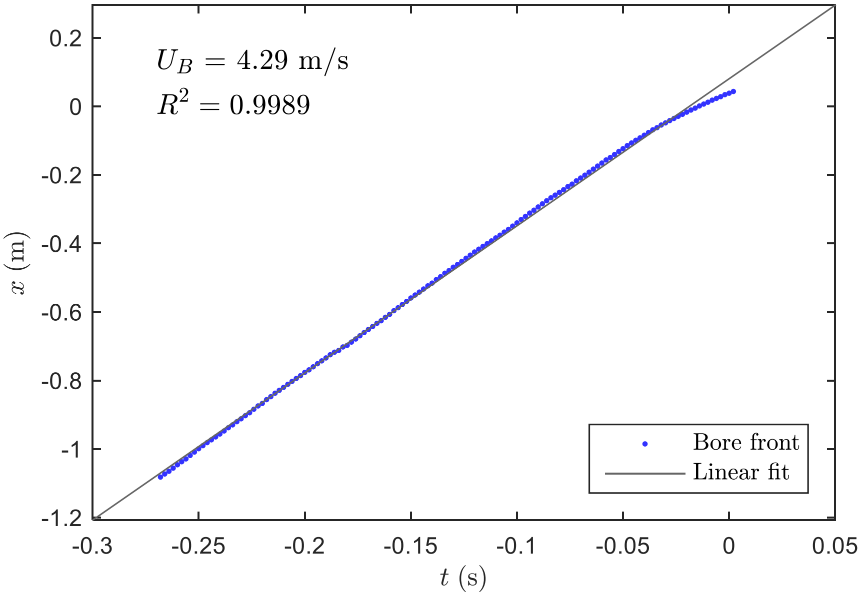

Figure 5.10 Time history of bore front propagation before impact.

5.3.3 Modeling tsunami bore as dam break flow

Figure 5.10 plots the time evolution of the bore front with a linear fit. Although the flow was propagating on a sloping beach, the duration (merely 0.3 sec) is so short that the deduction due to bed slope is not obvious and thus the bore front displacement evolved in a linear sense along the time axis. As a result, the bore front celerity (U_B) right before impact can be estimated as the slope of the linear fit or 4.29 m/s. Several studies (e.g., Kihara et al. 2015) suggested that the run-up motion may be described as a dam break flow. By modeling the tsunami bore as a dam break flow, Chanson (2006b) proposed a simple mathematic form with the consideration of bed slope to predict the celerity of the bore front and the formula reads as:

$$U_B = 2\sqrt{gh_D} + S_o g_n t_D \tag{5-2}$$

where h_D is the initial water depth of the reservoir, S_o $(= -\sin\theta_s)$ is the bed slope, t_D is time with $t_D = 0$ being the instant of dam removal, g_n is the gravitational acceleration normal to the beach face, and the solution is valid over $-\sqrt{g_n h_D} < x_D / t_D < 2\sqrt{g_n h_D}$ in which x_D is positive in the downstream direction with $x_D = 0$ at the dam. Unlike a typical dam break flow caused by a sudden release of large water mass, the transition between tsunami wave and bore (wave breaking on a sloping beach) is a continuous process such that the h_D is not explicitly defined in such flow. The breaking wave height may be the most appropriate substitute for h_D, but it is not practically available. On the contrary, the sum of water depth and tsunami wave amplitude or $h_D = h + A$ may be an acceptable way, and thus used in the present study. The impingement point ($x_D = 0$ or $x = -3.37$ m) is selected to match the initial location of dam, and the instant of the wave impinging on the bed slope is set to the instant of dam removal.

Table 5.3 Measured and predicted bore front velocity (U_B). Note $_D$ is the moment as the bore front reached the frontal wall of the model structure at the $\theta_b = 0°$ heading.

Measure U_B	Calculated U_B	$2\sqrt{g(h+A)}$	$S_o g t_D$
4.29 m/s	5.09 m/s	5.84 m/s	-0.75 m/s

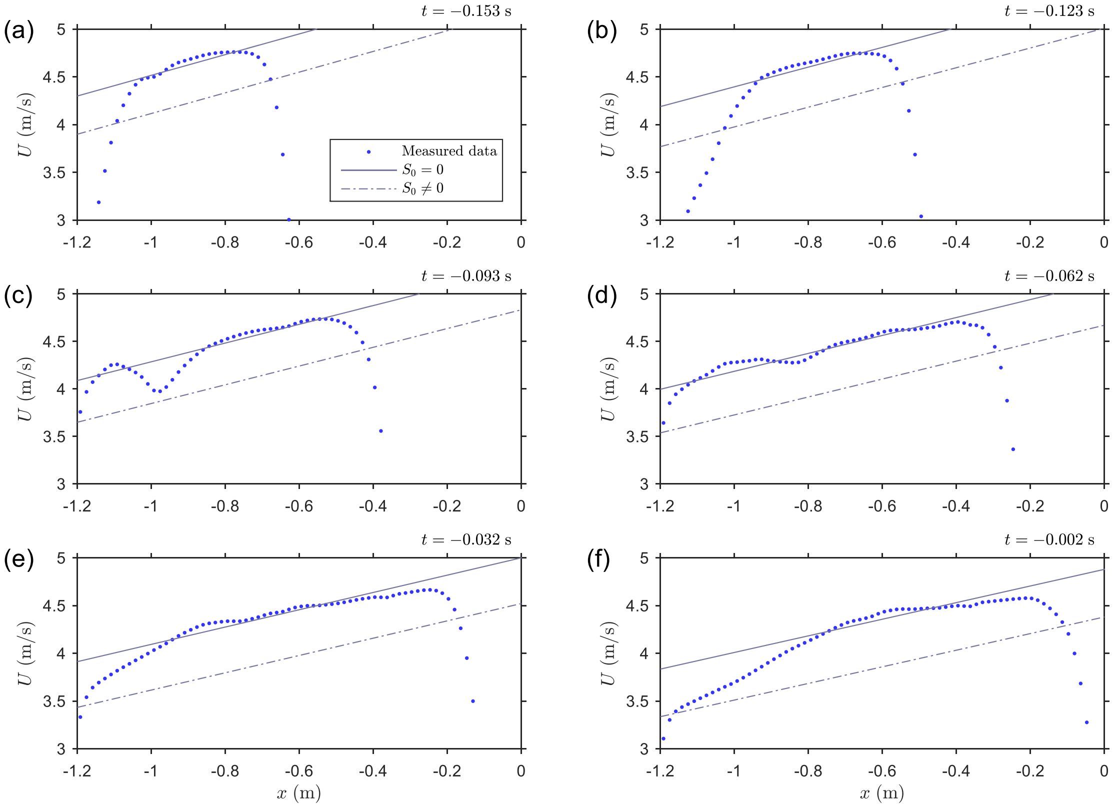

Figure 5.11 Comparison of measured U velocity distribution and analytical solutions for the flow before impact. *Solid line*, the analytical solution from Ritter (1892); *dot-dashed* line, the analytical solution from Chanson (2006b).

Table 5.3 lists the measured bore font celerity and the calculated results for each term in Eq. (5-2). The predicted value overestimates by 19%. The overestimation implies that friction slope is not negligible. However, the estimation of the friction slope is possible with the measurement of roughness (or estimating equivalent roughness height) on the beach face, but the required value is not available in the present study.

Assuming a dam break flow as an ideal fluid in a frictionless channel with zero bed slope, Ritter (1892) proposed an analytical solution to the Saint-Venant equations. The solution to a 1-D, linear *U* velocity distribution reads as:

$$U = \frac{2}{3}\left(\sqrt{gh_D} + \frac{x_D}{t_D}\right) \tag{5-3}$$

Chanson (2006b) extended Eq. (5-3) by adding the reduction due to bed slope:

$$U = \frac{2}{3}\left(\sqrt{gh_D} + \frac{x_D}{t_D} + S_o g_n t\right) \tag{5-4}$$

Figure 5.11 compares the measured *U* velocity distribution (averaged over the *y* axis) with Eq. (5-3) and Eq. (5.4) before impingement. Surprisingly Eq. (5-3) fits the measured *U* distribution very well, but the consideration of bed slope effect leads to an underestimation in magnitude. Having said that, the plunge of the *U* velocity near the bore front is resulted from the average-out due to the bore waterline variation among repeated tests. In short, the Eq. (5-3) provides an acceptable quantitative description on the *U* velocity distribution on tsunami bore.

Seeing from Figs. 5.11(a) to 5.11(b), the tail of the *U* velocity distribution (in decreasing time axis) is swelling. A convex curve ($x = -1.2 \sim -1\ \text{m}$) even appears in Fig 5.11(c). The examination of high speed images showed that a more aerated flow was catching up the leading flow. Figures 5.11(e) and 5.11(f) further shows that the more aerated flow merged with the leading flow and appeared a heavy tail in *U* velocity distribution before $t = -0.9\ \text{s}$ comparing to the earlier stages. Videos captured by digital camera from different angles of view can fully explain what creates such signature on the *U* velocity distribution. Upon the wave impingement on the sloping beach, a forward shooting flow, formed upon the contact between breaking wave tongue and beach face, took the lead and propagated toward the structure. Soon or later, the broken wave (more aerated flow) caught up the leading wave before impinging the structure.

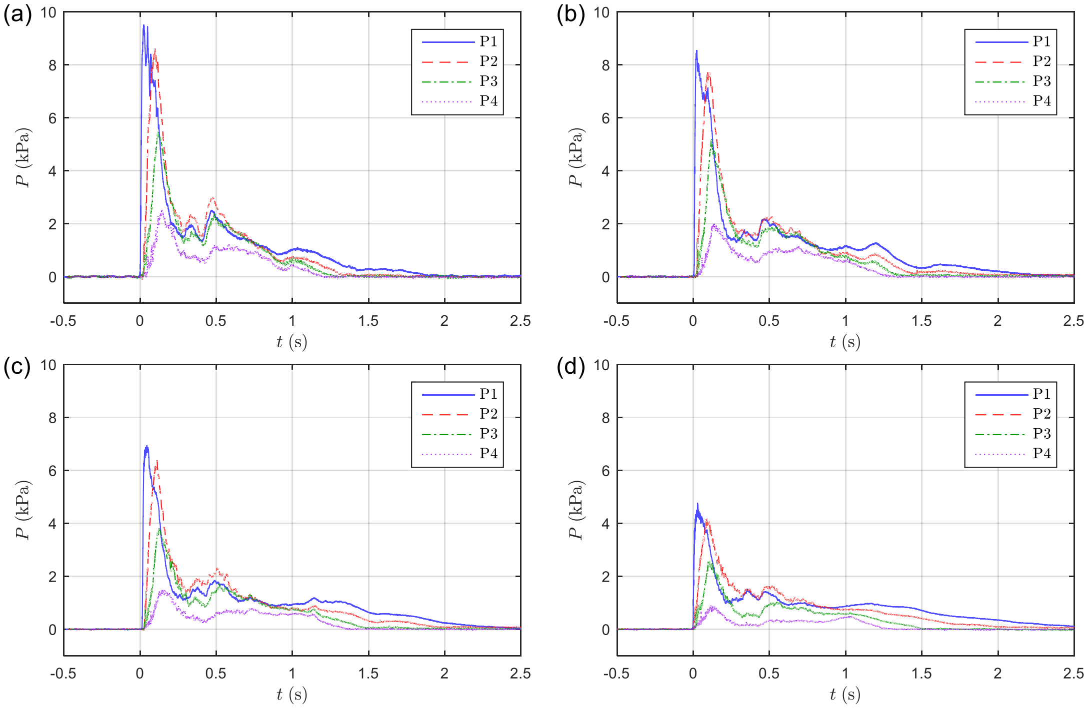

Figure 5.12 Pressure time histories at four elevations for four headings.

5.3.4 Tsunami bore impact pressure

Table 5.4 summarizes the maximum pressure ($P_{\max}$), rise time (t_r), and impulsiveness at four elevations for four different headings. The impulsiveness is a measure proposed by Ariyarathne et al. (2012) to determine if an impact pressure is impulsive (value greater than 100). The impulsiveness is defined as:

$$\left(\frac{P_{\max}}{t_r}\right)\Bigg/\left(\frac{0.5\rho U_{\max}^2}{T}\right) \tag{5-5}$$

where T is the wave period. The T in the present study was estimated by the duration (6 sec) that the wavemaker reached its maximum stroke. From Table 5.4, it can be concluded that only the measurement point at P1 experienced impulsive pressures. Typically, an impulsive impact pressure features a high pressure rising in a very short rise time (Nouri et al. 2010; Kihara et al. 2015), as the *blue lines* at $t = 0$ in Fig. 5.12. In the present study, the rise time (t_r) ranges from 22 ms to 117 ms, and the value increases with higher elevation or larger angle of heading. Maximum pressure measured is 11 kPa, located at P1 at the $\theta_b = 0^\circ$ heading. Figure 5.13 visualizes the vertical distribution of measured pressure maxima for four different headings. The pressure maxima is positively proportional to increasing elevation and angle of heading. Surprisingly, the projected lines of all headings intercept the *z* axis at nearly the same location. In most cases, zero pressure means no contact with flow. The intercept may be related to the maximum height of reverse flow (to be discussed later).

Table 5.4 Summary of pressure measurements and impulsiveness.

Measurement point	z (mm)	θ_b (deg)	$P_{\max}$ (Pa)	t_r (ms)	$\left(\frac{P_{\max}}{t_r}\right) \Big/ \left(\frac{0.5\rho U_{\max}^2}{T}\right)$
P1	20	0	11267	22	290
		15	10068	17	346
		30	8094	30	151
		45	6262	30	120
P2	50	0	9456	75	71
		15	8783	69	72
		30	7111	81	50
		45	4846	87	32
P3	80	0	6449	90	41
		15	5835	96	35
		30	4658	95	28
		45	3374	99	19
P4	110	0	3236	116	16
		15	2808	104	15
		30	2343	117	11
		45	1626	115	8

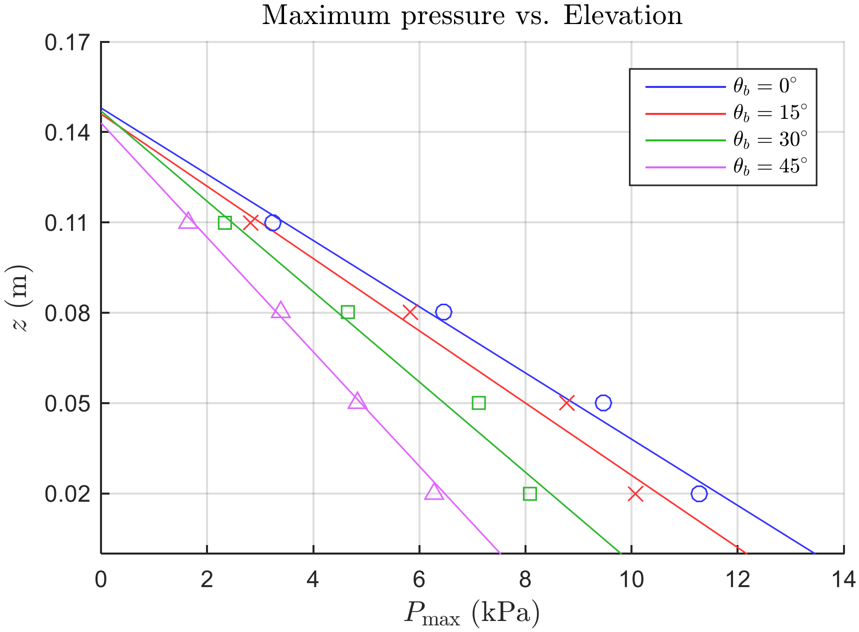

Figure 5.13 Vertical distribution of $P_{\max}$ for four headings.

By correlating the pressure maximum with the local kinetic energy density at the measurement point P1 for four headings, as shown in Fig. 5.14, a linear trend was found, and the slope or so-call impact coefficient is 0.548. Unlike the breaking wave impacts that the impact coefficient can reach up to 90 (Chan and Melville, 1988) due to air compressibility, the air bubbles seems play little role in tsunami bore impact. The use of Bernoulli equation may be valid in evaluating the maximum impact pressure with known velocity and the angle between dominant flow and impact face. However, it should be noticed that the scale effects are not examined in the present study. The further investigation on the scale effects in the future studies are important to confirm the validity of Bernoulli equation for tsunami bore impact pressures at different scales.

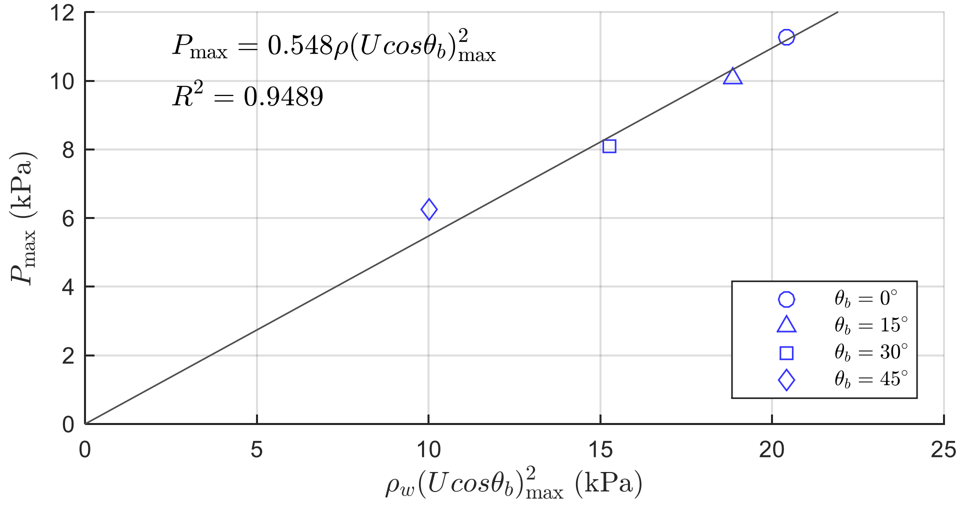

Figure 5.14 Correlation of peak pressure and local kinetic energy density.

5.3.5 Back-calculate the tsunami bore height

To measure the velocity using image-based velocimetry without intrusion and blockage, the bore height measurement was not performed. Nevertheless, the bore height is an important information for estimating the forces acting on the model structure. By simulating the tsunami bore as a dam break flow in open channel, several researchers have proposed a number of empirical equation to estimate bore velocity with measured bore height in a form:

$$U_B = \lambda\sqrt{g_n h_B} \tag{5-6}$$

Shafiei et al. (2016) reported that λ ranges from 0.66 ~ 2.0. With $U_B = 4.29$ m/s, the h_B is estimated as 0.94 ~ 2.84 m. This range is way above the observed h_B (< 0.05 m) estimated from videos. Eq. (5-6) was developed on the basis of breaking wave tsunami intrusion type. This may lead to overestimation in h_B since the run-up velocity is usually much higher in high run-up intrusion type. According to the comparison of measured U velocity profile and dam break flow solution, using Ritter's solution may be valid. According to Ritter (1892), the local bore height can be estimated as:

$$h_B = \frac{1}{9g}\left(2\sqrt{gh_D} - \frac{x_D}{t_D}\right)^2 \tag{5-7}$$

The use of Eq. (5-7) gives $h_B = 0.024\ \mathrm{m}$ at $x_D = 3.37\ \mathrm{m}$ or frontal wall of the model structure. This value is close to the observed but slightly underestimated. As discussed in the previous section, the use of Bernoulli equation may be used as another approach to estimate h_B and the form reads as:

$$P_{\max} = \rho_w g_n h_B + 0.5\rho_w \left(U_B \cos\theta_b\right)^2_{\max} \tag{5-8}$$

The use of Eq. (5-8) gives $h_B = 0.128\ \mathrm{m}$.

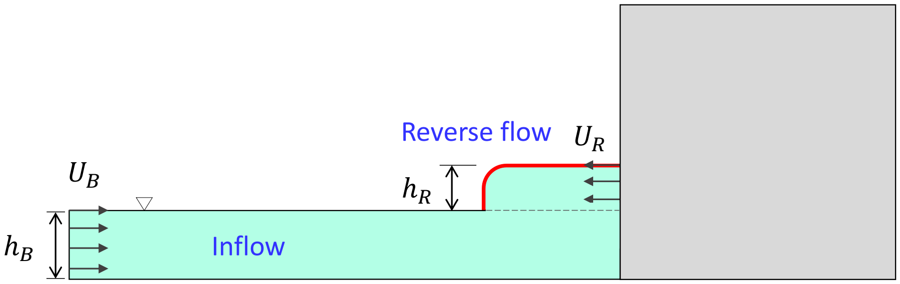

Figure 5.15 Sketch of reverse flow.

Table 5.5 Summary of the height of reverse flow obtained from different approaches.

Approach	h_B (m)
Empirical equation	0.94~2.84
Ritter's solution	0.024
Bernoulli equation (w/o reverse flow)	0.128
Bernoulli equation (w/ reverse flow)	0.041
Observation from videos	< 0.050

Upon the impact, partial water climbed up along the contacted wall face and even bounce off the wall face, creating “reverse flow” as sketched in Fig. 5.15. The reverse flow exerted additional hydrodynamic and hydrostatic pressure. In the present study, the reverse flow velocity (U_R) is very small (< 0.05 m/s) so that the additional pressure can be considered hydrostatically dominant. To estimate the height of reverse flow (h_R), Roberson et al. (2011, 2013) proposed a simple formula on the basis of continuity equation and conservation of momentum:

$$h_R = \left(\frac{U_B h_B}{\sqrt{g}} \right)^{2/3} \tag{5-9}$$

By replacing h_B with h_B + h_R (ponding height) in Eq. (5-8), the h_B was estimated as 0.041 m, which closely matches the observed value. The h_B obtained from different approaches were listed in Table 5.5.

5.3.6 Computation of the streamwise force

In the present study, the estimation of *x*-axis force or surge force (F_X) using measured pressure (sum of hydrostatic and hydrodynamic pressure) can be expressed as:

$$F_X = F_{s,\max} + F_{PS} \tag{5-10}$$

where F_{PS} is the force obtained by the integration of measured pressure, and $F_{s,\max}$ is the maximum static friction force:

$$F_{s,\max} = \mu_{s,\max} m_b g_n \tag{5-11}$$

where $\mu_{s,\max}$ is the maximum static friction force coefficient (measured as 0.971 in the present experiment) and m_b (= 18 kg) is the mass of model structure. As early mentioned, the model structure was attached to the force transducer, and its bottom side was sitting on the sloping beach. The model structure stood still during the impact. However, during the interaction with flow, the non-fixed bottom side more or less contributes the friction force that would be sensed by the model structure as well as the force transducer in positive

x direction upon the impact. As a result, the static friction is not negligible in modeling the surge force.

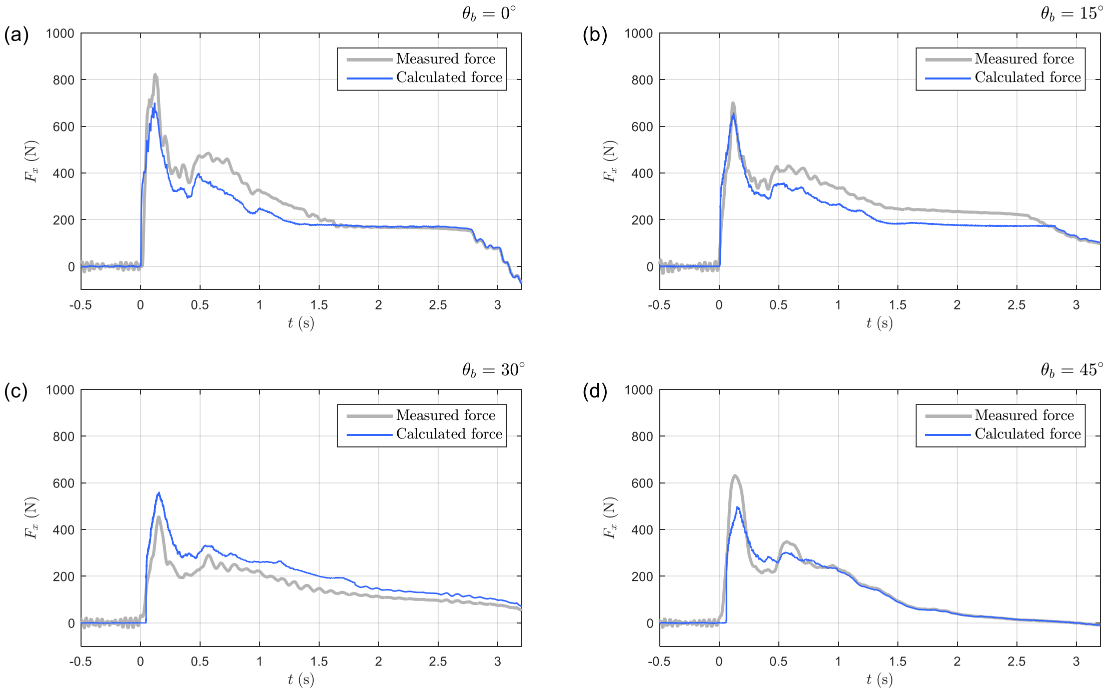

Figure 5.16 Time histories of calculated force and measured force for four headings.

To calculate F_{PS} by integrating the measured pressure, the vertical range covered by pressure sensors were evenly spaced with respect to each sensor's center, and the assumption was made that the pressure in each interval is constant. With the consideration of reverse flow, the vertical range dominated by P4 was extended to the ponding height. For headings $\theta_b = 15^\circ$ and $\theta_b = 30^\circ$, the pressure measurements were only carried out on one of both vertical walls that faced incoming flow. As recalled in Fig. 5.5, the y-axis distribution of the tsunami bore U velocity is uniform. Based on this fact, it may be appropriate to assume that the pressure distribution is uniform over the width of the structure before impingement. As a result, the pressure time histories on the vertical wall face without pressure sensors can be approximated by transforming the measured pressure time histories on another vertical wall faces. At the $\theta_b = 45^\circ$ heading, the pressure and forces are expected to be symmetric with respect to the center line. Therefore, the measured pressure time history on one side can be doubled in magnitude, and the result directly represents the total surge force induced by incoming flow.

Figure 5.16 presents the comparison of measured and calculated F_x time histories for four headings. Overall, the time histories in each comparison set are perfectly in phase, especially at the moment coincident to the peak force. However, at both headings $\theta_b = 0^\circ$ and $\theta_b = 45^\circ$, the calculated peak F_x is roughly 100 N less than the measured one. At the $\theta_b = 15^\circ$ heading, the calculated peak F_x agrees well with the measured one, but at the $\theta_b = 30^\circ$ heading, the calculated peak F_x is even larger by roughly 100 N. Two possible causes may account for the discrepancy:

a) Horizontal variation – a vertical array of pressure measurement at single horizontal point may be unable to represent the surge force variation on *x*-*y* plane. For example, at the $\theta_b = 45^\circ$ heading, the horizontal point on the wall close to the leading edge may sense larger pressure than the present measurement point.

b) Inappropriate formula for estimating the height of reverse flow – The Eq. (5-9) was derived based on the assumption of 1-D potential flow. Table 5.6 lists the calculated and observed ponding heights ($h_R + h_b$). The comparison shows the discrepancy between calculated and observed values, implying that a more suitable formula is needed in accurately predicting the height of reverse flow. Note the observed ponding height was determined by the highest point where waterline could reach on the vertical wall face of the model structure throughout the impact.

Table 5.6 Summary of calculated and observed ponding height ($h_R + h_b$).

θ_b	Calculated h_R+h_b (mm)		Observed h_R+h_b (mm)	
	Long side	Short side	Long side	Short side
0°	240	N/A	313	N/A
15°	235	98	250	125
30°	218	151	208	125
45°	191	191	208	208

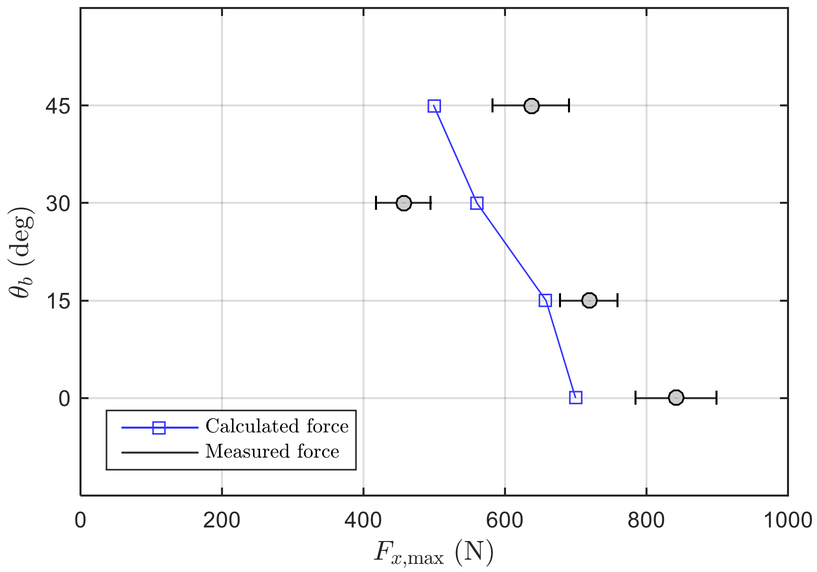

Figure 5.17 Calculated force versus measured force for four headings.

Figure 5.17 compares the measured and calculated F_x for four headings. The maximum peak F_x was measured at the $\theta_b = 0^\circ$ heading, with a magnitude up to 823 N; while the minimum peak F_x 455 N is measured at the $\theta_b = 30^\circ$ heading. The narrow error bars indicates the variation of peak F_x is moderate. The calculated peak F_x is linearly related to the angle of heading. However, the peak F_x for the heading $\theta_b = 30^\circ$ keeps the relation between angle of heading and measured peak F_x from consistent. It fact, it is unexpected that the peak F_x for the $\theta_b = 30^\circ$ heading is lower than that for the $\theta_b = 45^\circ$ heading. It is interesting to give additional attention to the $\theta_b = 30^\circ$ heading in the further studies since the tsunami bore surge force is reduced the most at this heading.

5.4 Conclusions

Measurements, including wave elevation, fluid velocity, impact pressure, forces, were carried out to investigate the flow kinematics and dynamics of a tsunami bore impact on a coastal structure at four different angles of heading on a 1/10 sloping beach. A high run-up tsunami intrusion type was considered in the investigation. The flow patterns were visualized as streamline maps calculated from instantaneous velocity fields determined by the BIV technique. The maximum U and V velocities were measured 4.6 m/s (at the moment of initial impingement on the frontal structure wall at the $\theta_b = 0^\circ$ heading) and 2.79 m/s (at the $\theta_b = 45^\circ$ heading). The maximum turbulence intensity is estimated as $0.39U_{\max}$. The use of the dam break flow solution with the consideration of bed slope (Chanson 2006b) overestimated the measured bore celerity by 19%, implying that friction slope should be considered. The measured U velocity distribution can be well described by the Ritter's solution.

The pressure time histories measured at P1 for different headings were all characterized as impulsive pressure. The largest peak pressure was measured at P1 at the $\theta_b = 0^\circ$ heading, with a magnitude up to 11.3 kPa. The peak pressure and elevation are linearly correlated, and the similar relationship is also found between peak pressure and angle of heading. The correlation between peak pressure and local kinetic energy density shows that the peak pressure caused by tsunami bore impact may be modeled as Bernoulli process. Among four different angles of heading, the maximum peak surge force is 823 N at the $\theta_b = 0^\circ$ heading, while the minimum peak surge force is 455 N at the $\theta_b = 30^\circ$ heading. Furthermore, the surge force is modeled as the sum of the integration of measured pressure and the maximum static friction force. The comparison between calculated and measured surge force shows good agreement. However, the discrepancy in magnitude points out that the horizontal pressure variation may have to be considered and a better formula for estimating the height of reverse flow is desired to accurately model the surge force magnitude.

CHAPTER VI
SUMMARY AND RECOMMENDATIONS FOR FUTURE STUDY

6.1 Summary

This dissertation contains a thorough experimental investigation of extreme waves interacting with coastal and offshore structures by emphasizing hydrodynamics. A general overview as well as the scope of this dissertation was given in CHAPTER I. The concluding remarks of each chapter are as follows.

In CHAPTER II, fluid kinematics of a plunging breaking wave impinging a TLP structure was experimentally studied. The present experiment confirms that the BIV technique is capable of simultaneously measuring structure motion and the fluid velocity in aerated region. The BIV measurement on two perpendicular view planes, side view and top view, was further validated through the comparison of the time histories of maximum U velocity. The flow behavior and dominant velocities at each stage were found similar to those reported by Ryu et al. (2007a) in which a fixed structure under similar wave condition was considered. The average turbulence levels were calculated as 0.16 and 0.18 for the side view measurements and the top view measurements, respectively. In addition, the average ratio k/k' was calculated as 1.35, agreeing with the $k/k' = 1.33$ widely used in two-dimensional breaking wave modeling. By modeling the green water as dam break flow, the comparison suggests that the Ritter solution may be valid in quantitatively describing the velocity distribution of the green water on moving platforms. Based on self-similar velocity profiles, two prediction equations were obtained with coefficients determined by measured data.

In CHAPTER III, by reproducing the identical test conditions performed in CHAPTER II, plunging breaking wave impacts on the frontal wall of a 2D TLP model structure were investigated with simultaneously measured pressure, void fraction, fluid velocity, and structure motion. The time evolutions of pressure and void fraction were exhibited, and the cause of the double-peak in the pressure time histories was elucidated. The examination in histogram suggested that the relative peak pressure may follow the lognormal distribution. A dimensionless formula was proposed to quantify the negative relationship between peak pressure and its corresponding rise time. The correlation between peak pressure and fluid velocity was done by using various approaches. Overall, linear trend was found among all approaches. The value of obtained impact coefficient, whether from instantaneous or ensemble-averaged data, is within the historical range. By modeling the plunging breaking wave impact as a filling flow, the pressure-aeration relationship was examined and compared with approximation solution. The negative correlation indicates that the cushioning effect induced by entrained air bubbles is significant in plunging breaking wave impact. In addition, the portion of compressed air pressure was found proportional to the squared void fraction.

In CHAPTER IV, the green water induced by focusing wave and random waves was experimentally investigated on a fixed offshore platform in a large wave basin. The focusing wave train generated two types of green water event: wall impingement event (wave breaks in front of structure) and deck impingement event (wave breaks onto a deck). Ensemble-averaged pressure, fluid velocity, void fraction, and free surface elevation were obtained from 20 repeated synchronized measurements and image recordings. The time histories of maximum velocities were presented. The relationship between peak impact pressure and rise time was examined and quantified with the dimensionless formula proposed by Chuang et al. (2017). The highest pressure, 11.23 kPa or $0.62\rho_w C_2^2$, was measured in the deck impingement event, at where is the lowest measurement point at mid-deck. The correlation between peak impact pressure and aeration level shows that the effect of entrained air bubbles only applied to the non-breaking overtopping wave in the deck impingement event. For a strong, full-developed green water flow, the gain of peak impact pressure might be associated with higher compressed air pressure. According to the similarity of flow behaviors, random green water events may be divided into three categories: (I) collapse of overtopping wave, (II) fall of bulky water, and (III) breaking wave crest, and Categories I occurred more often than another two combined. By examining the maximum *U* velocity histogram over 179 events, it is concluded that the lognormal distribution may be better used to evaluate the probable maximum *U* velocity for random green water events. A prediction equation was determined based on the self-similarity of green water *U* velocity profiles. In addition, by comparing the measured green water velocity with Ritter's solution, the present study shows that the dam break flow model may be valid to model the green water impacts induced by either focusing breaking wave or random waves.

In CHAPTER V, experimental modeling of a tsunami bore impact on a coastal structure at four different angles of heading on a sloping beach was performed with the consideration of high run-up tsunami inland intrusion type. Repeated measurements of fluid velocities, impact pressure, and forces were carried out to evaluate the ensemble averages. The flow patterns at four different headings were visualized as streamline maps and the comparison was made. The maximum velocities and turbulence intensity were examined, and the peak values were determined. The comparison between measured and calculated bore front celerity implied that considering friction slope is necessary. By modeling the bore as dam break flow, the Ritter's solution fits the measured *U* velocity distribution better than the solution with the consideration of bed slope. Maximum peak impact pressure was measured at where is the lowest measurement point at the $\theta_b = 0^\circ$ heading. The peak impact pressures were found linearly proportional to both elevation and angle of heading. Furthermore, according to the correlation between peak pressure and local kinetic energy density, the Bernoulli equation seems appropriate for predicting the peak pressure due to tsunami bore impact. By modeling the surge force using measured pressure, the calculated value is in good agreement with the measured.

6.2 Recommendations for future study

A measurement technique/tool that is able to quantify violent flows (e.g., impact velocity, overtopping, or run-up) on realistic, mobile offshore platforms under random seas at a general model scale (1:50) is probably the ultimate goal. By achieving a success in applying the BIV technique to a TLP model and to random green water events in a large-scale wave basin, the present study have pushed steps toward the goal. Nevertheless, there are still challenges, such as illumination, triggering, blockage due to geometry, and 3-D structure motion.

In this study the breaking wave impact pressure and air compressibility were investigated at a relatively small scale based on Froude scaling. However, it is known that Froude law does not hold for these two physical quantities. Although there are studies addressing the scaling of wave impact pressure and the effect of compressed air bubbles, more measurements at different scales are still desired to validate the existing theories or propose new mathematical relationships to scale up the wave impact pressures derived from any physical models at laboratory scales.

On the study of the tsunami bore impact on a coastal building, the pressure on the impact side without pressure sensors was approximated by assuming the uniform pressure along the y axis. It is worth confirming the assumption in near future experiment by taking pressure measurements on both impact sides. On the other hand, the present experiment did not account for the horizontal variation of the pressure sensed by the model walls. This might also be the cause that leads to discrepancy between measured and calculated surge force.

The model structure considered in the present investigation on tsunami bore impact was intended for a conceptual study. As a result, a scale-down model for the future study is needed to identify the hydrodynamics that can be incorporated into practical designs. In addition, debris flows and defensive strategies (e.g. plantation) are very important topics and should be considered in the future studies.

REFERENCES

Ariyarathne, K., Chang, K.-A. and Mercier, R., 2012. Green water impact pressure on a three-dimensional model structure. *Exp Fluids*, 53(6): 1879-1894.

Asakura, R. et al., 2000. An experimental study on wave force acting on on-shore structures due to overflowing tsunamis. *Proceedings of Coastal Engineering*, 47: 911-915.

Azarmsa, S.A., Yasuda, T. and Mutsuda, H., 2001. Cause and characteristics of impact pressure exerted by spilling and plunging breakers on a vertical wall. *Coastal Engineering Proceedings* (25).

Bagnold, R.A., 1939. Interim report on wave-pressure research. *Institution of Civil Engineeris*, 12: 201-226.

Bird, P.A.D., Crawford, A.R., Hewson, P.J. and Bullock, G.N., 1998. An instrument for field measurement of wave impact pressures and seawater aeration. *Coast Eng*, 35(1–2): 103-122.

Blackmore, P.A. and Hewson, P.J., 1984. Experiments on full-scale wave impact pressures. *Coast Eng*, 8(4): 331-346.

Bredmose, H., Bullock, G.N. and Hogg, A.J., 2015. Violent breaking wave impacts. Part 3. Effects of scale and aeration. *J Fluid Mech*, 765: 82-113.

Bredmose, H., Peregrine, D.H. and Bullock, G.N., 2009. Violent breaking wave impacts. Part 2: Modelling the effect of air. *J Fluid Mech*, 641: 389-430.

Bryant, E., 2001. Tsunami: The underrated hazard. Cambridge University Press.

Buchner, B., 1995. The impact of green water on FPSO design. *Offshore Technology Conference*, Houston, Texas, USA, pp. 47-57.

Buchner, B. and Bunnik, T., 2007. Extreme wave effects on deepwater floating structures, *Offshore Technology Conference*, Houston, Texas, U.S.A.

Bullock, G.N., Crawford, A.R., Hewson, P.J., Walkden, M.J.A. and Bird, P.A.D., 2001. The influence of air and scale on wave impact pressures. *Coast Eng*, 42(4): 291-312.

Bullock, G.N., Obhrai, C., Peregrine, D.H. and Bredmose, H., 2007. Violent breaking wave impacts. Part 1: Results from large-scale regular wave tests on vertical and sloping walls. *Coast Eng*, 54(8): 602-617.

Cawley, J.G., 2014. Review of guidelines for the design of tsunami vertical evacuation buildings, Oregon State University, 92 pp.

Chan, E.S., Cheong, H.F. and Tan, B.C., 1995. Laboratory study of plunging wave impacts on vertical cylinders. *Coast Eng*, 25(1-2): 87-107.

Chan, E.S. and Melville, W.K., 1988. Deep-water plunging wave pressures on a vertical plane wall. *Proceedings of the Royal Society of London. Series A, Mathematical and Physical Sciences*, 417(1852): 95-131.

Chang, K.A. and Liu, P.L.F., 1999. Experimental investigation of turbulence generated by breaking waves in water of intermediate depth. *Phys Fluids*, 11(11): 3390-3400.

Chang, K.-A., Ariyarathne, K. and Mercier, R., 2011. Three-dimensional green water velocity on a model structure. *Exp Fluids*, 51(2): 327-345.

Chang, K.-A., Lim, H.-J. and Su, C.-B., 2003. Fiber optic reflectometer for velocity and fraction ratio measurements in multiphase flows. *Rev Sci Instrum*, 74(7): 3559-3565.

Chanson, H., 2006a. Tsunami surges on dry coastal plains: Application of dam break wave equations. *Coastal Engineering Journal*, 48(04): 355-370.

Chanson, H., 2006b. Analytical solutions of laminar and turbulent dam break wave. *International Conference on Fluvial Hydraulics River Flow*, Lisbon, Portugal, pp. 465-474.

Chinnarasri, C., Thanasisathit, N., Ruangrassamee, A., Weesakul, S. and Lukkunaprasit, P., 2013. The impact of tsunami-induced bores on buildings. *P I Civil Eng-Mar En*, 166(1): 14-24.

Christensen, E.D., 2006. Large eddy simulation of spilling and plunging breakers. *Coast Eng*, 53(5-6): 463-485.

Chuang, W.-L., Chang, K.-A. and Mercier, R., 2015. Green water velocity due to breaking wave impingement on a tension leg platform. *Exp Fluids*, 56(7): 1-21.

Chuang, W.-L., Chang, K.-A. and Mercier, R., 2016. Impact pressure, void fraction, and green water velocity due to plunging breaking wave impingement on a 2d tension-leg structure. *ASME 2016 35th International Conference on Ocean, Offshore and Arctic Engineering*, Busan, South Korea, pp. V007T06A065.

Chuang, W.-L., Chang, K.-A. and Mercier, R., 2017. Impact pressure and void fraction due to plunging breaking wave impact on a 2d TLP structure. *Exp Fluids*, 58:68.

Cox, D. and Shin, S., 2003. Laboratory measurements of void fraction and turbulence in the bore region of surf zone waves. *Journal of Engineering Mechanics*, 129(10): 1197-1205.

Cross, R.H., 1967. Tsunami surge forces. *Journal of the Waterways and Harbors Division ASCE*, 93(4): 201-231.

Cuomo, G., Allsop, W., Bruce, T. and Pearson, J., 2010b. Breaking wave loads at vertical seawalls and breakwaters. *Coast Eng*, 57(4): 424-439.

Cuomo, G., Allsop, W. and Takahashi, S., 2010a. Scaling wave impact pressures on vertical walls. *Coast Eng*, 57(6): 604-609.

Davis, M.C. and Zarnick, E.E., 1964. Testing ship models in transient waves. *In: Symposium on naval hydrodynamics*, Bergen, Norway, pp. 507.

Efron, B. and Tibshirani, R., 1993. An introduction to the bootstrap. Chapman & Hall, New York.

Fritz, H.M., Synolakis, C.E. and McAdoo, B.G., 2006. Maldives field survey after the December 2004 Indian Ocean Tsunami. *Earthquake Spectra*, 22(S3): 137-154.

Ghobarah, A., Saatcioglu, M. and Nistor, I., 2006. The impact of the 26 December 2004 earthquake and tsunami on structures and infrastructure. *Eng Struct*, 28(2): 312-326.

Goda, Y., 2000. Random seas and design of maritime structures, 2nd edition Advanced Series on Ocean Engineering, 15. World Scientific, pp. 443.

Hamoudi, B. and Varyani, K.S., 1998. Significant load and green water on deck of offshore units/vessels. *Ocean Eng*, 25(8): 715-731.

Hattori, M., Arami, A. and Yui, T., 1994. Wave impact pressure on vertical walls under breaking waves of various types. *Coast Eng*, 22(1–2): 79-114.

Hull, P. and Muller, G., 2002. An investigation of breaker heights, shapes and pressures. *Ocean Eng*, 29(1): 59-79.

Johannessen, T.B., Haver, S., Bunnik, T. and Buchner, B., 2006. Extreme wave effects on deep water TLPs - lessons learned from the Snorre a model tests, DOT Conference, Houston, Texas, U.S.A.

Kihara, N. et al., 2015. Large-scale experiments on tsunami-induced pressure on a vertical tide wall. *Coast Eng*, 99: 46-63.

Kirkgoz, M.S., 1990. An experimental investigation of a vertical wall response to breaking wave impact. *Ocean Eng*, 17(4): 379-391.

Kirkoz, M., 1983. Breaking and run-up of long waves, tsunamis: Their science and engineering. *Proceedings of the 10th IUGG International Tsunami Symposium*, pp.

Kisacik, D., Troch, P. and Van Bogaert, P., 2012. Experimental study of violent wave impact on a vertical structure with an overhanging horizontal cantilever slab. *Ocean Eng*, 49: 1-15.

Kisacik, D., Troch, P., Van Bogaert, P. and Caspeele, R., 2014. Investigation of uplift impact forces on a vertical wall with an overhanging horizontal cantilever slab. *Coast Eng*, 90: 12-22.

Lim, H.-J., Chang, K.-A., Huang, Z.-C. and Na, B., 2015. Experimental study on plunging breaking waves in deep water. *Journal of Geophysical Research: Oceans*, 120(3): 2007-2049.

Lim, H.-J., Chang, K.-A., Su, C.B. and Chen, C.-Y., 2008. Bubble velocity, diameter, and void fraction measurements in a multiphase flow using fiber optic reflectometer. *Rev Sci Instrum*, 79(12): 125105.

Lin, C., Hsieh, S.-C., Kuo, K.-J. and Chang, K.-A., 2008. Periodic oscillation caused by a flow over a vertical drop pool. *Journal of Hydraulic Engineering ASCE*, 134(7): 948-960.

Lin, C., Hsieh, S.-C., Lin, I.-J., Chang, K.-A. and Raikar, R.V., 2012. Flow property and self-similarity in steady hydraulic jumps. *Exp Fluids*, 53(5): 1591-1616.

Lin, P.Z. and Liu, P.L.F., 1998. A numerical study of breaking waves in the surf zone. *J Fluid Mech*, 359: 239-264.

Liu, H. et al., 2013. The 11 march 2011 Tohoku tsunami survey in Rikuzentakata and comparison with historical events. *Pure and Applied Geophysics*, 170(6): 1033-1046.

Lugni, C., Brocchini, M. and Faltinsen, O.M., 2006. Wave impact loads: The role of the flip-through. *Phys Fluids*, 18(12): 122101.

Lugni, C., Brocchini, M. and Faltinsen, O.M., 2010b. Evolution of the air cavity during a depressurized wave impact. Ii. The dynamic field. *Phys Fluids*, 22(5): 056102.

Lugni, C., Miozzi, M., Brocchini, M. and Faltinsen, O.M., 2010a. Evolution of the air cavity during a depressurized wave impact. I. The kinematic flow field. *Phys Fluids*, 22(5): 056101.

Ma, Z.H. et al., 2016. Pure and aerated water entry of a flat plate. *Phys Fluids*, 28(1): 016104.

Matsutomi, H. and Okamoto, K., 2010. Inundation flow velocity of tsunami on land. *Island Arc*, 19(3): 443-457.

Moon, W.C., Tan, K.C. and Lau, T.L., 2014. An experimental study on wave forces of tsunami on simplified onshore buildings at Penang Island, Malaysia. *Journal of Civil Engineering Research*, 4(3a): 164-172.

Mori, N. and Chang, K.-A., 2003. Introduction to MPIV, online PIV software from http://www.Oceanwave.Jp/softwares/mpiv.

Mori, N. and Cox, D.T., 2003. Dynamic properties of green water event in the overtopping of extreme waves on a fixed dock. *Ocean Eng*, 30(16): 2021-2052.

Murty, T.S., 1977. Seismic sea waves: Tsunamis, Dept. of Fisheries and the Environment, Fisheries and Marine Service, Ottawa, Canada.

Na, B., Chang, K.-A., Huang, Z.-C. and Lim, H.-J., 2016. Turbulent flow field and air entrainment in laboratory plunging breaking waves. *Journal of Geophysical Research: Oceans*, 121(5): 2980-3009.

Nielsen, K.B. and Mayer, S., 2004. Numerical prediction of green water incidents. *Ocean Eng*, 31(3-4): 363-399.

Nouri, Y., Nistor, I., Palermo, D. and Cornett, A., 2010. Experimental investigation of tsunami impact on free standing structures. *Coastal Engineering Journal*, 52(1): 43-70.

Ochi, M.K. and Tsai, C.H., 1984. Prediction of impact pressure-induced by breaking waves on vertical cylinders in random seas. *Appl Ocean Res*, 6(3): 157-165.

Oumeraci, H. et al., 2001. Probablilistic design tools for vertical breakwaters. Balkema Publishers, New York.

Palermo, D., Nistor, I., Al-Faesly, T. and Cornett, A., 2012. Impact of tsunami forces on structures: The University of Ottawa experience. *5th International Tsunami Symposium*, pp.

Pedrozo-Acuña, A., de Alegría-Arzaburu, A.R., Torres-Freyermuth, A., Mendoza, E. and Silva, R., 2011. Laboratory investigation of pressure gradients induced by plunging breakers. *Coast Eng*, 58(8): 722-738.

Peregrine, D.H., 2003. Water-wave impact on walls. *Annu Rev Fluid Mech*, 35: 23-43.

Peregrine, D.H. and Kalliadasis, S., 1996. Filling flows, cliff erosion and cleaning flows. *J Fluid Mech*, 310: 365-374.

Peregrine, D.H. and Thais, L., 1996. The effect of entrained air in violent water wave impacts. *J Fluid Mech*, 325: 377-397.

Perlin, M., He, J.H. and Bernal, L.P., 1996. An experimental study of deep water plunging breakers. *Phys Fluids*, 8(9): 2365-2374.

Rahman, S., Akib, S., Khan, M.T.R. and Shirazi, S.M., 2014. Experimental study on tsunami risk reduction on coastal building fronted by sea wall. *Sci World J*.

Ray, S., 2002. Applied photographic optics Taylor & Francis.

Ritter, A., 1892. Fortpflanzung der wasserwellen. *Vereine Deutscher Ingenieure Zeitswchrift*, 36(33): 947-954.

Rivillas-Ospina, G., Pedrozo-Acuna, A., Silva, R., Torres-Freyermuth, A. and Gutierrez, C., 2012. Estimation of the velocity field induced by plunging breakers in the surf and swash zones. *Exp Fluids*, 52(1): 53-68.

Robertson, I.N., Paczkowski, K., Riggs, H.R. and Mohamed, A., 2011. Tsunami bore forces on walls. *ASME 2011 30th International Conference on Ocean, Offshore and Arctic Engineering*, Rotterdam, The Netherlands, pp. 395-403.

Robertson, I.N., Paczkowski, K., Riggs, H.R. and Mohamed, A., 2013. Experimental investigation of tsunami bore forces on vertical walls. *Journal of Offshore Mechanics and Arctic Engineering*, 135(2): 021601-021601-8.

Rudman, M. and Cleary, P.W., 2013. Rogue wave impact on a tension leg platform: The effect of wave incidence angle and mooring line tension. *Ocean Eng*, 61: 123-138.

Ryu, Y. and Chang, K.-A., 2008. Green water void fraction due to breaking wave impinging and overtopping. *Exp Fluids*, 45(5): 883-898.

Ryu, Y., Chang, K.-A. and Lim, H.J., 2005. Use of bubble image velocimetry for measurement of plunging wave impinging on structure and associated greenwater. *Measurement science & technology*, 16(10): 1945-1953.

Ryu, Y., Chang, K.-A. and Mercier, R., 2007b. Application of dam-break flow to green water prediction. *Appl Ocean Res*, 29(3): 128-136.

Ryu, Y.G., Chang, K.-A. and Mercier, R., 2007a. Runup and green water velocities due to breaking wave impinging and overtopping. *Exp Fluids*, 43(4): 555-567.

Schonberg, T. and Rainey, R.C.T., 2002. A hydrodynamic model of green water incidents. *Appl Ocean Res*, 24(5): 299-307.

Shafiei, S., Melville, B.W. and Shamseldin, A.Y., 2016. Experimental investigation of tsunami bore impact force and pressure on a square prism. *Coast Eng*, 110: 1-16.

Shimozono, T. et al., 2012. Propagation and inundation characteristics of the 2011 Tohoku Tsunami on the central Sanriku coast. *Coastal Engineering Journal*, 54(01): 1250004.

Song, Y.K., Chang, K.-A., Ariyarathne, K. and Mercier, R., 2015. Surface velocity and impact pressure of green water flow on a fixed model structure in a large wave basin. *Ocean Eng*, 104: 40-51.

Song, Y.K., Chang, K.-A., Ryu, Y. and Kwon, S.H., 2013. Experimental study on flow kinematics and impact pressure in liquid sloshing. *Exp Fluids*, 54(9): 1-20.

St-Germain, P., Nistor, I., Townsend, R. and Shibayama, T., 2014. Smoothed-particle hydrodynamics numerical modeling of structures impacted by tsunami bores. *J Waterw Port C*, 140(1): 66-81.

Svendsen, I.A., 1987. Analysis of surf zone turbulence. *J Geophys Res-Oceans*, 92(C5): 5115-5124.

Takahashi, S. et al., 2011. Urgent survey for 2011 great east japan earthquake and tsunami disaster in ports and coasts - Part I (tsunami), English Abstract Technical Note, No. 1231, Port and Airport Research Institute (PARI), Yokosuka, Japan.

Thusyanithan, N.I. and Madabhusi, S.P.G., 2008. Tsunami wave loading on coastal houses: A model approach. *P I Civil Eng-Civ En*, 161(2): 77-86.

Tomita, T., Imamura, F., Arikawa, T., Yasuda, T. and Kawata, Y., 2006. Damage caused by the 2004 Indian Ocean tsunami on the southwestern coast of Sri Lanka. *Coastal Engineering Journal*, 48(02): 99-116.

Veldman, A.E.P. et al., 2011. Extreme wave impact on offshore platforms and coastal constructions. *ASME 2011 30th International Conference on Ocean, Offshore and Arctic Engineering*, Rotterdam, The Netherlands, pp. 365-376.

Wang, D.W., Mitchell, D.A., Teague, W.J., Jarosz, E. and Hulbert, M.S., 2005. Extreme waves under hurricane Ivan. *Science*, 309(5736): 896-896.

Weggel, J.R. and Maxwell, H.C., 1970. Numerical model for wave pressure distributions. *Journal of the Waterways, Harbors, and Coastal Engineering Division*, 96: 623-642.

Wood, D.J., Peregrine, D.H. and Bruce, T., 2000. Wave impact on a wall using pressure-impulse theory. I: Trapped air. *Journal of Waterway Port Coastal and Ocean Engineering ASCE*, 126(4): 182-190.

Wuebbles, D.J., Kunkel, K., Wehner, M. and Zobel, Z., 2014. Severe weather in United States under a changing climate. *Eos, Transactions American Geophysical Union*, 95(18): 149-150.

Xu, L. and Barltrop, N., 2008. Bow impact loading on FPSOs 2—theoretical investigation. *Ocean Eng*, 35(11–12): 1158-1165.

Xu, L., Barltrop, N. and Okan, B., 2008. Bow impact loading on FPSOs 1—experimental investigation. *Ocean Eng*, 35(11–12): 1148-1157.

Yeh, H., 2007. Design tsunami forces for onshore structures. *Journal of Disaster Research*, 2(6): 531-536.

Yeh, H.H., 1991. Tsunami bore runup. *Natural Hazards*, 4(2): 209-220.

Zhou, D., Chan, E.S. and Melville, W.K., 1991. Wave impact pressures on vertical cylinders. *Appl Ocean Res*, 13(5): 220-234.

APPENDIX A

Time evolution of the velocity maps of the tsunami bore impingements on a stationary cubic coastal structure at four different headings.

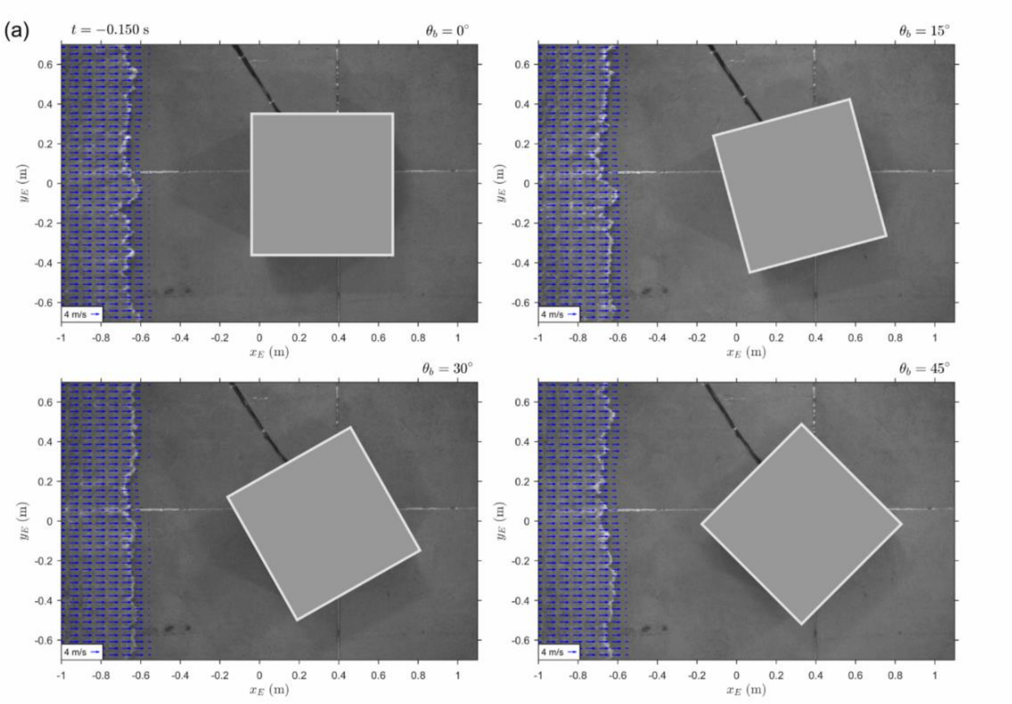

Figure A-1 Velocity maps at (a) *t* = -0.15 s, (b) *t* = -0.05 s, (c) *t* = 0.07 s, (d) *t* = 0.15 s, (e) *t* = 0.20 s, (f) *t* = 0.33 s.

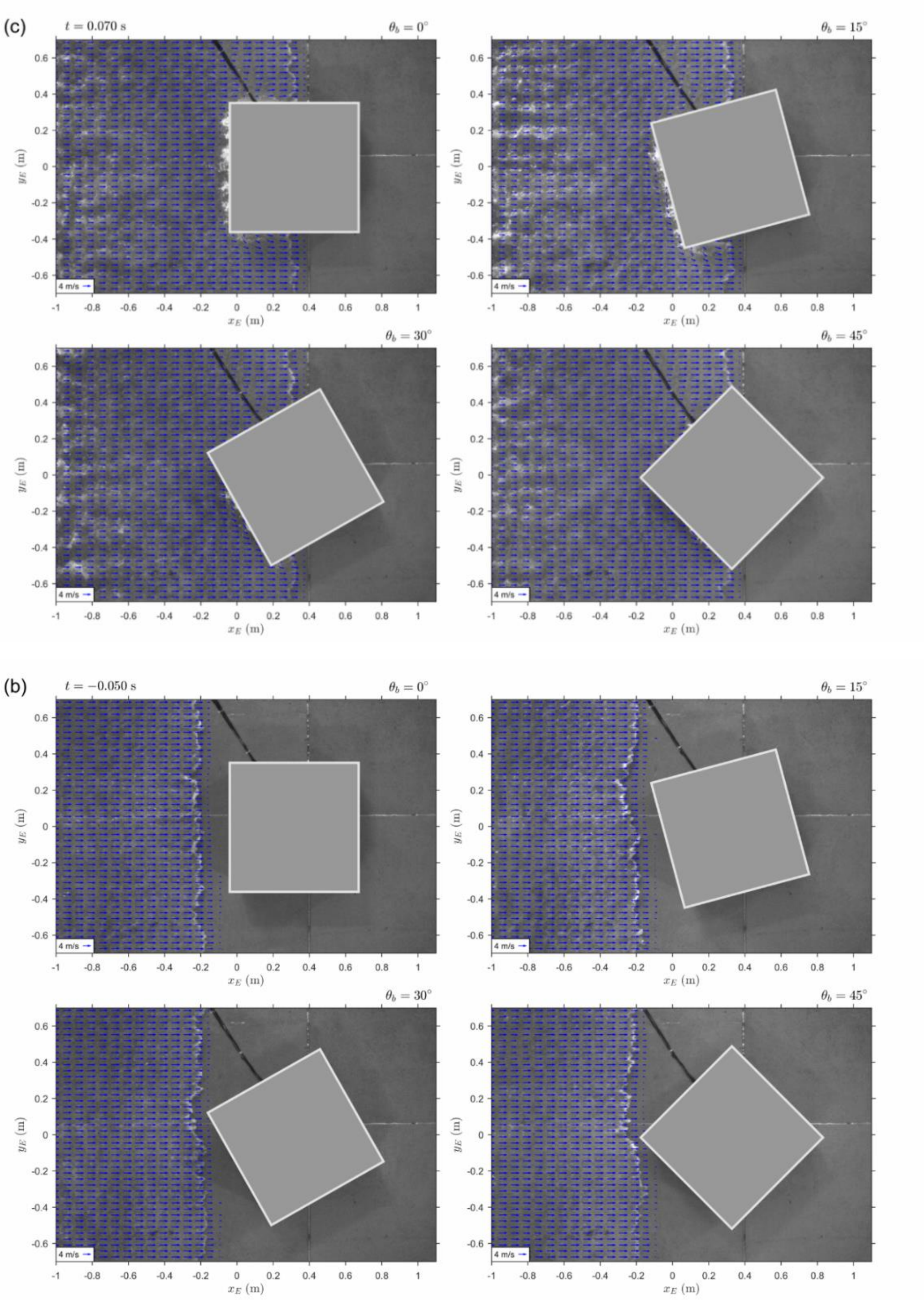

A-1 Continued.

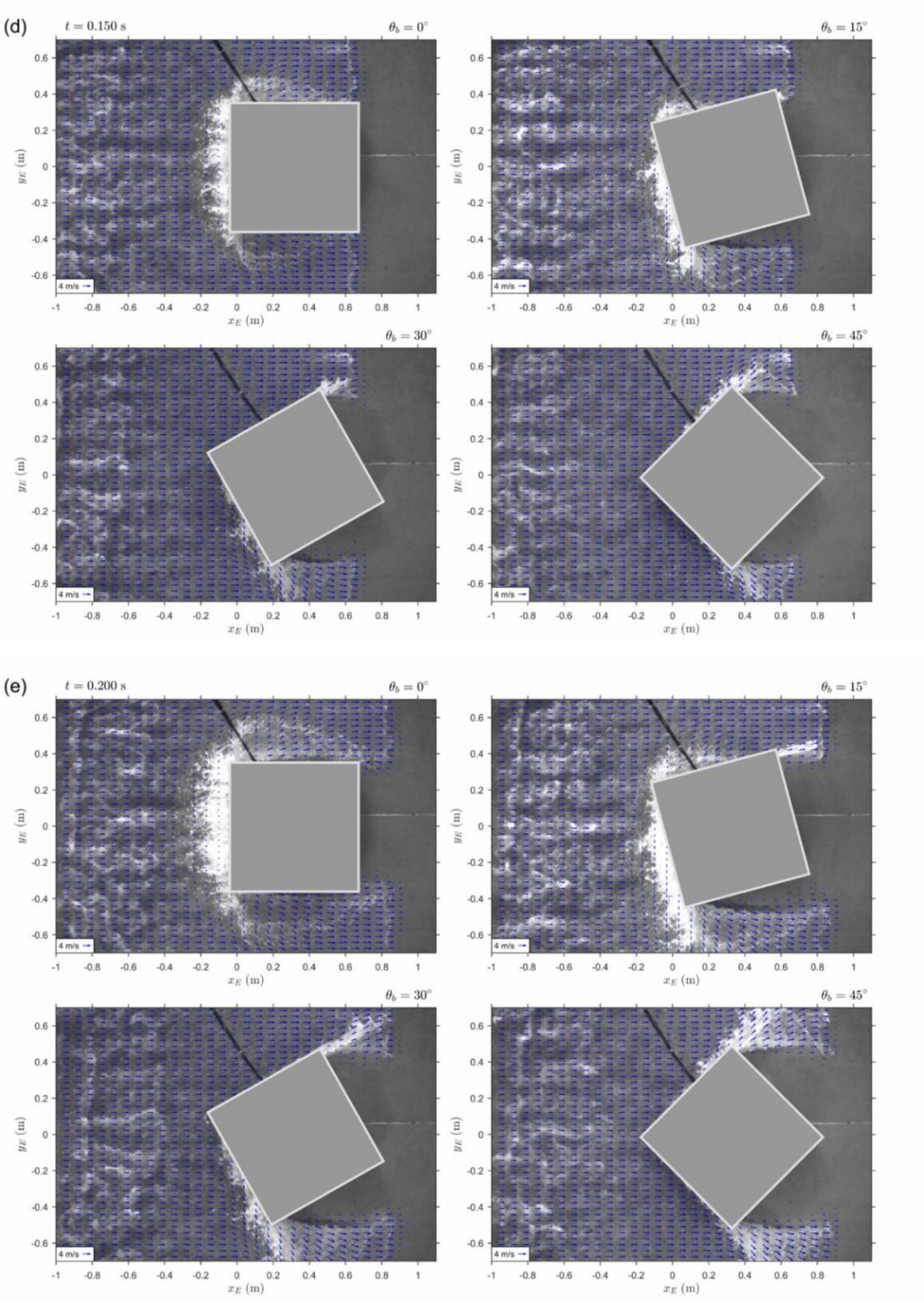

A-1 Continued.

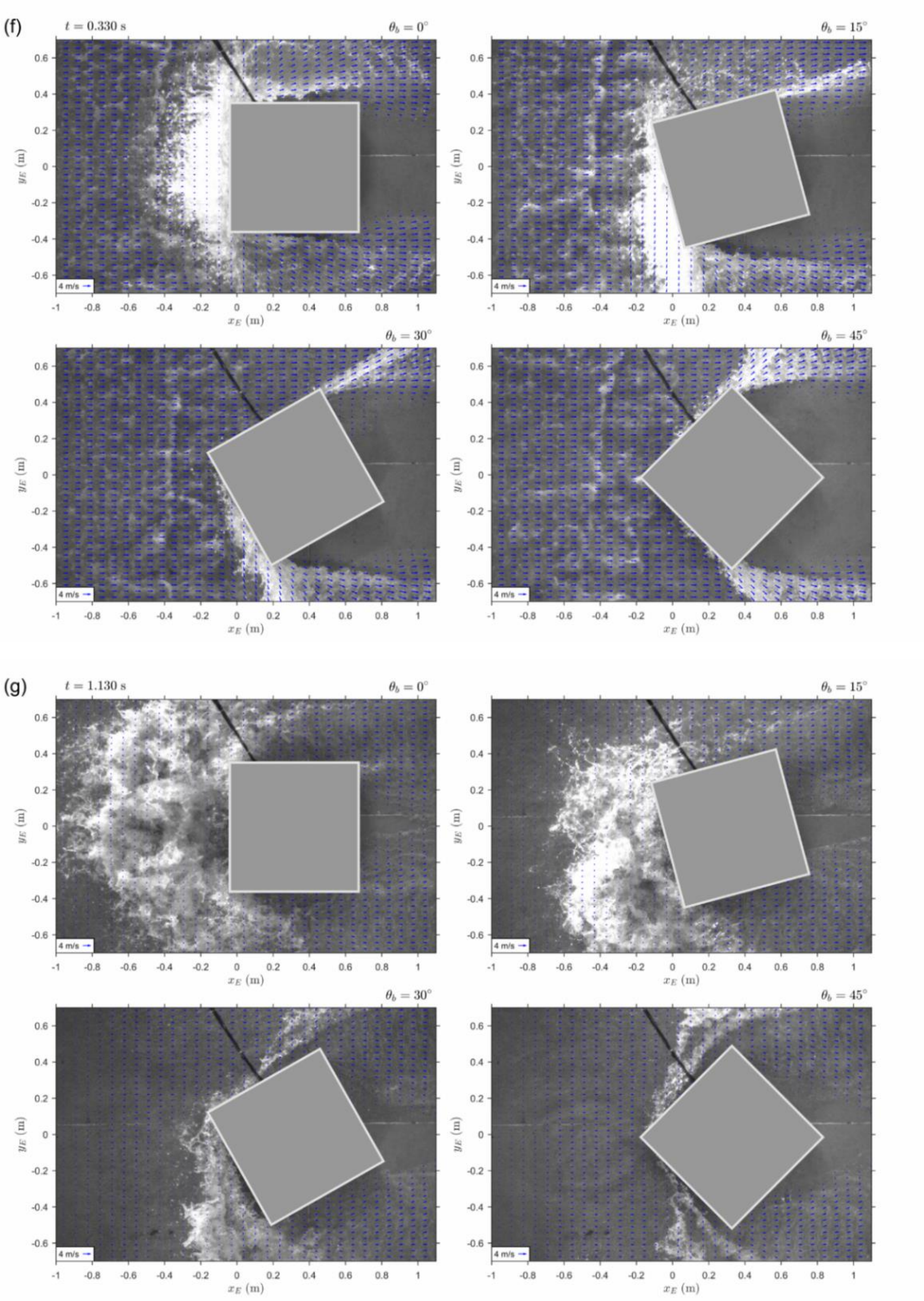

A-1 Continued.

APPENDIX B

The figure below shows the comparison of tsunami bore impact force (surge force only) between measured result and the calculated results with and without consideration of reverse flow. The comparison indicates that the consideration of reverse flow not only affects magnitude but also shift the time moment of peak force close to the measured one.